



## Tesis Doctoral

# The dynamics of small bodies suspended in low Reynolds number flows: Applications in physics and biology.

Idan Tuval Gefen

*Departament de Física*  
*Universitat de les Illes Balears*

June 1, 2005

La presente Tesis Doctoral ha sido dirigida  
por el Doctor Oreste Piro



# Contents

<b>1 Eureka</b>	<b>5</b>
<b>2 Passive bodies:</b>	<b>25</b>
2.1 Introduction . . . . .	25
2.2 The Equation of Motion . . . . .	27
2.2.1 Inertial Particles: Massive Passive Scalars . . . . .	28
2.2.2 Neutrally Buoyant Particles . . . . .	30
2.3 Three-dimensional unsteady flows and Liouvillian maps . . . . .	37
2.4 Opening Three-Dimensional Flows . . . . .	45
2.5 Bailout Embeddings . . . . .	53
2.6 The Bailout Embedding in Three Dimensional Flows . . . . .	58
2.7 Noisy Bailout Embeddings . . . . .	62
2.8 Bifurcations in Bailout Embedding . . . . .	67
2.8.1 Bubbling and blowout bifurcations . . . . .	69
2.8.2 Bailout effect and blowout bifurcation . . . . .	71
2.8.3 Blowout bifurcations in the presence of noise: Bubbling and avoidance . . . . .	74
2.9 Conclusions . . . . .	78
<b>3 Growing bodies: Symmetry Breaking in Stirred Crystalliza- tion.</b>	<b>81</b>
3.1 Introduction . . . . .	81
3.2 Secondary Nucleation . . . . .	84
3.3 Symmetry breaking . . . . .	86
3.4 The Model . . . . .	88
3.5 Comparison With Experiments: Whisker Crystals . . . . .	95
3.6 Conclusions . . . . .	98
<b>4 Biological bodies: Left Hand – Right Hand.</b>	<b>101</b>
4.1 Introduction . . . . .	101
4.2 Left – Right Pattering . . . . .	103
4.3 Hydrodynamic considerations . . . . .	108
4.4 The Model . . . . .	109
4.5 Comparison With Experiments . . . . .	114
4.6 In vivo vs. In vitro . . . . .	116

---

4.7	Symmetry breaking . . . . .	119
4.8	Conclusions . . . . .	123
<b>5</b>	<b>Living bodies: Bacterial Swimming and Oxygen Transport Near Contact Lines.</b>	<b>129</b>
5.1	Introduction . . . . .	129
5.2	Materials and Methods . . . . .	134
5.3	Results . . . . .	135
5.4	Mathematical Model . . . . .	137
5.5	Comparison With Experiments . . . . .	138
5.6	Chemotactic Singularity . . . . .	141
5.7	Conclusions . . . . .	144
5.8	Appendix . . . . .	145
<b>6</b>	<b>Forced bodies: The Control of Particles in Micro – electrode Devices.</b>	<b>147</b>
6.1	Introduction . . . . .	147
6.2	The Device . . . . .	149
6.3	Electro-Thermal-Hydrodynamics . . . . .	151
6.4	The Model . . . . .	156
6.5	Results . . . . .	158
6.6	Breaking The Traps . . . . .	160
6.7	Comparison With Experiments . . . . .	162
6.8	Conclusions . . . . .	163
<b>7</b>	<b>Final Remarks</b>	<b>165</b>
	<b>Bibliography</b>	<b>168</b>
	<b>Curriculum vitae</b>	<b>191</b>



# Chapter 1

## Eureka



People have been aware of objects floating (or sinking) on water since before recorded history. It was not until Archimedes of Syracuse came along, that the theory of flotation and the buoyancy principle were defined. The principle called after him is still learned at school by most of us, interested or not in science. And the story I want to start with is one of the most famous scientific stories.

Archimedes was born at Syracuse on the island of Sicily in 287 BC. He is often described as being absentminded, self-absorbed, and somewhat eccentric. Despite these personal attributes, he was recognized in his own time as a genius, and is revered today as one of the greatest figures in the history of science and mathematics. Despite his mathematical skills, Archimedes is perhaps best remembered for an incident involving the crown of King Hiero.

As the story goes, the king of Syracuse had given a craftsman a certain amount of gold to be made into an exquisite crown. When the project was completed, a rumor surfaced that the craftsman had substituted a quantity of silver for an equivalent amount of gold, thereby devaluing the crown and defrauding the king. Archimedes was tasked with determining if the crown was pure gold or not. The Roman architect Vitruvius relates the story:

While Archimedes was considering the matter, he happened to go to the baths. When he went down into the bathing pool he observed that the amount of water which flowed outside the pool was equal to the amount of his body that was immersed. Since this fact indicated the method of explaining the case, he did not linger, but moved with delight, he leapt out of the pool, and going home naked, cried aloud that he had found exactly what he was seeking. For as he ran he shouted in Greek: Eureka! Eureka! (eureka translated is "I have found it").

Although there is speculation as to the authenticity of this story, it remains famous. Probably no other tale in all of science combines the elements of brilliance and bareness quite so effectively. Whether the story is true or not, there is no doubt to the truth of Archimedes understanding of buoyancy.

Here is what Archimedes had found. Since an object immersed in a fluid displaces the same volume of fluid as the volume of the object, it was possible to determine the precise volume of the crown by immersing it in water. After determining the volume of water, a piece of pure gold could easily be made to match the volume of the water, and thus the volume of the crown. In theory, if the volume of the crown and the volume of the gold block are the same, they should also have the same mass. The only reason they would not have the same mass is if one of them was not pure gold. When the two objects were placed in a balance they did not have equal mass. Faced with this evidence the craftsman confessed to his crime.

Extending this idea further, if the mass of the water displaced is greater than the mass of the object, the object will float (Note: this calculation will require that the object be forcibly submerged). If the mass of the water is less than the mass of the object, the object will sink. If by chance the two masses are equal, the object will be suspended in the water at varying depths depending on the initial conditions. Every vessel that has ever sailed on water, every submarine that has ever launched, and in short, all objects that come in contact with a body of water, are governed by the principle of buoyancy defined by the great mind of Archimedes.

Archimedes founded the field of Hydrostatic. His principle gave us the first idea of how a body behaves when immersed in a fluid environment. However, even our daily experience give us the certainty that the behavior of a body in a

fluid media is much more complex than what the static picture describes. More than twenty centuries of further investigation have confirmed the richness of phenomena that conforms such complex scenario.

This Thesis is an exploration of that behavior. The main characters of the research developed here are depicted in Figure. (1.1): a small body of an undetermined shape and characteristic size  $a$ , surrounded by a fluid media of an unspecific nature with density  $\rho$  and dynamic viscosity  $\eta$ , and moving in it with certain velocity  $v$  at low Reynolds number.

This figure has been taken from the famous paper "Life at low Reynolds number" in which Purcell discussed several interesting points about the motion of organisms in that regime. But I find that it is a really good sketch for the core of this Thesis. I will come back to low Reynolds number flows later on, but now I want to focus on the particle velocity  $v$ . As Fig. (1.1) illustrate, we will be considering particles moving with certain velocity  $v$  in a fluid media. Therefore, since fluid motion is present in our problems we will find ourselves forsaking the equilibrium world of Hydrostatic and coming into the reign of Hydrodynamics. Hydrodynamics is the study of the macroscopic physical behavior of moving fluids. The solution of a fluid dynamic problem typically involves calculating various properties of the fluid, such as velocity, pressure, density, and temperature, as functions of space and time. Hydrodynamics has a wide range of applications. It is used, for example, for computing forces and moments on aircrafts or the mass flow of oil through pipelines, for the prediction of weather patterns, etc. But hydrodynamics may be also viewed through a broader scope, since it is sometimes used in fields unrelated to fluids such as traffic engineering, where traffic is often treated as a continuous flowing fluid. Hydrodynamics thus offers a mathematical structure that underlies many practical disciplines which often also embrace empirical and semi-empirical laws, derived from flow measurement, to solve practical problems.

The fundamental axioms of hydrodynamics are the conservation laws, specifically, conservation of mass (written in the form of the continuity equation), conservation of momentum (also known as Newton's second law), and conservation of energy. The conservation laws are based on classical mechanics and they naturally lead to the central equations for fluid dynamics.

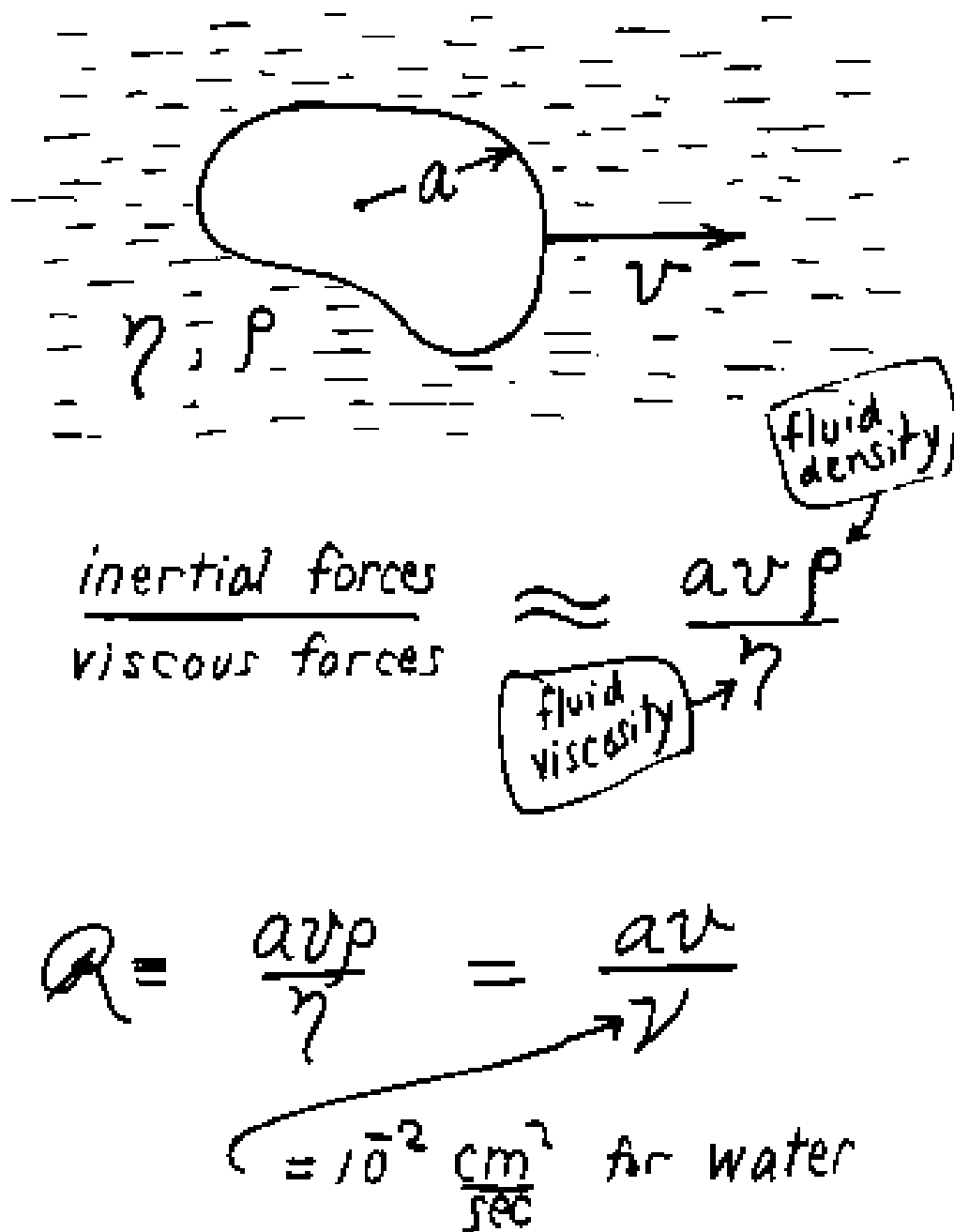


**Figure 1.1:** The dynamics of small bodies suspended in low Reynolds number flows.

---

*The Navier-Stokes equations:*

$$\begin{aligned}\frac{\partial \mathbf{u}}{\partial t} + (\mathbf{u} \cdot \nabla) \mathbf{u} &= -\frac{1}{\rho} \nabla \mathbf{p} + \frac{\eta}{\rho} \nabla^2 \mathbf{u} + \mathbf{f} \\ \frac{\partial \rho}{\partial t} + \rho \nabla \cdot \mathbf{u} &= 0\end{aligned}\tag{1.1}$$

Where:

- $\mathbf{u}$  - is the fluid velocity field,
- $p$  - is the pressure,
- $\eta$  - is the dynamic fluid viscosity,
- $\rho$  - is the fluid density,
- and  $\mathbf{f}$  - are the applied external forces (e.g. gravity).

Named after Claude-Louis Navier and George Gabriel Stokes, the Navier-Stokes equations are non-linear partial differential equations that describe the flow of a fluid whose stress depends linearly on velocity and on pressure. The equations in this raw form do not have a general closed-form solution. It is an open and difficult question whether smooth initial conditions always lead to smooth solutions for all times; it is literally "a million dollar question" since prizes of this size have been offered for the answer to this question. The equations, however, can be simplified in a number of ways to make them easier to solve. Some approximations allow appropriate fluid dynamics problems to be solved in closed form. These solutions depend on the fluid properties (such as viscosity, specific heats, and thermal conductivity), and on the boundary conditions of the domain of study. Representing as they do a general framework for the study of completely different fluids, Navier-Stokes equations have a long variety of interesting limits and simplifications. Several dimensionless numbers characterize those limits. Some of the most used are the following:

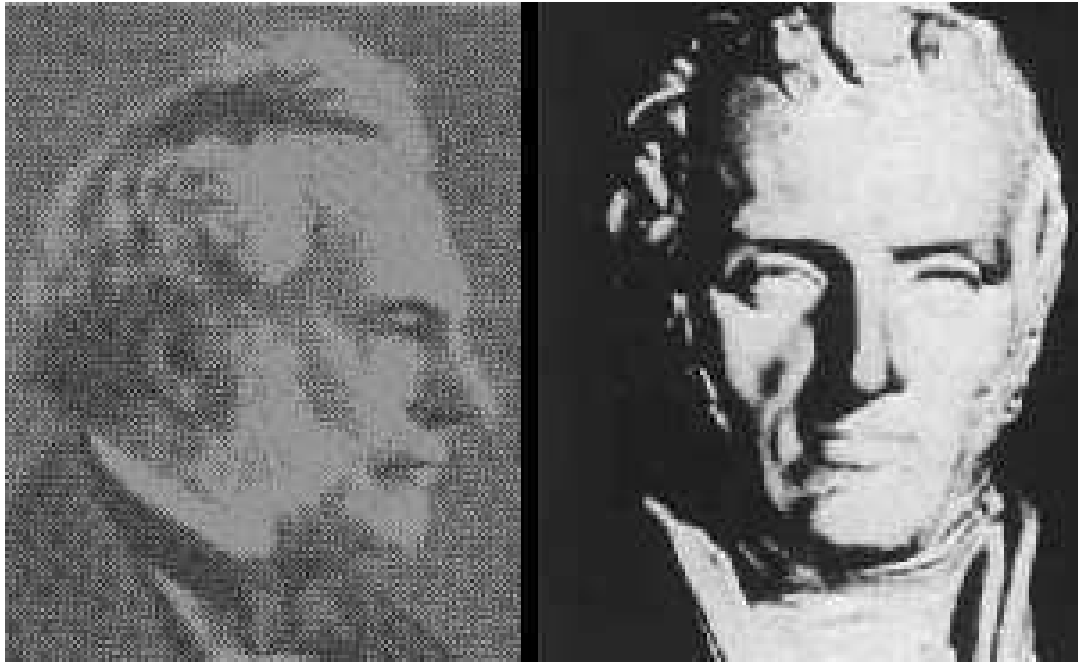


**Figure 1.2:** George Gabriel Stokes and Claude-Louis Navier.

- **COMPRESSIBLE VS INCOMPRESSIBLE FLOW**

A fluid problem is called compressible if changes in the density of the fluid have significant effects on the solution. If the density changes have negligible effects on the solution, the problem is called incompressible and the changes in density are ignored. The incompressible Navier-Stokes equations are simplifications of the Navier-Stokes equations in which the density,  $\rho$ , has been assumed to be constant. The continuity equation (Eq. 1.1b) is then reduced to:

$$\nabla \cdot \mathbf{u} = 0 \quad (1.2)$$

The Mach number,  $Ma$ , represents the balance between inertial forces and compressibility forces, and is defined as:

$$Ma = \frac{U}{c} \quad (1.3)$$

where  $U$  is a characteristic fluid velocity, and  $c$  is the speed of sound in the medium in case.

If the flow has a low Mach number the fluid will behave as being incompressible, i.e. at constant density. It can be shown that the fluctuations

of the density roughly scale with the Mach number squared. Thus already at  $Ma = 0.2$  the density fluctuations are down to less than 5%. The high sound speed of a liquid (because of its high density) results in comparably small Mach numbers in liquid flows. This can be seen as the basic reason why a liquid is less compressible as a gas.

In order to determine whether to use compressible or incompressible fluid dynamics, the Mach number of the problem is evaluated. At standard sea level conditions, Mach 1 is 1,225 km/h in the atmosphere. The incompressibility hypothesis for fluids in motion is only valid when the fluid velocities are much smaller than sound speed ( $Ma \ll 1$ ). Nearly all problems involving liquids as those considered in this thesis, and, in particular most of the fluids related to the process of life are in this regime and can accurately treated as incompressible.

- **STEADY VS UNSTEADY FLOW**

Another simplification of fluid dynamics equations is to set all changes of fluid properties with time to zero. This is called steady flow, and is applicable to a large class of problems, such as lift and drag on a wing or flow through a pipe. The steady fluid condition implies:

$$\frac{\partial \mathbf{u}}{\partial t} = 0 \quad (1.4)$$

Whether a problem is steady or unsteady depends on the frame of reference. For instance, the flow around a ship in a uniform channel is steady from the point of view of the passengers on the ship, but unsteady to an observer on the shore. Fluid dynamicists often transform problems to frames of reference in which the flow is steady in order to simplify the problem.

- **VISCOUS VS INVISCID FLOW**

Viscous problems are those in which fluid friction have significant effects on the solution. Problems for which friction can safely be neglected are called inviscid.

The standard equations of inviscid flow are the Euler equations, result-

ing from the  $\eta = 0$  limit in the Navier-Stokes equation.

$$\frac{\partial \mathbf{u}}{\partial t} + (\mathbf{u} \cdot \nabla) \mathbf{u} = -\frac{1}{\rho} \nabla p + \mathbf{f} \quad (1.5)$$

Another often used model, especially in computational fluid dynamics, is to use the Euler equations far from the body and the boundary layer equations close to the body.

- **NEWTONIAN VS NON-NEWTONIAN FLUIDS**

Sir Isaac Newton showed how stress and the rate of change of strain are very close to linearly related for many familiar fluids, such as water and air. These Newtonian fluids are modelled by a constant viscosity  $\eta$ , which depends on the specific fluid but does not depend on the fluid motion.

However, the viscosity of some fluids that are very important for life, such as milk and blood, and also some plastic solids, depends on the gradient of the velocity. Hence, they present more complicated non-Newtonian stress-strain behaviors. The analysis of this dependence is named *rheology*.

- **LAMINAR VS TURBULENT FLOW**

Turbulence is flow dominated by recirculation, eddies, and apparent randomness. Flow in which turbulence is not exhibited is called laminar. Mathematically, turbulent flow is often represented via Reynolds decomposition where the flow is broken down into the sum of a steady component and a perturbation component. The Reynolds number is the most important dimensionless number in fluid dynamics and provides a criterion for determining dynamic similarity. Where two similar objects in perhaps different fluids with possibly different flow rates have similar fluid flow around them, they are said to be dynamically similar.

Reynolds number is named after Osborne Reynolds (1842-1912), who proposed it in 1883. Typically it is given as follows:

$$Re = \frac{\rho UL}{\eta} \quad (1.6)$$

or

$$Re = \frac{UL}{\nu} . \quad (1.7)$$



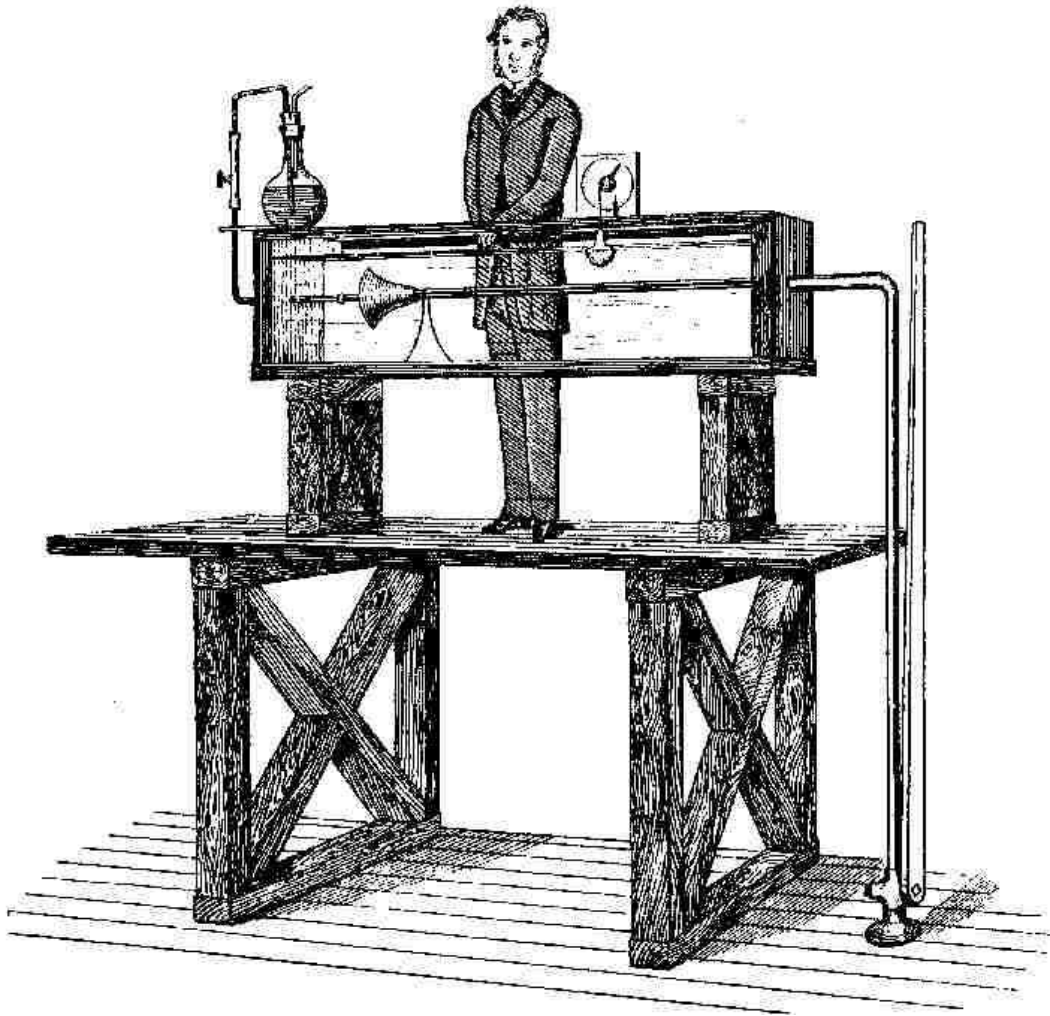


**Figure 1.3:** Osborne Reynolds and his famous experiment.

where  $L$  is a characteristic length and  $\nu$  is the kinematic fluid viscosity ( $\nu = \eta/\rho$ , and it is easier to remember its magnitude for water:  $\nu \approx 10^{-2} \text{cm}^2/\text{sec}$ ). The Reynolds number is used for determining whether a flow will be laminar or turbulent. Laminar flow occurs at low Reynolds numbers, where viscous forces are dominant, and is characterized by smooth, constant fluid motion, while turbulent flow, on the other hand, occurs at high Reynolds numbers and is dominated by inertial forces, producing random eddies, vortices and other flow fluctuations.

High Reynolds numbers indicate that the inertial forces are more significant than the viscous forces. However, even in high Reynolds number regimes certain problems require that viscosity be included. In particu-

lar, problems calculating net forces on bodies (such as wings) should use viscous equations. As illustrated by d'Alembert's paradox, a body in an inviscid fluid will experience no force.

Creeping flow is flow at very low Reynolds numbers ( $Re \ll 1$ ), such that inertial forces can be neglected compared to viscous forces. The simplified equation in the Creeping flow regime is known as the Stokes equation:

$$\nabla \mathbf{p} = \eta \nabla^2 \mathbf{u} + \mathbf{f} \quad (1.8)$$

The transition between laminar and turbulent flow is often indicated by a critical Reynolds number ( $Re_c$ ), which depends on the exact flow configuration and must be determined experimentally. Within a certain range around this point there is a region of gradual transition where the flow is neither fully laminar nor fully turbulent, and predictions of fluid behavior can be difficult. For example, within circular pipes the critical Reynolds number is generally accepted to be 2300, where the Reynolds number is based on the pipe diameter and the mean velocity  $U$  within the pipe, but engineers will avoid any pipe configuration that falls within the range of Reynolds numbers from about 2000 to 4000 to ensure that the flow is either laminar or turbulent.

It is believed that turbulent flows obey the Navier-Stokes equations. Direct numerical simulation, based on the Navier-Stokes and incompressibility equations, makes it possible to simulate turbulent flows with moderate Reynolds numbers (restrictions depend on the power of computer). The results of direct numerical simulation agree with the experimental data.

Only recently has it been generally appreciated that high Reynolds number turbulent flow is not necessary for complex particle trajectories occur in fluid dynamics. It turns out that laminar flow, once thought to have simple dynamics, can instead give rise to chaotic behavior of Lagrangian particle trajectories, even though the Eulerian velocity at any given point in space is fixed or periodic in time. Chaotic advection is the complex behavior a passive scalar a fluid particle, or a passively advected quantity such as temperature or concentration of a second tracer

fluid can attain, driven by the Lagrangian dynamics of the flow. The surprise is that even laminar flow at low Reynolds number is capable of producing such behavior.

- **OTHER APPROXIMATIONS**

There are a large number of other possible approximations to fluid dynamic problems. The Euler equations can be integrated along a streamline to get Bernoulli's equation. When the flow is everywhere irrotational ( $\omega = \nabla \times \mathbf{u} = 0$ ) as well as inviscid, Bernoulli's equation can be used to solve the problem.

The Boussinesq approximation neglects variations in density except to calculate buoyancy forces.

If a problem is incompressible, irrotational, inviscid, and steady, it can be solved using potential flow, governed by Laplace's equation. Problems in this class have elegant solutions which are linear combinations of well-studied elementary flows.

Throughout this Thesis we will assume that the studied fluid flows are incompressible, viscous, Newtonian, laminar, but we will face both steady and unsteady instances. These are realistic simplifications for many real situations and, in particular, they hold accurately for all the problems that we will discuss here. However, some of the phenomena that we will find and explore are not restricted to hold only in this approximation but can be shown to appear in more general flows. Our world here, though, will largely be the world of low Reynolds numbers flows.

When Reynolds number is very small, inertia is negligible and viscous forces play the main rôle. From the definition, low Reynolds number arise in situations where the velocities are small, the viscosity high or the scales small. This is the case in examples ranging from the microscopic world of swimming microorganisms to the macroscopic world of high viscous geological flows. To get useful insight on the Reynolds let us relate it to more intuitive physical quantities. By combining  $\rho$  and  $\eta$  we can obtain, for instance, a force. Indeed, the so called *kinematic viscosity*

$$[\nu] = \left[ \frac{\eta}{\rho} \right] \quad (1.9)$$

has dimensions of  $Length^2/Time$ . Therefore, a characteristic force is:

$$\left[ \frac{\eta^2}{\rho} \right] = Force \quad (1.10)$$

In water,  $\eta \approx 10^{-2}$  and  $\rho \approx 1$ , which implies that this force is  $\simeq 10^{-9}$  Newtons; but the force generated by, for example, a microscopic animal is much less than this, on the order of pico-Newtons. In fact, we can say that  $\eta^2/\rho$  is a force that will tow anything, large or small, but with a Reynolds number of order of magnitude 1. In other words, to tow a submarine with Reynolds number 1 (or strictly speaking  $1/6\pi$  if it were an spherical submarine) it is enough with a force  $10^{-9}$  Newtons in water. It is then clear that small Reynolds numbers are associated with small forces in absolute sense, since no other dimensions come in place. This, in fact, provides an independent measure of the Reynolds number by observing that for a given fluid:

- If the applied force  $\gg$  characteristic force, then Re is high.
- If the applied force  $\ll$  characteristic force, then Re is low.

Since the characteristic force is proportional to  $\eta^2$ , small changes in the viscosity are significant. Changing from water to glycerin means  $\eta$  increases by  $10^3$  and thus the characteristic force increases by  $10^6$ . For further comparison, while in glycerin the low Reynolds number regime holds for objects weighting of the order of less than 10 grams, in molten rock the characteristic force is  $\simeq 10^{36}$  Newtons, large enough to make any object driven by forces of the human range into the low Reynolds number domain. The very flow of the mantle of the Earth is, indeed, one with a very small Reynolds number.

Let us now get into the central problem to which this Thesis is devoted: the motion of bodies through fluids at low Reynolds number regimes. A human body swimming in water might reach a Reynolds number of around  $10^4$ ; a shrimp of reasonable dimensions might instead, swim at about  $Re = 10^2$ . The table in Fig. (1.4) shows some characteristic values for a variety of swimming organisms. Bacteria and other small microorganisms that we will study in this Thesis, swim at Reynolds numbers of about  $10^{-4}$  or  $10^{-5}$ . For these inertia is totally irrelevant, with their micron size they are unable to feel any consequences of the  $F = ma$  Newton's law of motion. In water, where the kinematic viscosity is  $10^{-2}$  cm/sec, these objects move around with a typical speed

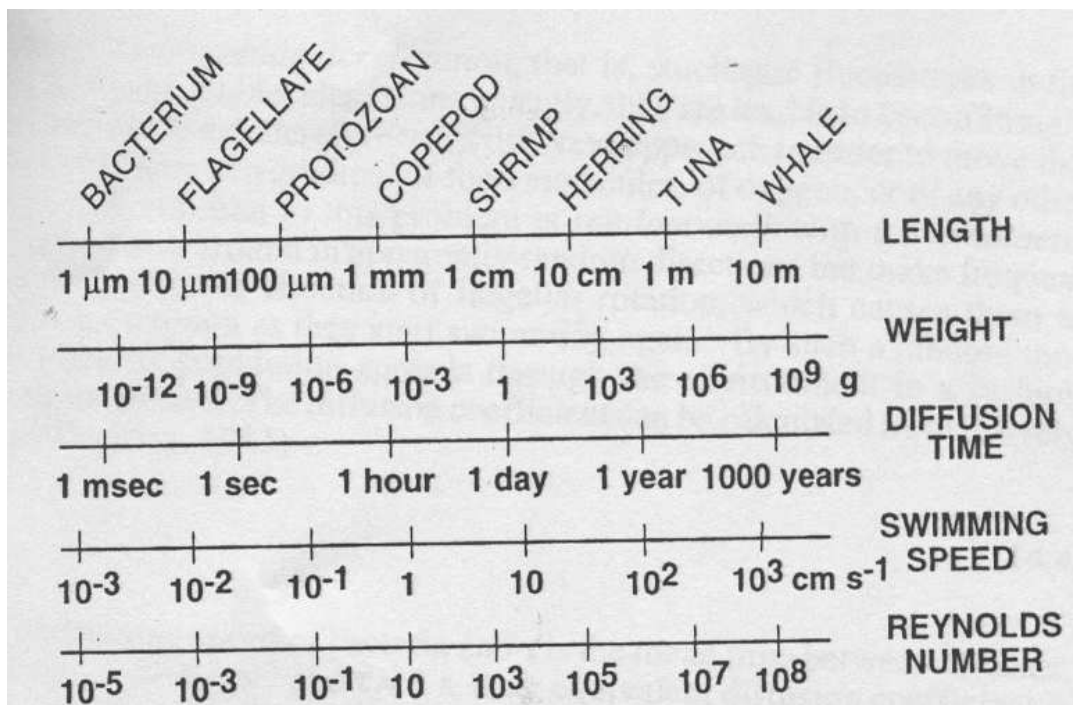


**Figure 1.4:** Size spectrum of living organisms and the biological and physical properties associated with their scale: lengths of typical aquatic organisms (top row), biomasses of these size classes (second row), mean diffusion time of small molecules such as oxygen over the scale of the organisms (third row), typical swimming speeds of aquatic organisms (fourth row), and Reynolds numbers associated with swimming or with fluid flows in the respective scale (bottom row).

of 10 micron/sec. If the force driving such animal to move this way suddenly stops, the small body will only drift an extra distance of about 0.1 angstrom before it comes to a full stop, and this drifting will last no more than about 0.6 microsec. This the fundamental aspect of the extremely low Reynolds number regime: inertia plays no rôle whatsoever. What the bodies are doing at one moment is entirely determined by the forces that are acting on it at that moment, and not by the past state of motion.

In order to gain intuition about the motion in the low Reynolds numbers domain from our perspective of animals dominated by inertia, we can say that swimming at the same Reynolds number as a sperm cell, for instance, would be for us something like swimming in a pool full of molasses and only being allowed to move any part of our body no faster than 1 cm/min. It is worth to mention that if in these conditions we were able to progress say, a meter per day, we would be as an efficient low Reynolds number swimmer as the sperm

is.

Fluid motion at low Reynolds number is normally thought of as slow and regular since they not only imply small velocities but also the absence of turbulence. But the accuracy of this image actually depends on the nature of the features we are concentrating on. As it was mentioned before, chaotic advection makes particle motion and fluid trajectories much more complex than what the fluid velocity field suggests. Chaotic particle trajectories are indeed as usual at low Reynolds number as they are at higher ones. Analogously, while it is true that motion is slow in absolute value, micro swimmers move actually very fast its speed is measured in terms of their own body sizes per time. While a tuna fish swims at ten times its own size per second and a highly trained swimmer, at most, at once her/his own size per second, the typical swimming speed of an unicellular organism is about a hundred times its own body a second.

There is a very important property of the motion at low Reynolds number that is crucial to understand the necessary conditions for a body movement in order to produce a net displacement: low Reynolds number flows are time reversible. This property, straightforwardly obvious from the mathematics of the fluid equations, has impressive consequences that were dramatically demonstrated by Taylor in the educational film "Low Reynolds Number Flows," [177]. In this, blobs of dye as well as rigid and flexible bodies suspended in an annulus of glycerin are set into motion by rotating one of the cylinder walls forming the annulus. Then, the movie shows how the original shape and position of the objects are recovered by simply reversing the rotation of the cylinder as each element retrace its path back to its original position.

This time reversibility has a strong effect on the way an animal can propel itself through a fluid. In a low Reynolds number environment, a creature having a single joint that just allow it to flap in the way a fish does, has a motion pattern that is time reversible, one could not say whether a film of this animal is being run forwards or backwards by just watching the motion of its tail. But since in the world of low Reynolds number the fluid motion is also time reversible, the forward motion produced by one swish of the tail of such fish-like creature is cancelled exactly by the motion produced by the reversed

movement of the tail returning to its initial position. Purcell popularized this phenomenon by stating what is known the "scallop theorem": a scallop, an object with only one joint, cannot swim in a viscous fluid.

The generalization of this particular type of swimming motion is known as a reciprocal motion. In this, the swimming body changes into a certain shape through a sequence of movements and then changes back to the original shape by performing the reversed sequence. But at low Reynolds number everything reverses as well. Moreover, time makes no difference at all, only configuration matters. The pattern of motion is exactly the same no matter how quick or slow the changes are. If in this environment an animal tries to swim by a reciprocal motion, as it happens in the simple example described above the progress that it eventually achieve during the direct sequence will be cancelled by the motion induced by the reversed one. Either fast or slow, it exactly retraces its trajectory and get back to its initial position, unless it moves its parts fast enough to get the Reynolds number higher thus making the inertial terms in the Navier-Stokes equation to play a rôle and achieve propulsion due to the inertial reaction. Therefore, at low Reynolds number, reciprocal motion is futile to swimming. Systems having only one degree of freedom in the configuration space, only one joint for example, are bound to perform reciprocal motion and then, unable to swim. The simplest animal that can swim must be configured with at least two joints. This would allow it to go through a non reciprocal sequence of configurations that return to the original one after a loop in its space of configurations space which is now two dimensional. By performing such loops an animal is now able to swim, i.e, to recover its shape in a translated position. We can see that at low Reynolds number:

Non-reversible motion  $\Leftrightarrow$  Net motion.

This ability constitutes an intriguing instance of a geometrical concept in mechanics known as Non-holonomy; the failure of some systems to recover their original state after a closed excursion in their configuration space.

This discussion provides only a taste of the difficulties in getting ahead in a low Reynolds number regime. The dynamics of swimming is complex enough to warrant material for several Thesis by their own. In this one, however,

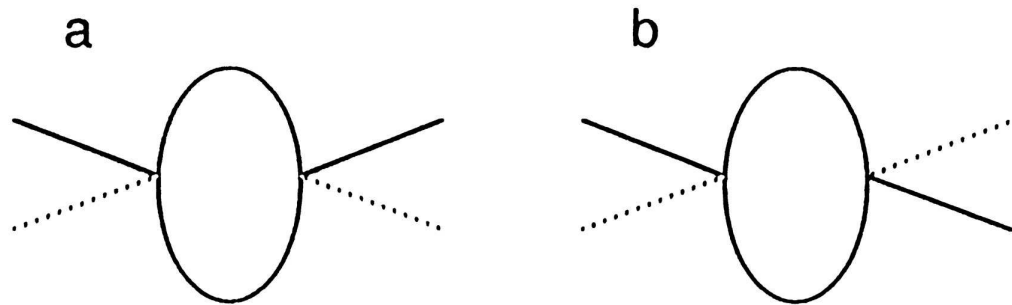


**Figure 1.5:** An organism propelled by two rigid oars. (a) If the organism strokes reciprocally, pulling both oars rapidly downwards, then returning them slowly upwards, and repeating this motion, it could swim upwards if macroscopic but not if microscopic. The position of the oars at the beginning of the power stroke is shown by the solid lines. Their position at the end of the power stroke is shown by the dotted lines. (b) If, instead, the organism stroked cyclically by moving its oars one by one, in the sequence right down, left down, right up, left up, and repeating this motion, it could swim, even if microscopic. The position of the oars at the end of the first step of the cycle is shown by the solid lines.

swimming would be just one more topic on a more general scope of focusing on problems related to transport, growth, reaction, control and mixing of bodies suspended in low Reynolds number fluid flows.

At low Reynolds number mixing also represents a challenge. The condition of no turbulence strongly limits the available mixing strategies. Hence, low Reynolds number flows are a natural instance where the chaotic advection paradigm become very important. Mixing is achieved through the interplay of chaotic advection and molecular diffusion. The relative importance of both mechanisms is characterized by another dimensionless number, the Peclet number:

$$Pe = \frac{UL}{D} \quad (1.11)$$

where  $D$  is the diffusion coefficient. For biological macromolecules like proteins,  $D$  is typically in the range from  $10^{-11}$  to  $10^{-10} \text{ m}^2\text{s}^{-1}$  from which we can estimate a diffusive mixing time as  $\tau_d = L^2/D$ . Mixing by molecular diffusion is generically a slow process. Some realistic values are shown in the third row of Fig. (1.4). Although at the micro scale diffusion is quite fast, the absence of turbulence at low Reynolds number reduces the contact interface through which molecules diffuse. Effective mixing at this scale requires that fluids be manipulated to increase the interfacial surface area between initially distinct fluid regions so that diffusion can complete the mixing process in a reasonable



time. The occurrence of chaotic advection typically indicates rapid distortion and elongation of material interfaces. This process significantly increases the area across which diffusion occurs, which leads to rapid mixing. Nearby particles quickly separate, ideally with an exponential rate, allowing an efficient mixing process in reasonable time scales. The advective contribution to mixing can be controlled by increasing fluid velocities. On the other hand, molecular diffusion is independent of fluid flow and takes place at a rate determined by the diffusivity of the body, which depends on its molecular mass. For a swimmer of micron scale  $L$ , moving at a speed  $U$  of several body lengths per second, and  $D \sim 10^{-5} \text{cm}^2 \text{s}^{-1}$  a solute diffusion constant, we have  $Pe \sim 10^{-2}$ . Therefore, the smallness of the Peclet number expresses the irrelevance of advection compared to diffusion for an isolated micro swimmer. Throughout this Thesis we will show how the opposite is true for many interesting situations such as the collective behavior of micro colonies, or the generation of electro-hydrodynamic flows in micro devices. This last instance constitutes a problem where high Peclet numbers are desirable. In the fast expanding field of miniaturization, mixing of reagents in a microspace is an important task. At the low Reynolds numbers present in those cases, situations where high Peclet numbers are induced must be exploited.

In summary, the space of problems involving bodies suspended in fluids is vast and very complex. This thesis intends to draw a path in this highly dimensional space. It is neither a systematic study trying to cover the whole space nor it is meant to be an exhaustive investigation on each of selected phenomena. Instead, the spirit of this Thesis is to open and follow a trail through a particular set of problems interesting themselves to several different scientific disciplines, but all sharing as a common feature the display of a variety of dynamical phenomena related to the motion of bodies immersed in a flowing fluid. My purpose is that such a trail can lead us uphill in two different directions of increasing complexity, one in sense of the body internal dynamics and the other relative to the body-fluid interaction. Thus my subjects of research went, on one hand, from spherical passive particles, to growing crystals in fluids, to complex molecular machineries and to living organisms. On the other hand, I also went from studying passive transport, to unidirectional body-fluid interaction (either when the body internal dynamics

is influenced by the fluid flow or when a fluid flow is perturbed or generated by the body internal dynamics) to end up considering situations with a bidirectional interaction where the body and the fluid flow are mutually influenced.

The problems that I picked as landmarks of my trail are open questions from completely unrelated fields that include chaotic dynamics, crystallography, microfluidics, developmental embryology and micro-ecology. Therefore these problems also configure the landscape of the Thesis, by illustrating the broad impact of its central theme to such different scientific disciplines.

Because of the multifaceted nature of this task it is impossible to carry it out with only a single research tool. Largely, this Thesis is based on theoretical work, but in some instances direct laboratory experimentation was also included. The mathematical concepts used throughout this Thesis mainly belongs to the theory of dynamical systems. However, at each step, more specific additional tools such as some from classical hydrodynamics, numerical simulations, direct experimentation, agent-based modelling, etc. were needed. In each chapter, any theoretical argument has been compared to numerical simulations of the corresponding models. In most of the cases, theory and models were motivated in experimental facts and the results predicted unobserved behavior that inspired new experiments to confirm them.

During my travel along this rather long path, I have found a large number of interesting side-trips leading to problems that while apparently being not essential for the main purpose of the travel, make it even more interesting and pleasant. Some of them have been worked out and the results included in the corresponding chapters, many others, however, have been left for future research.

The plan of the Thesis is as follows. Chapter. (2) is devoted to study the dynamics of small but finite size particles advected by three dimensional fluid flows. First I give an overview of the state of the knowledge on passive advection in three dimensional laminar flows. Later, the effect of the particle inertia on the dynamics of small neutrally buoyant spherical particles of finite size suspended in fluid flows is reviewed as well as the mathematical concept of bailout embedding of a dynamical system that was developed inspired in such dynamics. I then describe my contribution to the extension of these results to three dimensional volume preserving mappings and flows. The conceptual

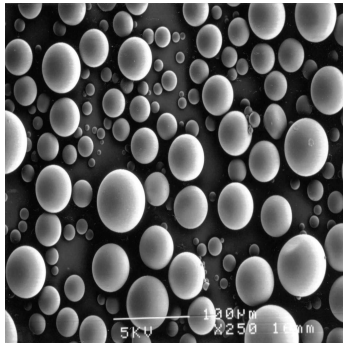
---

connection between the dynamics of the bailout embedding of a Hamiltonian system and the dynamical regimes associated with the occurrence of bubbling and blowout bifurcations are then established and investigated. Finally, as a side dish, we apply the *leaking method* to provide some extra insight into the phase space structures of chaotic 3D incompressible flows. In Chapter. (3) I address some phenomena related to the growth of crystals in a fluid environment subject to continuous stirring. One effect of the stirring on the crystallization of chiral molecules is the breakdown of the chiral symmetry in the distribution of produced crystals. Here, this phenomenon is conjectured to be the consequence of an autocatalytic property, effectively induced by the stirring mediated break up of the primary crystals, in the process of secondary nucleation. Chapter. (4) briefly surveys the the dynamics of cilia and flagella and, in particular, their recently discovered surprising rôle in setting up the vertebrate body plan. It turns out that a unidirectional left-right fluid flow induced by rotating cilia in an embryonal chamber-like structure known as the *node*, has a fundamental rôle in the determination of the left-right asymmetry in the body. However, the hydrodynamics of this flow was puzzling; symmetrically placed rotating cilia were apparently unable to generate such a unidirectional flow. On the basis of a simple model that I constructed with elementary solutions of the Stokes equation known as rotlets, we have conjectured that to generate this flow without a previous chiral-symmetry breaking, the cilia in the node must be tilted towards the posterior side of the embryo. This conjecture has been recently confirmed by experiments. We also discuss how the transport by this flow may lead to asymmetric concentrations of morphogenic substances. Chapter. (5) is devoted to the collective dynamics of swimming bacteria. I describe some of their cooperative behavior when, as a colony, they collaborate to survive in a variable environment. Specifically, I theorize and experiment on the dynamics of aerobic bacteria, namely *Bacillus Subtillis* in the neighborhood of the three-phase contact line in a drop of culture fluid. In these circumstances, the biology of chemotaxis, metabolism, and cell-cell signaling is intimately connected to the physics of buoyancy, diffusion, and mixing. The above mentioned contact line acts as a singular source of fresh oxygen driving the bacteria to crowd around it. We have found an interesting mechanism, the chemotactic analogue of the *Boycott effect* in sedimentation,

by which persistent vortices driven by the swimming bacteria appear. As these vortices favor the distribution of oxygen through the whole colony, we are here in the presence of a physical mechanism naturally connecting the individual behavior to the collective survival strategy. Chapter. (6) addresses the motion and control of particles suspended in micro-flows. Here I focus on the problem of small particles driven by dielectrophoresis, i.e. the force exerted on dielectric particles by nonuniform electric fields, in a micro-channel device built on top of an array of interdigitated micro-electrodes. The applied electric fields, however, normally influence also the state of motion of the fluid generating several types of electro-convective flows. We studied the combined dynamics induced by both electro-convective advection and dielectrophoresis and found dynamically originated traps that constitute an efficient mechanism for control and manipulation at these scales. Finally, in the concluding Chapter. (7), I knot all these different threads together and discuss the possibilities for future work.

# Chapter 2

## Passive bodies:



### 2.1 Introduction

*How complex is the dynamics of a simple spherical particle, passively advected by a laminar fluid flow when its own inertia is also considered? This is the first question that I address in this Thesis. Although this starting question seems to be an apparently solved, old and well-known problem, we will show that it still keeps interesting surprises.*

The development of the equation of motion of spherical particles in fluid flows has been in progress for more than one hundred and fifty years. The first work on the transient equation of motion of a particle appeared two decades before the development of what we now call the Navier–Stokes equations. Poisson [148] examined the potential sinusoidal flow past a rigid sphere. His calculations revealed what we now call the “added mass term” in the equation of motion. Green [76] independently obtained a solution for the potential flow of a rigid ellipse in an infinite fluid and pointed out the added mass component. Stokes [165] developed his theory on the unsteady sinusoidal motion of

a sphere in a viscous fluid as solutions to what we now know as the Stokes equations. Another result of Stokes' pioneering work is the formulation of the steady-state equation of motion of a sphere in a viscous fluid and the expression for the steady-state drag coefficient, which now bears his name. About thirty years after Stokes, Boussinesq [29] developed the mathematical framework and the expression for the unsteady motion of a solid sphere, starting from rest, inside an infinite, viscous and quiescent fluid. The steady-state drag term, the added mass term, and the history integral appear prominently in Boussinesq's expression of the hydrodynamic forces exerted by the fluid. Three years later, Basset [17], apparently unaware of the work by Boussinesq, derived independently the unsteady equation of motion of a sphere under the same conditions. Faxen [66] improved on the equation of motion of a particle by including terms due to the nonuniform fluid velocity field. All this work lead to a fairly well established equation of motion of a sphere in a creeping flow including steady-state drag, history and added mass terms.

Although subsequent and ongoing work has been aiming at the development of equations equally valid at finite Reynolds number, here we will concentrate on the dynamical properties implied by the former. It is apparent that the unsteady hydrodynamic force acting on a particle has a complex form even in the limit of zero Reynolds number. In this first Chapter we will simplify the problem *ad maximum*. The body will be small enough to neglect high order contribution in a perturbative expansion in the fluid-body interaction; it will be spherical in shape to easily evaluate any geometric integral; and we will even assume it to be neutrally buoyant to forget about Arquimedes type terms. Does anything interesting remain in such a problem? We will see next that this is the case. Contradicting the naive intuition, this simple model will show that the trajectories of the neutral spheres separate from those of a corresponding fluid parcel when they visit the most chaotic regions of the flow. These neutral tracers, though, dynamically tend to "escape" from chaos.

At least from the dynamical systems point of view, this surprising fact had a consequence, it inspired the concept of bailout embedding of a Hamiltonian system as a method to target small KAM islands. In this Chapter, we will extend this technique to a class of non-Hamiltonian dynamical systems, namely three-dimensional time-periodic volume preserving maps and

flows. Firstly, we will investigate the qualitative dynamics of small spherical particles in time-periodic flows, three-dimensional, incompressible fluid flows by the artificial embedding of the corresponding stroboscopic map, showing that this approach rightly describe behavior of the complete time-continuous flow. Secondly, we study the effects of noise and fluctuations on the dynamics of such particles, showing that a practical consequence of this analysis is to reveal structures in three-dimensional flows that would be largely hidden to other methods. In fact, we show that intricate but well defined structures may arise in a surprising way in the distribution of particles driven by extremely chaotic flows and the presence of noise. Bailout embedding is thus shown to be amenable to theoretical and experimental analysis of fluid dynamical problems, but the technique has many potential uses in the much broader community of physicists dealing in one way or another with nonlinear dynamical systems.

## 2.2 The Equation of Motion

The dynamics of small spherical particles immersed in a fluid flow have received considerable attention in the past few years from both the theoretical and experimental points of view. On one hand, these particles are the simplest models for impurities whose transport in flows is of practical interest, and, on the other, their motion is governed by dynamical systems that even in the most minimal approximations display a rich and complex variety of behavior. Properties of emulsions, dispersion of contaminants in the atmosphere or the oceans, sedimentation, and mixing, are just a few applications.

The passive advection paradigm assumes that the advected tracers are point-like and take on the velocity of the fluid instantaneously. Depending on the characteristic size of the flow and on the actual size of the tracers (like e.g. in the case of spores, plankton, rain droplets, buoys or ballons) this might turn out to be an oversimplification. A basic finite size effect is that a pronounced deviation appears between the trajectory of the particle and of a neighbouring fluid element. Recent results obtained in the field include the tendency of clustering (attractors), filamentation, transient chaos, and the effect of inertia on reactive processes in flows [180, 23]. When the density of the particles

does not match that of the fluid, it is intuitively clear that the trajectories of a particle and of a fluid parcel will in general differ. This has been demonstrated in two-dimensional flows in which particles with density higher than the basic flow tend to migrate away from the parts of the flow dominated by rotation — in the case of chaotic flows, the KAM (Kolmogorov–Arnold–Moser) islands — while particles lighter than the fluid display the opposite tendency [54, 175]. A more surprising result, however, is that neutrally buoyant particles may also detach from the fluid-parcel trajectories in the regions in which the flow is dominated by strain, to settle in the KAM islands [14]. The subtle dynamical mechanism responsible for the latter phenomenon has suggested the bailout embedding method we will describe in Section. (2) to target KAM islands in Hamiltonian flows and its extension to Hamiltonian maps as well [44].

### 2.2.1 Inertial Particles: Massive Passive Scalars

The equation of motion for a small, spherical tracer in an incompressible fluid may be written as

$$\begin{aligned} \rho_p \frac{d\mathbf{v}}{dt} = & \rho_f \frac{D\mathbf{u}}{Dt} + (\rho_p - \rho_f)\mathbf{g} \\ & - \frac{9\nu\rho_f}{2a^2} \left( \mathbf{v} - \mathbf{u} - \frac{a^2}{6}\nabla^2\mathbf{u} \right) \\ & - \frac{\rho_f}{2} \left( \frac{d\mathbf{v}}{dt} - \frac{D}{Dt} \left[ \mathbf{u} + \frac{a^2}{10}\nabla^2\mathbf{u} \right] \right) \\ & - \frac{9\rho_f}{2a} \sqrt{\frac{\nu}{\pi}} \int_0^t \frac{1}{\sqrt{t-\zeta}} \frac{d}{d\zeta} \left( \mathbf{v} - \mathbf{u} - \frac{a^2}{6}\nabla^2\mathbf{u} \right) d\zeta. \end{aligned} \quad (2.1)$$

$\mathbf{v}$  represents the velocity of the particle,  $\mathbf{u}$  that of the fluid,  $\rho_p$  the density of the particle,  $\rho_f$ , the density of the fluid it displaces,  $\nu$ , the kinematic viscosity of the fluid,  $a$ , the radius of the particle, and  $\mathbf{g}$ , gravity. The derivative  $D\mathbf{u}/Dt$  is along the path of a fluid element

$$\frac{D\mathbf{u}}{Dt} = \frac{\partial\mathbf{u}}{\partial t} + (\mathbf{u} \cdot \nabla)\mathbf{u}, \quad (2.2)$$

whereas the derivative  $d\mathbf{u}/dt$  is taken along the trajectory of the particle

$$\frac{d\mathbf{u}}{dt} = \frac{\partial\mathbf{u}}{\partial t} + (\mathbf{v} \cdot \nabla)\mathbf{u}. \quad (2.3)$$

The terms on the right of Eq. (2.1) represent respectively the force exerted by the undisturbed flow on the particle, buoyancy, Stokes drag, the added mass



due to the boundary layer of fluid moving with the particle, and the Basset–Boussinesq force ([29, 17]) that depends on the history of the relative accelerations of particle and fluid. The terms in  $a^2 \nabla^2 \mathbf{u}$  are the Faxén [66] corrections. Equation (2.1) is derived under the assumptions that the particle radius and its Reynolds number are small, as are the velocity gradients around the particle. The equation is as given by Maxey and Riley [110], except for the added mass term of Taylor [177, 12].

The most general description of the dynamics of these particles presents an enormous richness of phenomena (see, for example, [61, 175, 192, 117]). It is characteristic of the dynamics for small inertia that, in the time-independent case, what were invariant surfaces in the model without inertia are transformed into spirals, due to centrifugal forces. As a consequence, particles tend to accumulate at separatrices of the flow. Except in the proximity of fixed points, the relative velocity of particle and fluid tends to zero at long times. For large inertia, particles are no longer confined within vortices. Stokes drag is the most important force acting in this case, so to a first approximation one can discard the other terms in Eq. (2.1) to obtain

$$\frac{d^2 x}{dt^2} = -\mu \left( \frac{dx}{dt} - u_x(x, y, t) \right), \quad (2.4)$$

$$\frac{d^2 y}{dt^2} = -\mu \left( \frac{dy}{dt} - u_y(x, y, t) \right), \quad (2.5)$$

where we are considering a horizontal layer with  $\mathbf{v} = (dx/dt, dy/dt)$ , and  $\mu = 9\nu\rho_f/(2a^2\rho_p)$ . This is a highly-dissipative and singular perturbation of a Hamiltonian system, with a four-dimensional phase space:

$$\dot{x} = p_x, \quad (2.6)$$

$$\dot{p}_x = -\mu(p_x - u_x(x, y, t)), \quad (2.7)$$

$$\dot{y} = p_y, \quad (2.8)$$

$$\dot{p}_y = -\mu(p_y - u_y(x, y, t)). \quad (2.9)$$

In the time-dependent case, particles tend to accumulate in caustics, which correspond to the chaotic regions of the model without inertia, as the right panel of Fig. 2.1 shows. The relative velocity fluctuates chaotically, due to macroscopic, nonturbulent fluctuations, that act to give the particles deterministic but Brownian-like motion, illustrated in the left panel of Fig. 2.1.

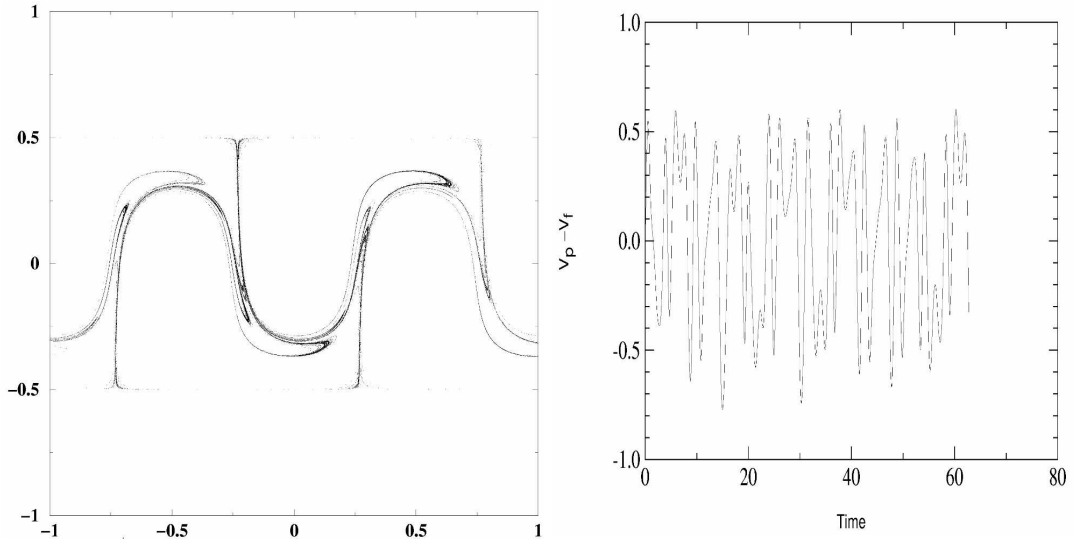


**Figure 2.1:** Right: dense particles collect in fractal structures around a separatrix. Left: in the large inertia limit the relative velocity of particle and flow fluctuates chaotically, in a Brownian-like fashion.

## 2.2.2 Neutrally Buoyant Particles

Let us now consider whether even in the most favourable case of neutral buoyancy a finite sized tracer particle may always be faithful to a flow trajectory. With this in mind, we set  $\rho_p = \rho_f$  in Eq.(2.1). At the same time we assume that it be sufficiently small that the Faxén corrections be negligible. Furthermore we exclude the Basset–Boussinesq term, for we wish to obtain a minimal model ([158, 54]) with which we may perform a mathematical analysis of the problem. If in this model there appear differences between particle and flow trajectories, with the inclusion of further terms these discrepancies will remain or may even be enhanced. If we rescale space, time, and velocity by scale factors  $L$ ,  $T = L/U$ , and  $U$ , we arrive at the expression

$$\frac{d\mathbf{v}}{dt} = \frac{D\mathbf{u}}{Dt} - St^{-1}(\mathbf{v} - \mathbf{u}) - \frac{1}{2} \left( \frac{d\mathbf{v}}{dt} - \frac{D\mathbf{u}}{Dt} \right), \quad (2.10)$$

where  $St$  is the particle Stokes number  $St = 2a^2U/(9\nu L) = 2/9(a/L)^2Re_f$ ,  $Re_f$  being the fluid Reynolds number. The assumptions involved in deriving Eq. (2.1) require that  $St \ll 1$ .

In the past it has been assumed that neutrally buoyant particles have trivial dynamics (e.g., [54, 61]), and the mathematical argument used to back this up is that if we make the approximation  $D\mathbf{u}/Dt = d\mathbf{u}/dt$ , which can be

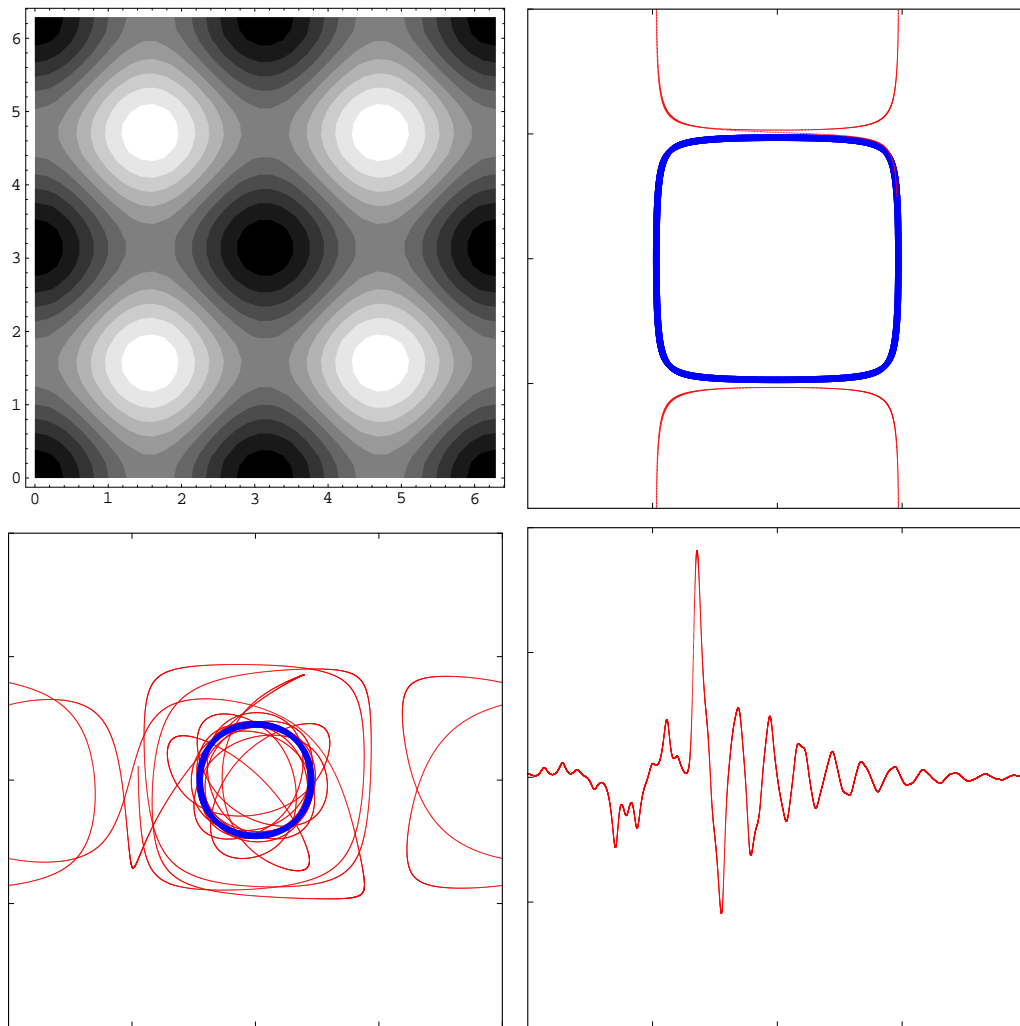


**Figure 2.2:** (Top left) Contour plot illustrating magnitude of  $Q$  — lighter is higher  $Q$  — for the time-independent model Eq. (2.19) (the flow is on a torus). (Top right) The separation of a neutrally buoyant particle trajectory (thin line) from the flow (thick line) in regions of high  $Q$  allows the particle to wander between cells. (Bottom left) After a complicated excursion, a particle (thin line) eventually settles in a zone of low  $Q$  of the flow; a KAM torus (thick line). (Bottom right) The velocity difference  $v_x - u_x$  between the particle and the flow against time.

seen as a rescaling of the added mass, the problem becomes very simple

$$\frac{d}{dt}(\mathbf{v} - \mathbf{u}) = -\frac{2}{3} St^{-1}(\mathbf{v} - \mathbf{u}). \quad (2.11)$$

Thence

$$\mathbf{v} - \mathbf{u} = (\mathbf{v}_0 - \mathbf{u}_0) \exp(-2/3 St^{-1} t), \quad (2.12)$$

from which we infer that even if we release the particle with a different initial velocity  $\mathbf{v}_0$  to that of the fluid  $\mathbf{u}_0$ , after a transient phase the particle velocity will match the fluid velocity,  $\mathbf{v} = \mathbf{u}$ , meaning that following this argument, a neutrally buoyant particle should be an ideal tracer. Although from the foregoing it would seem that neutrally buoyant particles represent a trivial limit to Eq. (2.1), this would be without taking into account the correct approach to the problem that has  $D\mathbf{u}/Dt \neq d\mathbf{u}/dt$ . If we substitute the expressions for the derivatives in Eqs. (2.2) and (2.3) into Eq. (2.10), we obtain

$$\frac{d}{dt}(\mathbf{v} - \mathbf{u}) = -((\mathbf{v} - \mathbf{u}) \cdot \nabla) \mathbf{u} - \frac{2}{3} St^{-1}(\mathbf{v} - \mathbf{u}). \quad (2.13)$$

We may then write  $\mathbf{A} = \mathbf{v} - \mathbf{u}$ , whence

$$\frac{d\mathbf{A}}{dt} = -\left(J + \frac{2}{3} St^{-1} I\right) \cdot \mathbf{A}, \quad (2.14)$$

where  $J$  is the Jacobian matrix — we now concentrate on two-dimensional flows  $\mathbf{u} = (u_x, u_y)$  —

$$J = \begin{pmatrix} \partial_x u_x & \partial_y u_x \\ \partial_x u_y & \partial_y u_y \end{pmatrix}. \quad (2.15)$$

If we diagonalize the matrix we obtain

$$\frac{d\mathbf{A}_D}{dt} = \begin{pmatrix} \lambda - 2/3 St^{-1} & 0 \\ 0 & -\lambda - 2/3 St^{-1} \end{pmatrix} \cdot \mathbf{A}_D, \quad (2.16)$$

so if  $Re(\lambda) > 2/3 St^{-1}$ ,  $\mathbf{A}_D$  may grow exponentially. Now  $\lambda$  satisfies  $\det(J - \lambda I) = 0$ , so  $\lambda^2 - \text{tr}J + \det J = 0$ . Since the flow is incompressible,  $\partial_x u_x + \partial_y u_y = \text{tr}J = 0$ , thence  $-\lambda^2 = \det J$ . Given squared vorticity  $\omega^2 = (\partial_x u_y - \partial_y u_x)^2$ , and squared strain  $s^2 = s_1^2 + s_2^2$ , where the normal component is  $s_1 = \partial_x u_x - \partial_y u_y$  and the shear component is  $s_2 = \partial_y u_x + \partial_x u_y$ , we may write

$$Q = \lambda^2 = -\det J = (s^2 - \omega^2)/4, \quad (2.17)$$

where  $Q$  is the Okubo–Weiss parameter ([129, 189]). If  $Q > 0$ ,  $\lambda^2 > 0$ , and  $\lambda$  is real, so deformation dominates, as around hyperbolic points, whereas if

$Q < 0$ ,  $\lambda^2 < 0$ , and  $\lambda$  is complex, so rotation dominates, as near elliptic points. Equation (2.14) together with  $d\mathbf{x}/dt = \mathbf{A} + \mathbf{u}$  defines a dissipative dynamical system

$$d\boldsymbol{\xi}/dt = \mathbf{F}(\boldsymbol{\xi}) \quad (2.18)$$

with constant divergence  $\nabla \cdot \mathbf{F} = -4/3 St^{-1}$  in the four dimensional phase space  $\boldsymbol{\xi} = (x, y, A_x, A_y)$ , so that while small values of  $St$  allow for large values of the divergence, large values of  $St$  force the divergence to be small. The Stokes number is the relaxation time of the particle back onto the fluid trajectories compared to the time scale of the flow — with larger  $St$ , the particle has more independence from the fluid flow. From Eq. (2.16), about areas of the flow near to hyperbolic stagnation points with  $Q > 4/9 St^{-2}$ , particle and flow trajectories separate exponentially.

To illustrate the effects of  $St$  and  $Q$  on the dynamics of a neutrally buoyant particle, let us consider a simple incompressible two-dimensional model flow defined by the stream function

$$\psi(x, y, t) = A \cos(x + B \sin \omega t) \cos y. \quad (2.19)$$

The equations of motion for an element of the fluid will then be  $\dot{x} = \partial_y \psi$ ,  $\dot{y} = -\partial_x \psi$ . As we observed earlier,  $\psi$  has the rôle of a Hamiltonian for the dynamics of such an element, with  $x$  and  $y$  playing the parts of the conjugate coordinate and momentum pair. Let us first consider the simplest case where the time dependence is suppressed, by setting  $B = 0$ . Thence  $\psi$  should be a constant of motion, which implies that real fluid elements follow trajectories that are level curves of  $\psi$ . In Fig. 2.2 are depicted contours of  $Q$ . Notice that the high values of  $Q$  are around the hyperbolic points, while negative  $Q$  coincides with the centres of vortices — elliptic points — in the flow. Figure 2.2 (top right) shows the trajectory of a neutrally buoyant particle starting from a point on a fluid trajectory within the central vortex, but with a small velocity mismatch with the flow. This mismatch is amplified in the vicinity of the hyperbolic stagnation points where  $Q$  is larger than  $4/9 St^{-2}$  to the extent that the particle leaves the central vortex for one of its neighbours, a trip that is not allowed to a fluid parcel. In the end a particle settles on a trajectory that does not visit regions of high  $Q$ , proper for a fluid parcel. While this effect is already seen at top right in Fig. 2.2b, it is more dramatically pictured in the trajectory

shown at bottom left, in which the particle performs a long and complicated excursion wandering between different vortices before it settles in a region of low  $Q$  of one of them. To illustrate the divergence of particle and fluid trajectories, and the fact that particle and fluid finally arrive at an accord, at bottom right we display the difference between the particle velocity and the fluid velocity at the site of the particle against time for this case. Notice that this difference seems negligible at time zero, and that it also converges to zero at long times, but during the interval in which the excursion takes place it fluctuates wildly.

Even more interesting is the case of time-dependent flow:  $B \neq 0$  in the above model. As in a typical Hamiltonian system, associated with the original hyperbolic stagnation points, there are regions of the phase space, which is here real space, dominated by chaotic trajectories. Trajectories of this kind, stroboscopically sampled at the frequency of the flow, are reproduced in Fig. 2.3. Such trajectories visit a large region of the space, which includes the original hyperbolic stagnation points and their vicinities where  $Q$  is large. Excluded from the reach of such a chaotic trajectory remain areas where the dynamics is regular; the so-called KAM tori. In the model these lie in the regions where  $Q < 4/9 St^{-2}$ . Now a neutrally buoyant particle trying to follow a chaotic flow pathline would eventually reach the highly hyperbolic regions of the flow. This makes likely its separation and departure from such a pathline, in search of another pathline to which to converge. However, convergence will only be achieved if the pathline never crosses areas of high  $Q$ . Figure 2.3 demonstrates this phenomenon: a particle was released in the chaotic zone with a small velocity mismatch. The particle followed the flow, until, coming upon a region of sufficiently high  $Q$ , it was thrown out of that flow pathline onto a long excursion that finally ended up in a regular region of the flow on a KAM torus. The regular regions of the flow then constitute attractors of the dissipative dynamical system Eq. (2.18) that describes the behaviour of a neutrally buoyant particle. The chaotic trajectories in a Hamiltonian system are characterized by positive Lyapunov exponents. The Lyapunov exponents are an average along the trajectory of the local rate of convergence or divergence. Such a rate is measured by the quantity  $\lambda$ . Hence, for a trajectory to be chaotic, it is a necessary condition that it visit regions of positive  $Q$ : an upper

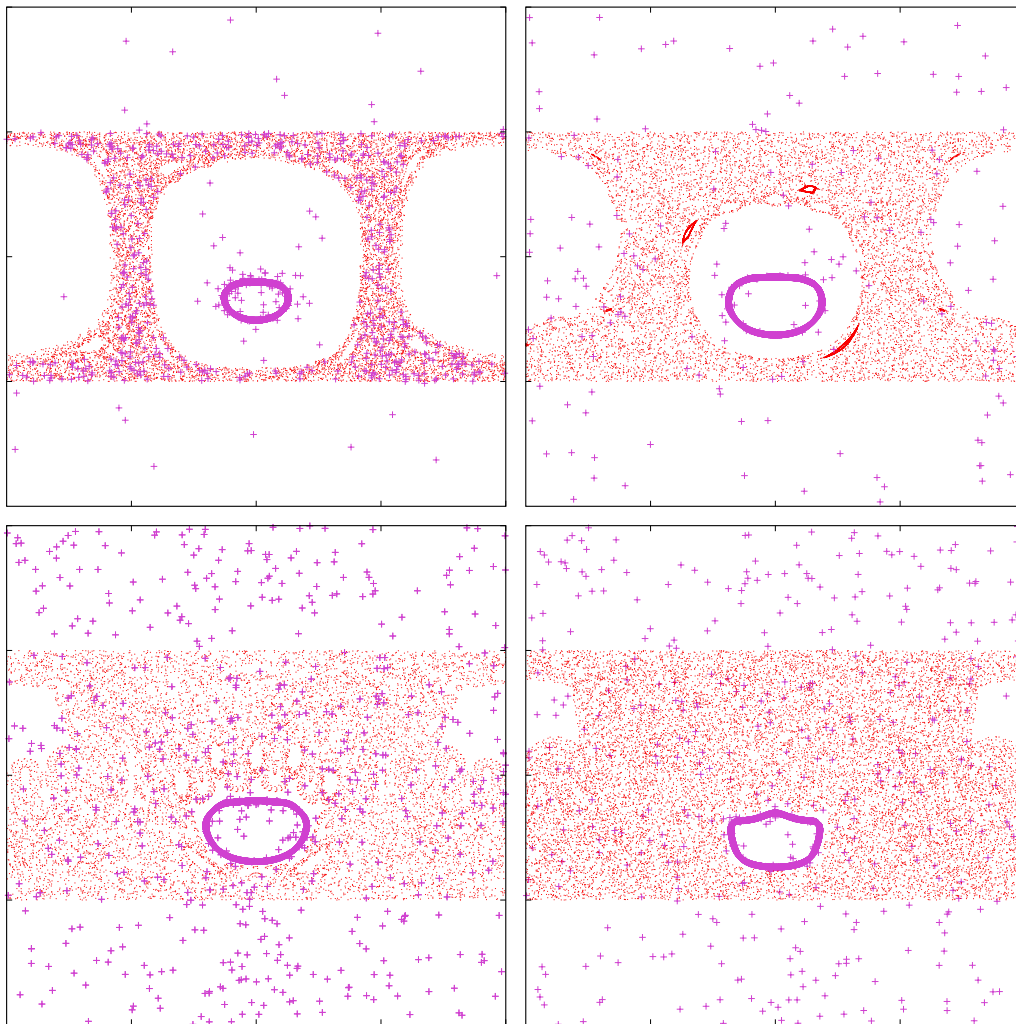


**Figure 2.3:** Poincaré sections of trajectories in the time-dependent flow of Eq. (2.19). From top left to bottom right are shown (dots) four increasingly chaotic examples of the flow, and (crosses), the trajectories of neutrally buoyant particles in the flows that in each case finally end up on a KAM torus within the regular region of the flow.

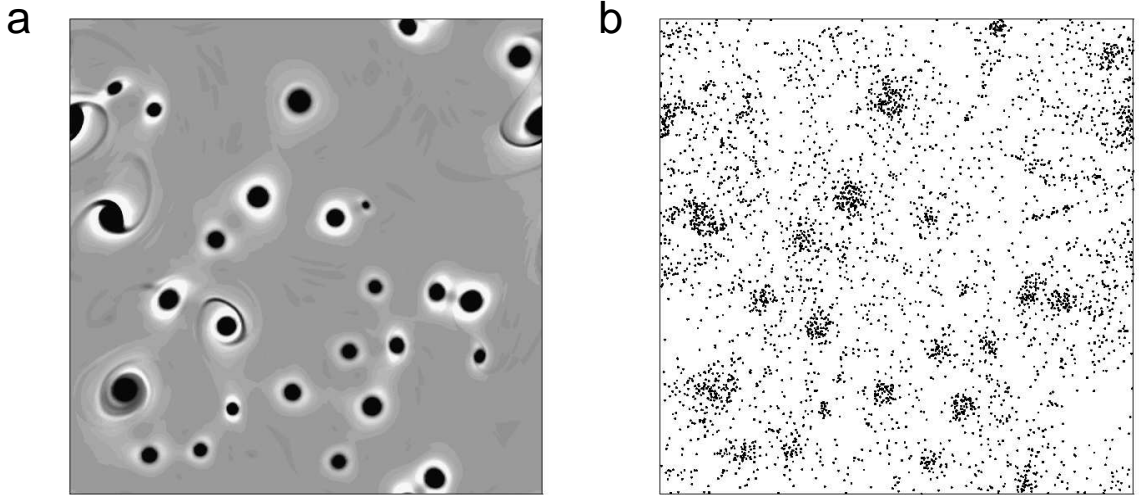


**Figure 2.4:** Small neutrally buoyant tracer particles with Stokes number  $St = 0.2$  collect in the centers of vortices in a two-dimensional turbulent flow simulation. (a)  $Q$  field at time  $t = 1$  (lighter shading is higher  $Q$ ), (b) distribution at time  $t = 1$  of particles that were uniformly distributed in the flow at time  $t = 0$ .

bound to  $Q$  is an upper bound to the Lyapunov exponent.

The implications of these results for two-dimensional turbulent flows have been considered, in which  $Q$  defines three regions: in the vortex centres it is strongly negative; in the circulation cells that surround them, strongly positive, while in the background between vortices it fluctuates close to zero (see, e.g., [64, 16, 86, 149, 150]). As a result of the dynamics, an initially uniform distribution of neutrally buoyant particles with finite size evolves in time towards an asymptotic distribution concentrated in the inner part of vortices where  $Q < 0$ , and with voids in the areas crossed by fluid trajectories that visit regions where  $Q > 4/9 St^{-2}$ , as we illustrate in Fig. 2.4.

To summarize, the simplest model for the force acting on a small rigid neutrally buoyant spherical tracer particle in an incompressible two-dimensional fluid flow leads to tracer trajectories which separate from the fluid trajectories in those regions where the flow has hyperbolic stagnation points. For flows with chaotic pathlines, the analysis shows that the tracer will only evolve on trajectories having Lyapunov exponents bounded by the value of the Stokes drag coefficient. Therefore, by making the value of this coefficient small enough, one can force the tracer to settle on either the regular KAM-tori dominated regions or to selectively visit the chaotic regions with small



Lyapunov exponents.

Interestingly enough, despite its obvious importance from the point of view of applications, the dynamics of finite size spherical particles in a base flow which is three-dimensional has been, in general, much less investigated. The probable reason for this is that very few simple realistic three-dimensional incompressible flow models exist. The few that are simple are not realistic — e.g., the ABC (Arnold–Beltrami–Childress) flow [59] — and those that are realistic are far more complex. In the study of the Lagrangian structure of three-dimensional incompressible time-periodic flows, where this difficulty is already present, the alternative approach of qualitatively modeling the flows by iterated three-dimensional volume-preserving (Liouvillian) maps has been successful in predicting fundamental structures later found both in more realistic theoretical flows and in experiments [69, 142, 42, 41]. However, no similar approach has been followed to describe the motion of impurities in this kind of flow. Later in this Chapter, we will introduce such a qualitative approach based on the method of bailout embedding of a map whose introduction was inspired by the real dynamics of neutrally buoyant particles. However, it is worthwhile to advance here that, in contrast to the two-dimensional case, in time-dependent three-dimensional flows the incompressibility condition only implies that the sum of the three independent eigenvalues of the Jacobian matrix in the 3D version of Eq.(2.14) must be zero. This less restrictive condition allows for many more combinations. Triplets of real eigenvalues, two positive and one negative or vice versa, as well as one real eigenvalue of either sign together with a complex-conjugate pair whose real part is of the opposite sign, are possible. Accordingly, chaotic trajectories may have one or two positive Lyapunov numbers, and a richer range of dynamical situations may be expected.

## 2.3 Three-dimensional unsteady flows and Liouvillian maps

Before entering into the study of finite size particles in 3D flows, let us first review the qualitative study of the dynamics of truly passive tracers in three-dimensional unsteady incompressible flows with periodic time dependence.

Such dynamics is well described by stroboscopic maps in three dimensions that preserve volume. These three-dimensional volume-preserving maps do not correspond to Hamiltonian systems, which have phase spaces of even dimensionality: Hamiltonians with two or three degrees of freedom produce volume-preserving stroboscopic maps of two or four dimensions respectively. Stressing the most general interpretation of the Liouville's theorem, volume-preserving maps on three dimensions, which dimensionally interpolate between the two Hamiltonian cases in the above enumeration, have been named *Liouvillian* maps [67, 68, 69, 142, 70, 40].

To study Liouvillian maps one can employ ideas from KAM theory and imagine perturbations of integrable action–angle models where the actions are fixed and the angles change at each iteration. A perturbation away from the integrable case then causes the actions to vary slowly. For two-dimensional area-preserving maps, or for any maps derived from Hamiltonian dynamical systems, the underlying symplectic structure provides the action–angle variables on which to build. Here with Liouvillian maps such symplectic structure is absent, so variables must be defined with respect to something else. Thus invariant tori have been used to define the action–angle variables.

We can consider integrable, Liouvillian maps that possess some variables, actions  $I$ , that do not change from iteration to iteration, whereas others, angles  $\theta$ , vary linearly as the map is iterated:

$$I' = I, \quad \theta' = \theta + \omega(I). \quad (2.20)$$

The following notation has been used  $L_k^0$  to represent an integrable Liouvillian map that possesses a set of action–angle variables  $I \in \mathbb{R}^k$ ,  $\theta \in \mathbb{T}^{3-k}$ . A  $k$ -action integrable Liouvillian map  $L_k^0$  has a family of  $(3 - k)$ -dimensional invariant tori, each of which is traversed by the  $3 - k$  angle variables that rotate at each iteration by an amount given by the corresponding component of the  $(3 - k)$ -dimensional vector  $\omega$ . In other words,  $L_k^0$  maps consist of uniform translations on  $(3 - k)$ -tori embedded in  $\mathbb{T}^3$ . We concentrate our attention on volume-preserving maps  $L : \mathbb{T}^3 \rightarrow \mathbb{T}^3$  on the three-dimensional torus of the form

$$(x', y', z') = (x + u(y, z), y + v(x', z), z + w(x', y')),$$

where  $u$ ,  $v$ , and  $w$  are doubly-periodic functions. In particular, the following

truncation of the Fourier expansions for these functions, will be considered:

$$\begin{aligned}x' &= x + A_1 \sin z + C_2 \cos y \pmod{2\pi}, \\y' &= y + B_1 \sin x' + A_2 \cos z \pmod{2\pi}, \\z' &= z + C_1 f(y') + B_2 g(x') \pmod{2\pi}.\end{aligned}\tag{2.21}$$

where the functions  $f$  and  $g$  are smooth on the circle.

Thus there are four possibilities for these integrable maps:

$L_0^0$  Zero actions; three angles. The frequency vector  $\omega$  is constant, and hence we have a uniform rotation on  $\mathbb{T}^3$ .

$L_1^0$  One action; two angles. The motion takes place on two-tori defined by constant  $I$ , and a point on one of these tori is given by the two angles  $\theta_1$  and  $\theta_2$ . Thus the motion on the tori is a uniform rotation with a frequency depending on the value of the action.

$L_2^0$  Two actions; one angle. The two actions parametrize a family of invariant circles (i.e., one-tori), and the angle variable rotates with a frequency  $\omega(I_1, I_2)$ .

$L_3^0$  Three actions; zero angles. Each point of space is parametrized by  $(I_1, I_2, I_3)$  and is hence invariant; the map is the identity.

Let consider now the effects of nonintegrable perturbations on  $L_k^0$  maps. The perturbations we wish to consider will act to couple the hitherto independent actions and angles whilst retaining the Liouvillian property of the map. Thyagaraja & Haas [178] have worked out the most general form that such perturbations can take, which in general leads to an implicit map. Below we shall discuss only the subset of perturbations that leave the map in explicit form. These explicit Liouvillian maps capture the dynamics of Liouvillian maps in general, whilst being easier to work with than implicit maps.

We deal first with the two extreme cases  $k = 0$  and  $k = 3$ . Results of Ruelle & Takens [157] and Newhouse, Ruelle & Takens [121] about perturbing quasiperiodic flows on a three-torus indicate that small perturbations of zero-action  $L_0^0$  maps will generically lead to completely chaotic behaviour. A

small nonintegrable perturbation added to three-action  $L_3^0$  maps is a small perturbation

$$I'_1 = I_1 + \epsilon F_1(I_2, I_3), \quad I'_2 = I_2 + \epsilon F_2(I'_1, I_3), \quad I'_3 = I_3 + \epsilon F_3(I'_1, I'_2), \quad (2.22)$$

of the identity. In the  $\epsilon \rightarrow 0$  limit we have a set of three autonomous ordinary differential equations, which takes us back to the case of three-dimensional steady flows. In other words, the perturbation represents the *Euler map* of the flow  $\dot{I} = F(I)$ ; the map (2.22) is derived from this flow by applying the forwards and backwards Euler numerical integration methods to discretize it. The dynamics of Euler maps are closely related to the flows from which they are derived [46].

For one-action  $L_1^0$  maps, it turns out that most of the invariant two-tori are preserved in a KAM-like manner under small nonintegrable volume-preserving perturbations. However, the resonant tori satisfying the equation

$$m\omega_1(I) + n\omega_2(I) = 2\pi k, \quad (2.23)$$

where  $k$ ,  $m$ , and  $n$  are integers, are destroyed, and in their place appear a finite number of invariant circles, half of which are stable and the other half unstable, in the same way as invariant circles are destroyed and fixed points appear in planar area-preserving maps following the Poincaré–Birkhoff theorem. Further invariant tori surround the stable invariant circles, whilst chaos appears around the unstable ones. The preserved invariant tori act as boundaries for the chaotic layers, so a single trajectory cannot cover the whole phase space until the perturbation is large enough to destroy the final invariant torus. The whole situation is like that governed by the KAM theorem in planar area-preserving maps, except that the structures have one additional dimension; that is the invariant tori are two rather than one-dimensional, the island chains interspersed amongst them contain invariant circles, not fixed points, and the stable (elliptic) and unstable (hyperbolic) invariant circles are centres for further invariant tori and for chaos respectively [69, 40]. The existence of a KAM-like theorem in this one-action case has been proven by Cheng & Sun [50], although as Mezić & Wiggins [116] point out, here in three dimensions we have no criterion similar to the irrationality of rotation numbers in two dimensions that enables one to predict in which order the

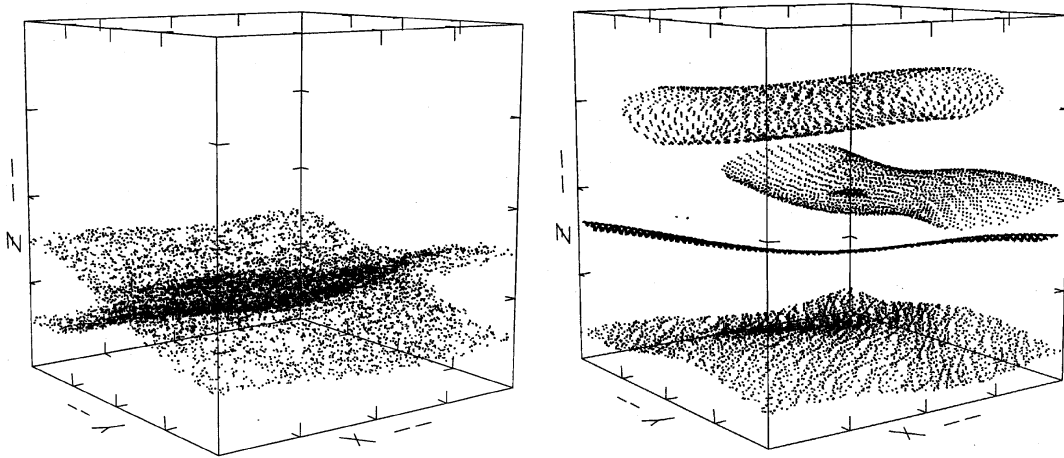


**Figure 2.5:** Numerically obtained invariant surfaces and chaotic volumes. The parameter values in Eq. (2.25) are  $A = 1.5$ ,  $\alpha_B = 1$ ,  $\alpha_C = 2$  and  $\epsilon = 0.1$ . (a) H-shaped chaotic volume associated with the *hyperbolic* line of the  $(0, 1, 0)$  resonance ( $x_0 = 0$ ,  $y_0 = 0.5$  and  $z_0 = 0.24$ ). All the initial conditions are indicated in fractions of  $2\pi$  and the box represents the  $[0, 2\pi]^3$  region. (b) In order of increasing  $z$ : non-resonant surface ( $x_0 = 0$ ,  $y_0 = 0.56$ ,  $z_0 = 0.11$ ) and tubular surfaces around the  $(1, -1, 0)$ ,  $(1, 0, 0)$  and  $(0, 1, 0)$  resonances  $-(x_0 = 0, y_0 = 0.9, z_0 = 0.395)$ ,  $(x_0 = 0.75, y_0 = 0, z_0 = 0.4626)$  and  $(x_0 = 0, y_0 = 0.5, z_0 = 0.828)$  respectively.

remaining invariant tori are destroyed as the nonintegrable perturbation is increased. An example of nearly-integrable maps with a single action is the map  $L_1$  given by the following restriction of Eq. (2.22):

$$\begin{aligned} x' &= x + A \sin z + \epsilon \alpha_C \cos y, \\ y' &= y + \epsilon \alpha_B \sin x + A \cos z, \\ z' &= z + \epsilon \alpha_C \sin y' + \epsilon \alpha_B \cos x'. \end{aligned} \tag{2.24}$$

At  $\epsilon = 0$  this map is integrable with only one action variable  $z$ . The motion in this limit takes place on the surfaces of constant  $z$ , and the angular variables  $x$  and  $y$  rotate at each iteration by constant angles  $\omega_x = A \sin z$  and  $\omega_y = A \cos z$  respectively. The map in Eq. (2.25) corresponds to a discretization of the ABC model proposed by Arnold [6] as an example of chaotic streamlines in a stationary 3-dimensional flow, and extensively studied by Dombre et al. [59] The discretization is equivalent to the addition of periodic time dependence to the flow. Numerically obtained invariant surfaces and chaotic volumes for this example are presented in Fig. (2.5).

With two-action  $L_2^0$  maps, on the other hand, small nonintegrable volume-preserving perturbations cause behaviour rather different to that detailed

above. The integrable case turns out to be a singular limit; as soon as a nonintegrable perturbation is switched on, the two-parameter family of invariant circles coalesce into invariant two-tori. To see why this should be so, one can use an argument based on an adiabatic approximation. Consider the perturbed two-action map

$$I'_1 = I_1 + \epsilon F_1(I_2, \theta), \quad I'_2 = I_2 + \epsilon F_2(I'_1, \theta), \quad \theta' = \theta + \omega(I'_1, I'_2). \quad (2.25)$$

Suppose that  $\omega$  is irrational, then when  $\epsilon$  is small, the angle  $\theta$  covers uniformly the entire interval  $(0, 2\pi)$  before the actions  $I$  change significantly. The variation of  $I$  is thus sensitive only to the average of  $F$  over  $\theta$ . Therefore the actions now iterate as

$$I'_1 = I_1 + \epsilon \bar{F}_1(I_2), \quad I'_2 = I_2 + \epsilon \bar{F}_2(I'_1). \quad (2.26)$$

where the bar represents the  $\theta$  average. Thus the dynamics of the actions  $I$  decouples from that of the angle  $\theta$  for non-resonant  $\omega$ . We are left with an area-preserving map, which leads in the limit  $\epsilon \rightarrow 0$  to the Hamiltonian system

$$\dot{I}_1 = \bar{F}_1(I_2) = \frac{\partial H}{\partial I_2}, \quad \dot{I}_2 = \bar{F}_2(I_1) = -\frac{\partial H}{\partial I_1}. \quad (2.27)$$

We obtain the Hamiltonian

$$H(I_1, I_2) = \int_0^{I_2} \bar{F}_1(I) dI - \int_0^{I_1} \bar{F}_2(I) dI = \beta. \quad (2.28)$$

In other words, in the  $\epsilon \rightarrow 0$  limit, the action variables evolve slowly along the level curves of (2.28). Including the fast motion in the  $\theta$  direction, we infer that the originally invariant circles parallel to the  $\theta$  axis coalesce into invariant tori  $\Sigma_\beta$  defined by the condition  $H(I_1, I_2) = \beta$ , the motion on which is fast in one direction and slow in the other. Resonances occur when the condition imposed above that  $\omega(I)$  be irrational is not satisfied and we have

$$n\omega(I_1, I_2) = 2\pi k, \quad (2.29)$$

where  $k$  and  $n$  are integers. The resonant condition defines a set of sheets that typically intersect a continuous set of invariant tori, which break down locally at the intersections. The remainder of the invariant torus survives, to a given order in the perturbation expansion. Invariant tori are thus connected

through resonances, meaning that, in contrast with the one-action case, a single trajectory can cover the whole of phase space [142, 70, 40]. This characteristic behaviour of two-action Liouvillian maps was termed *resonance-induced dispersion*. In order to exemplify the characteristic behaviour of  $L_2$  maps, we use an appropriate restriction of the family of maps defined in Eq. (2.22):

$$\begin{aligned}x' &= x + \epsilon\alpha_{A_1} \sin z + \epsilon\alpha_{C_2} \cos y, \\y' &= y + \epsilon\alpha_{B_1} \sin x' + \epsilon\alpha_{A_2} \cos z, \\z' &= z + C_1 f(y') + B_2 g(x').\end{aligned}\tag{2.30}$$

For  $\epsilon = 0$ , the map in Eq. (2.31) is integrable and has the form of Eq. (2.25). In this case the lines corresponding to constant values of  $x$  and  $y$  are invariant. Fig. (2.6a) shows some of these surfaces projected down to the  $z = 0$  plane. To illustrate the effect of the resonances, we plot in Fig. (2.6b) a trajectory of the map in Eq. (2.31) for a non-zero but very small value of  $\epsilon$ . The location of the lowest-order resonance  $\omega = 0$  for a particular election of the functions  $f$  and  $g$  is indicated by the dashed line. Close to this line, the trajectory oscillates wildly and jumps from one adiabatic surface to another. Finally, Fig. (2.6c) shows the extreme case in which the first-order resonance indicated by the dashed line intersects almost all the surfaces of Eq. (2.28). In this figure, the iterations of only one trajectory are shown. It is now apparent that this single trajectory visits all the available space.

Occupying as they do a position somewhere between symplectic maps of two and four dimensions from two and three-degree-of-freedom Hamiltonian systems, the Liouvillian maps that underlie three-dimensional unsteady flows can exhibit types of behaviour analogous to both their lower and higher-dimensional siblings. An important difference between Hamiltonians of two and three degrees of freedom is that Arnold diffusion exists in the latter but not in the former. With two degrees of freedom, the invariant KAM tori completely separate different regions of phase space. This is no longer true when another degree of freedom is added, and as a result Arnold diffusion can take place throughout the phase space. This occurs, albeit extremely slowly, for arbitrarily small values of the nonlinearity parameter  $\epsilon$ . Resonance-induced dispersion in two-action Liouvillian maps, although reminiscent of Arnold diffusion in the four-dimensional volume-preserving maps from three-degree-

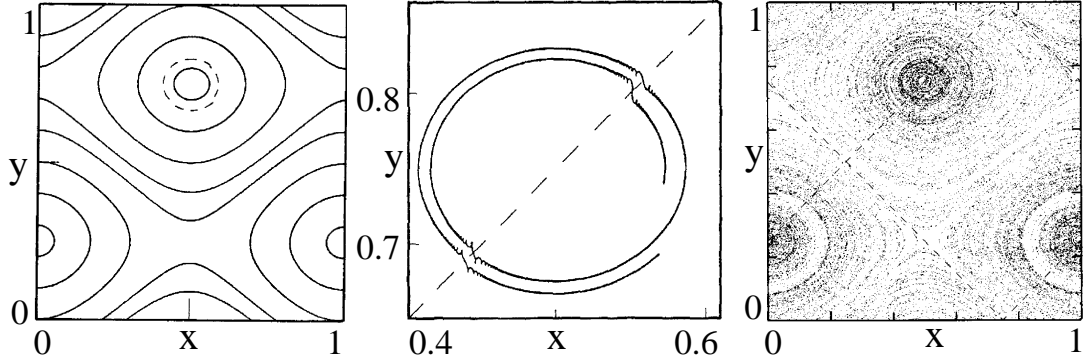


**Figure 2.6:** (a) A few members of the family of surfaces defined by Eq. (2.31) for  $\alpha_{B_1} = 1.5$  and  $\alpha_{C_2} = 2$  projected down to the  $z = 0$  plane. (b) One trajectory of the map in Eq. (17) for  $\alpha_{A_1} = 1$ ,  $\alpha_{A_2} = 2.5$ ,  $C_1 = B_2 = 4$  and  $\epsilon = 0.001$ ,  $f = \cos$  and  $g = \sin$ .  $\alpha_{B_1}$  and  $\alpha_{C_2}$  are the same as before. The dashed line indicates the location of the lowest-order resonance. (c) Only one initial condition is required to generate this picture.

of-freedom Hamiltonians, is engendered by a different mechanism. Whilst Arnold diffusion occurs through an interconnected web of resonances, in resonance-induced dispersion the available space is covered using the invariant tori, and the resonant surfaces are a means to jump from one torus to another. The consequence of this difference is that the rates of the two processes are radically different; with nonlinearity  $\epsilon$ , an estimate of the upper bound on the rate of Arnold diffusion is  $O(\exp(-\epsilon^{-1/2}))$ , whilst previous work on Liouvillian maps shows that resonance-induced dispersion has an  $O(\epsilon^2)$  dependence [142].

The presence of resonance-induced dispersion in two-action type flows, and its absence in those of one-action type, is from the mixing and transport point of view the crucial difference between these two classes of flows. In the one-action class of three-dimensional unsteady flows, as with two-dimensional unsteady flows, the existence of KAM-type theorems proves that complete mixing will not generically be achievable, as the invariant tori present barriers to transport. On the other hand, the addition of a third dimension to a two-dimensional unsteady flow leads in the two-action case to much faster dispersion than with two-dimensional flow alone, owing to the presence of resonance-induced dispersion. This should lead to better mixing. What we mean by efficient mixing here is that the density of an initial concentration of passive scalars should rapidly tend to a constant value throughout the region being mixed. This property is related to the Lyapunov exponents of the flow, one of which must be positive to allow the exponential separation of neigh-



bouring trajectories that is necessary for chaos. Even a small coupling between primary and secondary flows is effective in two-action flows in producing a large improvement in dispersion over two-dimensional chaotic advection alone through the action of resonance-induced dispersion, particularly when the flow period is relatively short when there is very little chaotic advection in two dimensions.

## 2.4 Opening Three-Dimensional Flows

This Section describes one of the interesting side-trips that, as I mentioned in the introduction, I took while progressing through the main theme of the Thesis . While it does not strictly concerns to the dynamics of finite size bodies in moving fluids, the research presented here is a contribution to the investigation structures and properties of 3D volume preserving flows and maps. As such, I find, therefore, pertinent to include its description following the previous review.

Although the dynamics of passive point-like impurities transported by incompressible fluid flows is conservative in the sense that the volume occupied by the particles remains constant under the evolution, there are situations, in which a peculiar type of effective dissipation comes naturally to the scene, namely, the elimination of particles in some place. Consider for example the following problem: the air of a room in which a controlled flow pattern has been established needs to be cleaned. The installation of purifier system is then planned at a specific location that has to be decided in order to maximize the cleaning efficiency. In a simplified view, we can think of the purifier as a volume of the space where the impurities are eliminated of the system without perturbing the flow. We are then facing a "leaking" dynamics in which trajectories evolve preserving the volume until they reach a specified region of the space where they disappear. Our problem is then deeply related to the investigation of the changes expected in the residence time of the particles in the allowed phase space —the room— as we modify the shape and location of the leak —the purifier design—.

Manifestations of the same problem arise in very different and otherwise unrelated contexts. In mesoscopic physics, for example the ballistic conduc-

tance of minute structures of both 2D and 3D character lead to conservative classical dynamics leaking through the feeding leads [163]. The problem is also relevant in other hydrodynamical contexts such as e.g. the mixing properties of open flows [91]. In the realm of oceanographic research, the leaking could be related to the loss of planktonic material due to its predation by larger species. Chemical reactions occurring at certain regions of the flow might also be responsible for the deactivation / annihilation of the particles arriving in these regions, modelled by the so-called resetting mechanism [141].

Leaking dynamics has largely been studied in the Hamiltonian framework [119, 160]. In particular leaking two-dimensional area-preserving maps have been thoroughly investigated as a function of the shape, location and orientation of the leaking regions as well as the characteristics of the basic dynamical system [161]. Fluid-dynamically, these results apply to flows that are two-dimensional and possibly periodically time-dependent. Although this case is important for some applications to geophysics, most of real life situations lead to three-dimensional incompressible flows.

Here we present the first study of this kind for a conservative but non-hamiltonian dynamical system, namely, volume preserving three-dimensional maps describing the basic features of incompressible time periodic flows. Apart from the applications, the study of leaked volume-preserving maps in three dimensions poses a few challenging questions to the theory of dynamical systems. For example, a key dynamical objects to understand leaked systems as well as many other open dynamical systems such as those describing scattering processes, are the so-called chaotic saddles and their associated stable and unstable manifolds. The chaotic saddle represents the set of points that never escape through the leak either forward or backward in time. The stable (unstable) manifold is the union of points which converge towards the chaotic saddle in the forward (backward) dynamics, and can also be interpreted as the complement of the union of all the pre-images (images) of the leak.

In 2D Hamiltonian systems the preservation of volume implies that the two Lyapunov exponents must be equal in magnitude and opposite in sign. Consistently with this, the invariant manifolds of the leaked system present some sort of statistical time reversal symmetry. For example, the fractal dimension of the stable and the unstable manifolds are the same. New to 3D

maps, however, is the fact that generically, the maps present either two positive and one negative expansion rates or viceversa. Consequently, a leaked 3D map is *not* a direct analog of a scattering problem since it is non-hamiltonian, although the original system is volume preserving, but only for a particular choice of the parameters it may be also time-reversal invariant. Here we investigate the impact of these features on the dimensionality and other statistical properties of the filamentation.

We study the behavior of time periodic three-dimensional incompressible flows modelled by three-dimensional volume preserving maps in the presence of a leakage. The distribution of residence times, and the chaotic saddle together with its stable and unstable invariant manifolds are described and characterized. They shed light on typical filamentation of chaotic flows whose local stable and unstable manifolds are always of different character (plane or line). We point out that leaking is a useful method which sheds light on typical filamentation of chaotic flows. In particular, the topology depends on the number of local expanding directions, and is the same in the leaked system as in the closed flow.

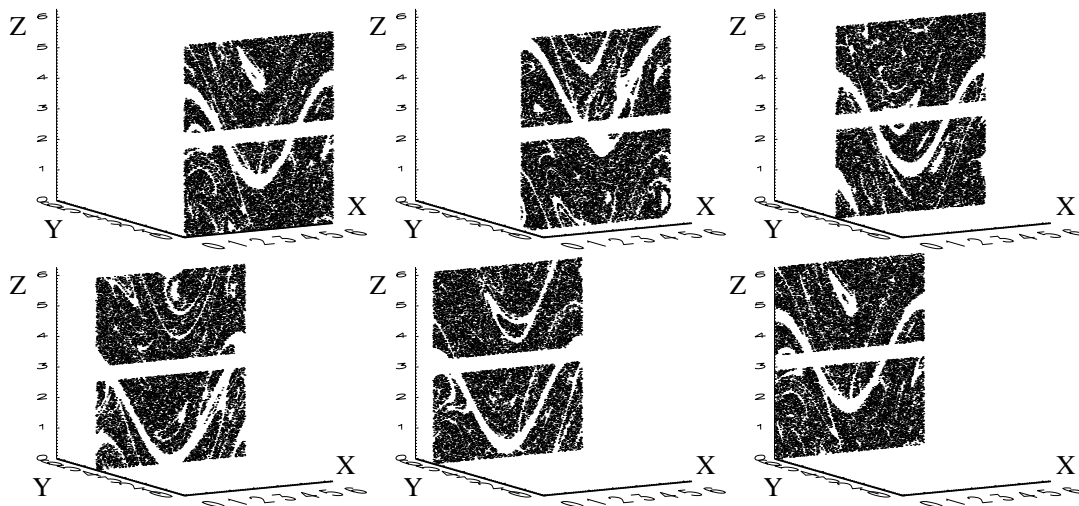


**Figure 2.7:** XY slices of the chaotic saddle for the leaked ABC map with  $A = B = C = 1.6$ . The leak is centered at  $z = \pi$  with a width of  $\epsilon = 0.5$ . The number of initially distributed particles is  $N_0 = 5000000$ . The width of slices is  $0.08\pi$ .

Some of these questions turn out to have unexpected importance from the point of view of applications.

An interesting case, for example, is the analysis of magma flows from

petrological data. Lavas often show in a freezed form the Lagrangian structures of these flows that can then be studied by image processing. Part of the processing may consist of band-pass filtering the greyscale levels of the images which is an indirect way of introducing leaking. Some empirical results [138] show that the resulting fractal dimensions of the structures are strongly correlated with the mixing efficiency of the corresponding magma flows. In this case, however, leaking does not imply a physical escape out of the system, rather it means that regions with a certain property (i.g. greyscale level) are filtered out. Considering the concentration as the filtering criterion, the same approach can be applied to the analyzis of chemical reactions in flows [161].

As a paradigm of this type of three-dimensional systems, we use the family of ABC and ABC-related maps introduced in previous Section [69]:

$\mathbf{T}(x_n, y_n, z_n) \longrightarrow (x_{n+1}, y_{n+1}, z_{n+1})$ , with

$$\begin{aligned} x_{n+1} &= x_n + A \sin(z_n) + C' \cos(y_n) \\ y_{n+1} &= y_n + B \sin(x_{n+1}) + A' \cos(z_n) \pmod{2\pi} \\ z_{n+1} &= z_n + C \sin(y_{n+1}) + B' \cos(x_{n+1}). \end{aligned} \tag{2.31}$$

Although the ABC map is the solution of the Navier-Stokes equation in the presence of a rather artificial space-time periodic forcing [73], it has been shown to capture the essential features of more realistic three-dimensional time-periodic flows [40, 41, 42] whose geometries are relevant to geophysical and environmental applications. This family of maps display a range of dynamical behavior that goes from nearly integrable to strongly chaotic ones that in some sense can be considered the equivalent in three dimensions of those found in even dimensional conservative Hamiltonian dynamics.

In the following, we will focus on the highly chaotic case, where no large scale sticky integrable regions are found numerically, and we will investigate the effect of introducing leaking regions. As an example, we define a rectangular box lying parallel to the  $x - y$ -plane of width of  $\epsilon = 0.5$ , centered at  $z = \pi$ , cutting through the whole system in  $z$ , as the leak. Particles which enter the leak during the simulations escape the system. Remaining particles then trace out fractal structures, which have a dimension less than 3, the dimension of the whole accessible space.

Starting with a large number  $N_0$  of particles initially distributed in the full phase space uniformly, all the nonescaping particles are followed over  $n$  number of iterations. For large enough  $N_0$  and  $n$ , the initial coordinates of the nonescaping particles should trace out the stable manifold, their final positions after  $n$  steps the unstable manifold, and the midpoints at time  $n/2$  the chaotic saddle itself [101].

For iterating  $n$  times, we obtain the chaotic saddle as shown in Fig. (2.7). In order to have a better view on the three-dimensional structure, the chaotic saddle is represented in slices at different width (centered at different  $y$ ) of the system. It can be seen in the pictures, that the sine structures appear both in the  $x$  and in the  $z$  direction.

As a tool of visualizing dynamical properties of the particles in the leaked ABC map, we calculated their residence times. A 2D slice of this function is depicted in Fig. (2.8a): regions with large lifetimes (particles need long time to reach the leak) are denoting regions close to the stable manifold, thus the structures traced out by the long-living particles practically coincide with the ones of the stable manifold. The residence times depend sensitively on the size and on the position of the leak [161]. For a fixed size of the leak, such as the purifier, calculations of the residence or escape times will give the optimal location for an extreme particle exchange.

Fig. (2.8b) depicts the chaotic saddle, refined with the PIM-triple method [125]. The method is based on so called PIM (Proper Interior Maximum) triples: three points (a, c, b) in a straight line segment such that the interior point c has the maximum residence time. Once a PIM-triple is found, is used to approach the stable manifold of the chaotic saddle, looking for refined segments in (a,b) that contain closer PIM-triples. This constitute an iterative scheme to approach the stable manifold. Initial conditions on the stable manifold in a XZ plane at  $y = 0$  are then evolved  $n/2$  times to obtain the chaotic saddle. A slice (with width  $0.01 \cdot \pi$ ) of this three-dimensional saddle is plotted in the figure. If the chaotic saddle has a large dimension, this implies that the emptying process is slow, that is, the location or size of the purifier is not optimal. The visualization of parts of its otherwise space-filling three dimensional unstable manifold is an important step to obtain the stretching filamentation [133], i.e. the routes of efficient transport, in a system. Fur-

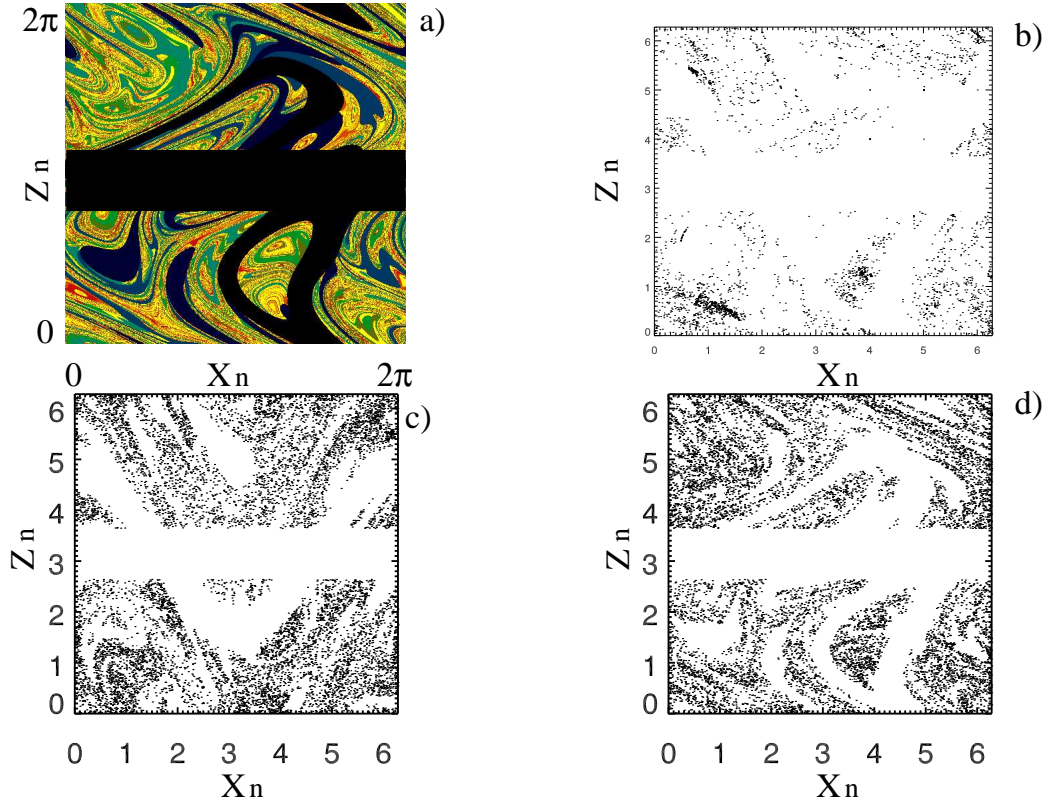


**Figure 2.8:** (a) XZ slice of the residence time function for the same parameters as in Fig. (2.7). The leak is centered at the same  $z$  value but with a width of  $\epsilon = 1.0$ . Dark colors mean small residence times, while light colors represent higher values. (b) XZ slice of the chaotic saddle refined with the PIM-triple method. (c) and (d) The associated unstable and stable manifolds. The average mean residence time of the associated chaotic transient is used to obtain the fractal dimensions, and its value is  $1/\tau = 0.192$ . All the slices are for  $y = 0$ .

thermore, visualizing different subsets of the unstable manifold by defining different leaks (different shapes, positions or sizes) corresponds to mimicking different concentration layers, traced out e.g. by chemical or biological processes or by magma mixing processes.

We have computed the fractal dimensions of the unstable and stable manifolds of the chaotic saddle of the leaked map in the case where the second Lyapunov exponent is zero (usually the highly chaotic  $A = A', B = B, C = C'$  case). We have used both the correlation dimension and the generalization of

the Kaplan-Yorke formula for the information dimension [88]:

$$\begin{aligned}
D_u &= U + I + \left[ \left[ \left( \sum \lambda_j^+ \right) - \frac{1}{\tau} \right] - (|\lambda_1^-| + \dots + |\lambda_I^-|) \right] / |\lambda_{I+1}^-| \\
D_s &= S + J + \left[ \left[ \left( \sum \lambda_j^+ \right) - \frac{1}{\tau} \right] - (\lambda_1^+ + \dots + \lambda_J^+) \right] / \lambda_{J+1}^+ \\
D_{saddle} &= D_u + D_s - N.
\end{aligned} \tag{2.32}$$

where  $\lambda_i^+$  and  $\lambda_j^-$  are the positive and negative lyapunov exponents, U and S are the number of positive and negative lyapunov exponents,  $N = U + S$ , and I and J are such that the following relations are fulfilled

$$\begin{aligned}
|\lambda_1^-| + \dots + |\lambda_{I+1}^-| &\geq \left[ \left( \sum \lambda_j^+ \right) - \frac{1}{\tau} \right] \geq |\lambda_1^-| + \dots + |\lambda_I^-| \\
\lambda_1^+ + \dots + \lambda_{J+1}^+ &\geq \left[ \left( \sum \lambda_j^+ \right) - \frac{1}{\tau} \right] \geq \lambda_1^+ + \dots + \lambda_J^+
\end{aligned}$$

In our simulations we have used  $A = B = C = 1.6$ . Analogously to the 2D case, the stable and unstable manifolds have then the same dimension.

$$\begin{aligned}
\lambda_1 &= +0.775, \lambda_2 = +0.001, \lambda_3 = -0.776 \\
D_u &= 2.752, D_s = 2.751, D_{saddle} = 2.50
\end{aligned}$$

In the more interesting case when the Lyapunov exponents of the maps are all nonzero new characteristics of the manifolds appear in comparison to the 2D case. Now, the manifold related to the two exponents of equal sign (i.e. the unstable manifold if the system shows 2 positive Lyapunov's, and the stable one in the case of two negative Lyapunov's) is locally a surface, while the other one is a line. Due to the foldings generated by the chaotic dynamics, their global form is a curtain like and a filamental fractal, respectively. The former possesses a larger dimension than the other one.

This can clearly be seen in a different volume preserving map, a 3D toral automorphism:

$$\begin{pmatrix} x_{n+1} \\ y_{n+1} \\ z_{n+1} \end{pmatrix} = \begin{pmatrix} 1 & 1 & 2 \\ 1 & 3 & 5 \\ 2 & 5 & 9 \end{pmatrix} \cdot \begin{pmatrix} x_n \\ y_n \\ z_n \end{pmatrix} \pmod{1}. \tag{2.33}$$

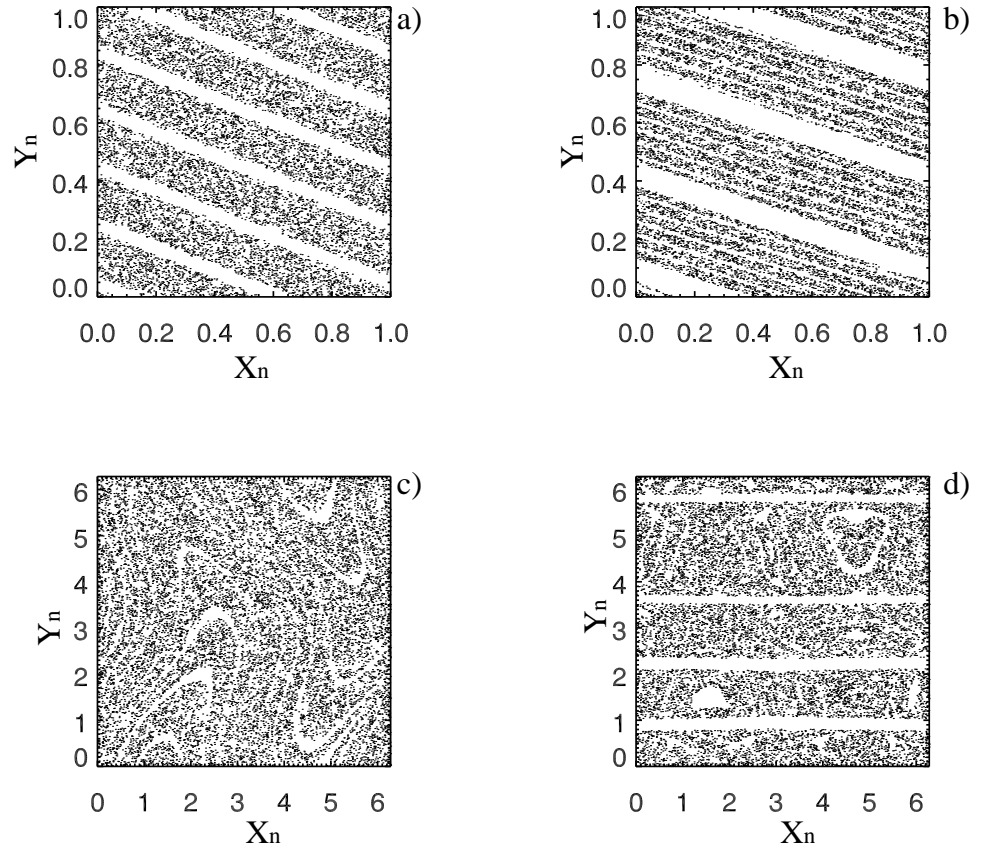


**Figure 2.9:** XY slices (for a value  $z = 0.8$  and  $z = 0.8 \cdot \pi$ , above the leak) of the stable and unstable manifolds for the 3D toral automorphism (a,b) and for the asymmetric ABC map (c,d). The leak is a rectangular box parallel to the XY plane and centered at  $z = 0.3$  ( $z = 0.3 \cdot \pi$ ) with a width of  $\epsilon = 0.25$  ( $\epsilon = 0.25 \cdot \pi$ ). The width of the slices is  $0.01$  ( $0.01 \cdot \pi$ ). The mean residence time values are  $1/\tau = 0.357$  and  $1/\tau = 0.227$  respectively.

This map is a constant matrix hyperbolic map whose Lyapunov exponents can be obtained analytically as the logarithm of the matrix eigenvalues. The fractal dimension of the invariant manifolds are consistent with the Lyapunov values. Slices of the stable and unstable manifolds are depicted in Fig. (2.9a,b):  $\lambda_1 = +2.5$ ,  $\lambda_2 = -0.53$ ,  $\lambda_3 = -1.97$ ,  $D_u = 2.315$ ,  $D_s = 2.857$ ,  $D_{saddle} = 2.172$

For the nonlinear ABC map these manifolds are no longer translation invariant. In the particular case of the ABC parameters as  $A = 3.6$ ,  $A' = 1.6$ ,  $B = 4.6$ ,  $B' = 0.06$ ,  $C = 5.06$ ,  $C' = 0.6$ , the map has two negative and one positive



exponent. Consequently, the dimension of the stable manifold is larger than of the unstable manifold.

$$\begin{aligned}\lambda_1 &= +2.53, \lambda_2 = -0.9, \lambda_3 = -1.63 \\ \mathbf{D}_u &= 2.864, \mathbf{D}_s = 2.91, \mathbf{D}_{saddle} = 2.774\end{aligned}$$

The topological difference of both manifolds is visible in these approximately two-dimensional slices (Fig. (2.9c,d)). The stable one appears to be filamental in this cut while the unstable one is a cloud of points consistently with the lower fractal dimension of the latter manifold.

## 2.5 Bailout Embeddings

Let us now come back to the simplified equation of motion for a small, neutrally buoyant, spherical tracer in an incompressible fluid (Eq. 2.13), rewritten in the following way:

$$\frac{d}{dt}(\dot{x} - u(x)) = -(\lambda + \nabla u) \cdot (\dot{x} - u(x)), \quad (2.34)$$

where  $\dot{x}$  represents the velocity of the particle,  $u$  that of the fluid,  $\lambda$  a number inversely proportional to the Stokes number of the particle — the ratio of the relaxation time of the particle back onto the fluid trajectories to the time scale of the flow — and  $\nabla u$  the Jacobian derivative matrix of the flow. We would like to point out here that this equation can be seen as a dynamical system whose state variable  $\dot{x} - u(x)$  when vanishing, defines, in turn, another dynamical system. While the solution of the latter is also a solution of the former, this one has a much larger set of solutions. Let us also remember, that the chaotic trajectories of the flow vector field are in some way unstable when viewed as trajectories of the finite size tracers, a properties that leads to the settling of these on the KAM islands of the flow.

In this Section, we discuss a mathematical abstraction built up on a generalization of this kind of dynamics that has been named *bailout embedding*. Given an arbitrary dynamical system  $\dot{x} = f(x)$ , we define a bailout embedding

as one of the form

$$\begin{aligned}\frac{d}{dt}(v - f(x)) &= -k(x)(v - f(x)), \\ \frac{dx}{dt} &= v.\end{aligned}\tag{2.35}$$

This is a dynamical system defined in the space of the variables  $x$  and  $v$ . Notice though that the original dynamics satisfying  $\dot{x} = f(x) = v$  also solves Eqs.(2.35). This implies that  $v = f(x)$  defines an invariant submanifold for the bailout embedding. The idea then, is that we can design an embedding to satisfy the condition that  $k(x) < 0$  on a set of unwanted orbits of the original dynamics while  $k(x) > 0$  on the others. We thus force the unwanted orbits to be unstable in the larger dynamics even though they are stable in the original system. In this way, trajectories in the embedding tend to detach or bail out from the unwanted set of the original system, bouncing around in the larger space until eventually reaching a stable region with  $k(x) > 0$ , where they may converge back onto trajectories of the original dynamical system. In other words, by means of a bailout embedding we can create a larger version of the dynamics in which specific sets of orbits are removed from the asymptotic set, while preserving the dynamics of another set of orbits — the wanted one — as attractors of the enlarged dynamical system.

The motion of finite-sized neutrally buoyant spherical particles suspended in an incompressible fluid flow thus embeds the Lagrangian dynamics of a perfect tracer satisfying  $\dot{\mathbf{x}} = \mathbf{u}(\mathbf{x})$  where  $\mathbf{u}(\mathbf{x})$  is the Eulerian velocity field describing the flow. In the full model of the drag on a sphere [110], this is a highly nontrivial embedding. For example, the contribution to the drag known as a Basset–Boussinesq force contains the difference between the fluid and particle accelerations integrated over the whole trajectory. However, in the limit where the particles are sufficiently small and the Basset–Boussinesq term can be disregarded, the dynamics reduce to a bailout embedding of the form given in Eq.(2.35) with  $\mathbf{u}(\mathbf{x})$  playing the role of  $f$ , and  $k(\mathbf{x}) = -(\gamma + \nabla f)$ , where  $\gamma$  turns out to be the Stokes coefficient [14]. In this case, it appears that the embedding — the finite-sized particle dynamics — detaches from the original dynamics — the passive scalar one — near saddle points and other unstable regions of the basic volume-preserving flow, converging back only in the KAM islands that act now as attractors of the embedding. This particular

type of bailout embedding can be immediately generalized and applied to any Hamiltonian and/or divergence-free flow by using a similar form of  $k(x)$ , and can be used as a method to target small KAM islands in these types of systems [44].

The notion of bailout embedding, Eq. (2.35), can also be extended to maps in a rather obvious fashion [44, 43]. Given a map  $x_{n+1} = f(x_n)$ , the bailout embedding is given by

$$x_{n+2} - f(x_{n+1}) = K(x_n)(x_{n+1} - f(x_n)). \quad (2.36)$$

The condition  $k(x) < 0$  over the unwanted orbits has to be replaced here by  $|K(x)| > 1$ , because the deviations from the original dynamics are multiplied by  $K$  in each iteration. The particular choice of the gradient as the bailout function  $k(x) = -(\gamma + \nabla f)$  in a flow translates in the map setting to  $K(x) = e^{-\gamma} \nabla f$ .

Let us illustrate the functioning of a map bailout embedding in the Hamiltonian framework by means of the prototypical area-preserving standard map introduced by Chirikov and Taylor [105]. This map is defined on the two-dimensional torus by

$$\begin{aligned} x_{n+1} &= x_n + \frac{k}{2\pi} \sin(2\pi y_n) \equiv f_x(x_n, y_n) \pmod{1}, \\ y_{n+1} &= y_n + x_{n+1} \equiv f_y(x_n, y_n) \pmod{1}. \end{aligned} \quad (2.37)$$

The parameter  $k$  controlling the nonlinearity takes the standard map from the integrable limit at  $k = 0$  to a highly chaotic regime when  $k \gg 1$ . At intermediate  $k$  this map shows a mixture of quasiperiodic trajectories on the KAM tori together with chaotic ones, depending on where we set the initial conditions. As the value of  $k$  is increased the region dominated by chaotic trajectories pervades most of the phase space except for increasingly small islands of KAM quasiperiodicity. Notice that the only factor that decides whether we are in one of these islands or in the surrounding chaotic sea is the initial condition of the trajectory. Therefore, in order to locate one of these islands, it would be necessary to make the initial condition scan the whole phase space while watching for quasiperiodicity in the resulting dynamics. In a bailout embedding, on the other hand, the KAM trajectories of the embedded system can be transformed into effective global attractors in the extended phase space. The

search for KAM islands then becomes a matter of simply iterating the bailout map forwards until its trajectories converge to those of the embedded one.

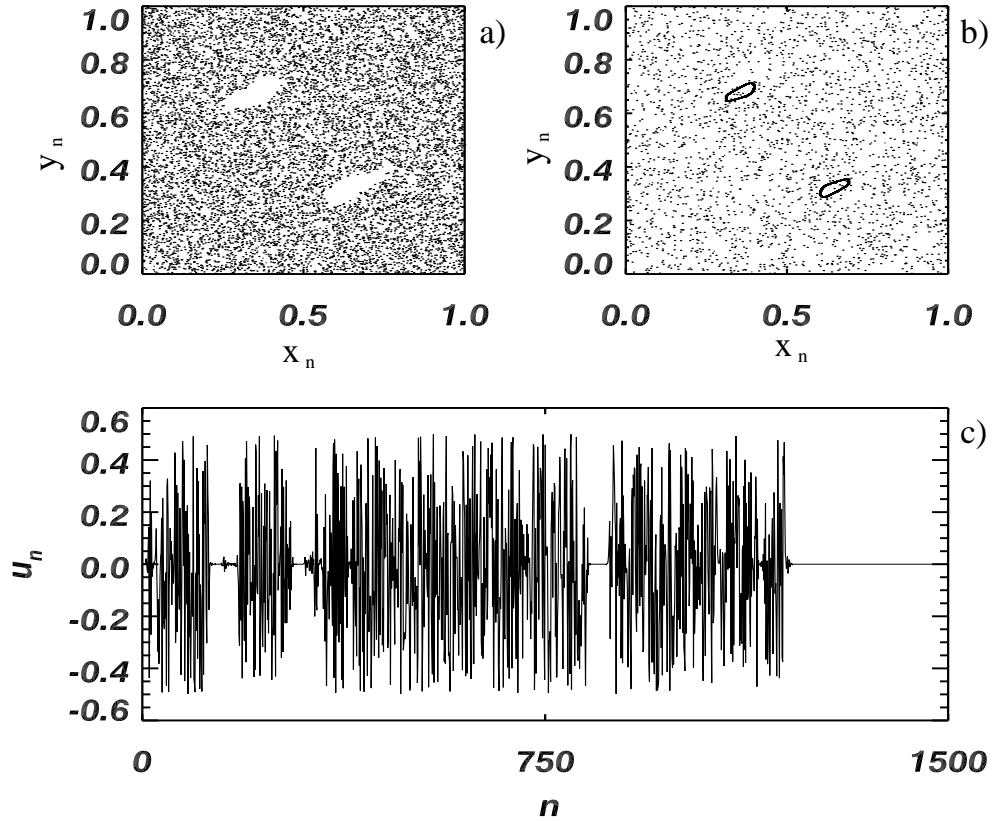


**Figure 2.10:** (a) Chaotic trajectory of the standard map for  $k = 5$  covering practically the whole phase-space except for a small period-2 KAM island. (b) Trajectory of a bailout embedding of the standard map with  $e^{-\gamma} = 0.85$ . After wandering around the phase space for a while, the trajectory finally settles inside the islands. (c) Deviation of the bailout embedding trajectory from the original dynamics showing transiently intermittent behavior as a function of time. The parameters here are the same as in (a) and (b).

The bailout embedding of the standard map is obtained by simply replacing  $f$  in Eq. (2.36) with the definitions from Eq. (2.37). Accordingly,  $K(x)$  in Eq. (2.36) becomes

$$K(x) = e^{-\gamma} \begin{pmatrix} 1 & k \cos(2\pi y_n) \\ 1 & k \cos(2\pi y_n) + 1 \end{pmatrix}. \quad (2.38)$$

These replacements then lead to the coupled second-order iterative system

$$\begin{aligned}
 x_{n+1} &= u_n + f_x(x_n, y_n), \\
 y_{n+1} &= v_n + f_y(x_n, y_n), \\
 u_{n+1} &= e^{-\gamma} (u_n + k \cos(2\pi y_n) v_n), \\
 v_{n+1} &= e^{-\gamma} (u_n + (k \cos(2\pi y_n) + 1) v_n).
 \end{aligned}
 \tag{2.39}$$

Notice that due to the area-preserving property of the standard map, the two eigenvalues of the derivative matrix must multiply to one. If they are complex, this means that both have an absolute value of one, while if they are real, generically one of them will be larger than one and the other smaller. We can then separate the phase space into elliptic and hyperbolic regions corresponding to each of these two cases. If a trajectory of the original map lies entirely in the elliptic regions, the overall factor  $e^{-\gamma}$  damps any small perturbation away from it in the embedded system. But, for chaotic trajectories that inevitably visit some hyperbolic regions, there exists a threshold value of  $\gamma$  such that perturbations away from a standard-map trajectory are amplified instead of dying out in the embedding. As a consequence, trajectories are expelled from the chaotic regions to finally settle in the safely elliptic KAM islands. This process can be seen clearly in Figs. 2.10(a) and (b).

The temporal behavior of the departure of the bailout embedding trajectory from the embedded dynamics is interesting by itself. This departure is measured by the components  $u_n$  and  $v_n$  of Eq. (2.39). Over the evolution, the embedding visits in turn areas where convergence and divergence from the original dynamics is reinforced. The result is typically a highly intermittent behavior where periods of exponentially small values of  $u$  and  $v$  alternate with periods with very large values of these components, as depicted in Fig. 2.10(c). Except for the fact that finally the fluctuations are bound to die-out at some stage, this behavior is reminiscent of the so called on–off intermittency taking place after a blowout bifurcation. In section 2.8 we investigate further the connection between these two dynamical phenomena.

## 2.6 The Bailout Embedding in Three Dimensional Flows

In this section we study the richer range of dynamical situations found in the dynamics of neutrally buoyant particles suspended in three-dimensional time-periodic flows. Instead of investigating all these in terms of a given fully fledged three-dimensional time-periodic model flow, we follow a qualitative approach based on iterated maps that roughly reproduces the properties of the impurity dynamics in a generic flow of this kind.

As was introduced in previous section, is rather easy to construct this type of embedding for map dynamics. Given a map  $X_{n+1} = T(X_n)$ , a general bailout embedding is given by

$$X_{n+2} - T(X_{n+1}) = K(X_n) \cdot (X_{n+1} - T(X_n)), \quad (2.40)$$

where  $K(X)$  is the bailout function whose properties determine which trajectories of the embedded map will be eventually abandoned by the embedding. The particular choice — naturally imposed by the particle dynamics — of the gradient as the bailout function in a flow translates in the map setting to

$$K(x) = e^{-\lambda} \cdot \nabla T. \quad (2.41)$$

Here we consider the bailout embedding of a class of non-Hamiltonian systems: three-dimensional volume-preserving maps. In particular, we choose to represent qualitatively chaotic three-dimensional incompressible base flows that are periodic in time by ABC maps, the family

$$T = T_{ABC} : (x_n, y_n, z_n) \longrightarrow (x_{n+1}, y_{n+1}, z_{n+1}), \quad (2.42)$$

where

$$\begin{aligned} x_{n+1} &= x_n + A \sin z_n + C \cos y_n \pmod{2\pi}, \\ y_{n+1} &= y_n + B \sin x_{n+1} + A \cos z_n \pmod{2\pi}, \\ z_{n+1} &= z_n + C \sin y_{n+1} + B \cos x_{n+1} \pmod{2\pi}, \end{aligned} \quad (2.43)$$

that displays all the basic features of interest of the evolution of three dimensional time periodic fluid flows. As remarked previously, depending on the

parameter values, this map possesses two quasi-integrable behaviors: the one-action type, in which a KAM-type theorem exists, and with it invariant surfaces shaped as tubes or sheets; and the two-action type displaying the phenomenon of resonance-induced diffusion leading to global transport throughout phase space [69].

Let us now study the dynamics defined by Eqs (2.40)–(2.43). We first concentrate on the cases in which the flow is dominated by one-action behavior. In these we find an interesting generalization of the behavior already seen in two dimensions: particles are expelled from the chaotic regions to finally settle in the regular KAM tubes. As an example, we take values of  $A$ ,  $B$ , and  $C$  that lead to almost ergodic behavior of the fluid map: a single fluid trajectory almost completely covers the phase space. However, from randomly distributed initial conditions, the particle trajectories inevitably visit some hyperbolic regions where they detach from the corresponding fluid trajectory. In this fashion they find their way inside the invariant elliptic structures where they can finally relax back onto a safe fluid trajectory. In Fig. (2.11) we show how a homogeneous distribution of particles in the fluid flow, after a large number of stabilization iterations, finally settles inside the tubular KAM structures for different values of the parameter  $\lambda$ . When the value of  $\lambda$  decreases, more random trajectories follow this evolution: more particles fall into the invariant tubes.

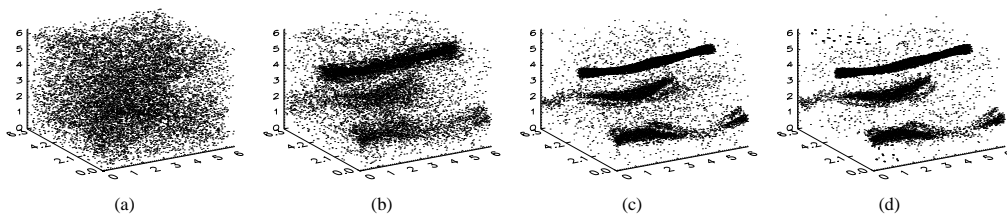


**Figure 2.11:** For a homogeneous distribution of one hundred initial conditions we plot only the last 1000 steps of the map evolution for different values of  $\lambda$ : (a)  $\lambda = 2$ , (b)  $\lambda = 1$ , (c)  $\lambda = 0.6$ , (d)  $\lambda = 0.5$ . The images represent the  $[0, 2\pi]$  cube in the phase space.

In the two-action case, the eigenvalues of the Jacobian are very small on large portions of the trajectory, so that separation may only occur sporadically during the short time intervals in which the fluid parcel crosses the fast-motion resonances [69]. Most of the time, particles and fluid parcels follow exponentially convergent trajectories, causing the separations to be practi-

cally unobservable except for very small values of  $\lambda$ . Most probably, once the particles converge to the fluid dynamics, they remain attached. However, by adding a small amount of white noise, we can continually force the impurity to fluctuate around the flow trajectory [45]. From the application point of view, this noise may be considered to represent the effect of small scale turbulence, thermal fluctuations, etc., but here we use it only as a dynamical device. With this, the particles arrive in the neighborhood of the resonances with a non-negligible velocity mismatch with the fluid that is considerably amplified during the transit across the resonance. The measure of this mismatch is then a good detector of the proximity of the resonance. Consider the

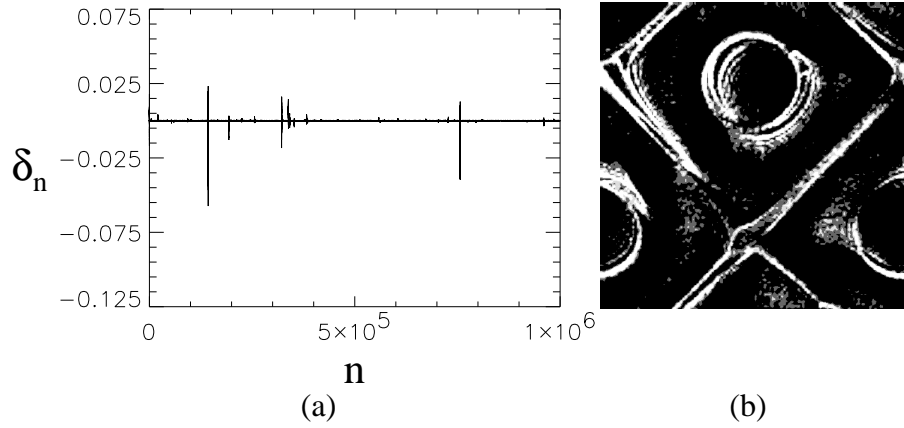


**Figure 2.12:** (a) The evolution of one component of the difference  $\delta_n$  between the particle and the fluid-flow velocities as a function of the number of iterations. (b) An  $xy$  slice of the phase space with those points where  $\delta_n$  is greater than  $\delta_0$ . The square is the region  $[0, 2\pi] \times [0, 2\pi]$ .

following stochastic iterative system:

$$X_{n+2} - T(X_{n+1}) = e^{-\lambda} \nabla T \cdot (X_{n+1} - T(X_n)) + \xi_n, \quad (2.44)$$

where the noise term  $\xi_n$  satisfies  $\langle \xi_n \rangle = 0$ , and  $\langle \xi_n \xi_m \rangle = \varepsilon(1 - e^{-2\lambda}) \delta_{mn} \mathbf{I}$ . We can recast Eq. (2.44) into

$$\begin{aligned} x_{n+1} &= T(x_n) + \delta_n, \\ \delta_{n+1} &= e^{-\lambda} \nabla T \cdot \delta_n + \xi_n, \end{aligned} \quad (2.45)$$

if we define the velocity separation between the fluid and the particle as  $\delta_n = x_{n+1} - T(x_n)$ . We illustrate the behavior referred above by studying the most ergodic two-action case, in which all the fluid trajectories intersect



the resonant lines. In Fig. (2.12a) we show how  $\delta_n$  grows strongly at some points, which correspond to the crossings of the resonant lines. In Fig. (2.12b) we plot an  $xy$  slice of the three-dimensional cube, choosing those points where the value of  $\delta_n$  is greater than a minimum value  $\delta_0$ . As shown, we recover the resonant structure previously noted [69, 142].

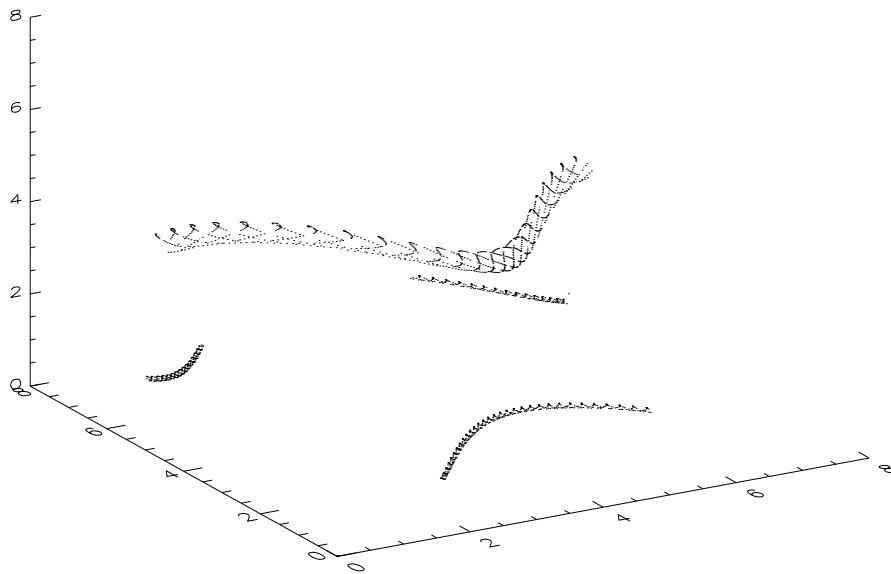


**Figure 2.13:** Stroboscopic sampling ( $\Delta t=1$ ) of the position of 10 particles initially distributed at random in a flow described by Eq. (2.46) with  $A=2$ ,  $B=0.4$ ,  $C=1.2$ . The dots represent the positions of these particles at the strobing periods 1000 to 2000.

In order to confirm that the above-described behavior is not an artefact of our mapping-based approach, we have performed analogous simulations using a continuous-time model as a base flow. We have considered neutrally buoyant particles immersed in a modified version of the ABC flow,

$$\begin{aligned} \dot{x} &= (1 + \sin 2\pi t) \cdot (A \sin z + C \cos y), \\ \dot{y} &= (1 + \sin 2\pi(t + 1/3)) \cdot (B \sin x + A \cos z), \\ \dot{z} &= (1 + \sin 2\pi(t + 2/3)) \cdot (C \sin y + B \cos x), \end{aligned} \quad (2.46)$$

in which each component of the velocity vector field is sinusoidally modulated with a relative phase shift of  $2\pi/3$ , and where  $x$ ,  $y$ , and  $z$  are to be considered modulo  $2\pi$ . While a detailed analysis of the dynamical aspects of this flow is

beyond the scope of this Thesis, we advance that it shows structures similar to those of the ABC maps, i.e., a complex array of KAM sheets and tubes surrounded by chaotic volumes. Neutrally buoyant particles evolved according to the true (simplified) Maxey–Riley equations, Eq. (2.34), based on this flow, show exactly the same tendency to accumulate inside KAM tubes as in the map case (Fig. 2.13).

## 2.7 Noisy Bailout Embeddings

In this Section we study the properties of bailout embeddings in the presence of an extremely small amount of white noise [45]. We show that there are two stages to the modulation of the invariant density in the small-noise limit. At first the bailout is everywhere stable, but fluctuations around the stable embedding may be restored towards the stable manifold at different rates and thus acquire different expectation values. These fluctuations leave a mark on the invariant density through a mechanism similar to spatially modulated temperature [37, 103], namely, the dynamics prefer to escape the hot regions. This is balanced in a nontrivial fashion by mixing in the map to create interesting scars in the invariant density. As the bailout parameter is changed, the noise prefactor can diverge, and the embedding loses stability at some points, so honest-to-goodness detachment ensues.

The study of Hamiltonian systems is hampered by the uninteresting features of the ergodic measures: if the system is ergodic, then it is Lebesgue automatically; if it is not, then it does not have a unique invariant measure to begin with: in the case of KAM systems, the measure disintegrates into a millefeuille of KAM tori and ergodic regions. The addition of a small amount of white noise — i.e., coupling to a thermal bath — renders the system automatically ergodic, and a unique stable invariant measure (in the Sinai–Ruelle–Bowen sense [62, 107]) appears; but it is still the Lebesgue measure, and thus all properties to be studied are necessarily higher order. This is even a problem for plotting what the phase space looks like. Bailout embeddings allow the use of measure-theoretical studies in Hamiltonian systems, by permitting the dynamics to leave nontrivial shadows upon an invariant measure.

We study the bailout embedding

$$x_{n+2} - f(x_{n+1}) = e^{-\gamma} \nabla f|_{x_n} (x_{n+1} - f(x_n)) + \xi_n \quad (2.47)$$

of a dynamical system  $x_{n+1} = f(x_n)$ , in which as before we have used the gradient of the map as the bailout function. New here is the noise term  $\xi_n$ , with statistics

$$\begin{aligned} \langle \xi_n \rangle &= 0, \\ \langle \xi_n \xi_m \rangle &= \varepsilon (1 - e^{-2\gamma}) \delta_{mn} \mathbf{I}. \end{aligned} \quad (2.48)$$

We can separate this two-step recurrence into two one-step recurrences

$$x_{n+1} = f(x_n) + \delta_n, \quad (2.49)$$

$$\delta_{n+1} = e^{-\gamma} \nabla f|_{x_n} \delta_n + \xi_n. \quad (2.50)$$

Note that now the second equation is affine, being linear in the  $\delta$  plus a homogeneously added noise process, so it could be solved analytically for  $\delta$  if we knew what the  $x$  were in the past. Under the assumption that the  $\delta$  are infinitesimally small, we get the classical orbits  $x_{n+1} = f(x_n)$ , and we can explicitly write down the solution for the  $\delta$

$$\begin{aligned} \delta_{n+1} &= \xi_n + e^{-\gamma} \nabla f|_{x_n} \\ &\quad \times \left( \xi_{n-1} + e^{-\gamma} \nabla f|_{x_{n-1}} \right. \\ &\quad \left. \times \left( \xi_{n-2} + e^{-\gamma} \nabla f|_{x_{n-2}} (\xi_{n-3} + \dots) \right) \right), \end{aligned} \quad (2.51)$$

or, after unwrapping,

$$\begin{aligned} \delta_{n+1} &= \xi_n + e^{-\gamma} \nabla f|_{x_n} \xi_{n-1} \\ &\quad + e^{-2\gamma} \nabla f|_{x_n} \nabla f|_{x_{n-1}} \xi_{n-2} \\ &\quad + e^{-3\gamma} \nabla f|_{x_n} \nabla f|_{x_{n-1}} \nabla f|_{x_{n-2}} \xi_{n-3} + \dots, \end{aligned} \quad (2.52)$$

which may be written more compactly as

$$\delta_{n+1} = \sum_{j=0}^n \left( \xi_{n-j} e^{-j\gamma} \prod_{k=0}^j \nabla f|_{x_{n-k}} \right). \quad (2.53)$$

Then, given that the  $\xi$  are uncorrelated, the expectation value of  $\delta^2$  is given as the sum of the squares of the terms, or

$$\frac{\langle \delta^2 \rangle}{\langle \xi^2 \rangle} = \sum_{j=0}^{\infty} \left( e^{-j\gamma} \prod_{k=0}^j \nabla f|_{x_{n-k}} \right)^2, \quad (2.54)$$

where the  $\langle \cdot \rangle$  are averages over the  $\xi$  process. Clearly, as  $\gamma \rightarrow \infty$  this expression tends to 1.

In the regime in which  $\gamma \gg 0$  and  $\langle \xi^2 \rangle \ll 1$ , the  $\langle \delta_{n+1}^2 \rangle \approx \langle \xi^2 \rangle \ll 1$  and hence the trajectories collapse upon the classical orbits:  $x_{n+1} = f(x_n) + \delta_n \approx f(x_n)$ . Under these circumstances, the embedding is always stable, and there is no detachment. In this regime we can compute explicitly the above expression Eq. 2.54 which depends only on the current value of the position:

$$T(x) = \frac{\langle \delta^2 \rangle}{\langle \xi^2 \rangle} = \sum_{j=0}^{\infty} \left( e^{-j\gamma} \prod_{k=0}^j \nabla f|_{f^{-k}(x)} \right)^2 \quad (2.55)$$

Thus  $T(x)$  defines a sort of temperature for the fluctuations  $\delta$ .

As long as the  $\delta$  are infinitesimally small, they do not — and cannot — affect the  $x$  dynamics, which has collapsed unto the classical trajectories; thus they do not affect the invariant density  $P(x)$  either, and hence  $P(x)$  is asymptotic to the Lebesgue measure. For infinitesimally small  $\langle \xi^2 \rangle$ , as  $\gamma$  is made smaller, the sum acquires more and more terms because the prefactor  $e^{-j\gamma}$  decays more and more slowly. For any value of  $\gamma$ , the products of the gradients grow or shrink roughly as the exponential of the Lyapunov exponent times  $j$ . Thus, when  $\gamma$  equals the local Lyapunov exponent at  $x$ , the series defining  $T(x)$  stops being absolutely convergent at  $x$  and may blow up. As  $\gamma$  is lowered further, more and more points  $x$  have local Lyapunov exponents greater than  $\gamma$  and so  $T(x)$  formally diverges at more and more points  $x$ .

Where  $T(x) = \infty$  it means that  $\langle \delta_n^2 \rangle$  is finite even if  $\langle \xi^2 \rangle$  is infinitesimally small. Thus the embedding trajectories have detached from the actual trajectories, and the approximations given above break down. Detachment is the process that was first envisioned as being characteristic of bailout embeddings [14, 44]. However, by employing noise in the embedding and carefully controlling its use, we can see the process that occurs before detachment. If  $T(x)$  is finite and smaller than  $1/\langle \xi^2 \rangle$ , then we have a regime in which the  $\delta$ s

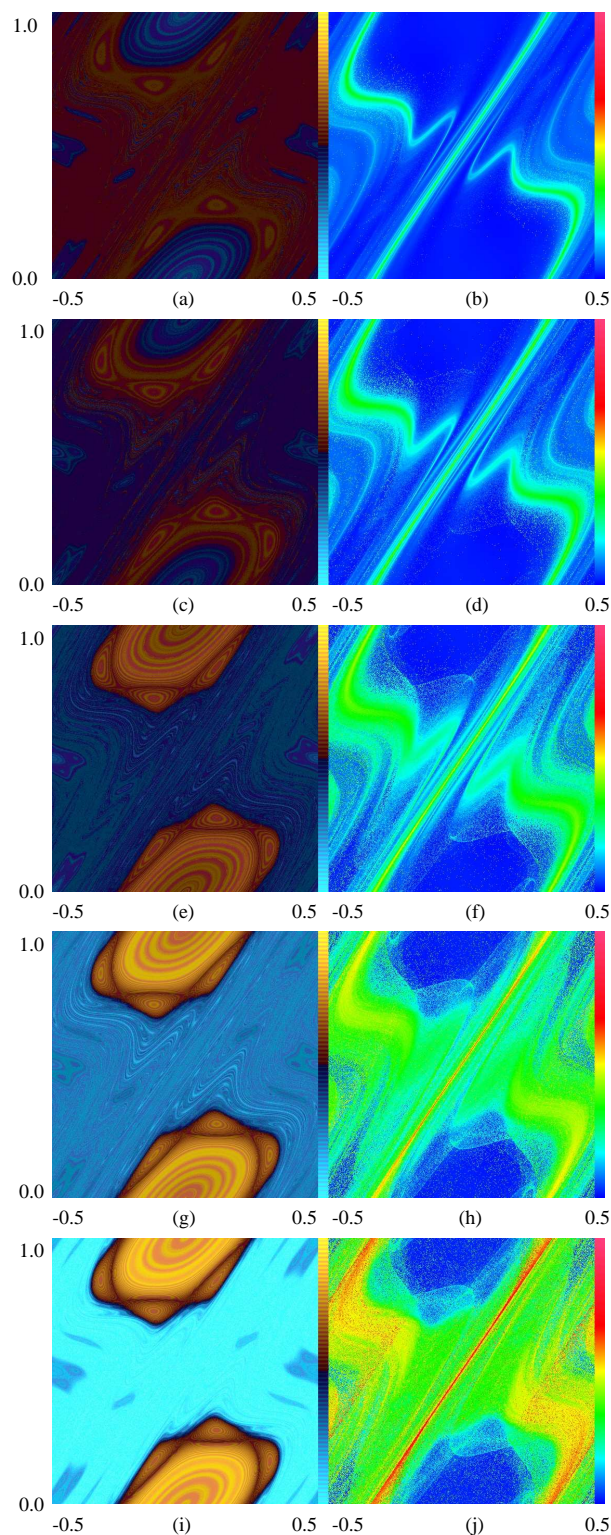


**Figure 2.14:** Noisy bailout embedding histograms (left) and temperature plots (right) for standard map nonlinearity parameter  $k = 1.5$ , noise parameter  $\varepsilon = 10^{-8}$ , and bailout parameter (a), (b),  $\gamma = 0.7$ ; (c), (d),  $\gamma = 0.65$ ; (e), (f),  $\gamma = 0.6$ ; (g), (h),  $\gamma = 0.55$ ; and (i), (j),  $\gamma = 0.5$ . The striped histogram color scale runs from yellow at high densities to cyan at low densities, while the temperature color scale runs from red (high) to blue (low).

behave as a noise term added to the classical trajectories:  $x_{n+1} = f(x_n) + \delta_n$  with  $\langle \delta_n^2 \rangle = \langle \xi^2 \rangle T(x)$ .

We have, alas, lost the whiteness of the process, since  $\delta_{n+1}$  and  $\delta_n$  are not any longer statistically independent. However, this is in this case a second-order effect compared with the fact that the noise process amplitude, being modulated as a function of position, will immediately lead to inhomogeneous coverage by the dynamics: hot regions will be avoided while cold regions will preserve the dynamics. All of this is in a context in which the embedding is essentially stable throughout. Thus this process is not detachment per se, but rather avoidance.

We can illustrate this best in the context of the standard map acting as before as the base flow. Figure 2.14 shows side by side the visit histogram — the invariant measure — (left-hand side) together with the corresponding space-dependent temperature (right-hand side) for a decreasing sequence of the bailout parameter  $\gamma$  and fixed values of the standard-map nonlinearity and noise parameters. While, for  $\gamma$  larger than 0.55, the temperature is a well-defined function of the space coordinates, it shows signs of divergence — the red regions, which become larger as  $\gamma$  decreases — for  $\gamma$  smaller than 0.55. On the other hand, however, the invariant measure displays features related to the structure of  $T$  on both sides of this transition, i.e., even before detachment occurs.

As we anticipated at the end of the previous Section, the noisy bailout can give us useful information about the dynamics in a non-Hamiltonian context as well. In Fig. 2.15 we illustrate this phenomenon. First we analyze a one-action situation showing the temperature amplitude, as well as the impurity dynamics; Figs 2.15a and 2.15b respectively. Again we use slices of the three-dimensional cube to show the situation more clearly. Fig. 2.15a shows the temperature in a scaled color code. Fig. 2.15b shows a histogram of visits that a single particle pays to each bin of the space. The agreement between the higher-temperature regions and the less-visited ones is evident. Next we plot the same pictures but in the two-action case studied before; Figs 2.15c and 2.15d. Finally, we apply this analysis to a generic chaotic case where we do not have any information about the phase space structure. We show in Fig. 2.15e how the invariant manifolds are very twisted, and in Fig. 2.15f how

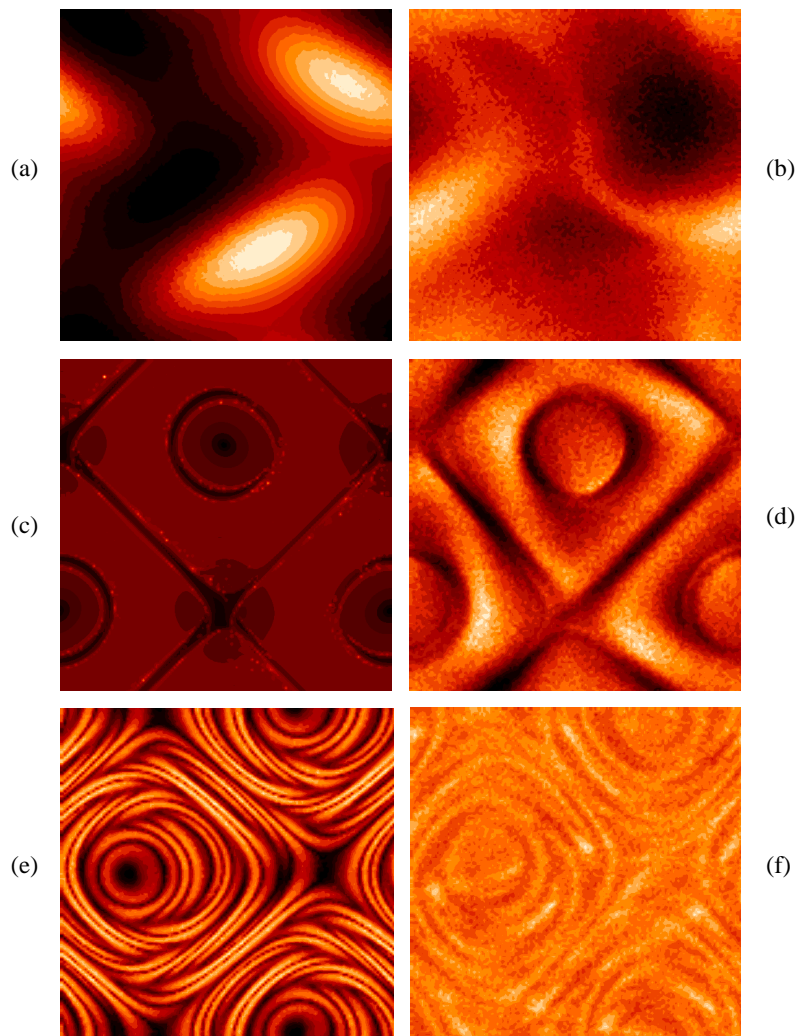


**Figure 2.15:** The temperature amplitude — lighter is hotter — for the one-action, two-action and most chaotic cases ((a), (c), and (e) respectively), together with the corresponding slices of the impurity dynamics (histogram) in the phase space ((b), (d), and (f)). All images are the  $[0, 2\pi] \times [0, 2\pi]$  region in the  $xy$  axis, for a slice in the  $z$  direction corresponding to the values  $z \in [0, 0.49]$ .

the particles, even so, try to find the coldest regions of the flow.

## 2.8 Bifurcations in Bailout Embedding

We will now explore some interesting connections of the dynamical behavior of the bailout embeddings with two bifurcation phenomena occurring in dynamical systems with a symmetry. These are the so called *bubbling* and *blowout* bifurcations which gives rise to a variety of dynamical behaviors among which,

the ones known as bubbling and on-off intermittency, are of special interest here.

In dynamics, the presence of symmetries usually implies the existence of lower-dimensional submanifolds of the full phase space that are dynamically invariant, because symmetric states must evolve into symmetric states. The motion restricted to these invariant manifolds is often chaotic. This occurs, for instance, in synchronized chaotic oscillators, and in extended systems with spatial symmetry. The existence of chaotic attractors in the restricted dynamics can have interesting consequences for the behavior of the full system [132, 9].

An interesting question is whether the attractors on invariant manifolds are also attractors of the unrestricted dynamics. Consider the case in which a parameter controls the dynamics transversal to the invariant manifold while leaving unaffected the dynamics restricted to the invariant manifold [9]. Below a critical value of this parameter, the manifold is transversally stable and any attractor within it is also a global attractor. When the parameter exceeds the critical value, some invariant set embedded in the attractor becomes transversally unstable. Although most trajectories initially close to the attractor in the invariant manifold may still remain close to it, there is now a small set of points in any neighborhood of the attractor that diverge from the invariant manifold. Increasing the parameter still further, the full attractor becomes transversally unstable. These two scenarios, named bubbling and blowout bifurcations, may lead either to so-called riddled basins [4] or to strong temporal bursting termed on–off intermittency [132, 83, 145, 182], depending on the nature of the dynamics away from the invariant manifold.

In the foregoing, we have supposed that both the restricted and the unrestricted dynamics are dissipative. But we might envision a case in which the global dissipative dynamics have an invariant manifold on which the restricted dynamics is conservative; described, for example, by a Hamiltonian flow or a volume-preserving (Liouvillian) map. The orbits on the invariant manifold then exhibit, instead of attractors, the typical Hamiltonian phase-space structure characterized by the coexistence of chaotic regions and Kolmogorov–Arnold–Moser (KAM) tori. However, since the full dynamics are dissipative, a part or even the whole family of the restricted Hamiltonian or-



bits may be global attractors. Furthermore, a parameter can now control the transversal stability of the invariant manifold in the same way as in blowout bifurcations, but now governing which part of the Hamiltonian dynamics is globally attracting, and which is not.

The aim of this section is to show that these dynamics are observed in a physical system of finite-sized particles driven by an incompressible fluid flow (Section. 6.15), and have been harnessed to work in the different context of the study of chaotic dynamical systems in the technique of bailout embedding, previously introduced in Section. (2.5). We establish and investigate the conceptual connection between the dynamics of the bailout embedding of a Hamiltonian system and the dynamical regimes associated with the occurrence of bubbling and blowout bifurcations. The roles of the invariant manifold and the dynamics restricted to it — required in bubbling and blowout bifurcating systems — are played in the bailout embedding by the embedded Hamiltonian dynamical system. The Hamiltonian nature of the dynamics is precisely the distinctive feature of this instance of a bubbling/blowout bifurcation. The detachment of the embedding trajectories from the original ones can thus be thought of as transient on–off intermittency, and noise-induced avoidance of some regions of the embedded phase space can be recognized as Hamiltonian bubbling.

### 2.8.1 Bubbling and blowout bifurcations

The behavior of a bailout embedding can be analyzed in connection with bubbling and blowout bifurcations. These bifurcations have been studied in dissipative dynamical systems which, due to symmetries or other constraints, have an invariant submanifold of the whole phase space that contains an attractor of the global dynamics. In such situations, one may wish to study the stability of the invariant manifold with respect to small departures in a transversal direction. This stability is indicated by the transversal Lyapunov exponent, which is the growth rate  $h_{\perp}$  of a transversal perturbation averaged over a trajectory on the manifold. Specifically, we may follow the evolution of an infinitesimal perturbation  $\delta_n$ , transversal to the invariant manifold, along the attractor trajectory  $X_n$ . The transversal Lyapunov exponent is then de-

defined as

$$h_{\perp} = \lim_{n \rightarrow \infty} \frac{1}{n} \ln[\delta_n/\delta_0]. \quad (2.56)$$

If  $h_{\perp} < 0$  for all orbits in the manifold then any transversal perturbation will eventually die out. In this case, if there is a unique topological attractor [34] for the dynamics restricted to the manifold, it will also be a topological attractor for the full dynamics.

The situation is far more complex if the attractor itself is transversally stable while one or more periodic orbits embedded in the attractor are not, so that  $h_{\perp} > 0$  for these orbits. When, as a consequence of changing a parameter, the system passes from the fully stable situation of the previous paragraph to one in which some transversally unstable orbits coexist with the stable attractor, it is said that a bubbling bifurcation has taken place.

In the new-born regime, named bubbling, when a trajectory visits the neighborhood of an orbit with positive  $h_{\perp}$ , a transversal perturbation temporarily grows. If the attractor in the manifold is the only attractor of the system, this local relative instability is inconsequential; at most it spoils temporarily the asymptotically safe convergence to the the attractor. But, on the other hand, if the attractor is not unique, the local instability provides a gateway for a trajectory apparently converging to the stable attractor to escape and end up on another attractor. In other words, the basin of attraction of one attractor is riddled by filaments of the basin of attraction of the other. Notice that this implies that the attractor is no longer of the topological type. It is, instead, a so-called Milnor attractor, because it attracts trajectories with initial conditions in a set of positive Lebesgue measure, but there is no neighborhood of the attractor from which all trajectories are attracted.

Even in the case where the attractor in the invariant manifold is unique, the bubbling regime has another interesting property that manifests itself when a small amount of noise is added to the deterministic dynamics. In the absence of noise the overall negative transversal Lyapunov exponent implies that fluctuations away from the invariant manifold are bound to asymptotically die out. A finite noise term, however, may be considered as a permanent source of finite-time fluctuations that now are amplified on the occasions when the dynamics passes near a transversally unstable orbit. The result is a kind of noise-sustained intermittency, where short intervals of relatively highly

fluctuating transversal motion alternate randomly with intervals where the motion occurs very close to the invariant manifold.

As the same parameter responsible for the bubbling bifurcation is increased further, a second threshold is commonly reached: a value at which the full attractor of the invariant manifold becomes transversally unstable. This transition is called a blowout bifurcation. Now, intermittent bursts of motion away from the manifold are unavoidable unless a very close matching of the initial condition of the trajectories is made to situate the trajectory on that manifold. It is enough to have a very small uncertainty in the initial condition to sustain the fluctuations. The regime called on–off intermittency has now been reached.

This behavior is illustrated by the well studied example of a system of two identical dissipative Hénon maps

$$\mathbf{x}(n+1) = \mathbf{T} \begin{pmatrix} x(n) \\ y(n) \end{pmatrix} \equiv \begin{pmatrix} y(n) + 1 - ax^2(n) \\ bx(n) \end{pmatrix}, \quad (2.57)$$

coupled through diffusive type of interaction [11]:

$$\begin{aligned} \mathbf{x}_1(n+1) &= \mathbf{T}(\mathbf{x}_1(n)) + \varepsilon (\mathbf{T}(\mathbf{x}_2(n)) - \mathbf{T}(\mathbf{x}_1(n))), \\ \mathbf{x}_2(n+1) &= \mathbf{T}(\mathbf{x}_2(n)) + \varepsilon (\mathbf{T}(\mathbf{x}_1(n)) - \mathbf{T}(\mathbf{x}_2(n))). \end{aligned} \quad (2.58)$$

Obviously, the manifold  $(x_1, y_1) = (x_2, y_2)$  is dynamically invariant and hosts the same attractor as the individual uncoupled maps; Fig. 2.16(a) displays the attractor. In Fig. 2.16(b) we show the temporal behavior of the mismatch between the  $x$  coordinates of each map for an  $\varepsilon$  value for which the computed transversal Lyapunov exponent is positive, i.e, in the regime of on–off intermittency. The relevance of this example here is to show the strong similarity with the behavior reported in Fig. 2.10(c). However, it should be remarked that while the wild fluctuations of  $x_1 - x_2$  in the present case never cease to occur, the fluctuations of  $u_n$  in the former only last for a finite period of time, until the trajectory finally settles within a KAM torus.

## 2.8.2 Bailout effect and blowout bifurcation

The discussion in Sec. 2.8.1 concerns dissipative systems. This is important in the sense that the invariant submanifold under consideration may contain

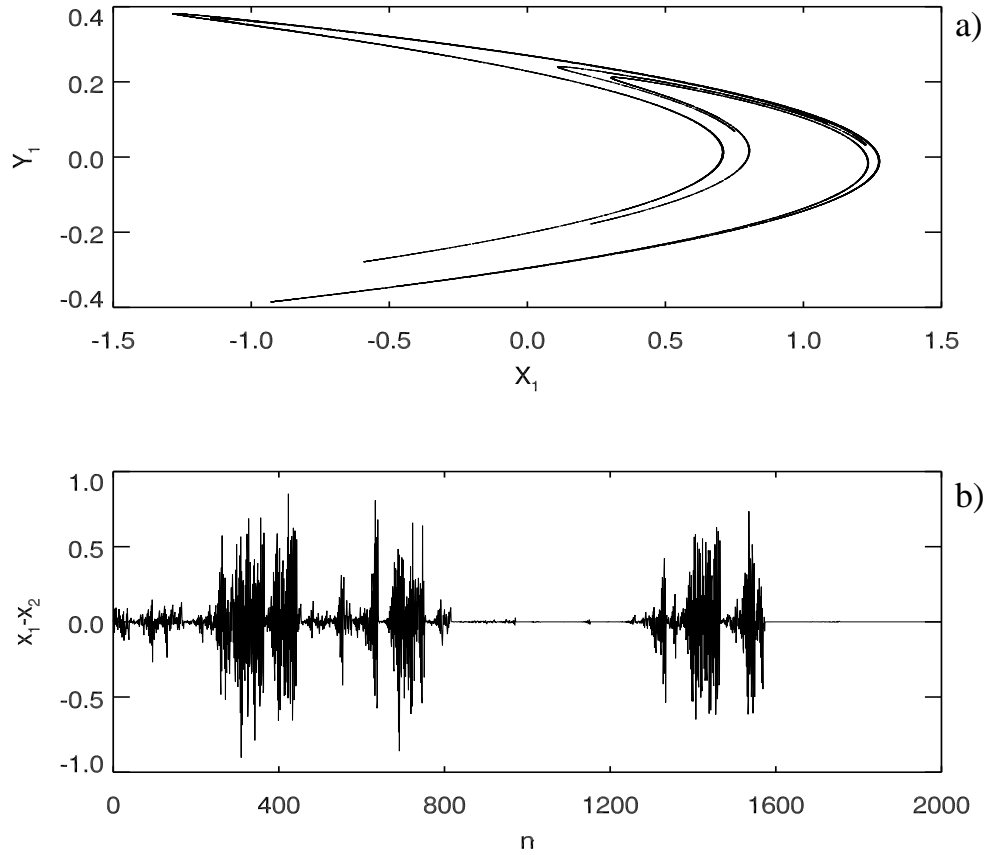


**Figure 2.16:** (a) The Hénon attractor for the individual uncoupled maps with  $a = 1.4$  and  $b = 0.3$ . (b) Time evolution for  $x_1 - x_2$  showing on-off intermittency.

an attracting set for trajectories starting either in the manifold itself or in the rest of the phase space.

In order to show that the bailout effect corresponds to the occurrence of a blowout bifurcation, we again consider the specific example of the standard map. The phase space for the bailout embedding of this problem is four dimensional, with coordinates  $(x_n, y_n, u_n, v_n)$ , and its dynamics was defined in Sec. 2. It is clear from the construction of the embedding that  $u_n = v_n = 0$  is an invariant two-dimensional submanifold of the four-dimensional phase space; if  $u_n = v_n = 0$  at  $n = 0$ , Eqs. (2.39) imply that this is so for all  $n > 0$ .

We now consider again the dynamics of infinitesimal perturbations  $(\delta u_n, \delta v_n)$  transverse to the invariant manifold. In order to compute the transversal Lyapunov exponent, one has to take a trajectory on the invariant manifold and plug it into the linearized equations for the perturbations. Notice that the last

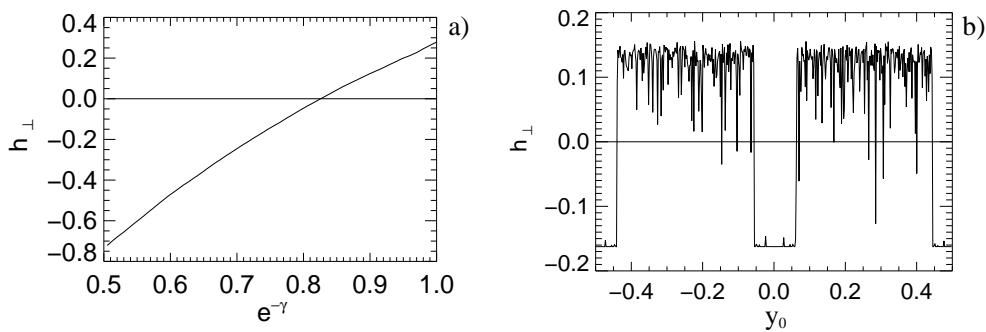


**Figure 2.17:** For the bailout embedding of the standard map with  $k = 1.5$ , the transverse Lyapunov exponent  $h_{\perp}$  versus (a) the parameter  $e^{-\gamma}$  for  $0.5 \leq e^{-\gamma} \leq 1$ , and (b) versus the initial condition  $y_0 \in [-0.5, 0.5]$ ,  $x_0 = -0.5$  for  $e^{-\gamma} = 0.85$ .

two Eqs. (2.39) are linear in  $u$  and  $v$ , and therefore represent also the evolution of  $\delta u_n$  and  $\delta v_n$ . Note also that the trajectories on the invariant manifold are the trajectories of the original standard map obtained by setting  $u$  and  $v$  to zero in the first two Eqs. (2.39). Plugging a typical chaotic solution  $(x_n, y_n)$  of the standard map into the last two we compute its transversal Lyapunov exponent  $h_{\perp}$  by setting  $\delta_n = \{[\delta u_n]^2 + [\delta v_n]^2\}^{\frac{1}{2}} = \{u_n^2 + v_n^2\}^{\frac{1}{2}}$  in Eq. (2.56).

Figure 2.17(a) shows a plot of  $h_{\perp}$  versus the parameter  $e^{-\gamma}$  for a specific chaotic trajectory of the standard map. We see that  $h_{\perp}$  increases with increasing  $e^{-\gamma}$ , changing sign at the critical value of  $\gamma = \gamma_c \approx 0.3$ . One can say that at this value, a Hamiltonian version of a blowout bifurcation occurs. Let us clarify the special characteristics imposed by the Hamiltonian dynamics. By definition,  $h_{\perp}$  is an average over the whole chosen chaotic trajectory, and therefore the change in its sign has the same implications as in the case of the dissipative dynamics in so far as that particular chaotic region is concerned. There are, however, two main differences. First, in the Hamiltonian case, no trajectory, and in particular, no chaotic trajectory, is an attractor. Therefore, the positiveness of the transversal Lyapunov exponent only has an effect on the trajectories starting in the corresponding chaotic region on the invariant manifold. On the other hand, in Hamiltonian systems one typically encounters a very complex coexistence of chaotic regions with nearly integrable ones — the KAM islands — and the corresponding  $h_{\perp}$  are completely unrelated since no trajectory can visit both regions. As a consequence one can typically find that while trajectories are forced to diverge from the invariant manifold

in some regions they may reconverge onto it in some others.

To demonstrate that this is the situation with the bailout embedding of Hamiltonian systems, we study the behavior of the transversal Lyapunov exponent as a function of the initial conditions in the bailout-embedded standard map. We compute  $h_{\perp}$  for a given value of  $\gamma$  above the bifurcation and initial conditions uniformly distributed on the one-dimensional line defined by  $y_0 \in [-0.5, 0.5], x_0 = -0.5$ . Since the dynamics in the invariant subspace are Hamiltonian, the line of initial conditions cuts both chaotic areas and KAM surfaces. Figure 2.17(b) shows the transversal Lyapunov exponent along this line, making it evident that it is positive for most chaotic trajectories, but negative in the regular regions where the embedding finally converges.

By construction, the bailout embedding of any dynamical system does not possess global attractors other than those in the invariant manifold. This is crucial to ensure that the blowout bifurcation leads to on–off intermittency. However, the Hamiltonian nature of the dynamics restricted to the invariant manifold implies the coexistence of sets of orbits that are transversally unstable with other sets that are not. Embedding trajectories starting in the neighborhood of the invariant manifold are repelled from it and bounce around the phase space, coming back to the invariant manifold and diverging away from it in an intermittent fashion, until they eventually arrive close enough to one of the transversally stable sets to become trapped. The on–off intermittency displayed in this case is therefore only transient, as we can appreciate in Fig. 2.18.

Lastly, we note that on decreasing  $\gamma$ , progressively more orbits on the invariant manifold become transversally unstable, and the number of trajectories starting from random initial conditions that eventually settle into the KAM tori in this way increases — as we anticipated in Sec. 2.

### 2.8.3 Blowout bifurcations in the presence of noise: Bubbling and avoidance

The alteration of the dynamical behavior around bubbling and blowout bifurcations in the presence of imperfect symmetry and noise has been studied by several authors [144, 83, 83, 145, 9, 182]. Among the many observed effects, it is particularly important for our purposes to recall that the addition of

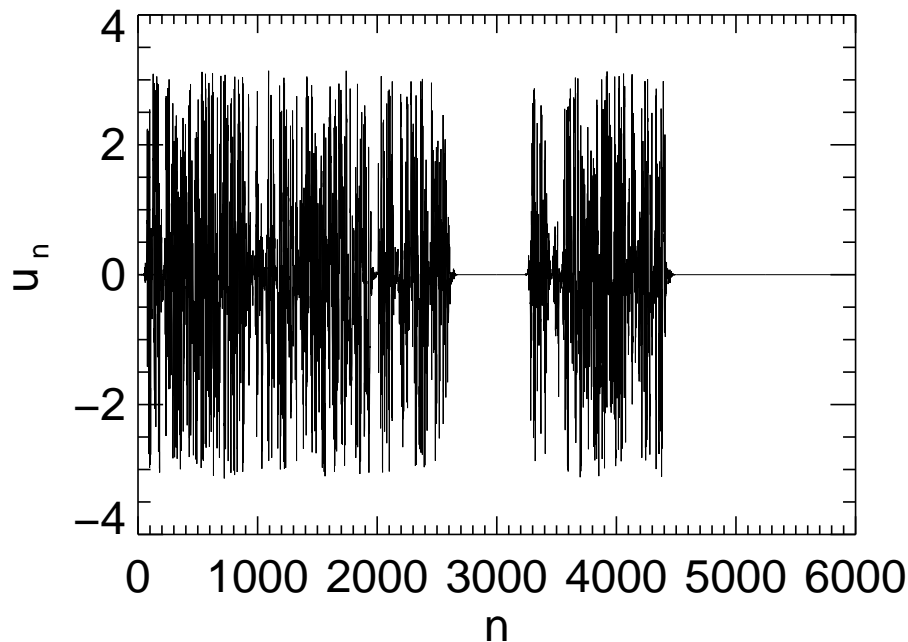


**Figure 2.18:** Time evolution of  $u_n$  for a randomly selected initial condition, for  $\gamma \leq \gamma_c$ . Transient on-off intermittency is clearly seen before the embedding finally collapses inside the KAM tori.

noise to a system that experiences a blowout bifurcation may lead to dynamics qualitatively similar to on-off intermittency, but appearing before the actual blowout bifurcation has occurred. This regime has been dubbed bubbling [9], because its onset is associated with the occurrence of a bubbling bifurcation.

In turn, the properties of bailout embeddings in the presence of a small amount of white noise have been studied in Section 2.7. It has been shown that as the bailout parameter is changed while keeping the noise intensity fixed, two regimes displaying increasingly strong modulations of the invariant density appear [45]. At first the bailout is globally stable, but fluctuations around the stable embedding are restored towards the stable manifold at different rates, thereby acquiring different expectation values at different points on the manifold. This behavior leaves a mark on the invariant density that can be described by means of a mechanism similar to spatially modulated temperature [37, 103]. Indeed, the transversal fluctuations can be shown to be locally proportional to the noise amplitude with a space-dependent prefactor that only depends on dynamical quantities. The dynamics thus prefer to escape the hot regions of the invariant manifold (the phase space of the embedded system) and to freeze onto the cold ones. This is balanced in a non-

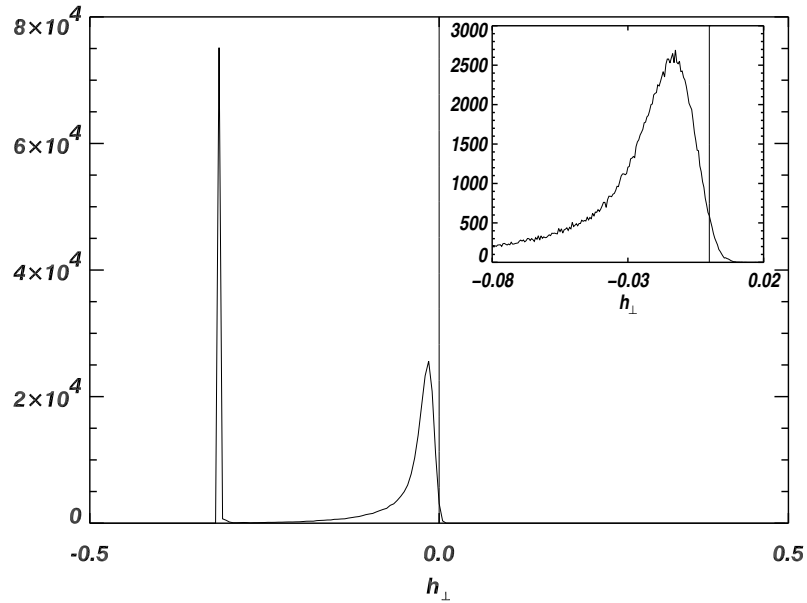


**Figure 2.19:** For a parameter setting below the blowout bifurcation,  $e^{-\gamma} = 0.65$ , a histogram of the finite-time transverse Lyapunov exponent  $h_{\perp}$  computed from 1000 initial conditions randomly chosen in the phase space of the standard map with  $k = 1.5$ . Although the asymptotic value of  $h_{\perp}$  for trajectories on the chaotic sea is slightly negative, at finite times there are many trajectories that experience repulsion from the invariant subspace, reflected by the spread of this histogram into the positive region.

trivial fashion by mixing in the map to create interesting scars in the invariant density. This regime has been called avoidance. As the bailout parameter is changed, the noise prefactor eventually diverges and the embedding loses stability at some points. This is the stage described in Sec. 2, in which the embedding trajectories detach from those of the original system; to distinguish it from the avoidance regime it has been termed detachment [45].

Let us now show that the avoidance regime is a Hamiltonian manifestation of bubbling. For this purpose, we first investigate the behavior of the finite-time transversal Lyapunov exponent  $h_{\perp}$  for a bailout parameter below the onset of detachment. In Fig. 2.19 we have plotted a histogram showing the values of such an exponent computed for a thousand different initial conditions for the bailout embedding of the standard map in a regime where relatively large KAM islands coexist with broad chaotic regions. The calculations were carried out over a large number of iterations. Notice first that the histogram is composed of two peaks centered around negative values of  $h_{\perp}$ . The most negative peaks correspond to initial conditions lying within KAM



islands where the embedding is known to be stable even for larger values of the bailout parameter. The second peak, closer to zero but still negative, corresponds to initial conditions within the chaotic sea. Notice that this peak has a tail that includes positive values of  $h_{\perp}$ . On average, however,  $h_{\perp}$  is clearly negative even if it is restricted to the individual peaks. Moreover, both peaks converge to Dirac distribution functions supported at negative values as the computation time for  $h_{\perp}$  increases. This behavior is the signature of a bubbling type of bifurcation within the chaotic region: a few individual unstable orbits acquire positive transversal exponents while the whole chaotic trajectory is still transversally stable.

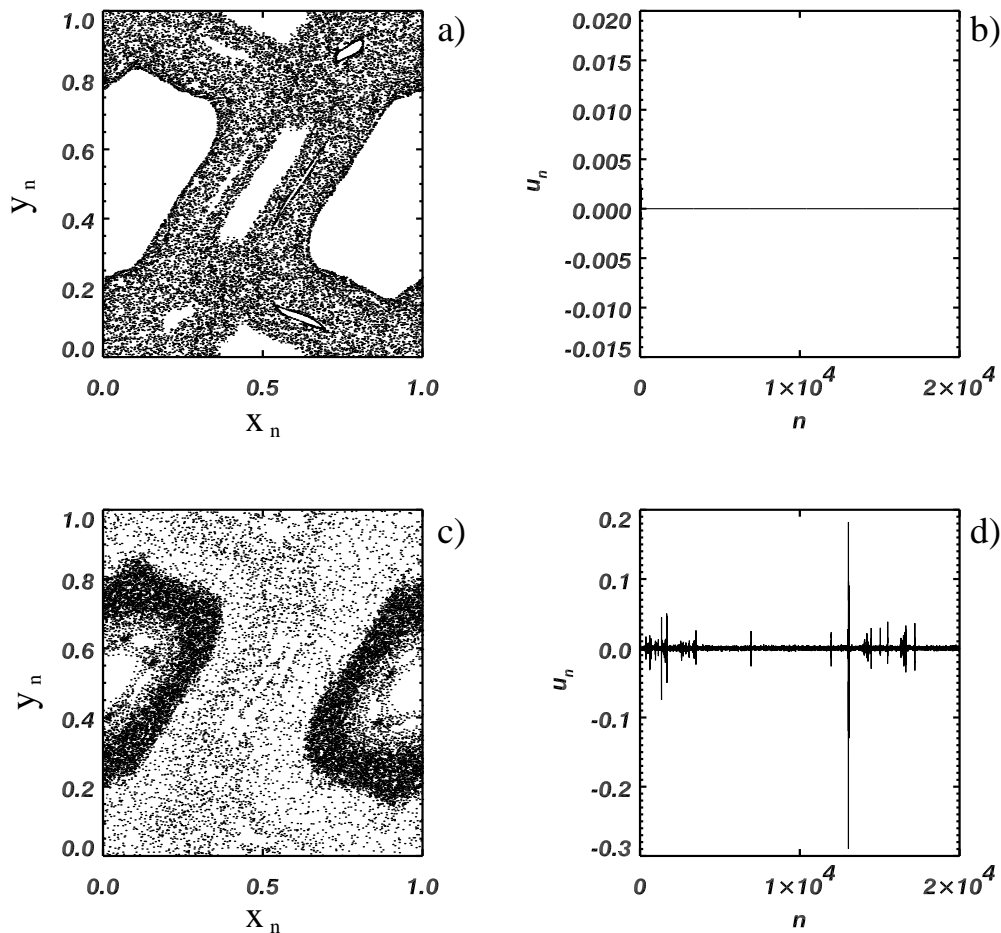


**Figure 2.20:** For the same parameters as in Fig. 2.19, (a and c respectively) a trajectory of the standard map with and without the added noise term; (b and d) the time evolution of the mismatch  $u_n$  in both cases.

The similarity of the bubbling and avoidance regimes is illustrated in

Fig. 2.20 with the same embedding of the standard map. The bailout parameter is the same as in Fig. 2.19, i.e., below the onset of detachment. Figures 2.20(a) and (b) represent the noise-free situation: the embedding trajectory coincides with a chaotic trajectory of the embedded system, and this coincidence is stable. In this situation, any initial mismatch transversal to the invariant manifold decays irreversibly to zero. In Figs. 2.20(c) and (d), on the other hand, a small amount of noise has been added to the embedding in the way indicated in Eq. (2.47). We can see that as a consequence of this noise term, on one hand the boundaries of the chaotic region have become fuzzier, and on the other a bursting mismatch between the embedding and the original system is now sustained over time. This noise-driven intermittent behavior is typical of systems in a bubbling regime.

## 2.9 Conclusions

Let us now summarize the variety of results described in this chapter. The main part of the original research presented here is the application of the method of bailout embedding to the description of the qualitative features of the dynamics of neutrally buoyant particles suspended in three dimensional time periodic incompressible flows. This is the first instance in which such a technique has been applied to a non-Hamiltonian, albeit volume preserving, dynamical system. Our approach has been pursued with two different goals in mind: on one hand, to contribute to the understanding of the physical behavior of impurities, and on the other, to provide a mathematical device to learn about the dynamical structures of the base flow in situations where these are very difficult to elucidate directly. Both bodies of information are important to improve our presently scant knowledge of the transport properties of three-dimensional fluid flows.

On a more theoretical avenue in the realm of dynamical systems, we have demonstrated here that two distinct behaviors, previously studied as unrelated phenomena, are different manifestations of a common situation. These are the ones induced by the blowout bifurcations, on one hand, and the detachment and avoidance phenomena in bailout embeddings. Blowout bifurcations, which arise naturally in the synchronization of chaotic oscillators,

or in continuum systems with spatial symmetry, are usually accompanied by undesirable phenomena like riddled basins or on–off intermittency that spoil the synchronism [10, 183, 48]. The difference between these scenarios and bailout embedding is the Hamiltonian nature of the dynamics restricted to the invariant manifold in the latter case. The nonexistence of an attractor in the invariant manifold of a bailout embedding permits one to avoid these undesirable phenomena, and, instead to exploit them positively. This is done by transforming a selected set of orbits into global attractors for the dynamics, allowing the embedding to target islands of order within the chaos.

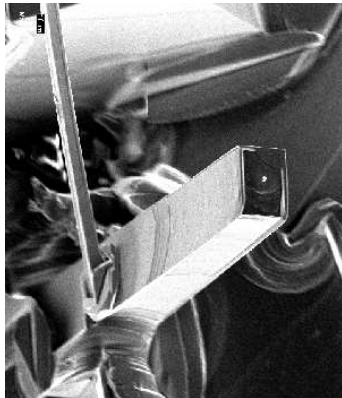
One interesting outstanding issue is whether the scaling behavior found in the intermittent dynamics of attractors experiencing bubbling and blowout bifurcations has a counterpart in the Hamiltonian case. This is a nontrivial question for two reasons. One is the transient nature of Hamiltonian on–off intermittency — the bailout effect — and the other is the fact that the statistics of the intermittent behavior of these systems under the action of noise is strongly sensitive to the statistics of KAM island sizes, which is highly non-universal. This strongly affects the typical time scale of transient intermittency in the absence of noise. We shall explore these problems in the future.

Finally, the application of the method of leaking provided further insight into the phase space structures of chaotic  $3D$  incompressible flows. In the example of the  $ABC$  map, which represents a general class of three-dimensional systems, it is shown to be a fast and suitable way in quantifying physical and geophysical systems. By measuring the fractal dimension in the highly chaotic  $ABC$  map with three non-zero Lyapunov exponents we found agreement with the theoretical expectations: the manifold related to the Lyapunov exponents with equal sign has the larger dimension. Fractal structures have recently been shown [138] to be quantifiers of mixing efficiency in magma processes. Until now, similar structures have been numerically reproduced only by following a dye droplet in closed  $3D$  flows, which, however cannot have a fractal dimension other than 3. Our method shows that by leaking the flow, we reproduce filaments whose fractal dimension and properties are even closer to the empirically observed.



# Chapter 3

## Growing bodies: Symmetry Breaking in Stirred Crystallization.



### 3.1 Introduction

*In this Chapter we will deal with the dynamics of crystallization. Five phenomena comprise its essence; they are: nucleation, crystal growth, movement and transport in space, aggregation and destruction of crystals. The diversity of realization of those phenomena makes crystallization one of its complicated forms of phase transformation, and its study a fascinating process.*

Crystallization is one of the most spread physical-chemical phenomena. It determines the properties of an enormous number of products of chemical, pharmaceutical and food industries. It is responsible for the formation of kidney stones and the development of bone tissue, for the accumulation of pollutants in the environment, for the rock formation and deposit in the seas and oceans,

and for a long etc. of natural instances.

Crystallization of chemical compounds from their solution is also an intriguing example of an active growing process of bodies, that strongly interact with the surrounding media, in a fluid environment. This interaction leads to an incredible number of surprising phenomena of which symmetry-breaking events are just an example.

A century and a half ago, Pasteur [135] discovered that inorganically synthesized tartaric acid differs from that obtained from plants in crystallizing as two mirror-image versions, or enantiomers, whereas only one of the two forms is found in biologically derived samples. This symmetry is broken in all biological systems, as amino acids, the building blocks of proteins, and thence of every living organism, are found in nature almost exclusively as the laevo (left-handed) enantiomers, while natural sugars are all dextro (right handed). In his famous experiment in 1848, Pasteur recrystallized a salt of tartaric acid and obtained two kinds of small crystals that were mirror images of each other. According to the Nobel laureate George Wald, 'No other chemical characteristic is as distinctive of living organisms as is optical activity.'

Pasteur's discovery arose at a meeting place of hitherto distinct disciplines. They were crystallography, physics and chemistry. He also showed that the fruits of the discovery benefited new branches in these sciences. But of course, not only material objects can have chirality or handedness. Bach's *The Art of the Fugue* is a beautiful example. Handedness is also an area of symmetry that is charged with philosophical implications. Immanuel Kant wrote about the puzzle of the isometric left and right hands that cannot be made to coincide in space and called the nonsuperposable mirror images 'incongruente Gegenstcke' (incongruent counterparts). Then, of course, Lord Kelvin gave a definition for chirality that has stood the test of time, 'I call any geometrical figure, or group of points, chiral, and say that it has chirality if its image in a plane of mirror, ideally realized, cannot be brought to coincide with itself.'

The discovery also brought about the realization that, in living organisms, biologically important substances occur in one of the two possible versions. This also led to the big question, 'How did it all start? What was the way one of the two was chosen?' This question deeply bothered Pasteur and a century later Vladimir Prelog called this a question of 'molecular theology' in

his Nobel lecture.

In contrast with Pasteur's discovery, inorganic chemical reactions involving chiral products commonly yield a racemic mixture of both laevo and dextro enantiomers [13]. So it came as a considerable surprise when a decade ago it was shown that simply stirring during the crystallization of sodium chlorate from solution was sufficient to produce a yield approaching 100% of just one enantiomer [98]. Whereas under normal conditions a distribution of the proportion of one or other enantiomer obtained in a series of experiments falls on a typical Gaussian curve, with the peak yield at 50% of each enantiomer, in the stirred experiments the distribution is bimodal, with the peak yield close to 100% of one or the other enantiomer (Fig.(3.1)). Similar results have been obtained in stirred crystallization of an organic molecule, 1,1'-binaphthyl, from its melt [99], and in the stirred synthesis of a chiral cobalt complex [7, 8]. Subsequent discussion has revolved around how this symmetry-breaking mechanism operates. The importance of the detachment of parts of the crystal surface upon contact with the stirring bar [108], and convection in the fluid [35], have both been proposed as possible mechanisms.

Our purpose here is to clarify the mechanism of chiral symmetry breaking during crystallization. Firstly, we show with numerical simulations that secondary nucleation — nucleation of new crystals caused by the presence of an existing primary crystal — is a nonlinear autocatalytic process capable of explaining the experimental results. Secondly, we present theoretical arguments to show that convection and mechanical crushing are on the microscale the same mechanism for secondary nucleation: detaching whiskers or other asperities from the surface of the primary crystal by supplying sufficient force to rupture the chemical bonds. Finally, we demonstrate with laboratory experiments that both sodium chlorate crystallizing from solution and 1,1'-binaphthyl crystallizing from its melt produce such whisker crystals.

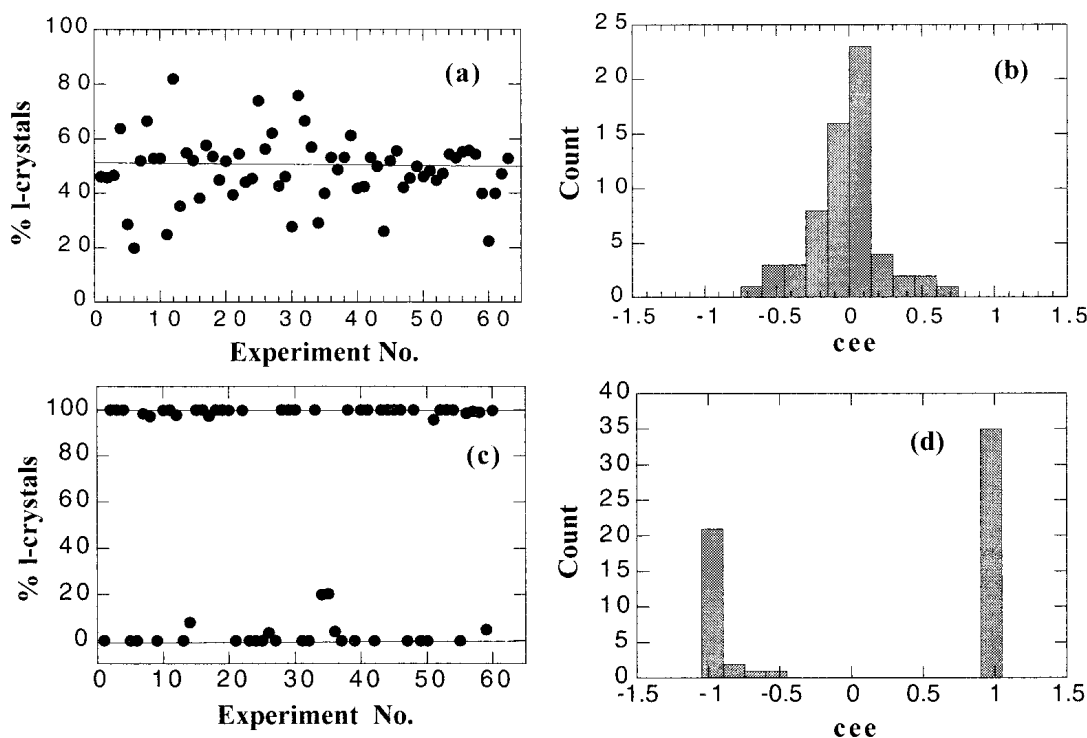


**Figure 3.1:** Spontaneous chiral symmetry breaking in  $\text{NaClO}_3$  crystallization. (a) The percentage of laevo crystals obtained in 63 independent unstirred crystallizations and (b) the corresponding histogram of crystal enantiomeric excess  $\varepsilon = (n_D - n_L)/(n_D + n_L)$ . (c) The percentage of laevo crystals obtained in 60 independent stirred crystallizations and (d) the corresponding histogram of  $\varepsilon$ .

## 3.2 Secondary Nucleation

To nucleate a crystal requires overcoming a certain energy barrier [74]. The height of the barrier is a function of the concentration of a solution, or the temperature of a melt. A supersaturated solution, concentrated beyond its saturation point, or a supercooled melt, cooled beyond its freezing point, are systems metastable to nucleation. With a solid surface already present, less energy is required to surmount the barrier (Fig.3.2). Thus functions secondary nucleation, in which the presence of one crystal facilitates the production of further crystals. Secondary nucleation, though easily observed and even noted in elementary books on crystallization, is a rather complex process: even after decades of studies, empirical rate laws are widely used because details of its mechanism are not known. Solid-solid contact between a crystal and the stir bar, or the impeller in industrial crystallizers, can generate a large number of



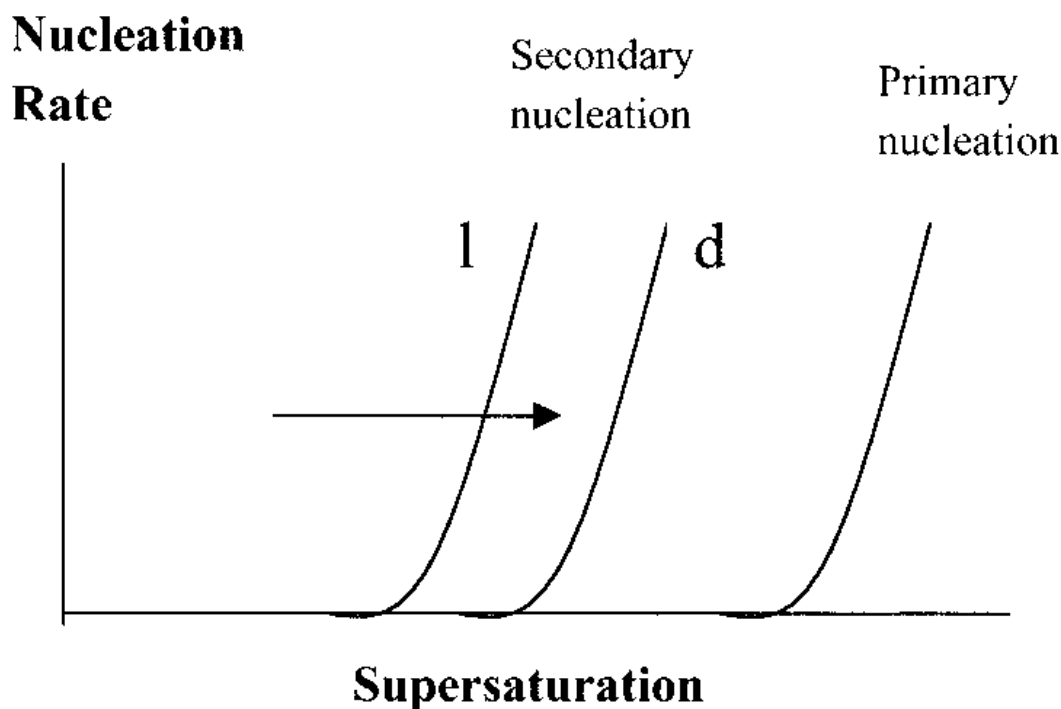


**Figure 3.2:** Nucleation rate as a function of supersaturation for laevo and dextro crystals near the surface of a laevo crystal.

secondary nuclei. However, solid-solid contact is not essential for the generation of secondary nuclei. Secondary nuclei can be generated from a suspended crystal due to fluid convection alone [153]. Secondary nucleation occurs at supersaturation levels at which the primary nucleation rate is negligible; at low supersaturation the secondary nucleation is highly enantioselective but at higher supersaturation it is less so. Recently, Qian et al. [152] formulated a theory of secondary nucleation, noting that forces between clusters and surfaces of crystals can lead to higher nucleation rates. The classical expression for the nucleation rate  $J$  is

$$J = J_0 \exp\left(-\frac{16\pi\gamma^3 V_m^2}{3KT\Delta\mu^2}\right) \quad (3.1)$$

in which  $\gamma$  is the interfacial energy,  $V_m$  is the molar volume of the solid phase, and  $\Delta\mu$  is the chemical potential difference between the solution and the solid phases. In the simplest approximation,  $\Delta\mu = RT\ln(C/C_S)$ , where  $C$  is the concentration and  $C_S$  the saturation concentration.  $J$  increases with  $(C/C_S)$  almost like a step function as shown in Fig.(3.2). Qualitatively, high chiral

selectivity at a low supersaturation and lower selectivity at higher supersaturation may be due to a shift in the nucleation rates in the vicinity of a chiral surface; chiral selectivity arises because laevo and dextro nucleation rates shift by different amounts. Thus, there is a supersaturation range in which only the laevo nuclei are produced in the vicinity of an laevo crystal surface, but both laevo and dextro nuclei are generated at higher supersaturation.

A half century ago, Frank [71] suggested that a form of autocatalysis in which each enantiomer catalyzes its own production, while suppressing that of its mirror image, might have nonlinear dynamics leading to the amplification of small initial fluctuations in the concentrations of the enantiomers. Secondary nucleation can act as just such a nonlinear autocatalytic process, as, in the case of chiral crystallization, secondary nuclei possess the same chirality as the mother crystal, so the presence of a crystal of a given chirality catalyzes the production of further crystals with the same chirality. When stirred, secondary crystal nuclei are generated from the surface (or the vicinity) of an existing crystal, and an overwhelming number of these secondary nuclei can have the same crystal structure, laevo or dextro, as the parent crystal. Symmetry breaking occurs because the first crystal rapidly clones itself through secondary nucleation and dominates the system. One must note that chirally autocatalytic generation of crystals alone is not sufficient for symmetry breaking. For the dominance of one enantiomeric form, the proliferation of crystals of one form must prevent the proliferation of crystals of the mirror image form. In stirred crystallization this happens because the concentration drops rapidly due to secondary nucleation, and this drop virtually stops the formation of more nuclei, primary or secondary, during the rest of the process.

### **3.3 Symmetry breaking**

To understand the origin of chirally asymmetric states, we must first note that the physical or chemical states that are generated by natural processes need not reflect process symmetries. Thus, though chemical reactions are chirally symmetric if we disregard the extremely small violation of this symmetry due to electro-weak interactions it does not mean that chemical reactions between achiral reactants always generate a racemic product. If there is appropriate

chiral *autocatalysis* and *cross inhibition* between enantiomers of the product, the process of spontaneous chiral symmetry breaking will generate unequal amounts of the product enantiomers. At thermodynamic equilibrium there can be no  $\varepsilon \neq 0$ . However, in nonequilibrium systems a state of nonzero  $\varepsilon$  can spontaneously arise from an achiral or a racemic state through a chiral-symmetry-breaking transition. When cast in the appropriate framework of thermodynamics, this process can be analyzed in a general manner and thus a general theory of chiral symmetry breaking could be formulated. As in the case of symmetry breaking phase transitions, the basic equations of the chiral symmetry breaking system, chemical or otherwise, derive from the two-fold mirror symmetry or parity. The instability of the symmetric state and the consequent transition to an asymmetric state has a rather simple mathematical description in terms of two variables  $\alpha$  and  $\lambda$ ;  $\alpha$  is a measure of the chiral asymmetry. In chemical systems,  $\alpha$  might be the difference between the amount of enantiomers;  $\lambda$  is a parameter, which is a measure of the displacement from a reference state, which is chirally symmetric. The value of  $\lambda$  above which the asymmetric states spontaneously arise is denoted by  $\lambda_c$ . For values of  $\lambda$  near  $\lambda_c$ , it is possible to derive an equation of the form

$$\frac{d\alpha}{dt} = -A\alpha^3 + B(\lambda - \lambda_c)\alpha. \quad (3.2)$$

in which the coefficients A and B are functions of the kinetic rate constants of the reactions. At a fixed  $\lambda$ ,  $\alpha$  will evolve to its steady state, at which  $d\alpha/dt = 0$ . For positive A and B and  $\lambda < \lambda_c$ , it follows from Eq.(3.2) that the symmetric state,  $\alpha = 0$  is the only stable steady state; any perturbation from  $\alpha = 0$  will decay back to zero. For  $\lambda > \lambda_c$ , two new steady states,  $\alpha = ([B(\lambda - \lambda_c)/A]^{1/2})$ , emerge or bifurcate from  $\alpha = 0$  at  $\lambda_c$ ; these are the asymmetric states, each dominated by one of the enantiomers. At  $\lambda_c$ , precisely when the asymmetric states emerge, the symmetric state begins to become unstable; when  $\lambda > \lambda_c$ , a small random perturbation from  $\alpha = 0$  will grow and produce an asymmetric state. The steady states of  $\alpha$  as functions of  $\lambda$  and the resulting bifurcation diagram are shown in Fig.(3.3a). The evolution of  $\alpha$  is not deterministic because we cannot predict, using Eq.(3.2), to which branch,  $\alpha > 0$  or  $\alpha < 0$ , the system will evolve. It is probabilistic with a probability distribution  $P(\alpha)$ . Below  $\lambda_c$ , due to small random fluctuations in  $\alpha$ , the probability distribution will

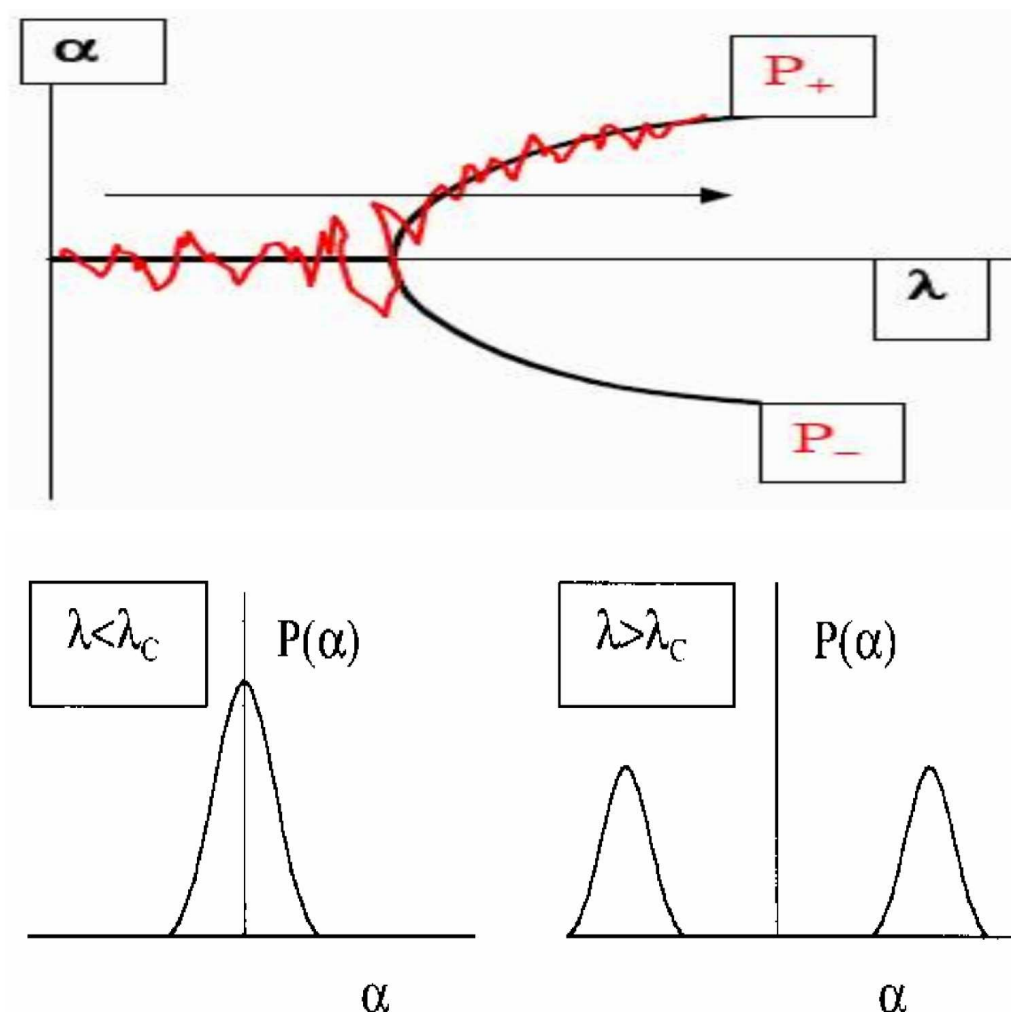


**Figure 3.3:** Spontaneous chiral symmetry breaking in nonequilibrium chemical systems. (a) Bifurcation of asymmetric states. (b) Probability distributions associated with stochastic behavior. (c) As the systems sweeps through the critical point, it makes a transition randomly to one of the two branches.

be monomodal centered around zero; above  $\lambda_c$  it will be bimodal (Fig.(3.3b)) because repeated runs will result randomly in both positive and negative values of  $\alpha$  (Fig.(3.3c)). A bimodal probability distribution is a clear signature of a symmetry-breaking transition.

### 3.4 The Model

To demonstrate that these ideas can explain the experimental observations, we construct a minimal model for chirality selection via secondary nucleation

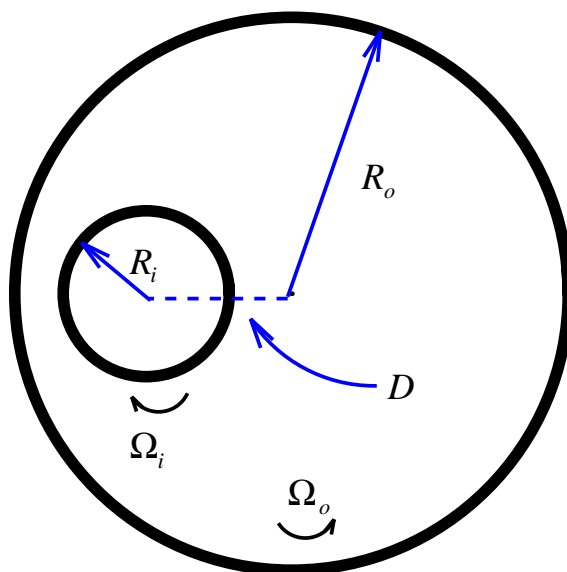


**Figure 3.4:** The geometry of journal bearing flow and the definitions of the parameters.

in solution or in the melt by building on the work on nonlinear autocatalytic processes in flows of Metcalfe and Ottino [115], to which we add a realistic but simple model for the physics of crystal nucleation and growth. The general problem of describing a growth process by detailing the various overlapping fluid-dynamics and kinetic phenomena is very complex and all growth models rely on more or less drastic simplifying assumptions. We use, as they did, the chaotic journal-bearing flow to illustrate the concept. This is a two-dimensional, carefully controlled, Stokes flow, that has an analytic solution and has been extensively studied [170]. Fluid resides between two parallel but offset cylinders. The perturbation from steady flow is governed by the linear displacement of the cylinders and parameterized by the total angle of rotation  $\theta$  of the outer cylinder.

This system is particularly well suited for the study of chaotic advection in two dimensions. First, for the steady problem an analytical solution of the Navier–Stokes equations is available in the creeping flow regime. Therefore, one obtains the unsteady flow by periodically switching between two different steady flows conditions. Second, experiments that are in close correspondence with the theoretical model can be easily designed. The geometry of steady journal-bearing flow (see Figure. 3.4) is uniquely determined by five parameters, namely, the radii of the two cylinders,  $R_i$  (inner) and  $R_o$  (outer), the

corresponding angular velocities,  $\Omega_i$  and  $\Omega_o$ , and the eccentricity,  $D$ , that is the distance between the centres of the cylinders. However, the corresponding stream function depends on only three parameters,  $r \equiv R_i/R_o$ ,  $\omega \equiv \Omega_i/\Omega_o$  and  $D$ . In the creeping flow limit, the Navier–Stokes equation reduces to a linear biharmonic one,

$$\nabla^4\psi = 0, \tag{3.3}$$

which together with the appropriate boundary conditions was solved by Wannier [188] using complex variables, and by Ballal & Rivlin [15] using bipolar coordinates. The topology of the stream lines for various values of the parameters is related to the competition between the two cylinders to impose their own flow, namely, the flow that would be obtained in the absence of the other cylinder. Due to the linearity of (3.3), the stream function can be expressed as a linear combination of single cylinder flow, that is,

$$\psi(x, y) = \psi_i(x, y)\Omega_i + \psi_o(x, y)\Omega_o. \tag{3.4}$$

The different situations can be classified in terms of the number of stagnation points that arise. These can be either enclosed by elliptical stream lines, being then stable, or alternatively, lie at the intersection of separatrix-type stream lines or endpoints of such stream lines on one of the cylinders, being then unstable. It appears that one can have at most two pairs of a stable and an unstable stagnation point for  $\omega$  positive (corotating cylinders) and large enough  $D$  and at least one such pair for negative  $\omega$  (counterrotating cylinders).

The simplest way to introduce time dependence in the journal-bearing stream function is to let either  $\Omega_i$  or  $\Omega_o$  (or both) alternate periodically between two different values. For example, we let  $\Omega_o$  take the value  $\Omega_{o,1}$  for time  $T_1$  and  $\Omega_{o,2}$  for time  $T_2$  such that the period,  $T = T_1 + T_2$ . Whenever inertial effects can be neglected this provides a mechanism for passive scalars that evolve along a streamline of the flow with  $\Omega_{o,1}$  during  $T_1$  to move over to a different streamline of the same flow for the next period by means of a streamline of a different flow, namely, that associated with  $\Omega_{o,2}$  during  $T_2$ . The dynamics ensuing from the process of switching from one streamline to another is no longer integrable. In order to study the new type of behavior, one strobos the motion at discrete times that are multiples of  $T$ . For  $T_2 \ll T_1$ , small regions of chaotic motion appear in the vicinity of the separatrix stream

lines of the  $\Omega_{o,1}$  flow while in the rest of the space the dynamics is regular and practically unchanged from the steady flow. However, as  $T_2$  becomes closer in value to  $T_1$ , a gradually larger fraction of space is taken over by the chaotic motion at the expense of the regular path lines.

A significant effort has been made to understand the consequence of the chaotic dynamics on the mixing properties of journal-bearing flow. For this purpose the time evolution of continuous distributions rather than that of a single passive scalar has been studied. Such distributions may for example represent a second fluid and can be either one or two dimensional. In regions surrounding stable stagnation points the distributions rotate and at the same time are sheared by the gradient of angular velocities of the elliptical trajectories enclosing the stagnation point. The deformation process is relatively slow (being linear in time) and leads to the emergence of *whorls* [26]. On the other hand, in the chaotic regions the evolution of distributions is guided by the homoclinic or heteroclinic tangle of the stable and unstable manifolds belonging to the unstable stagnation points. In this process exponentially fast deformation occurs, generating huge *tendrils* [26]. Consequently, the mixing efficiency in the chaotic domain is significantly enhanced over that in the regular regions. However, regular path lines which are the fluid mechanical analogue of KAM tori play an additional rôle in suppressing mixing efficiency for the case of two-dimensional flows. Whenever such path lines separate two chaotic domains, they form a barrier that prevents fluid on one side from mixing with the fluid on the other. Thus, good mixing throughout the volume of the flow can occur only for large enough nonlinearities, and appropriate values of the other parameters, where the fraction of regular path lines becomes negligible and these appear only in the form of very small elliptical islands.

Our crystallization model works as follows: we model supersaturation or supercooling as an initially uniform distribution of passive scalar particles in the journal-bearing flow. A large number  $n$  of particles are initially distributed uniformly throughout the domain. The flow advects particles as purely passive, without affecting the underlying flow. We allow primary nuclei to appear randomly at any point with a probability depending upon the supersaturation or supercooling. These are randomly assigned one of two chiralities  $L$  (laevo) or  $D$  (dextro). As nuclei appear they deplete their vicinity

of solute or increase the local temperature, so the supersaturation or supercooling in the fluid around them decreases. The nuclei move with the flow and accumulate putative secondary nuclei on their surfaces at a rate depending on the supersaturation or supercooling. Nuclei are labelled with a size label, initially fixed to one. During flow, when a nucleus comes within a distance  $\delta$  of a solute particle, there is an instantaneous crystallization process, whereby the nucleus absorbs the solute and the crystal size increases by one ( $C_i + S \rightarrow C_{i+1}$ ). Secondary nuclei are shed into the flow at a rate depending on the shear stress at their position. When a crystal of size  $i$  passes through a region of high shear, a number of secondary nuclei in the range  $[0, i - 1]$  break from it. The exact number of broken pieces is proportional to the shear stress at that point. The size of the mother crystal diminishes accordingly. These secondary nuclei have the same chirality as their parent. The choice of  $\delta$  and of a purely computational parameter fixing the number of times per periods to check for primary and secondary crystallization reactions, has been adopted following Metcalfe and Ottino work. With this model we can investigate how the ratio  $L/D$  depends on the advection rate and on the initial supersaturation or supercooling, and can evaluate the relative contributions of primary versus secondary nucleation.

Metcalfe and Ottino investigated a model in which there are two competing reaction pathways, but in which there is neither primary nor secondary nucleation. Starting from two initial seeds, one of each chirality, they observed the dominance of one of the competing chiralities upon the advection of the seeds in the flow. But if we allow in the Metcalfe and Ottino model the random introduction — as in primary nucleation — of seeds of both enantiomers, there is no longer chiral selection, and the final result is that there is 50% of each enantiomer. In Fig. (3.5) we present simulations with black dots representing the uniformly distributed supersaturation or supercooling, and red and green dots, which are crystal nuclei of different chiralities. We had introduced the enantiomeric excess  $\varepsilon = (n_D - n_L)/(n_D + n_L)$ , where  $n_D$  and  $n_L$  are the numbers of crystals of each enantiomer, as a means to quantify the symmetry breaking. In the two upper plots we have the Metcalfe and Ottino model with primary nucleation. Initially there is 50% of each enantiomer, and after many flow periods there is still 50% of each ( $\varepsilon = 0.001$ ). But if we



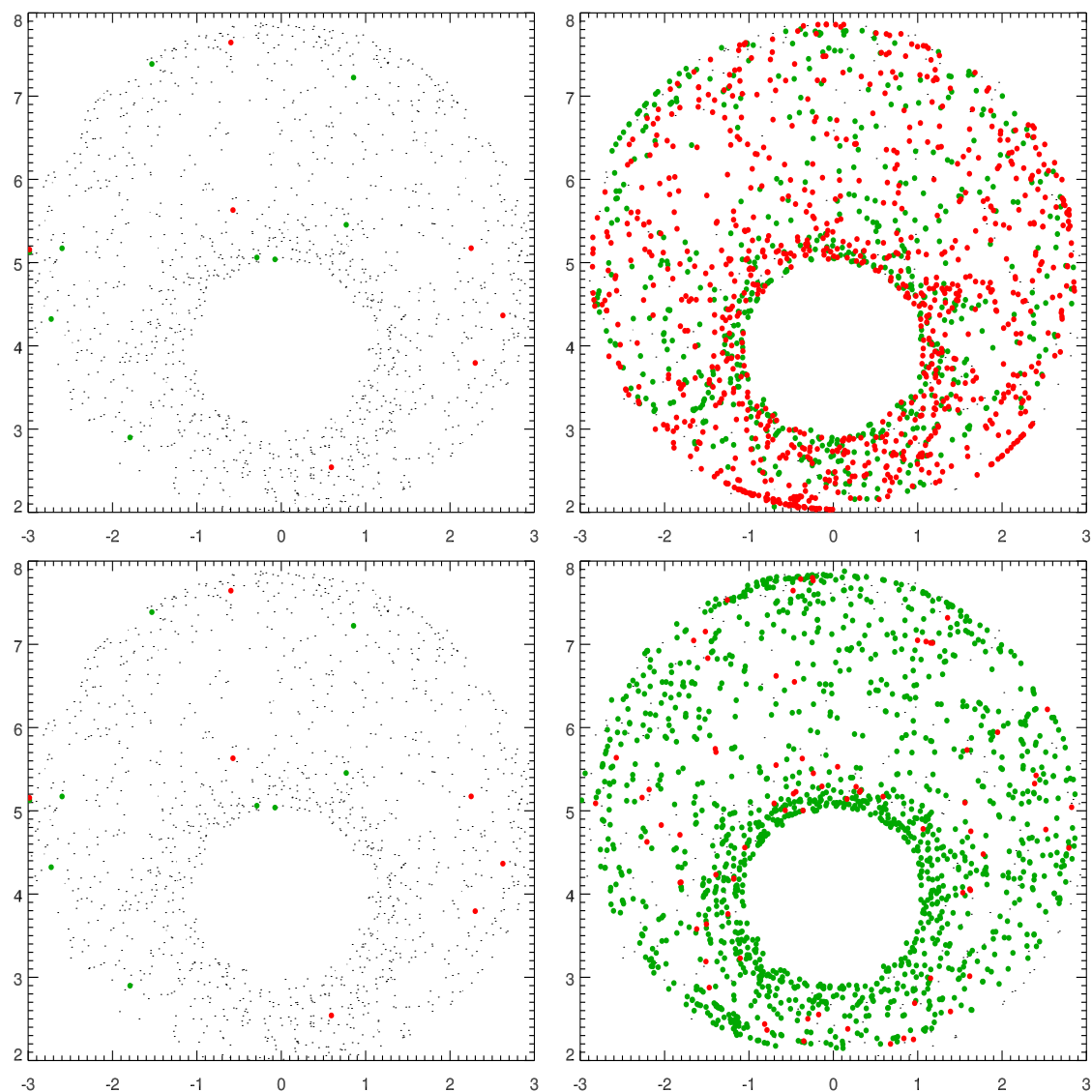


**Figure 3.5:** Simulations of (top) the Metcalfe and Ottino model with primary nucleation and (bottom) our model, demonstrating the importance of secondary nucleation for the production of an enantiomeric excess. Initial conditions are shown on the left; on the right are the final states after seven periods of the flow.

add the production and growth of secondary nuclei to the model, and their detachment from the mother nucleus and dispersal when they pass through a region of high shear, the results change dramatically, as we display in the two lower plots. At first, as before, there is no enantiomeric excess, but by the end we observe an overwhelming predominance of the green enantiomer, corresponding to a value of  $\varepsilon$  of 0.899. In summary, the addition of primary nucleation to the Metcalfe and Ottino model restores enantiomeric parity, and

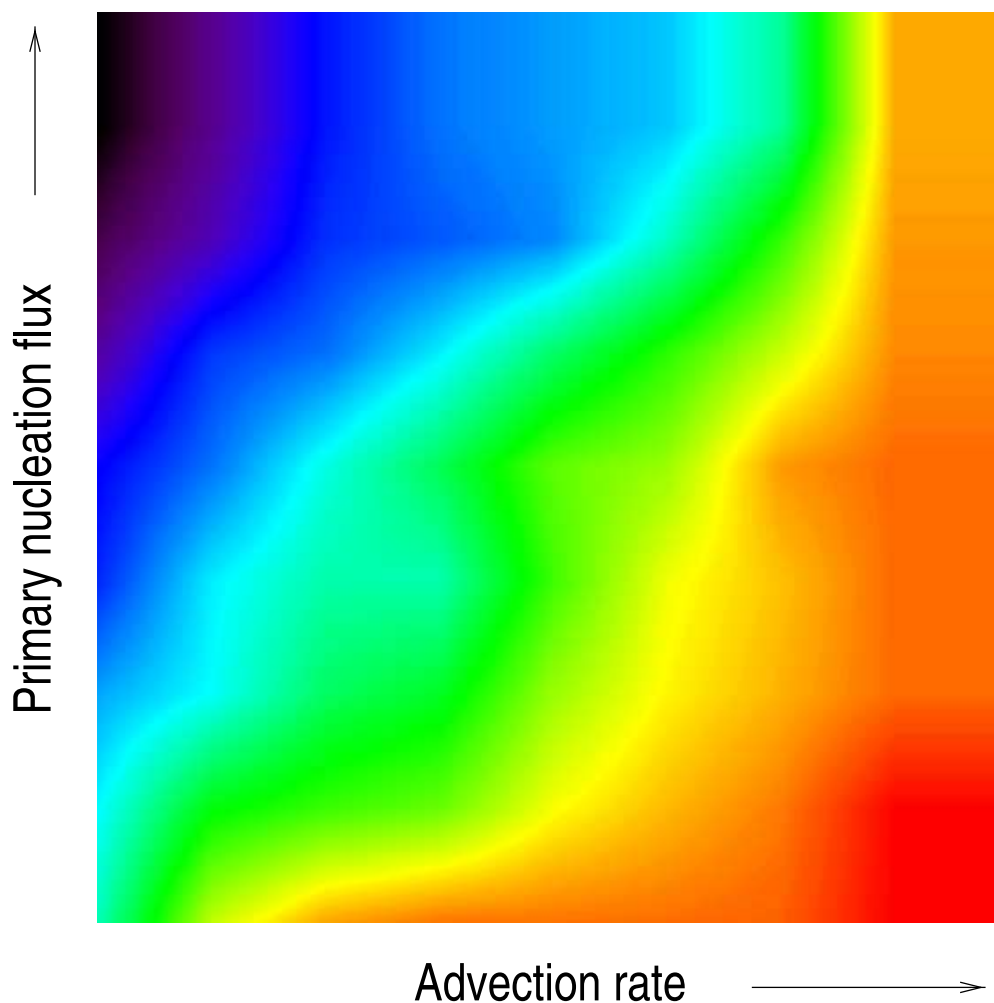


**Figure 3.6:** Plot of absolute value of enantiomeric excess  $|\varepsilon|$  for our model against rate of introduction of primary nuclei (nucleation flux, defined as the fraction of primary crystals produced per rotation cycle, in the range  $[0.01, 0.5]$ ) and against advection rate (parametrized by the total angle of rotation  $\theta \in [4\pi, 12\pi]$ ). The color scale is as a rainbow, with red representing  $|\varepsilon| = 1$ , and black  $|\varepsilon| = 0$ .

that secondary nucleation can reintroduce symmetry breaking. In Fig. (3.6), we plot the enantiomeric excess with our model against the rate of introduction of primary nuclei (the nucleation flux, controlled experimentally by the supersaturation or supercooling), and against the advection rate, upon which secondary nucleation depends [97]. We see that, even for high supersaturation or supercooling, when primary nucleation has most influence, secondary nucleation can overwhelm primary nucleation for fast enough advection, and produce a large enantiomeric excess. This accounts for some recent experimental results showing chiral symmetry breaking in stirred crystallization of

sodium chlorate at very high supersaturations [184].

### 3.5 Comparison With Experiments: Whisker Crystals

We have shown with these simulations that secondary nucleation can explain the earlier experimental results, but by what means is it operating? Secondary nucleation has been extensively investigated, particularly for its relevance to industrial crystallization [168, 126]. The mechanism on the microscale of homochiral secondary nucleation must presumably involve the surface of the mother crystal. Contact nucleation, in which collisions between one crystal and another, or between a crystal and the fluid boundaries (container walls, stirring bar, etc) break pieces off the surface, and fluid shear, which may also detach fragments from the crystal surface, have each been put forward as responsible for homochiral secondary nucleation [108, 35]. Both of these mechanisms involve the idea of the production and subsequent removal of relatively weakly attached homochiral material from the crystal surface. Other forms of secondary nucleation operate without regard to chirality. These involve crystal embryos (prenuclei) in the fluid adjacent to the mother crystal, which, in chiral crystallization, may be of either chirality. These achiral mechanisms may well be important, especially at high supersaturations or supercoolings at which crystal embryos in the fluid are more numerous [153]. Here, however, we are interested in understanding the dynamics of homochiral secondary nucleation.

For either mechanical or fluid forces to break material off from the growing crystal surface, that material must be relatively weakly attached, which implies that the surface must be rough, rather than smooth. While crystals at low supersaturations or supercoolings grow by the addition of material at the edges of smooth layers (so-called tangential growth), at increasing supersaturations or supercoolings the surface grows in a more disordered manner (normal growth) [51]. It is clear that the larger the number and size of asperities on the crystal surface, the greater the probability of detaching fragments by mechanical shock or fluid shear. The detached fragments will possess the same chirality as the mother crystal of which they previously formed a part.

At the highest supersaturations or supercoolings, these asperities can be the result of normal growth, but even with tangential growth at more moderate supersaturations or supercoolings it is possible to have structures that are easily detached. Whisker crystals are an example. In this crystal-growth morphology, long thin crystallites, or whiskers (defined as crystals with aspect ratio greater than 10:1), grow out from the substrate beneath.

It is not hard to see how whisker crystals may cause secondary nucleation, as their shape makes them easy to detach from the primary crystal. Let us estimate the force that the fluid flow or contact with a stirring bar or the wall could impart, and compare it with the force needed to break off a whisker. Consider a cuboidal whisker  $b$  m long, and  $a$  m in its other two dimensions, giving it an aspect ratio  $R = b/a$ . Assume the whisker to be a flat plate of surface area  $ab$  m<sup>2</sup> orthogonal to a fluid flow of  $v = 1$  m s<sup>-1</sup>. The force exerted on the whisker by the fluid is the mass of fluid deflected per second  $\rho abv$  ( $\rho = 10^3$  kg m<sup>-3</sup> is the fluid density) multiplied by its velocity  $v$ . As the whisker is a cantilever projecting from the crystal surface, the force acting to open a crack at its base is the above force multiplied by the mechanical advantage  $R$ , which gives us an estimate  $F_f = \rho b^2 v^2 = 10^3 b^2$  N. If, on the other hand, we consider the force imparted to the whisker by its mother crystal of mass  $M = 2 \times 10^{-3}$  kg hitting the wall or the stirring bar and decelerating from the fluid velocity  $v$  to zero in the length  $b$  of the whisker, we obtain  $Mv^2/(2b)$ , which again should be multiplied by the mechanical advantage  $R$  to give  $F_w = Mv^2/(2a) = 10^3/a$  N. Let us compare these estimates with the force needed to break off a whisker. This breakage will preferentially occur at its base, where, as indicated above, the loading is the greatest. The whisker has a cross-sectional area of  $a^2$  m<sup>2</sup>. A cross section then contains of order  $10^{18}a^2$  atoms (assuming  $10^9$  atoms m<sup>-1</sup>). Let us assume that each possesses a single chemical bond linking it to the mother crystal below. Then breaking off the whisker consists in rupturing  $10^{18}a^2$  bonds, each of which requires of order  $10^{-8}$  N. This gives the total force required as  $F_b = 10^{10}a^2$  N. This rough estimate assumes that the whisker crystal is defect free, and in fact the figure arrived at is rather close to much more sophisticated calculations of the theoretical maximum strength of defect-free materials [140]. Although the whisker itself is likely to be without defects, it may be attached to the mother

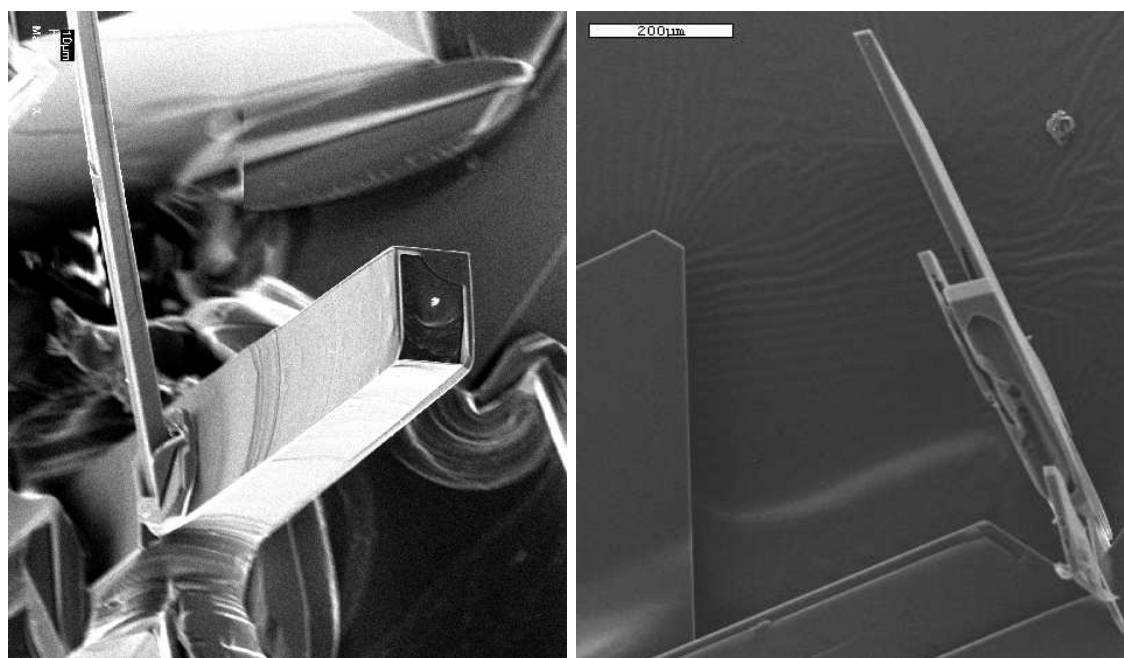


**Figure 3.7:** Whiskers of (left) sodium chlorate crystallized from solution, and (right) 1,1'-binaphthyl crystallized from its melt.

crystal by a dislocation, which would lower the strength by several orders of magnitude [140], and make it easier to snap off at its base. In any case, we can now observe the relative importance of fluid and mechanical forces  $F_f/F_w = ab^2$  on the whisker, which will normally be considerably less than unity; the fluid forces are weaker. However,  $F_f/F_b = R^2/10^7$ , so fluid forces can detach a whisker with aspect ratio  $R > 10^{7/2}$ , which appears quite plausible. The stronger mechanical forces can break off any sufficiently small whisker when  $F_w/F_b = 10^{-7}/a^3 > 1$ , implying  $a < 10^{-7/3}$ . Both fluid and mechanic forces appear then to be eminently capable of breaking off whiskers during stirred crystallization. Sodium chlorate ( $\text{NaClO}_3$ ) is an achiral ionic compound that crystallizes in the cubic space group  $P2_13$  as two chiral forms [1]. Its crystallization has been much studied, and it is with sodium chlorate that the phenomenon of the selective crystallization of one enantiomer with stirring was first seen [98]. Its propensity to produce whisker crystals has been noted [162, 100]. We have crystallized sodium chlorate from solution and have observed the morphology of the crystals with scanning electron microscopy. As we see in Fig. (3.7), whisker crystals are notable features of the

crystal surface at higher supersaturations. An interesting study has shown growth hillocks on the faces of solution-grown sodium chlorate crystals [171]. Many of these resulted from dislocation defects in the substrate crystal structure. These may be incipient whiskers, and the defects at the base would make them easy to break off, as we discussed above. We wished to see whether whisker crystal growth may be a general mechanism capable of explaining similar results with different compounds that show the same enantiomer selection behaviour on crystallization. 1,1'-binaphthyl is an organic molecule that when crystallized from its melt accompanied by stirring shows similar enantiomer selectivity to sodium chlorate [99]. 1,1'-binaphthyl differs from sodium chlorate in that its chirality is present at the molecular level: a single molecule possesses a chemical bond with restricted rotation leading to there existing below a certain critical temperature two enantiomeric forms of the molecule. Hence sodium chlorate is achiral before crystallization, as it exists in solution as more or less dissociated ions or clusters without a fixed chirality, but forms a chiral crystal, while 1,1'-binaphthyl exists in the melt below a certain critical temperature as chiral molecules that form a chiral crystal. We crystallized 1,1'-binaphthyl from the melt. In this case too, whisker crystals growing out from the primary crystal feature prominently; see Fig. (3.7). The presence of whiskers in these two chemically diverse systems strengthens the idea that whisker growth is a common mechanism for secondary nucleation. Although we have shown the existence of large (mesoscale) whiskers with these laboratory experiments, if these exist, ergo smaller whiskers must too, right down to incipient whiskers on the molecular scale.

### 3.6 Conclusions

We have been discussing chiral symmetry breaking during stirred crystallization. However, the mechanism at work in these experiments is not stirring *per se*, but the formation and dispersion of homochiral nuclei throughout the fluid by flow produced by whatever means. The direction of stirring is not important here — one sense does not produce one enantiomer, and the opposite sense, the other — unlike in experiments on larger molecules that stack together to form chiral mesoscale structures which are susceptible to

macroscopic hydrodynamic interactions, in which the chirality does depend on the direction of stirring [155]. With sodium chlorate, an enantiomeric excess can sometimes be obtained in unstirred solutions too, as natural convection caused by concentration or temperature differences within the solution can play the role of stirring (forced convection) to propagate secondary nuclei [172]. This reinforces the idea that dislocations at the base of the whiskers play an important part in the mechanism, for typical fluid velocities in natural convection around a growing crystal of  $0.1\text{--}1\text{ mm s}^{-1}$  — three to four orders of magnitude less than the forced convection velocity we considered above — would not break off a typical whisker unless the material strength were some orders of magnitude below the theoretical maximum. The nucleation of a crystal of one or other chirality is a symmetry-breaking event on the microscale, but the nonlinear autocatalytic dynamics of secondary nucleation amplify this to the macroscale, to the extent that an entire experiment may be influenced by the chirality of a single mother crystal: an ancestral Eve for the whole population.

Recently, Viedma [185] shows that a large and symmetric population of L and D crystals can move into complete chiral purity, with one of the enantiomers completely disappearing, in a stirred solution with the addition of glass balls. He suggests that this process become possible by the combination of the nonlinear autocatalytic dynamics of secondary nucleation and the recycling of crystallites when they reach the achiral molecular level in the dissolution-crystallization reaction, through an abrasion-grinding process. Is this a different symmetry-breaking process? It seems, at least, to be independent of the chirality of a "mother crystal". Our model could be easily modified to include such a dissolution process, through which the final stage of any crystallite is at the achiral level. Therefore, any crystal can feed other crystals independently of its chirality. Is our model able to reproduce the experimental results under these modifications? I am still working on that.





# Chapter 4

## Biological bodies: Left Hand – Right Hand.



### 4.1 Introduction

*The small bodies considered in this Chapter are slender oscillators that are responsible for the propulsion of fluid in biological environments. They are called cilia or flagella, but the latter term is somewhat ambiguous because it is used for two evolutionary unrelated structures: prokaryotic and eukaryotic flagella. Furthermore, cilia and eukaryotic flagella are closely related organelles having essentially the same structure.*

Cilia and flagella appeared very early in evolution to provide unicellular organisms with motility in water. They were retained and employed through adaptation for a wide variety of functions requiring fluid movement in complex multicellular animals. The functions of cilia in diverse processes such as leftright axis pattern formation, cerebrospinal fluid flow, sensory reception, mucociliary clearance and renal physiology indicate that cilia have been adapted as versatile tools for many biological processes.

A typical cross-sectional view of a cilium is shown in Fig.(4.1). Within a

membrane there is the "axoneme", which consists of longitudinal fibrils or tubules (one of the structural elements of which is tubulin) arranged as a number of peripheral pairs plus a central pair. The number of outer pairs is often nine (hence the reference to a "9+2" pattern), although many other numbers and modifications of this basic pattern have been observed. For instance, the monocilia protagonists of this Chapter are sometimes termed "9+0" cilia in contradistinction to the "9+2" cilia, since they lack the central pair. Based on whether the axoneme has a 9+0 or a 9+2 structure, cilia have been defined as primary cilia or motile cilia, respectively. Recent findings indicate that there are many exceptions to this definition and favor the distinction into four subtypes: motile 9+2 cilia (e.g. respiratory cilia), motile 9+0 cilia (e.g. nodal cilia), sensory 9+2 cilia (e.g. vestibular cilia), and sensory 9+0 cilia (e.g. renal monocilia and photoreceptor connective cilia). "Arms" consisting of dynein project from the outer pairs of fibrils. The dynein and tubulin are believed to interact in a manner analogous to heavy meromyosin and actin in striated muscle, although the precise mechanical details of this interaction have yet to be clearly identified. It has, however, been well established that the energy source, namely ATP, is the same for both systems.

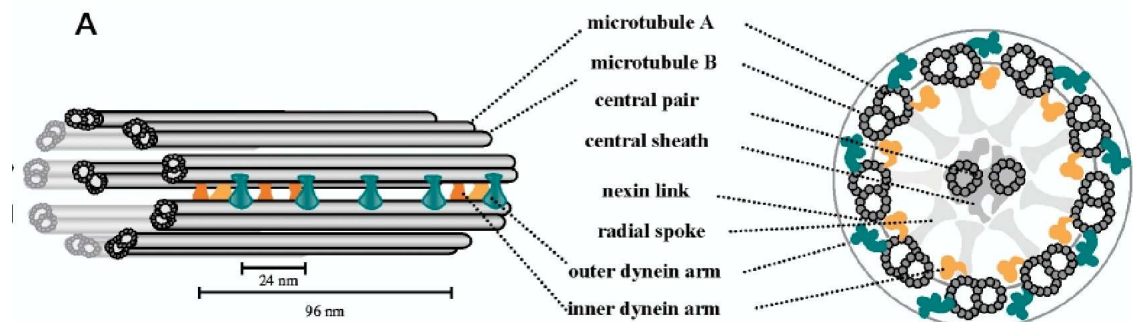


**Figure 4.1:** A diagrammatic representation (a) of a cilium; (b) through a cross section of a cilium.

In our particular trail uphill the complexity in the fluid-body interaction, the motion of these complex biological machineries represent a further step towards the full bidirectional reality. In this case, we will address the problem of a body, the cilia, that through its internal dynamics is capable of generating a fluid flow. The internal motion is caused by ATP consumption, and we assume that there is plenty of it available from whatever source. Although

the produced flow necessarily influence the cilia dynamics, in this Chapter we will discard this influence as a first simplified approach. Nevertheless, it is worth to keep in mind that in some cases this assumption will be invalid. For example, cilia sometimes appear in large arrays and produce fluid motion by a collaborative action arising from a definite phase relationship between the beats of neighboring cilia. The presence of such a relationship is known as *metachrony*, which often results in a wave, known as a metachronal wave, travelling over the array (Fig.4.2). It is also known that metachrony is established mainly through the hydrodynamics interaction of neighboring cilia [75]. In order to model such cases, the existence of a more complex bidirectional fluid-cilia interaction can not be ignored.

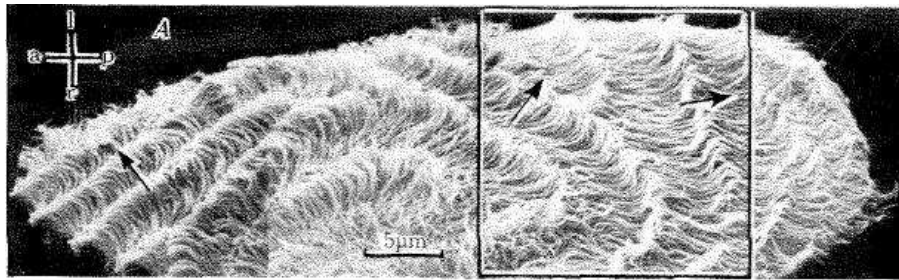


**Figure 4.2:** A metachronal wave in the ciliated protozoan *Opalina*.

## 4.2 Left – Right Patterning

The motivation of our research is the recent experimental work in developmental biology showing that, in mice, a fluid flow driven by rotating cilia in the node, a structure present in the early stages of growth of vertebrate embryos, is responsible for determining the normal development of the left–right axis, with the heart on the left of the body, the liver on the right, and so on. The rôle of physics, in particular of fluid dynamics, in the process, is one of the important questions that remain to be answered. We will show with an analysis of the fluid dynamics of the nodal flow in the developing embryo that the leftward flow that has been experimentally observed may be produced by the monocilia driving it being tilted toward the posterior. We propose a model for morphogen transport and mixing in the nodal flow, and discuss how this might initiate the development of left–right asymmetry.

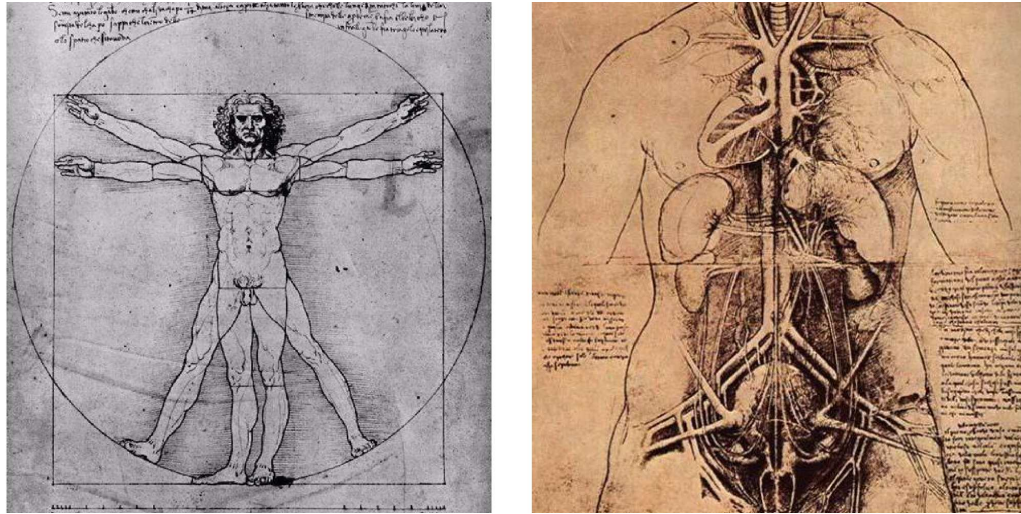


**Figure 4.3:** External human symmetric appearance, and its internal asymmetry.

The bilaterally symmetric external appearance of vertebrates is deceptive, for beneath the skin asymmetry reigns. In the early stages of development of an organism, in the embryo are laid down the anterior–posterior, dorsal–ventral, and left–right axes of the vertebrate body plan [20]. The left–right symmetry axis is decided after the anterior–posterior and dorsal–ventral axes have been laid down. The symmetry breaking involved is qualitatively different from the two earlier cases. In those, it matters only that the symmetry is broken, and not in what sense, as the opposite choice in each instance — interchanging up with down, or front with back — would lead to exactly the same result. This is not so for the third axis, as the two possible outcomes are chiral (Fig. 4.4a); the opposite choice would lead to an animal having all its internal structure mirror reversed from the norm — so called *situs inversus*. That nature does distinguish left from right is shown by the fact that animals normally have their hearts on the left (*situs solitus*), and *situs inversus* is a rare variation that in humans, for example, is found in only around one person in ten thousand [179, 112]. This is curious, since an organism with complete *situs inversus* can function just as well as one with normal chirality.

Recently, elegant experiments with mice have shown that a structure on the surface of the embryo, the node, is responsible for determining left–right chirality [123, 127, 3, 39, 169, 65, 122, 81]. The node is liquid filled, and lined

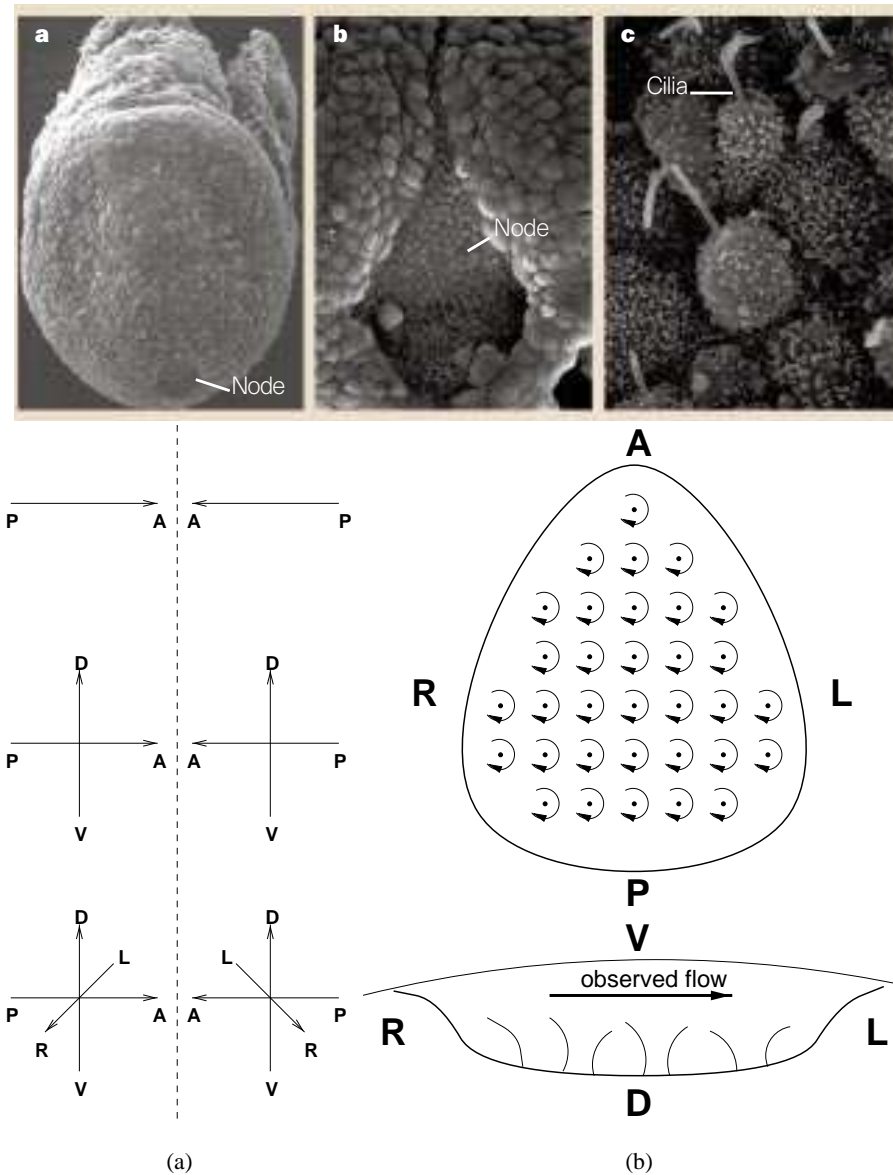


**Figure 4.4:** (a) The node is at the apex of the egg cylinder, and the head process, which will give rise to the notochord, extends anteriorly. (b) Closeup showing the cup-like shape of the node. The anterior is orientated towards the top. (c) Higher magnification showing the monocilia on each cell in the head process and on the ventral surface of the node. (d) Anterior–posterior, dorsal–ventral, and left–right axes provide a coordinate system for the vertebrate body plan. When only one or two of the axes are defined, the result is achiral — the mirror image is the same as the original. But when the final, left–right axis is added there are now two chiral forms. (e) Ventral and posterior sketch views of the node of the mouse embryo, and its rotating monocilia, showing also the experimentally observed leftward nodal flow.

with cells possessing monocilia, or primary cilia. Nodal cilia are seen to rotate

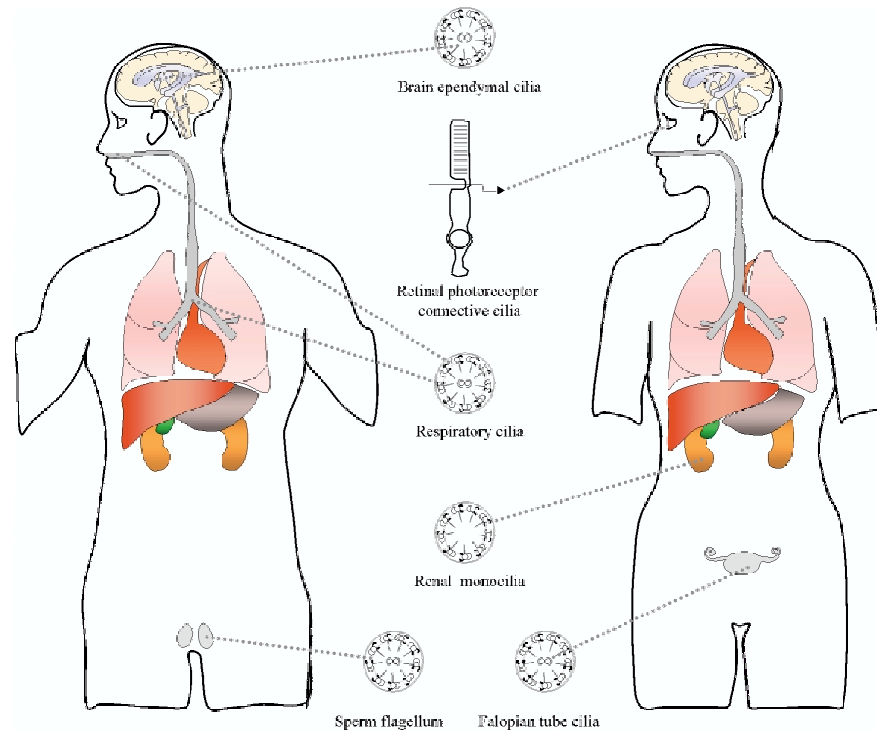


**Figure 4.5:** Cilia malfunction in diverse human disorders. Representation of a male and a female individual, showing the sites of action of cilia that have been implicated in human disease. Also indicated are the different axonemal structures of each particular cilia type. In the brain, the ependymal cells lining the ventricles carry motile cilia with a 9+2 ultrastructure. In the retina, the light sensitive photoreceptor cells consist of an outer and an inner segment which are linked by a connective cilium which might have a 9+0 ultrastructure. The back-side of the cornea carries monocilia as well. In the upper and lower respiratory tract, epithelial cells are covered with motile cilia of 9+2 ultrastructure. In kidney, monocilia of presumably a 9+0 structure are present in glomerulus and tubular cells. The axoneme structure of renal monocilia and photoreceptor connective cilia is supposed to be 9+0 but no electron microscopy has verified yet whether these cilia have the microtubule central pair and/or dynein arms. The sperm flagellum and cilia of the testis efferent ducts have a 9+2 structure. Similarly, motile cilia of a 9+2 structure line the uterus and fallopian tubes.

clockwise as viewed from above [123, 122]. These monocilia are curved, hence, as they rotate, the tip of each cilium traces out a circular path. When passive tracers — sub-micrometre-sized spherical particles — are introduced into the nodal fluid above the cilia, they move leftwards — meaning towards the left of the embryo, not towards the observer's left — across the node, following the flow in the extraembryonic fluid in which they are immersed. That this movement is induced by the cilia is demonstrated by genetic abnormalities in laboratory mice and in humans that lead to the monocilia of the node being



immobile; for example, Kartagener’s syndrome in humans, in which the dyein arms are missing from the microtubules of the molecular motors that normally drive the cilia [2]. A check with passive tracers in such mice shows no fluid flow, only Brownian motion. The same developmental error illustrates the rôle of this nodal flow in left–right symmetry breaking: in half of the animals with this abnormality the internal organs are mirror reversed from the norm [127], as without the nodal flow, symmetry is broken randomly. This confirms a hypothesis of Afzelius [2], who first surmised that the movement of cilia might be crucial in this symmetry breaking. Moreover, normal embryos can be made to develop *situs inversus* by using external forcing to artificially change the flow direction in the node from leftwards to rightwards [122].

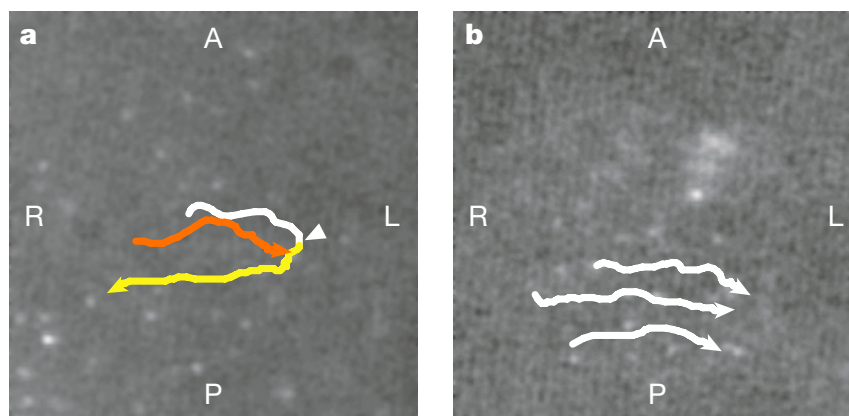


**Figure 4.6:** Reversal of the intrinsic nodal flow by fast, but not by slow, rightward artificial flow. Embryos at the one-somite stage were placed in the flow chamber, and the fluid flow in the node was visualized with fluorescent beads. Arrows indicate the direction of individual beads. (a) Fast rightward flow. The pump was initially off, then it was turned on to impose the fast rightward flow, and it was then turned off again. In the absence of the artificial flow, a bead moved leftward (white line), but it turned rightward (yellow line) when the pump started (arrowhead). After the pump stopped, a bead resumed its original leftward movement (orange line). (b) Slow rightward flow. The flow in the node was observed under the slow rightward flow. The flow remained leftward even when the slow rightward flow was imposed (white lines). A, P, L and R refer to anterior, posterior, left and right sides of the node, respectively.

How does the clockwise motion of tens of monocilia drive a leftward flow in the node? And, if the observed flow is leftwards, how is the fluid recirculating within the node, as it must, since the node is a closed structure? Finally, how does the nodal flow lead to left–right symmetry breaking in the embryo? These questions are within the realm of fluid physics [164].

### 4.3 Hydrodynamic considerations

In the mouse, the most studied case, the node is a depression on the surface of the embryo, roughly pear shaped when viewed from above — that is, from the ventral side — some  $50 \mu\text{m}$  across, and  $10 \mu\text{m}$  deep; see Fig. (4.4b). It is covered by Reichert’s membrane, and filled with extraembryonic liquid. Arrayed over its base are a few tens of monocilia some  $2\text{--}3 \mu\text{m}$  in length. These rotate clockwise, as viewed from above, at circa  $10 \text{ Hz}$ . The flow velocity produced by the monocilia has been measured with passive tracers to be some  $20\text{--}50 \mu\text{m s}^{-1}$  in normal embryos [127]. This implies that the Reynolds number of the node,  $Re_n = vL/\nu$ , the relative importance of inertial to viscous forces in the flow, where  $v$  is the flow velocity,  $L$  the size of the node, and  $\nu$  the kinematic viscosity of the extraembryonic fluid (an aqueous solution of proteins), is of order  $10^{-3}$ . We can obtain another Reynolds number from the cilium rotation velocity:  $Re_c = \omega a^2/\nu$ , where  $\omega$  is the angular velocity  $2\pi f$  and  $a$  is the length of a cilium. From the ciliary frequency  $f = 10 \text{ Hz}$ ,  $Re_c \sim 5 \cdot 10^{-4}$  here. The two estimates are close, and, whether we take  $Re_n$  or  $Re_c$  as the more representative, the Reynolds number of the flow is certainly very low. This means that viscosity dominates inertia; if the monocilia were to stop, the flow would instantly cease. Under this condition, known as creeping flow, the Navier–Stokes equations that describe the movement of fluid may be linearized to the Stokes equations, which are amenable to analytical solution.

The analysis of the detailed hydrodynamics of creeping flows due to cilia has been greatly aided by the development of methods to construct the flow fields by means of distributions of fundamental singularities. For the purpose of describing these methods we must dwell briefly on the nature of the fundamental solutions to the equations of motion for an incompressible inertialess Newtonian fluid. They consist of a continuity condition on the fluid velocity  $\mathbf{u}$ :

$$\nabla \cdot \mathbf{u} = 0 \quad (4.1)$$

and since there are no inertial forces, a condition of force equilibrium

$$\nabla p = \mu \nabla^2 \mathbf{u} \quad (4.2)$$

containing the fluid pressure,  $p$ . This is the Stokes equation for a steady flow. From this it follows that  $p$  is a harmonic function, and since  $\nabla^4 \mathbf{u} = 0$ , the



velocity is a bi-harmonic function. The primary fundamental solution to these equations due to a single point force,  $\mathbf{F}$ , was first obtained by Oseen (1927), developed further by Burgers (1938), and named a *stokeslet* by Hancock (1953) [130, 36, 82]. If one represents the strength and direction of the singular force at the origin of a coordinate system  $\mathbf{x}$  by  $8\pi\mu\alpha$ , where  $\alpha$  denotes the stokeslet strength and direction, the resulting fluid velocity and pressure are, respectively [52],

$$\mathbf{u}(\mathbf{x}; \alpha) = \frac{\alpha}{r} + \frac{(\alpha \cdot \mathbf{x})\mathbf{x}}{r^3} \quad (4.3)$$

$$p(\mathbf{x}; \alpha) = \frac{2\mu\alpha \cdot \mathbf{x}}{r^3} \quad (4.4)$$

where  $\mathbf{u}$  is the induced flow velocity,  $\mathbf{F} = 8\pi\mu\alpha$  the applied force,  $\mathbf{x} = (x, y, z)$  the coordinate in three-dimensional space, and  $r = \sqrt{x^2 + y^2 + z^2}$  the distance from the origin. It follows that a derivative of any order of this solution is also a solution to the basic equations. Thus, one can construct higher-order singularities such as a Stokes doublet, Stokes quadrupole, etc. Batchelor[19] indicated how a Stokes doublet could be decomposed into an antisymmetric component representing the flow field due to a singular moment of strength  $8\pi\mu\gamma$  and called a *rotlet* with velocity and pressure

$$\mathbf{u} = \frac{\gamma \times \mathbf{x}}{r^3} \quad (4.5)$$

$$p = 0 \quad (4.6)$$

and a symmetric component representing a pure straining of the fluid and termed a *stresslet* (Fig.4.7).

## 4.4 The Model

As the monocilia lining the floor of the node rotate, each produces a vortex about itself in the flow. A ciliary vortex can then be modelled as a rotlet. The vortical flow produced by a rotlet is shown in Fig. (4.8a). As the Stokes equations are linear, an array of vortices is simply a combination of rotlet solutions. An array of rotlets can be given the same topology as the array of rotating monocilia in the node, and in this way transport in the nodal flow can be investigated with this rotlet model.

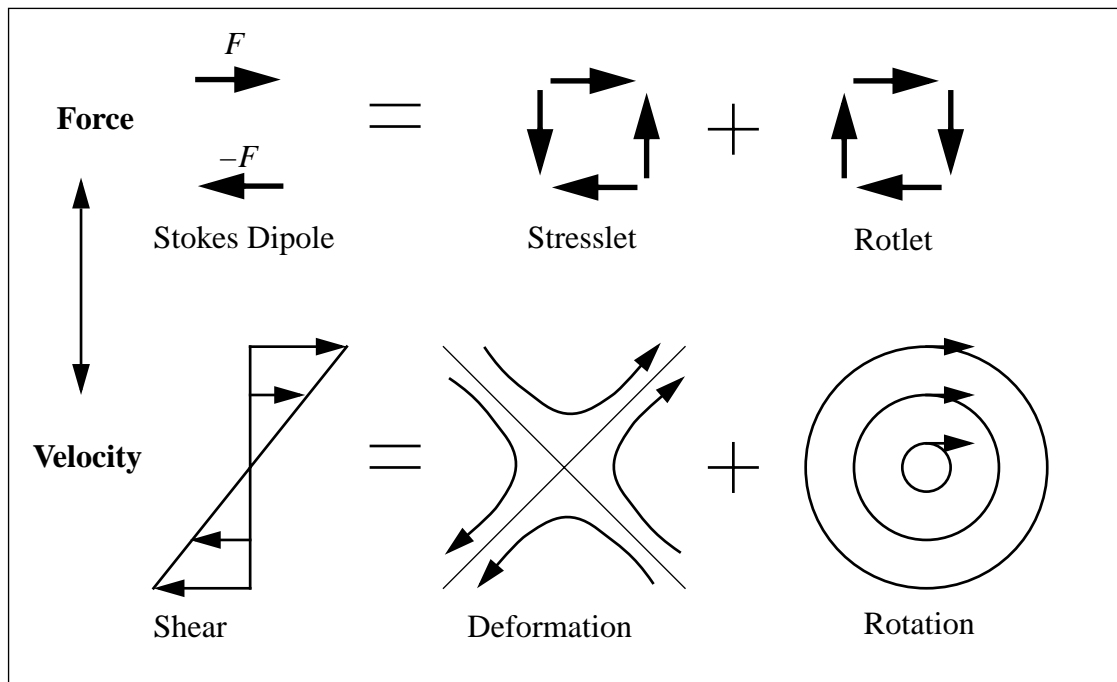


**Figure 4.7:** A scheme representing the decomposition of the Stokes doublet into a rotlet and a stresslet.

If the monocilia rotate about vertical axes, they create a set of vortices, one per cilium, but not a directional flow in the fluid above. Instead, as depicted in Fig. (4.8b), there is a flow consisting of a cellular network of vortices, in which a general circulation only occurs at the edges of the network; elsewhere, movement is vortical. This does not correspond with the experimental observations of a general leftward flow above the cilia. Nonaka et al.[123, 122] suggest that the key to producing such a flow is in the shape of the node; it is elongated, or pear shaped (Fig. 4.4b), and so the array will be not a rectangle, but a triangle of vortices. As we can see in Fig. (4.8c), however, merely changing this aspect of the geometry does not qualitatively change the flow field; it is still vortical within the triangular array, with a general circulation only at the edges. A further possibility would be cilia shaped like oars, which, if feathered during part of the rotation, could produce a directional flow; but all observations show cylindrical cilia. To envisage how a general circulation within the node may be produced by cylindrical cilia, a useful analogy is to a kitchen blender; if this is held vertically in the fluid it is mixing, so that the blades rotate about a vertical axis, the surface flow is a vortex around the stem of the blender.

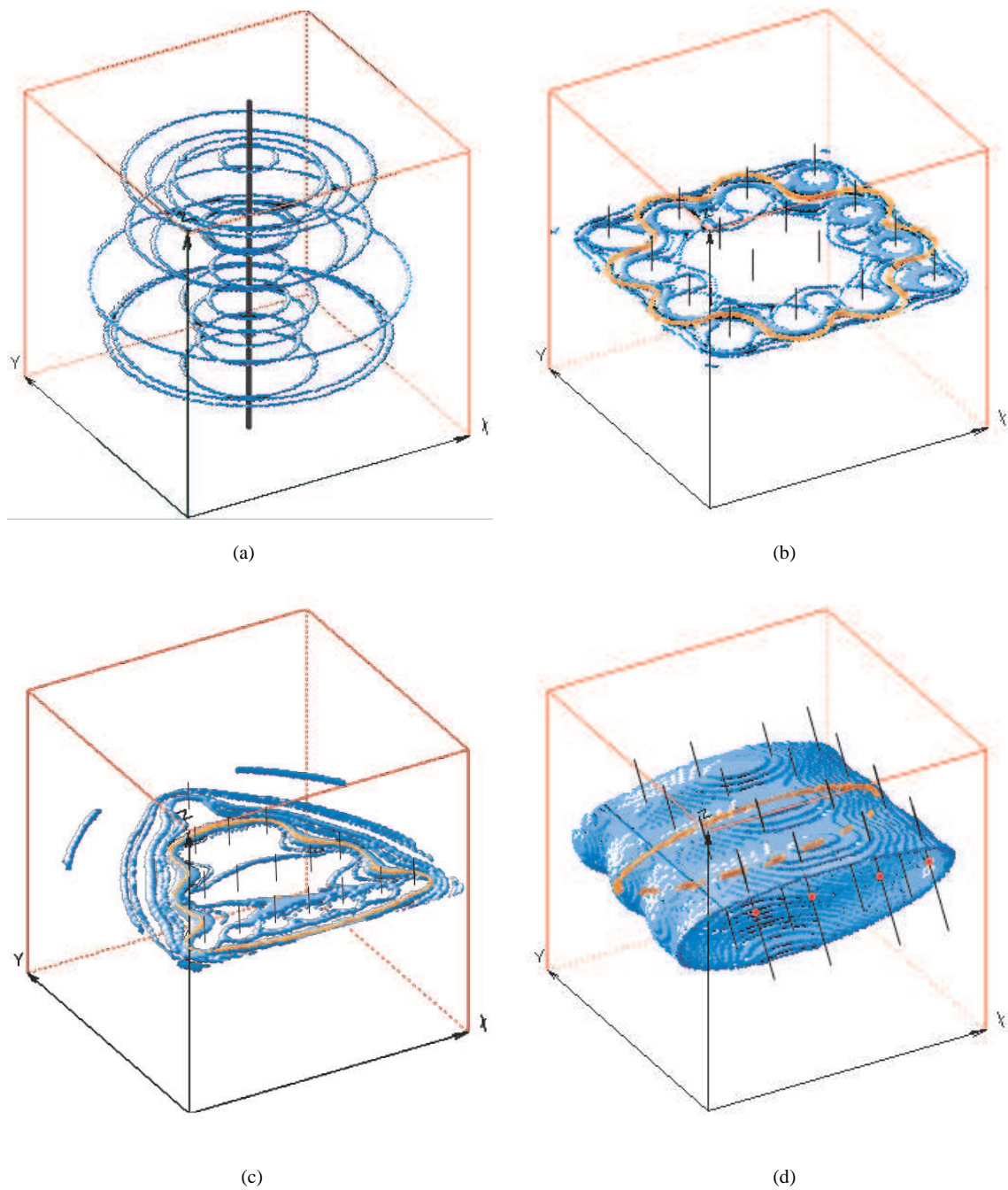


**Figure 4.8:** (a) Vortical flow structure produced by a single rotlet. (b) Rectangular array of rotlets with axes vertical, showing cellular structure of vortices with a general circulation only occurring at the edges. (c) Triangular array of rotlets with axes vertical, to correspond more closely with the shape of the node. As in (b), there is a general circulation only at the edges. (d) Result of tilting the rotlet axes: array of tilted rotlets with tilt angle  $\alpha = 24^\circ$ , showing directional flow above and below the array.

But if the blender is tilted, the surface shows a general flow in the direction in which the blades are turning when they are closest to the surface. In the node, then, we should consider the possibility that the cilia are all inclined, so that they sweep out circles at an angle to the horizontal. If each one is tilted in the same direction, there will be a directional flow across the chamber above them, due to the fluid overhead being entrained in their direction of rotation; the greater the tilt, the stronger the directional flow above the vortices. It may be objected that this tilt implies a prior symmetry-breaking event. This is so, but the symmetry broken is the already defined anterior–posterior, and not left–right; for to obtain the observed leftwards flow, given that they rotate clockwise, the monocilia ought to be tilted towards the posterior.

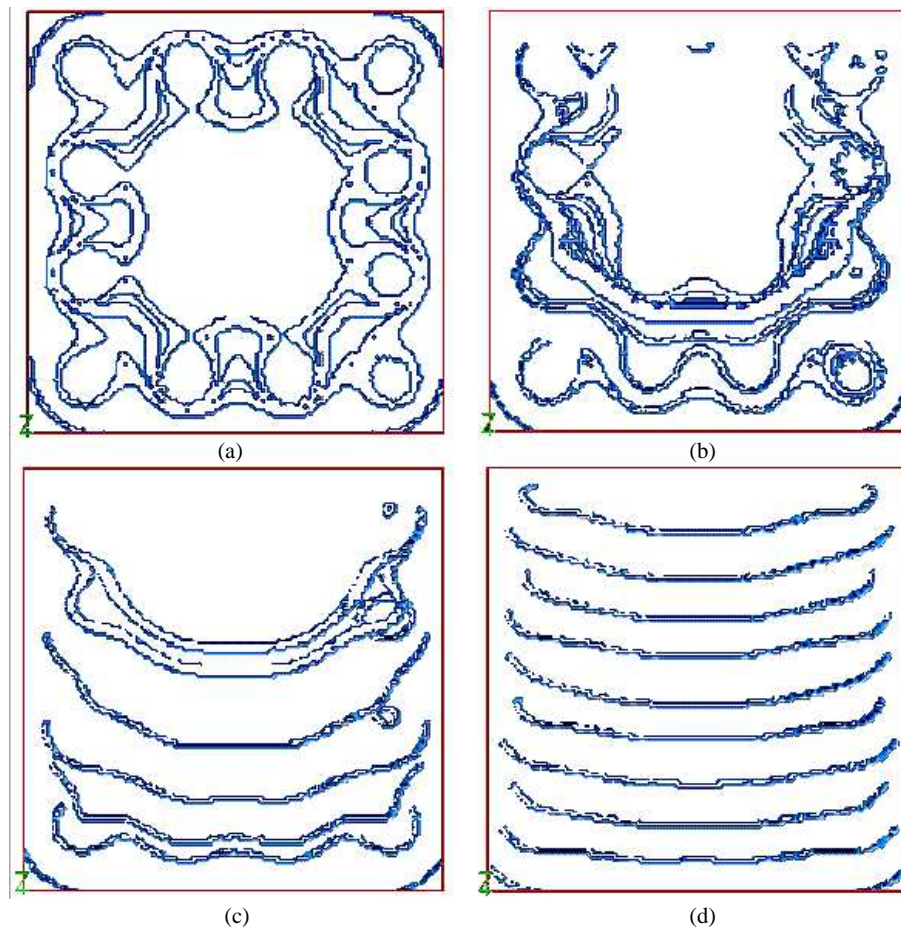


**Figure 4.9:** Views of the  $xy$  plane for  $\alpha$  varying between 0 and  $24^\circ$ : (a)  $0^\circ$ , (b)  $8^\circ$ , (c)  $16^\circ$ , and (d)  $24^\circ$ . For small  $\alpha$  the flow is vortical, while for larger  $\alpha$  it is increasingly linear. The small- $\alpha$  pictures are similar to what is seen in *Inv* mutant mice, while the larger- $\alpha$  cases correspond to experiments on normal mouse embryos.

Consider a single rotlet as in Fig. (4.8a), but now inclined at an angle  $\alpha$  to the vertical. For a general leftward flow as is seen in the node to emerge from a cellular network of such vortices, what angle of tilt  $\alpha$  would be necessary? We can estimate this from the observed tip velocity  $V = 2\pi af$  of a cilium and the flow velocity  $v$  of the nodal fluid. Close to the tips of the cilia, the flow velocity will match the tip velocity. The component of the tip velocity contributing to a directional flow is  $V \sin \alpha$ , so we can estimate  $\alpha = \arcsin(v/2\pi af)$ . If we substitute the ranges of values for  $v$  and  $a$  mentioned earlier, plus  $f = 10$  Hz, we find the range of angles of tilt to be between around  $5^\circ$  to  $25^\circ$  from the vertical. We model such an array of tilted rotlets in Fig. (4.8d), and we see there that a directional flow above the rotlets arises exactly as predicted. From the biological point of view, one can envisage two possibilities for inclined cilia: either the inclination is active, requiring the shaft to bend and straighten as it rotates, or it is passive, with the embedded bearing of the cilium inclined at an angle and no active bending of the shaft being necessary. Our rotlet model covers both these cases, as the fluid dynamics is substantially the same, and with either passive or active inclination, the cilia must be oriented towards the posterior as they rotate. As the angle of tilt varies, the strength of the directional flow compared to the vortical flow alters with it. There is an intriguing genetic abnormality in mice, *Inv*, in which all of the animals have their viscera mirror reversed from the norm. The nodal cilia are present, and rotate at the same 10 Hz and in the same direction as in normal mice. The nodal flow is present in these animals, but altered; instead of a strong leftward flow, passive-tracer experiments show a much more vortical flow structure [127]. It has been speculated that this may be caused by a difference in the shape of the node in *Inv* mice, which is appreciably narrower and rougher than normal [127]. But the node remains left–right symmetric — otherwise the implication would be that left–right symmetry is broken at an earlier embryonic stage — and we have demonstrated above that the tilt of the cilia is much more influential than the precise shape of the node in producing the flow pattern. Our hypothesis is that this mutant mouse may have its monocilia less tilted than normal; a smaller tilt would make the flow more entrained in vortices, and the leftwards component slower, which is just what is observed. The *Inv* mouse node displays very similar flow characteristics to those observed in the node

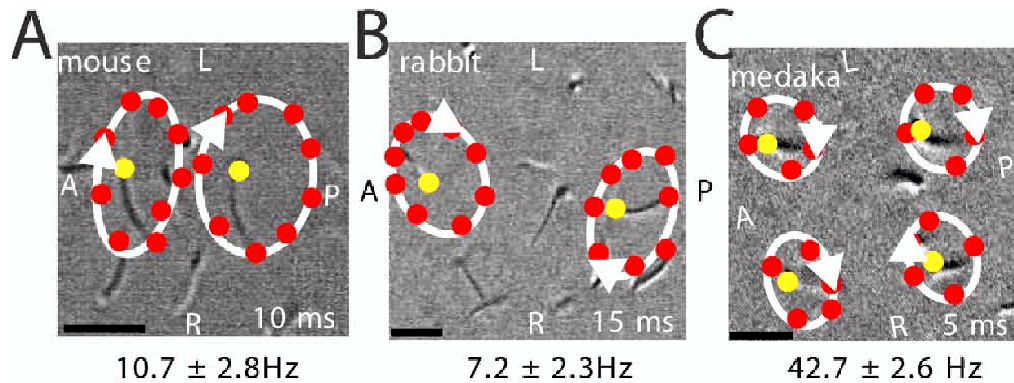


**Figure 4.10:** Posteriorly tilted rotation-like beating of the cilia (A-C) Traces of the cilia. Orientation, the species of the animal, the time interval of the trace, and the frequency of the beating are indicated in the figure. Red circles show the position of the end of the cilia at each time point, and the yellow circles show the position of the root of the cilia. White ellipses show the trajectory of the tip. In these panels, only cilium with its root well separated from the trajectory of the tip is presented for better reproduction. Bars,  $5\mu\text{m}$ .

of normal mice in the early stages of its development, before a strong leftward flow appears [127]. Thus it may be that the tilting of the cilia occurs in normal mice as the node matures, while in *Inv* mice this tilting of the mature cilia never takes place. In Fig. (4.9) we plot just the  $xy$  plane for four different values of  $\alpha$  increasing from 0 to  $24^\circ$ ; for small  $\alpha$  we see exactly the same flow behavior observed in experiments on *Inv* mutant mice embryos.

## 4.5 Comparison With Experiments

Our tilt prediction has now been confirmed by several experiments [128, 124]. Unlike other moving cilia –for example, the ones lying on the airway epithelium– where a fast effective stroke is followed by a slow recovery stroke with a planar or half-teardrop-like trajectory [28], the motile monocilia in the node exhibit, as previously reported, a clockwise rotational-like motion with an elliptic or circular trajectory when observed from above (Figures (4.10)A–C). Interestingly, a more careful inspection in these experiments reveals that cilia swing almost perpendicular to the apical surface of the nodal pit cell and then sweep back almost parallel just above the apical surface, thus moving around an axis tilted toward the posterior. This motion was most evident with the oblique side view of the ventral node of the medakafish. For further quanti-



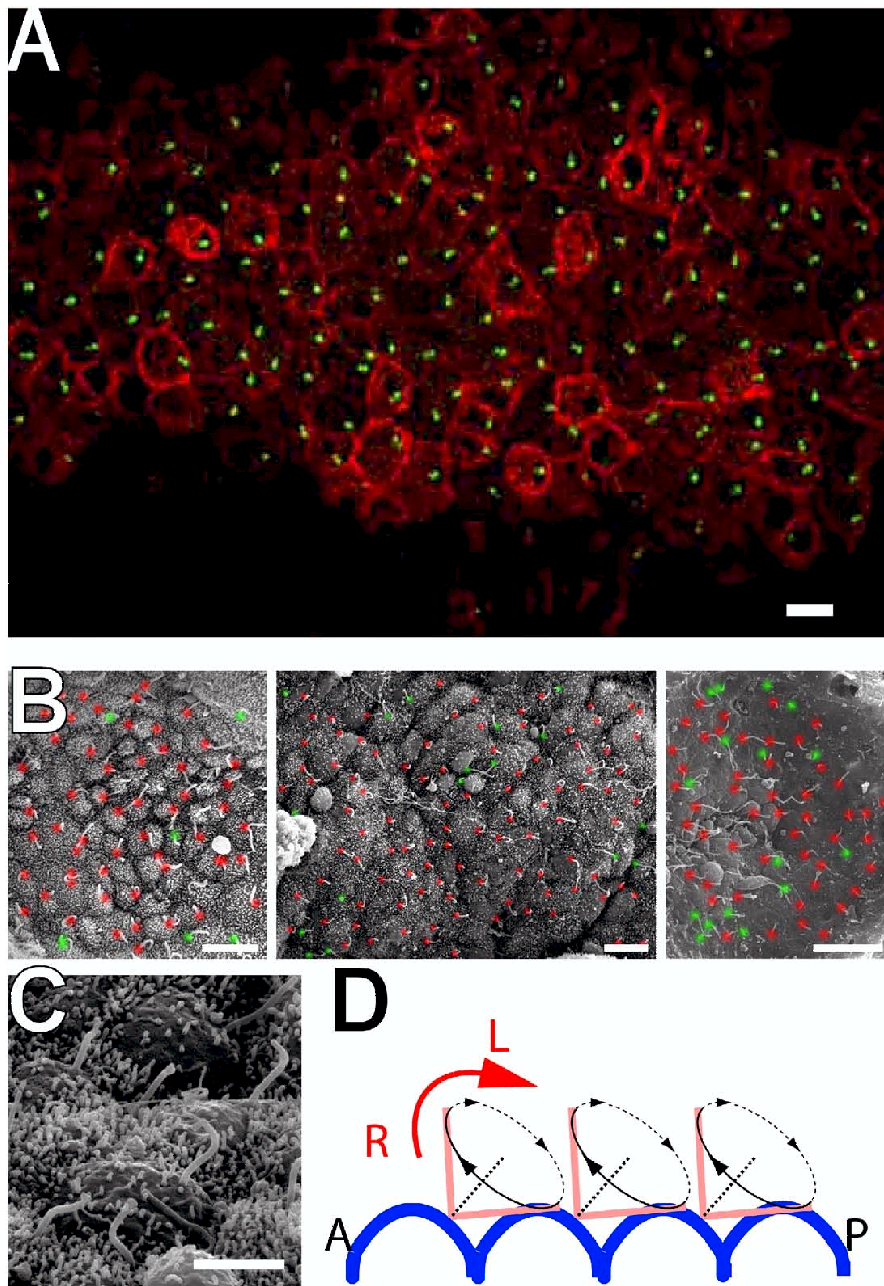


**Figure 4.11:** Ventro-Posterior projection of monocilia by the posteriorly positioned basal body. All micrographs and schema are shown with the anterior side on the left. (A) This panel shows the optically sectioned image of the ventral node of the rabbit embryo. Basal body is stained with anti- $\gamma$ -tubulin antibody in green, and the cell surface is stained with anti-rabbit antibody in red. Bar,  $10\mu m$ . (B) SEM micrographs of ventral nodes of mouse (left), rabbit (middle), and medaka (right). Roots of cilia are colored red when they are located in the posterior side of the apical cell surface, and otherwise they are colored green. About 85% of cilia are projected from the posterior side of the nodal cell (245/302 in mouse, 809/882 in rabbit, and 115/156 in medaka). Bars,  $10\mu m$ . (C) Higher magnification SEM micrograph of rabbit nodal ciliated cells. Note the dome-like curvature of the apical plasma membrane and the posteriorly tilted projection of the monocilia nearly perpendicular to the plasma membrane. Bar,  $5\mu m$ . (D) Schematic representation of the ventro-posterior projection of monocilia.

tative description of this posteriorly tilted rotation-like beating of nodal cilia, the trajectory of the tip of the cilium were analyzed. The trajectory is nearly circular, especially when observed from the direction nearly parallel to the circulating axis of the ciliary movement [127]. When the nodal cilium was observed from the direction perpendicular to the nodal cell layer, the trajectory of its tip was mostly elliptic, with the center located more posteriorly than the root of the cilium (Figures (4.10)A–C). This elliptic trajectory is the projection of the circular trajectory in the real three-dimensional space to the imaging plane parallel to the nodal cell layer. Thus, from this elliptic trajectory, the direction of the axis around which the cilium is circulating can be estimated. This analysis thus demonstrated that the nodal cilia moves around the posteriorly tilted axis. By reviewing the SEM images in light of this finding, it was noticed that most of these cilia project from the posterior side of the apical plasma membrane (Figure (4.11)B). To confirm this posterior projection of nodal cilia, the position of the basal body in the monociliated cells were examined in the rabbit embryo, whose flat and large ventral node allows easier visualization. Immunofluorescent staining of the basal body (Figure (4.11)A) clearly demonstrated that more than 70% of the basal bodies were found near the posterior end of the apical dome-like surface of the monociliated cells. Some basal bodies were near the center of the apical dome, but very few were found on the anterior side.

## 4.6 In vivo vs. In vitro

In all experiments, Reichert's membrane covering the node is of necessity removed. To what degree does the observable *in vitro* flow with the membrane removed differ from the unobservable *in vivo* flow with it in place? Is it for this reason that the return flow we predicted on the *in vivo* case has not been observed experimentally in the *in vitro* flow?

Our rotlet simulations of Fig. (4.8) take place in an infinite medium. We can see in Fig. (4.8d) that corresponding to the directional flow above the rotlets there is an equal and opposite flow below them. We should expect this counterflow in the node also, except that there it will be modified by the presence of the node walls. Moreover, in the embryo *in vivo*, the node is a



closed structure from the point of view of advective flow, being covered by Reichert's membrane [123] (beyond the limits of the nodal chamber, there may be diffusion but not advection under this membrane), so fluid flowing leftwards must return rightwards. If the outward flow takes place in the centre of the chamber, as experiments show, the return flow has no choice but to follow the walls, both close to the node floor around the bases of the cilia, as Fig. (4.8d) indicates, and, additionally, close to the other walls; we sketch the complete flow pattern that would be expected, with recirculatory vortices in the upper and lower halves of the node, in Fig. (4.13a). As flow close to a wall is slower than in the bulk of the fluid, the return flow will be slower than the primary flow, but as it necessarily transports the same volume of fluid as the outward flow, it must be more spatially extended. It has not yet been seen experimentally. This is probably for two reasons: firstly, in the embryo *in vitro*, in order to obtain access to the nodal flow, Reichert's membrane is removed, and the embryo is immersed in a much larger liquid-filled container [123]. Under these experimental conditions there is an open rather than a closed flow as *in vivo*, the return flow above the outward flow is eliminated, and that below it is diminished. Secondly, the passive tracers are injected into the flow above, and not below the cilia, so they experience only the outward flow.

To dilucidate these ideas we represent the node by a fluid-filled box of dimensions  $50 \times 50 \times 10 \mu\text{m}$ , either completely closed as *in vivo*, or open at the top and placed within a much larger fluid-filled volume to model the *in vitro* bead-tracking experiments. We solve the steady-state Navier–Stokes equations for the nodal fluid set into motion by the cones that form the surfaces of revolution of the cilia. These (length  $3 \mu\text{m}$ ; half-angle  $45^\circ$ ; rotation frequency 10 Hz) rotate clockwise viewed from above inclined at an angle  $\alpha = 25^\circ$  to the posterior. The ciliary Reynolds number is of order  $10^{-4}$ . We present our results in Fig. (4.12). In both the *in vivo* and the *vitro* node there is a general leftward flow across the center of the node that corresponds well to that observed in experiments. In the *in vivo* case, this fluid recirculates within the node following the walls (Fig. (4.12a)), so the general scheme is of two vortices, one each in the upper and the lower halves of the node; fluid flows to the left across the middle and returns to the right along the ceiling and floor

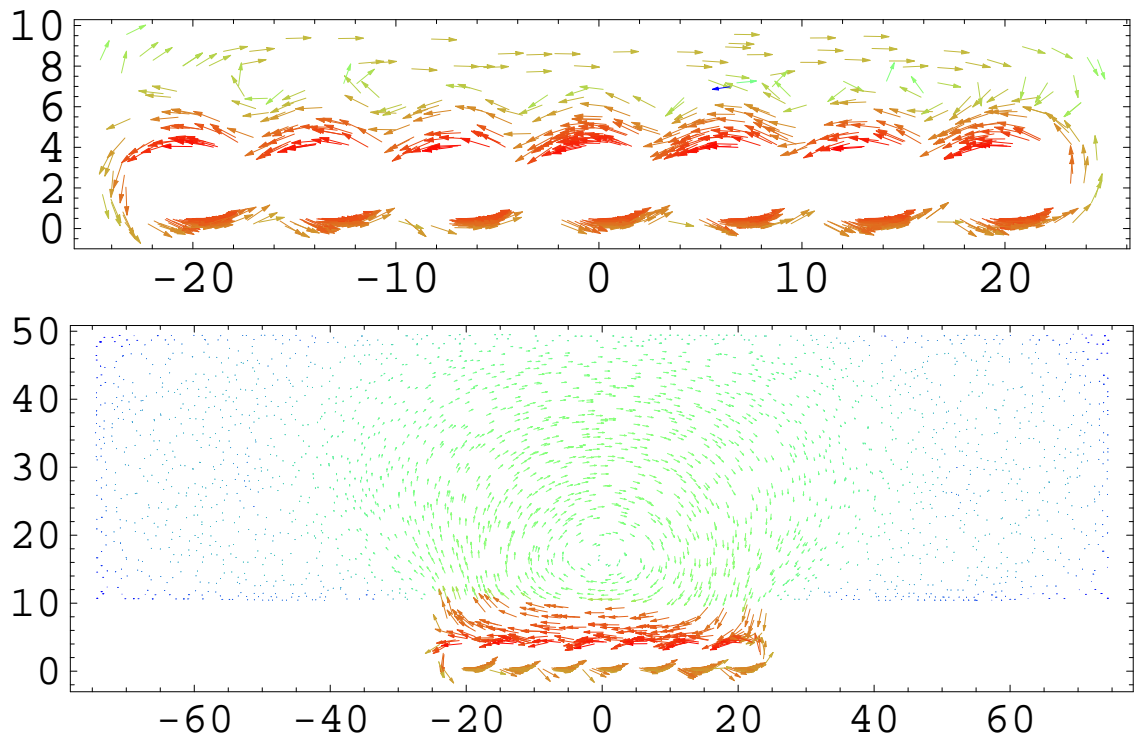


**Figure 4.12:** Vertical slices of the velocity field in the node: (a) *in vivo*, and (b) *in vitro*.

of the node. The flow in the lower vortex is more complex than in the upper vortex owing to the presence of the cilia; while there is a general recirculation across the floor of the node, some pathlines representing fluid parcels become trapped in the vicinity of a cilium and may spend some time there before rejoining the general circulation once more. In contrast, in the *in vitro* case, the opening of the node completely eliminates the upper recirculatory vortex within the node (Fig. (4.12b)). Fluid is now free to enter and leave the node to flow around a much larger surrounding volume, so the upper recirculation occurs around the whole of the box containing the node. As the fluid volume is larger, velocities are lower, and the rightward return current occurs far beyond the limits of the node in a manner so diffuse as to be almost imperceptible compared to the leftward flow. The strong leftward current above the cilia is, as before, the most prominent feature of the flow. The flow in the lower half of the node persists, but the general rightward component is diminished compared to recirculatory flow about individual cilia. Thus, while the main feature of the nodal flow, the central leftward current, is present

both *in vivo* and *in vitro*, there are significant differences in other aspects of the flows. This explains why the recirculation of fluid rightwards predicted in the *in vivo* case has not been observed *in vitro*, and should make one wary of using *in vitro* bead tracking experiments as the sole basis for understanding the *in vivo* flow; they ought to be interpreted together with a knowledge obtained from simulations of the differences between the *in vivo* and *in vitro* flows. These differences should be taken into account when weighing the various alternatives for the — as yet unknown — sensory mechanism through which the information about the directionality of the fluid flow is passed to the embryo.

## 4.7 Symmetry breaking

How is the information on the symmetry broken by the nodal flow transmitted to the embryo? The *Inv* mutant mice mentioned earlier provide an important clue to the mechanism. Although the nodal flow in these animals is still leftwards, albeit slower than normal, they all have *situs inversus*. A mechanism must be sought that would lead *Inv* mice to have opposite chirality. Two means have been proposed for how information may be extracted from the nodal flow: chemosensing and mechanosensing. On one hand, it has been suggested that the nodal fluid may be carrying a morphogen, a signalling molecule — probably a protein — that is released into the flow, and whose concentration is detected by chemoreceptors within the node [123]. On the other, very recent experimental work has shown that there appear to be two populations of monocilia in the node, and has speculated that the second may be nonrotating mechanoreceptors [111]. Below we first treat the morphogen hypothesis, and develop a model for morphogen transport and mixing in the node compatible with the observations and with the physics. We then discuss why mechanosensing is unlikely to be the mechanism operating in the node.

The morphogen hypothesis proposes that a difference in morphogen concentration detected by receptors placed on both the left and right sides of the node should be the factor that determines the chirality of the left–right axis. This implies that the concentration of active morphogen should reach a steady state that in normal embryos is higher on one side of the node, and

in *Inv* embryos on the other. To see how this might come about, we have to comprehend how a morphogen would be transported and mixed by the nodal flow. Mixing in the creeping flow in the node is very different to that we are more accustomed to seeing at higher Reynolds numbers, for example when we stir milk into our tea or coffee. In particular, turbulent mixing plays no rôle here; for there is no turbulence at low Reynolds numbers. We emphasize this as some articles on nodal flow have described the slow vortical flow in the *Inv* mouse as turbulent; it is not. What is seen in the node is always laminar flow, and the complex particle paths observed in low-Reynolds-number flows arise not from turbulence, but from another phenomenon, that of chaotic advection [133]. Two factors are important in mixing in creeping flows; advection by the flow, and molecular diffusion. Advection can be quantified by an advective mixing time  $\tau_a = L/v$ , where  $L$  and  $v$ , as given earlier, provide us with the estimate  $1 < \tau_a < 5$  s for the time for a morphogen to be advected across the node in normal mice. On the other hand, molecular diffusion is independent of fluid flow and takes place at a rate determined by the diffusivity of the morphogen, which depends on its molecular mass. For biological macromolecules like proteins, the diffusion coefficient  $D$  is typically in the range from  $10^{-11}$  to  $10^{-10}$   $\text{m}^2\text{s}^{-1}$ . We can then estimate a diffusive mixing time  $\tau_d = L^2/D$  for a morphogen in the node, which lies in the range  $25 < \tau_d < 250$  s, and compare the relative importance of advection and diffusion with the ratio  $\tau_d/\tau_a$  of these mixing times. This dimensionless ratio is called the Péclet number  $Pe = vL/D$ . Our estimate for the Péclet number is then in the range  $5 < Pe < 250$ ; greater than unity — if it were not advection would be unimportant — but relatively small, so the contribution of diffusion is fundamental to mixing and cannot be ignored. In physical terms then, morphogen transport and mixing is an advection–diffusion system. The implication of this analysis for the biology is that the morphogen must be degraded and become inactive rapidly after its release — in a time scale shorter than the diffusive mixing time — otherwise it would reach a constant concentration throughout the node and be of no use for initiating symmetry breaking through concentration differences.

There are *a priori* many possibilities for the positions of the sources and receptors of morphogen within the node. Okada et al. analysed a series of

models for compatibility with the genetic and biochemical evidence [127, 186]. We, in addition, ask that it be faithful to the fluid-dynamical, transport, and mixing properties of the nodal flow. We present a model that fulfils all these requirements in Figs. (4.13b) and (4.13c), in which we exhibit the results of numerical simulations of advection–diffusion equations in a rectangular domain representing the flow in a cross section of the node as in Fig. (4.13a). Morphogen is released from the perinodal regions at the left and right edges of the node, and detected by receptors across the whole floor of the node. As the sources are in the upper part of the node, the morphogen finds itself to begin with in the upper recirculatory vortex. The morphogen coming from the right side is swept leftwards across the node in the central leftward current, while that from the left side is pushed rightwards across the roof of the node by the upper recirculatory vortex. While it is advected by the flow, the morphogen diffuses. Diffusion allows it to cross flow streamlines and so to penetrate into the lower recirculatory vortex, where it can come into contact with the receptors on the floor of the node. As the leftward flow is approximately  $5\ \mu\text{m}$  above the floor of the node, the characteristic vertical diffusion time down to the floor of the node is of order 0.25–2.5 s. If we compare this with the advection time across the node, 1–5 s for normal animals, and twice as long or more for *Inv* mice, it is clear that on which side of the node the maximum concentration of morphogen reaches the node floor will depend crucially on this advection time. In a normal animal the morphogen in the central leftward current is swept to the left side of the node before it arrives by diffusion at the node floor, but with the slower nodal flow in *Inv* mice the advection time is longer, so the diffusing morphogen arrives at the node floor on the right side of the node, and activates the right side receptors instead of the left. Shortly thereafter, the morphogen must become degraded, so that although it will continue circulating within the node, it is now in an inactive form and unable to dock with the receptors. As a result, the steady-state active morphogen concentration pattern at the floor of the node is as shown in Figs 4.13d and 4.13e, with the maximum on the left in normal animals, but on the right in *Inv* mice. This steady state, maintained for the duration of the nodal flow — for some hours [127] — during the relevant stage of embryonic development, must be the signal to activate the biochemical machinery that should inform

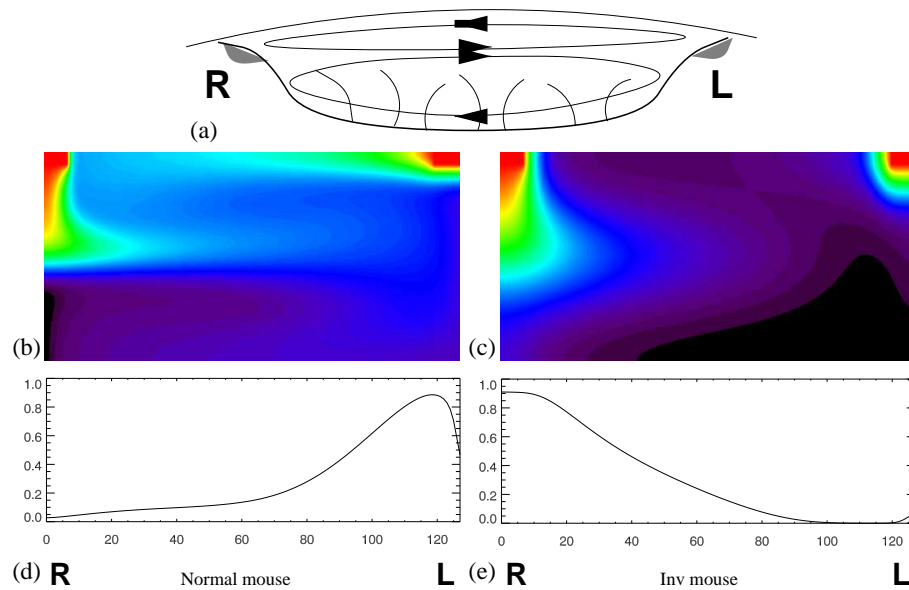


**Figure 4.13:** (a) Sketch of how fluid will recirculate within the node *in vivo* with diffuse return flows above and below the more intense outward flow in the centre. Also shown is the putative placement of morphogen sources (grey areas) at the left and right sides adjacent to the upper recirculatory vortex. Numerical simulations of our model depicting the steady-state concentration of a morphogen with a finite lifetime within the node with (b) normal, and (c) *Inv* mice. The colour scale is as for a rainbow, with red the highest concentration, and violet the lowest. Graphs of the concentration of morphogen at the floor of the node in the above simulations with (d) normal, and (e) *Inv* mice (arbitrary units).

the rest of the embryo about visceral positioning [81].

Our model thus explains the symmetry breaking seen in both normal and *Inv* mice. In the earlier delayed-activation model proposed by Okada et al. [127], a signalling molecule is released at the left and right sides of the node in an inactive form, while receptors are present across the whole of the floor of the node. Some time after release, the molecule becomes activated and can dock with the receptors. Following this hypothesis, in a normal animal the activated morphogen would dock with more receptors on the left side, while in an *Inv* mouse the slower flow would allow the morphogen to become activated while still on the right side of the node, producing *situs inversus*. By taking into account the fluid dynamics we have seen that delayed activation is not necessary — although it is perfectly compatible with our model — as the molecular diffusion time from the central nodal current to the floor ensures that a morphogen does not immediately come into contact with its receptors. Furthermore, by taking into consideration the closed nature of the node and

the recirculation pattern of flow it implies, we have shown that while an activation time for the morphogen is not necessary, an inactivation time is. The morphogen must have a window of activity, between an initial time which could be zero (instant activation), or nonzero (delayed activation), and a final time less than  $\tau_d$ , the diffusive mixing time in the node. The second population of monocilia recently observed in the node [111] has been speculated to be mechanoreceptors for the flow. Monocilia possess the necessary biochemical machinery for both mechano- and chemoreception [136]. We suspect that in the node they may not be mechanoreceptors, but instead are chemoreceptors for the morphogen.

These two alternative mechanisms about how fluid flow is sensed by the embryo are still under discussion: the unidirectional transport of a morphogen protein, and the asymmetric deformation of mechanosensory cilia (the two-cilia hypothesis [173]). In a recent work, Tanaka et al. [174] provide the first experimental support for the former model, showing that Sonic hedgehog (Shh) protein and retinoic acid are encapsulated into membrane-wrapped nodal vesicular parcels (NVPs), which are asymmetrically transported by the flow across the node. The NVPs are membrane-sheathed objects  $0.3 - 5\mu m$  in diameter that carry Sonic hedgehog and retinoic acid. These NVPs are transported leftward by the fluid flow and eventually fragment close to the left wall of the ventral node. Once there, they trigger the cascade that initiates left-right patterning, through the formation of morphogen gradients. Tanaka and coworkers directly visualize the transport of NVPs in the node through scanning and transmission electron microscopy and the concentration of  $Ca^{+2}$  in both wild type and *iv* mutants (Fig. 4.14).

## 4.8 Conclusions

Biological symmetry breaking is a problem that has long interested physical scientists. In his pioneering work on the chemical basis of morphogenesis, Turing [181] proposed the mechanism of pattern formation through the interaction of diffusing morphogens that now bears his name. He recognized the special problem for his theory posed by left-right symmetry breaking in vertebrates; how to explain that nature almost always breaks left-right sym-

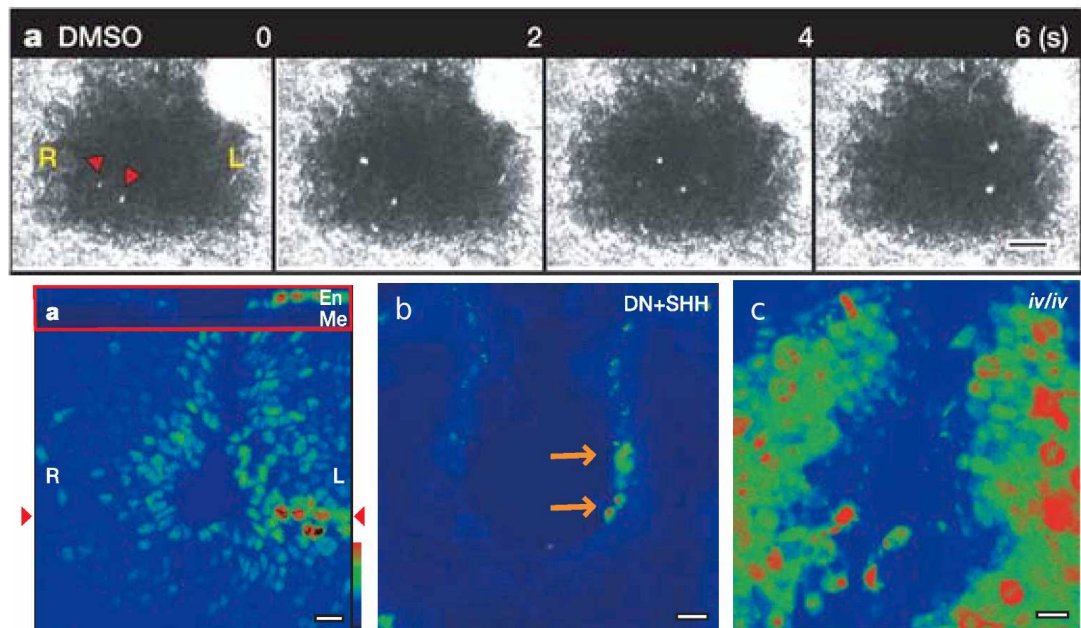


**Figure 4.14:** (a) Time-lapse images of the ventral nodes showing NVP flow. Scale bar is 10mm. Red arrowheads show detached NVPs. (b) Ventral view of  $Ca^{+2}$  imaging of wild type (WT) (a-b) and *iv/iv* mutant (c) embryos, represented by pseudocolour (signal intensity: red > green > blue > black). Upper, anterior; lower, posterior. The upper part of (a), boxed in red, is a transverse section reconstructed from a Z-series of images at the level between the red arrowheads.

metry in a given sense, whereas his mechanism would lead to approximately equal numbers of animals with *situs inversus* and *situs solitus*? He proposed that the input to the system must somehow be biased. Almirantis & Nicolis [5] later showed in detail how an initial gradient could seed the process. Brown & Wolpert [32] hypothesized a chiral molecule with a fixed orientation relative to the anterior–posterior and dorsal–ventral axes, which would provide the necessary information on left and right for the initial biasing. But nature, it seems, in mice at least, prefers to use not a chiral molecule, but a chiral structure — a molecular motor — to provide advection in a given direction relative to the anterior–posterior and dorsal–ventral axes to seed the symmetry breaking. The information on which side is which is then carried to the rest of the embryo by diffusion. Hamada et al. [81] propose that the subsequent phase of propagation of the broken symmetry could function by exactly the mechanism Turing imagined, with the initial small concentration difference produced by the nodal flow magnified by a nonlinear interaction between two diffusing proteins, Nodal and Lefty. A further possibility is that



the interaction may involve the fluid flow itself, which would make this a biological instance of a recently proposed generalized Turing pattern-formation mechanism including fluid flow [159].

We have discussed here experiments on mice, but similar structures to the node with its monocilia are found in other vertebrate embryos (Fig.4.15), so it has been surmised that this left–right symmetry-breaking mechanism may be universal among vertebrates [65]. On the other hand, experimental evidence has been put forward for asymmetries in chick and frog embryos before the emergence of the nodal structures [114]. If these observations prove to be correct, then nodal flow is not the earliest left–right symmetry breaking event in some vertebrates. If the initial symmetry-breaking mechanism differs across species, the chiral molecule or structure, equivalent to the chiral monocilium of the node, that bootstraps the process must be sought for those cases. Moreover, the rôle of the nodal flow in those species would need to be clarified: would it then be acting as a means to preserve or amplify an initial asymmetric signal from the earlier symmetry-breaking event, or would it constitute a second, independent, mechanism for determining left and right? Might this be a case of two independent mechanisms creating extra security through redundancy? More evidence needs to be collected.

Diffusion is ubiquitous in biology. Nature also often uses advection to achieve its ends, for example in the cardiovascular system, and it has recently been found to be fundamental in the development of the heart [85]. The use of cilia to move fluid is also common, for example in the lung. Microbes use cilia and flagella for propulsion, just as the node uses them to advect fluid, and the similarity of scale implies a similarity of environment. This highlights the resemblance of the situation to that of microbial swimming. In both cases, we are talking of life at low Reynolds number [151]. The problems of moving fluids at the microscale, with their associated low Reynolds numbers, are also now interesting engineers who design fluid flow microsystems; so-called microfluidics devices [72]. We humans inhabit a world of much higher Reynolds number, and our intuition on how fluids behave is not straightforwardly transferrable into this alien inertialess environment, which is why some ideas put forward for producing a directional flow from rotating cilia cannot work. In creeping flow, algorithms like varying the angular velocity

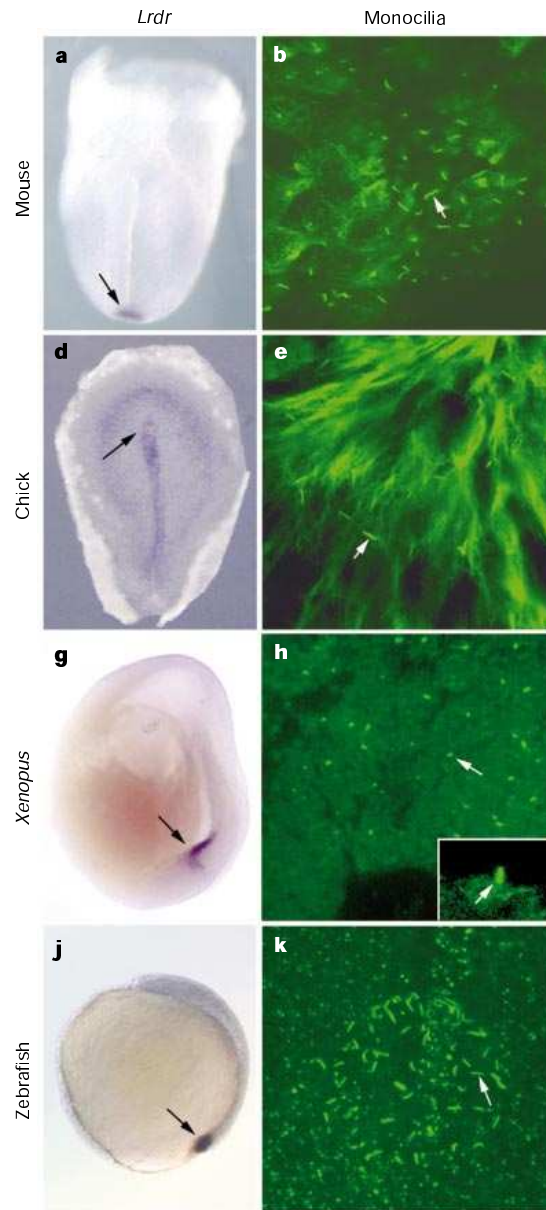


**Figure 4.15:** Regions of potential leftright signalling in mouse, chick, *Xenopus* and zebrafish. These regions were identified by in situ hybridization with *Lrd* probes (left) and immunofluorescence with an antibody against acetylated tubulin to detect cilia (right). (a) Frontal view of a mouse embryo 7.5 days post-fertilization (d.p.f.), showing *Lrd* expression at the node. (b) Ventral view of a mouse embryo at 7.5 d.p.f., showing cilia on the ventral surface of the node. (d) Dorsal view of a HamburgerHamilton (HH) stage-4 chick gastrula-stage embryo showing *Lrd* expression in Hensens node and in the primitive streak. (e) In chick, cilia are present at Hensens node at HH stage-4 in the space between the dorsal epiblast and the ventral endoderm. (g) Lateral view of a stage-13 *Xenopus* embryo, showing *Lrd* expression in the ventral cells of the dorsal blastopore. (h) After the completion of gastrulation in *Xenopus*(stage 14), cilia begin to form on the ventral surface of the dorsal blastopore. Inset, lateral view of a single cilium. (j) Lateral view of a late gastrula, or 90% epiboly, zebrafish embryo, showing expression in the dorsal forerunner cells ahead of the organizer region. (k) In zebrafish at the 10-somite stage (dorsal view), cells in Kupffers vesicle are ciliated on their inner surface. Anterior is towards the top in all panels; black arrows show regions of *Lrd* expression where cilia are found (or subsequently develop); white arrows show cilia.

of the cilia in different parts of the rotation cycle do not obtain the desired effect, because there is no fluid inertia. Similarly, the idea of the mechanical sensing of the shear stress on the node walls, or the velocities of the flow at the side walls, rather than a morphogen, being responsible for the symmetry breaking is not tenable, since at low Reynolds number the magnitudes of the shear stresses and flow velocities are symmetric across the node; it is only the direction that breaks the symmetry. Mechanosensing of the flow by cilia [173, 136] could then provide the signal for symmetry breaking only if the sensors could detect not just the magnitude, but also the direction of the flow; however there are no reports that monocilia possess this vectorial capability (such a signal is produced, for example, by the hair cells of the ear [156], but these are cells possessing bundles of cilia). Producing the nodal flow is not like waving your arms about in a swimming pool [190], but more akin to finding oneself “in a swimming pool that is full of molasses, and . . . forbid[den] . . . to move any part of [the] body faster than 1 cm/min” [151]. In the nodal environment, nine orders of magnitude lower in Reynolds number than the above person in a swimming pool, the lack of inertia constrains the fluid physics that the biology can exploit, leaving our proposed mechanisms of a posterior tilt of the cilia and the chemosensing of the flow as the best hypotheses, compatible with the facts, for producing the observations reported in experiments.

The direction of rotation of a monocilium is determined by the motor proteins that power its molecular motor. These, like the vast majority of naturally occurring proteins, are made up of chiral amino acids in just one of their two possible forms: they are all laevo. An equivalent molecular motor using the same amino acids in their opposite, dextro, configuration would rotate in the reverse direction. In this way left–right symmetry breaking here is ultimately determined by the chirality of natural amino acids, not directly through a chiral molecule, but by setting the direction of the nodal flow. There are several schools of thought as to how this natural chirality has arisen. One supposes it to be a frozen accident, and that life could equally have chosen to use dextro amino acids, but a competing idea points out that laevo amino acids are slightly more stable than the dextro forms owing to the broken parity of the weak nuclear force [109]. This provides us with the fascinating idea that we may have our hearts on the left because, as Wolfgang Pauli famously

put it, God is weakly left handed [112]. But, whether or not there turns out to be a causal link between parity violation and the asymmetry of the vertebrate body plan, after answering the *how* part of the symmetry-breaking problem, the most intriguing question that remains may be: *why* does nature take care to break the symmetry in a given direction, rather than leaving things to chance and allowing half the population to have *situs inversus*?

# Chapter 5

## Living bodies: Bacterial Swimming and Oxygen Transport Near Contact Lines.



### 5.1 Introduction

*This Chapter is devoted to the dynamics of living organisms. Eons before we came into existence, bacteria had already invented many of the features that we immediately think of when asked what is life?. Bacteria, being the first form of life on Earth, had to devise ways to convert inorganic substance into living matter. This is not a solitary endeavor for the bacteria; under natural conditions, they use chemical communication to form hierarchically structured colonies, consisting of  $10^9 - 10^{13}$  bacteria each. By acting jointly, they can make use of any available source of energy and imbalances in the environment to reverse the spontaneous course of entropy production and synthesize life-sustaining organic molecules for themselves and in the service of all other organisms.*

Bacteria have come up with sophisticated modes of cooperative behavior to cope with adverse and varying environmental conditions. They developed intricate communication capabilities, including a broad repertoire of chemical signalling mechanisms, collective activation and deactivation of genes and even exchange of genetic materials. With these tools they can communicate and self-organize their colonies into multicellular hierarchical aggregates, out of which new abilities emerge.

During colonial development, bacteria create a wealth of patterns, some of which are reminiscent of those observed in abiotic systems. Therefore, it could be expected that the principles of abiotic self-organization would help us to understand the colonial behavior. Still, some words of caution are warranted here. One must avoid ‘mathematication’ of biotic systems, and keep in mind that bacteria can exhibit much richer behavior that reflects their sophisticated communication capabilities. As in abiotic systems, patterns emerge through the singular interplay between individual bacteria (micro-level) and the colony (macro-level). However, inherent in the growth of a colony is an additional degree of complexity: the building blocks are themselves biotic systems, each with internal degrees of freedom, internally stored information and internal processing (interpretation) of information. These afford each bacterium a certain freedom to respond and alter itself, sometimes even by altering gene expression and bringing about changes in other bacteria via emission of signals in a self-regulated manner.

In most natural aquatic ecosystems, microorganisms are advected more or less passively in the large-scale flows generated by various imbalances of the environment. In a quiescent fluid, however, even their slow motion (typically a couple of meters per day) and physical interactions can result in considerable spatial rearrangements, and influence the dynamics of the system [113]. Bioconvection is one of the oldest documented collective behaviors of independent microorganisms [187, 106, 143, 146], arising spontaneously in suspensions of diverse swimming microorganisms such as bacteria, algae or ciliated protozoa [94, 137, 96]. Typically, bioconvective pattern formation occurs in shallow suspensions at high cell concentration if the density of cells is 5 – 15% larger than that of water and the average direction of the microorganisms swimming is upward in response to some external stimulus, e.g. gravity, light

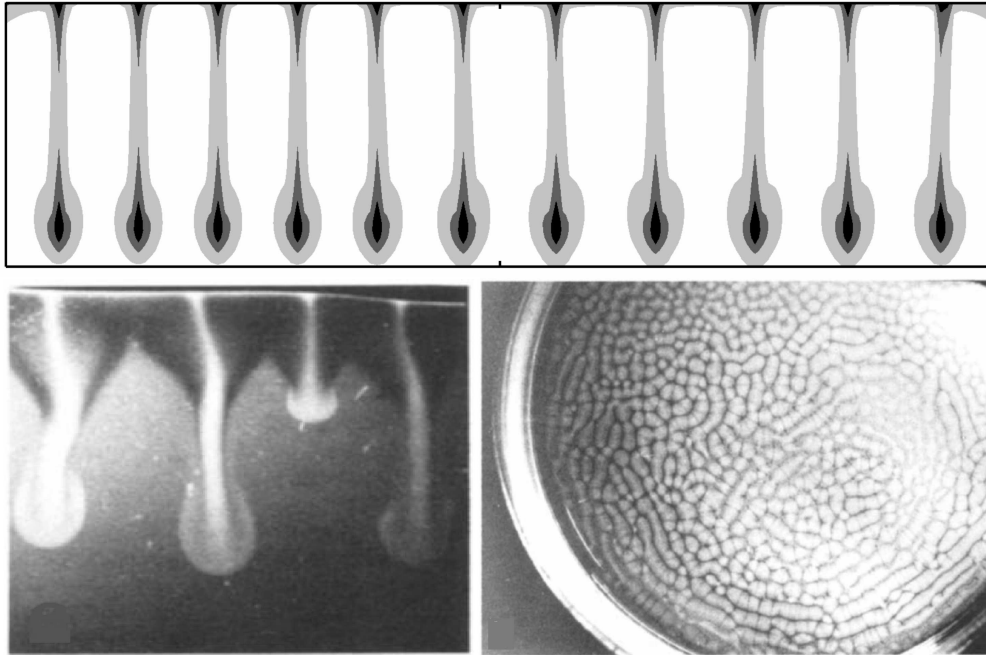


**Figure 5.1:** Numerical and experimental bioconvective plumes.

or oxygen-concentration gradient. For instance, in non-aerated suspensions of *B. subtilis* (aerobic, soil-living bacteria) upward swimming is a chemotactic behavior directed by the oxygen gradient [176]. The continuous upward swimming results in a density inversion, i.e. the surface layer of the suspension becomes denser than the bulk. This configuration is mechanically unstable, and through a Rayleigh-Taylor instability [146] the top layer sinks in vertical plumes (Fig.(5.1)). As the velocity of the emerging fluid motion is larger than the swimming speed of the microorganisms, they are dragged along from the surface into the bulk of the liquid. Recently, a number of theoretical [137, 95] and experimental [21, 90, 55] studies analyzed the physical aspects of bioconvection.

Bacterial chemotaxis, oriented swimming along chemical gradients, is generally viewed as locomotion in an otherwise quiescent fluid [24]. Yet, the very flagella which propel the cell inevitably stir up the fluid through their high-speed rotation, bundling, and unbundling. Conventional arguments [25] showing the irrelevance of advection compared to diffusion are based on the smallness of the Peclet number  $Pe = UL/D$ . For a swimmer of micron scale  $L$ , moving at a speed  $U$  of several body lengths per second, and  $D \sim 10^{-5} \text{cm}^2 \text{s}^{-1}$

a solute diffusion constant, we have  $Pe \sim 10^{-2}$ , confirming this for an isolated swimmer. Yet, the collective hydrodynamics of concentrated assemblies of cells greatly changes this situation, yielding  $Pe > 1$ . Such assemblies can arise due to the joint action of chemotaxis, a symmetry breaking source of metabolites, and gravity. Once concentrated, the collectively driven hydrodynamics globally outcompetes diffusion.

Aerobic bacteria often live in thin fluid layers near solid-air-water contact lines, where the biology of chemotaxis, metabolism, and cell-cell signaling is intimately connected to the physics of buoyancy, diffusion, and mixing. Using the geometry of a sessile drop we demonstrate in suspensions of *B. subtilis* the self-organized generation of a persistent hydrodynamic vortex which traps cells near the contact line. Arising from upward oxygentaxis and downward gravitational forcing, these dynamics are related to the Boycott effect in sedimentation, and are explained quantitatively by a mathematical model consisting of oxygen diffusion and consumption, chemotaxis, and viscous fluid dynamics. The vortex is shown to advectively enhance uptake of oxygen into the suspension and the wedge geometry leads to a singularity in the chemotactic dynamics near the contact line.

The interplay of chemotaxis and diffusion of nutrients or signaling chemicals in bacterial suspensions can produce a variety of structures with locally high concentrations of cells, including phyllotactic patterns [33], filaments [27], and concentrations in fabricated microstructures [134]. Less well explored are situations in which concentrating hydrodynamic flows actually arise from these ingredients. Here we report a detailed experimental and theoretical study of an intriguing mechanism termed the *chemotactic Boycott effect*. Briefly described earlier [60], it is intimately associated with buoyancy-driven flows, metabolite diffusion, and slanted air-water menisci. The ubiquity of contact lines and their transport singularities [57] suggest importance of these observations in biofilm formation [131]. The large-scale stirring created by these flows illustrate important advective contributions to intercellular signaling, as in quorum sensing [18].

The chemotactic Boycott effect takes its name from a phenomenon in sedimentation [30] that occurs when the chamber containing a fluid with settling particles is tilted from vertical. Settling depletes the fluid near the upper



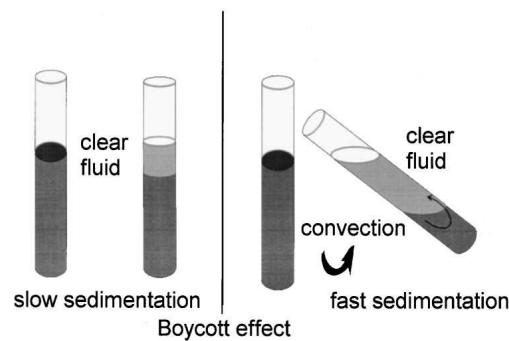


**Figure 5.2:** The Boycott effect as it works in sedimentation.

wall, making it buoyant relative to nearby fluid, whereupon it rises (Fig.5.2). This boundary flow stirs up the entire medium, greatly accelerating the settling process. In the chemotactic version, negatively-buoyant aerobic bacteria swim up to the free surface of a sessile drop, and slide down the slanted meniscus, producing high concentrations of cells near the three-phase contact line. In earlier work where this was observed [60], the detailed nature of hydrodynamic flows near the contact line was unclear. Here, by direct visualization and particle-imaging velocimetry (PIV) we show that the sliding surface layer drives a circulating hydrodynamic *vortex* in the meniscus region that is central to the microecology. While counterintuitive in viscous flows, persistent circulation driven by forcing at the free surface is consistent with the classic analysis for vortex generation in wedge geometry [118].

The initial discussion of the chemotactic Boycott effect lacked a quantitative explanation in terms of the coupled dynamics of oxygen transport and consumption, chemotaxis, and viscous fluid dynamics. Here we present numerical and analytical results on one such model, and show they provide a good accounting of the major experimental observations. The characteristic fluid velocity  $U$  and length scale  $L$  associated with the vortex are both significantly larger than those of a single bacterium. We find the Boycott-like flows lead to  $Pe \gg 1$ , indicating the advection-dominated regime, just the opposite of the situation at the scale of a single bacterium. In addition, by analogy with evaporative singularities in sessile drops [57, 58], we find a singularity in the oxygen uptake rate at the contact line. Along with the large-scale stirring of fluid in the drop, this significantly enhances the overall oxygen concentration

in the medium, showing that collective effects can improve the viability of the population, as demonstrated by remarkable collective activity [60] of the extremely concentrated organisms near the drop edge.

## 5.2 Materials and Methods

Experiments were conducted with *B. subtilis* strain 1085B. Samples were prepared by adding 1 ml of  $-20^{\circ}$  C stock to 50 ml of Terrific Broth (TB; Ezmix Terrific Broth, Sigma: 47.6g broth mix and 8 ml glycerin in 1 l dH<sub>2</sub>O) and incubating for 18 h (shaker bath;  $37^{\circ}$  C, 100 rpm), after which 1 ml was added to 50 ml of TB and incubated for 5 h. The 5 h culture was then slowly added to the chamber with a syringe (21G needle). The  $-20^{\circ}$  stock was prepared by adding spores on sand to 10 ml. Terrific Broth at room temperature in a petri dish and allowing for  $\sim 24$  h of growth. 1 ml of 24 h stock was added to 50 ml TB and incubated for 18 h. 1 ml of the 18 h culture was added to 50 ml of TB and incubated 5 h. Aliquots composed of 0.75 ml of 5 h culture mixed gently with 0.25 ml glycerin were placed in cold storage. The chambers (Fig.(5.3A)) were constructed from microscope slides cemented together with UV-curing adhesive (Norland); care was taken to remove excess adhesive to avoid interference with visualizations near the contact line, and to seal the chamber adequately to avoid evaporation and associated flows. The space between the vertical slides which form the front and back of the chamber was typically 1 mm. Imaging was achieved with a digital ccd camera (Hamamatsu C7300,  $1024 \times 1024$  pixels, 12 bit) under computer control (National Instruments), attached to a macrophotography bellows (PB-6, Nikon) with a 105 mm f/2.8 lens. Darkfield illumination was a 4 cm diameter fiber optic ring light (Navitar) behind the sample chamber. PIV measurements were conducted by adding  $5 \mu\text{l}$  of fluorescent microspheres (Molecular Probes, F8825 Carboxylate-modified,  $1.0 \mu\text{m}$ , Nile red) to 1 ml of suspension, illuminating with a DPSS laser (100 mW, 532 nm) reflected from a dichroic mirror (Z542RDC, Chroma Technology), and visualizing through a longpass filter (HQ542LP, Chroma). Analysis was performed with PIV software (Dantec Dynamics).

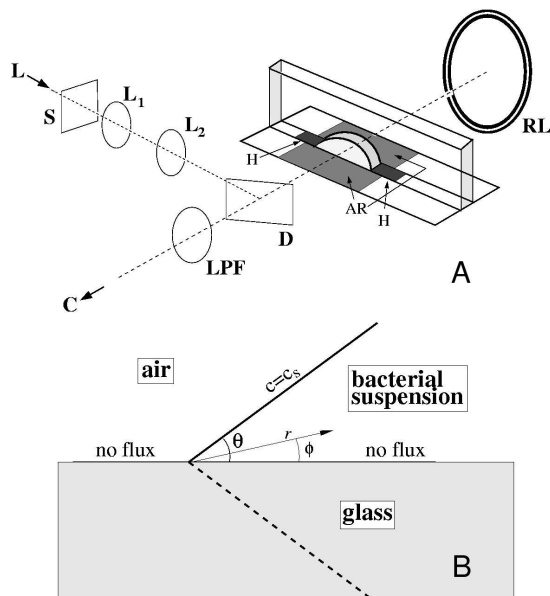


**Figure 5.3:** (A) Apparatus for simultaneous darkfield and fluorescence imaging of fluid drops. Laser (L), shutter (S), beam expander lenses ( $L_1$  &  $L_2$ ), dichroic beamsplitter (D), long-pass filter (LPF), fiber-optic ring light (RL), digital camera (C). Chamber has anti-reflection areas (AR) to reduce glare and hydrophobic areas (H) to pin the drop. (B) Boundary conditions and coordinates in the wedge, described in text.

## 5.3 Results

Figures (5.4A-C) show images of the mainstages of the chemotactic Boycott effect. After a drop of well-mixed suspension is placed in the chamber, the first spatial structure that forms is a “depletion layer” of thickness  $\ell \sim 1$  mm below the fluid-air interface, which appears dark in our imaging method because of the absence of cells. This region arises from the consumption of dissolved oxygen by the uniformly dispersed cells, followed by their chemotactic migration up the oxygen gradient to the source of oxygen - the free surface. No cellular motion is seen below the depletion layer, suggesting that the oxygen concentration there has fallen to the critical value, denoted  $c^*$ , below which motility vanishes. In a flattened sessile drop the bottom of the depletion layer follows the shape of the air-water meniscus, displaced downward by the layer thickness. This layer forms within 100 s, consistent with consumption of the saturation dissolved oxygen concentration  $c_s \sim 10^{17} \text{ cm}^{-3}$  by cells at concentration  $n_0 \sim 10^9 \text{ cm}^{-3}$ , with a consumption rate  $\kappa \sim 10^6$  oxygen molecules per second. This is also consistent with the time  $t_\ell = \ell/v_c$  for a cell with a typi-

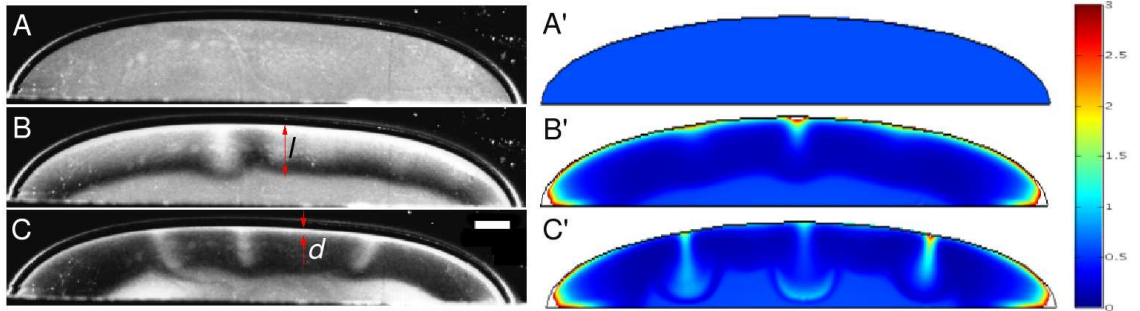


**Figure 5.4:** Stages leading to self-concentration in a sessile drop, observed experimentally (left) and by numerical computations with the model described in text (right). (A,A') drop momentarily after placement in chamber. (B,B') formation of depletion zone after 150 s, prior to appreciable fluid motion, (C,C') lateral migration of accumulation layer toward drop edges and creation of vortex (shown in Fig.(5.3)), after 600 s. Color scheme describes the rescaled bacteria concentration  $\rho$ . Scale bar is 0.5 mm.

cal chemotactic velocity  $v_c \sim 10\mu\text{m/s}$  to traverse the thickness  $\ell$ . Ultimately, the cells congregate in a narrow surface “accumulation layer” whose thickness  $d \sim 100\mu\text{m}$ . While the accumulation layer slides along the meniscus to the contact line it is unstable to plume formation on a length scale comparable to the layer thickness, consistent with the fundamental instability of bioconvection in fluids with a horizontal meniscus [137]. The Boycott effect occurs at the slant region; the resultant surface and return flows distort the plumes that would otherwise fall straight down. This surface flow is opposite to that of the conventional Boycott effect, whereas the depletion layer here is buoyantly forced in the usual direction, creating a unique shear double layer. Typical fluid velocities at the free surface are in the range  $20 - 200 \mu\text{m/s}$ , accelerating as the meniscus slope increases near the contact line. Finally, due to incompressibility requirements, a well-developed vortex appears near each of the contact lines and shows persistence over many tens of minutes. The closed streamlines (Fig.(5.5A)) show the sense of circulation created by the downward gravitational forcing on the accumulation layer and the recirculation into the bulk required by fluid incompressibility. Despite the outward flow at the bottom of the vortex, the optical density indicates that cells are trapped near the contact line.

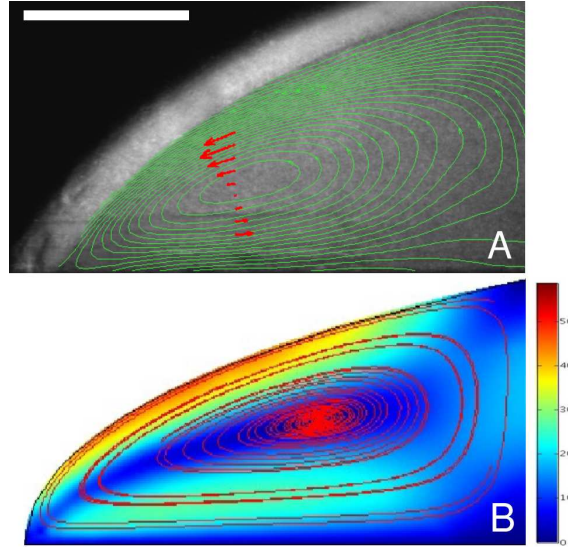


**Figure 5.5:** Hydrodynamic vortex near three-phase contact line. (A) velocity contours obtained from PIV measurements, averaged over 750 frames acquired at intervals of 0.2 s. Scale bar is 1 mm. Region immediately above PIV contours is the curved fluid-air interface beyond the slice viewed in cross section. (B) Numerical results obtained from finite-element calculations using the model in Eqs. 5.1-5.3. Closed streamlines are shown along with velocity magnitude in color.

## 5.4 Mathematical Model

The dynamics of the oxygen concentration  $c$ , cell concentration  $n$ , and fluid velocity  $\mathbf{u}$ , are described by coupled PDEs [84],

$$c_t + \mathbf{u} \cdot \nabla c = D_c \nabla^2 c - n \kappa f(c) \quad (5.1)$$

$$n_t + \mathbf{u} \cdot \nabla n = D_n \nabla^2 n - \nabla \cdot [\mu r(c) n \nabla c] \quad (5.2)$$

$$\rho (\mathbf{u}_t + \mathbf{u} \cdot \nabla \mathbf{u}) = -\nabla p + \eta \nabla^2 \mathbf{u} - V_b g n \Delta \rho \hat{\mathbf{z}}. \quad (5.3)$$

In (5.1) the oxygen diffusion constant is  $D_c \sim 2 \times 10^{-5} \text{ cm}^2/\text{s}$ , and the dimensionless function  $f(c)$  modulates the oxygen consumption rate  $\kappa$ , asymptoting to unity at large  $c$ , but vanishing as  $c \rightarrow 0$ . As the experimental timescales are minutes and the cell division time is  $\sim 100$  minutes, the dynamics (5.2) of  $n$  conserve the total number of cells. The bacterial diffusion constant  $D_n$  arises as a consequence of the random swimming trajectories and is estimated to be  $D_n \sim 10^{-6} - 10^{-5} \text{ cm}^2/\text{s}$ . Chemotaxis is described by the second term on the r.h.s. of (5.2), with a velocity proportional to the oxygen gradient [93]; the coefficient  $\mu$  may be interpreted as  $\mu = av_0/c_s$ , so that the chemotactic velocity is

$v_0$  when the gradient is  $c_s/a$ , where  $a$  is a characteristic length. Like the function  $f(c)$ , the motility function  $r(c)$  is unity at large  $c$  and vanishes rapidly for  $c$  below the motility cutoff  $c^*$ ; we approximate it and  $f(c)$  by the step function  $\Theta(c - c^*)$ . Subject to incompressibility,  $\nabla \cdot \mathbf{u} = 0$ , the fluid equations (5.3) utilize the Boussinesq approximation in which the density variations due to bacteria appear only in the buoyant forcing, with  $\Delta\rho = \rho_b - \rho$ , where  $V_b$  and  $\rho_b$  are the bacterial volume and density and  $\rho$  is the pure fluid density. In the Appendix we provide a non-dimensionalization of these equations convenient for numerical studies.

The boundary conditions on  $c$ ,  $n$ , and  $\mathbf{u}$  are central to the global flows and possible singularities. As shown in Fig.(5.3B), there is no flux (of cells or of oxygen) through the substrate, under the drop and to its side, and no cell flux through the fluid-air interface. That interface is stress-free, while the fluid-glass boundary has no slip. Since the oxygen diffusion coefficient in the air is three orders of magnitude larger than that in the fluid, the oxygen concentration outside the drop can be assumed equal to its saturation value  $c_s$  inside the fluid and on the free surface. Oxygen diffusion in the drop is equivalent to that in the enlarged space whose bottom is the reflection of the meniscus across the fluid-glass interface. This lens-shaped region has a sharp point which is the source of a chemotactic singularity in the same way that a pointed electrical conductor produces a singular electric field.

## 5.5 Comparison With Experiments

The phenomena shown in Figs.(5.4 and 5.5) can now be explained, beginning with formation of the depletion and accumulation layers. Forming first in the absence of fluid flow, we need only consider Eqs. 5.1 and 5.2 with  $\mathbf{u} = 0$ , and even more simply in a one-dimensional vertical cut through the drop. Quasi-steady-state profiles of  $c$  and  $n$  are found in which  $c$  varies exponentially down from the free surface until it intercepts  $c^*$ . From this one deduces

$$\ell = \left( \frac{D_c (c_s - c^*)}{\kappa n_0} \right)^{1/2}, \quad d = \frac{D_n}{v_c}. \quad (5.4)$$

The result  $\ell \sim n_0^{-1/2}$  can be verified by a dilution experiment. Figs.(5.6B & 5.6C) show two drops, the first from the standard bacterial suspension with

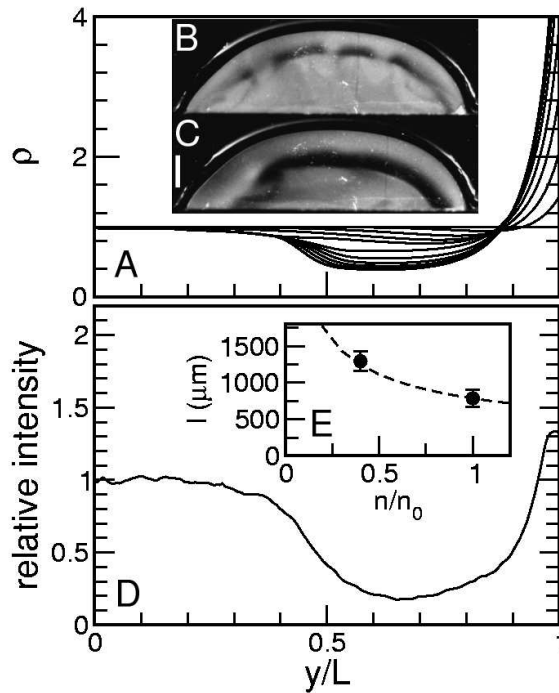


**Figure 5.6:** Depletion layers in sessile drops. (A) Numerical solution of (5.1) and (5.2) for the rescaled cell concentration as a function of rescaled height. (B) depletion layer forming in stock solution and (C) in a 40% dilution. Scale bar is 0.5 mm. (D) averaged intensity trace in the stock solution, normalized to intensity at bottom of drop. (E) depletion layer thickness as a function of relative concentration. Dashed line is theoretical prediction.

cell concentration  $n_0$ , the second a dilution to  $0.4n_0$ . The increase in  $\ell$  is apparent. Vertical traces of the optical intensity through the height of the drop, averaged over 40 s, yield profiles like that shown in Fig.(5.6D), from which  $\ell$  is determined. We see good agreement with the numerical results in Fig.(5.6A) although at the very high cell concentrations in the accumulation layer the optical intensity saturates, the likely explanation for the relatively small intensity there. With parameters discussed above, we fit  $\ell$  for the undiluted solution with  $c^* = 0.3c_s$ , and then  $\ell$  of the diluted solution lies accurately on the prediction (Fig.(5.6E)).

Numerical studies of the PDEs with a curved fluid-air interface are readily accomplished with finite-element methods. Calculations were done with Femlab (Comsol, Inc.). The coupled PDEs for handled using the “general” form, with high order Lagrange elements (quintic for Eqs. 5.1 & 5.2 and quartic-quadratic for Eq. 5.3), on a triangular mesh consisting of  $\sim 1000$  nodes, and a fifth-order time integration scheme in the nonlinear time-dependent solver.

We focus here on two-dimensional dynamics, equivalent to the assumption of translational invariance with respect to the direction *along* the contact line. The essential features of the flow are found as well in numerical studies using Darcy's law for flow between the vertical plates of the experimental chamber. Overhead views of sessile drops reveal that in the third dimension the vortex breaks up into a radial form of bioconvective plumes [60]. Elsewhere we discuss these in more detail. Our two-dimensional computations, shown in Figs.(5.4A'-C'), reproduce the observations; the depletion layer tracing the shape of the meniscus, the variations in thickness of the accumulation layer over the boundary of the drop, and the plume instability. Figure (5.5B) shows that the vortex is also captured accurately.

Except close to the contact line, the accumulation layer is very thin compared to the depth of the drop, so the gravitational forcing that acts on it is essentially concentrated at the surface. When combined with the no-slip boundary condition at the bottom of the drop, this defines one of the scenarios in Moffatt's analysis of viscous eddies in sharp corners [118]. Theory predicts a set of progressively smaller vortices adjacent to the main vortex. We have not seen evidence of these, either in experiment or simulations, but they are expected to be extremely weak and are likely outside the resolution of both approaches. Theory also suggests that the conditions under which vortices develop can depend sensitively on the far-field conditions and the wedge angle. Our numerical results indicate the existence of a vortex at least over a range of angles from  $\pi/4$  to  $\pi/2$ .

The velocities  $U$  in the vortex can reach 0.01 cm/s, with a size of 0.1 cm, so the Peclet number can approach  $\sim 10^2$ . Numerical studies show that the combination of accumulated bacteria and greatly-enhanced stirring in the wedge lead to (i) a near-singular variation in oxygen flux near the contact line (Fig.(5.7A)), and (ii) an increase in oxygen uptake into the drop. Figure (5.7B) shows that the average oxygen concentration initially drops precipitously as consumption dominates, but it slowly returns to a high value as stirring enhances the uptake from the air above. Without the hydrodynamic coupling between cell concentration and buoyancy, the oxygen concentration remains low after the initial consumptive drop. Not only oxygen, but also nutrients will be ferried to the contact line region from areas in the bulk of the drop.



## 5.6 Chemotactic Singularity

Some insight into the oxygen flux near the contact line is obtained by making use of the electrostatic analogy mentioned above. Close enough to the contact line the numerics indicate that the velocity along the upper free surface tends to zero, so advective contributions vanish asymptotically there. The simplest steady-state oxygen diffusion problem, for which  $\nabla^2 c = 0$  inside the drop and  $c = c_s$  on the free surface, is mathematically equivalent to the equation defining the electrostatic potential in that same region, the exterior of the drop being a conductor [57]. This mapping reveals [89] that a singularity arises from a solution of the form

$$c(r, \phi) \sim c_s + \sum_{m=1}^{\infty} a_m r^{m\pi/2\theta} \cos(m\pi\phi/2\theta), \quad (5.5)$$

with polar coordinates  $(r, \phi)$  as in Fig.(5.3B). This form enforces the condition  $c = c_s$  on the drop surface ( $\phi = \theta$ ) and the no-flux condition on the glass substrate ( $\phi = 0$ ). Upon successive differentiation, the potentially most singular term is  $m = 1$ , and we expect  $a_1 < 0$  since  $c \leq c_s$  in the drop interior. Noting that  $|\nabla c| \sim r^{\pi/2\theta-1}$  and  $\nabla^2 c \sim r^{\pi/2\theta-2}$ , singularities appear in two cases:

1.  $\theta > \pi/2$ , an overhanging meniscus. This case is like the familiar “lightning rod” effect. Both the Fick’s law oxygen flux,  $-D_c \nabla c$ , and the chemotactic flux,  $\mu r n \nabla c$ , diverge as  $r \rightarrow 0$ , leading to a singular accumulation at the contact line.
2.  $\pi/4 < \theta < \pi/2$ , as in Figs.(5.4-5.6): Here,  $|\nabla c|$  is finite as  $r \rightarrow 0$ , but has a diverging slope. Expanding the chemotaxis term in the dynamics (5.2), we see terms of the form  $\mu r [\nabla n \cdot \nabla c + n \nabla^2 c]$ , the former implying a potential cusp in the cell concentration  $n$ . Although weaker than case 1, there still is a singular accumulation driven by the diffusional singularity of oxygen.

Let us consider in more detail the typical case  $\theta < \pi/2$ . There is a positive, bidirectional feedback loop involving the chemotactic response to the oxygen singularity. The singularity is reinforced by the accumulation of bacteria which consume the oxygen. A rough idea of this can be gleaned by examining a steady state balance between the dominant terms in the chemotaxis

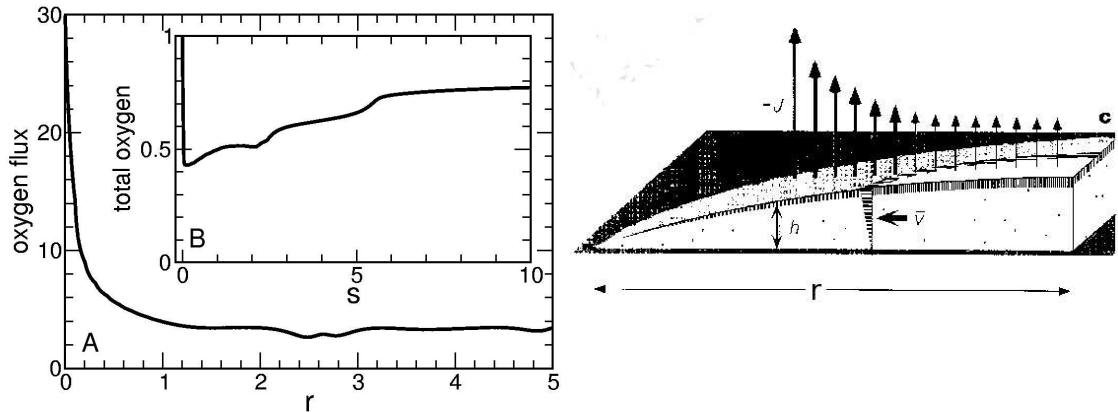


**Figure 5.7:** Oxygen dynamics from numerical studies. (A) Inward flux of oxygen along upper surface of a drop, in units of  $D_c c_s / L$ , as a function of distance  $r$  from the contact line, showing near-singular behavior. (B) Average oxygen concentration in the drop as a function of rescaled time  $s$ , normalized to initial value. (C) Schematic representation of the Inward flux of oxygen along upper surface of a drop.

equation (5.2), setting  $D\nabla^2 n \sim \mu r n \nabla^2 c$  to find a distribution  $n \sim \exp(-\Gamma r^{\pi/2\theta})$ , with  $\Gamma > 0$ , that decays away from the contact line very sharply. Since the local oxygen consumption rate is proportional to  $n$ , the inward flux of oxygen mirrors the bacterial concentration distribution, as in Fig.(5.7B). While a more precise treatment requires a fully self-consistent calculation of the coupled oxygen and bacterial concentrations, this result illustrates the dramatic accumulation of bacteria in the contact region.

The development of the self-trapping vortex and the associated high concentration of bacteria near the contact line depend crucially on the no-flux boundary conditions at the substrate. A dramatic demonstration of this is seen in the flows in a “supported” drop. This geometry was achieved by turning over the experimental chamber, allowing a previously sessile drop to slide down from the chamber base toward the opening at the opposite end. Surface tension supports the drop, with free uptake of oxygen around the whole meniscus. As shown in Fig.(5.8), the bottom interface is very flat, giving an effective contact angle exceeding  $\pi/2$ , but with no substrate the dynamics are nonsingular. We see the key stages in the chemotaxis and fluid instabilities in this geometry. Development of the depletion zone occurs rather symmetrically around the entire perimeter of the drop, producing the non-motile re-

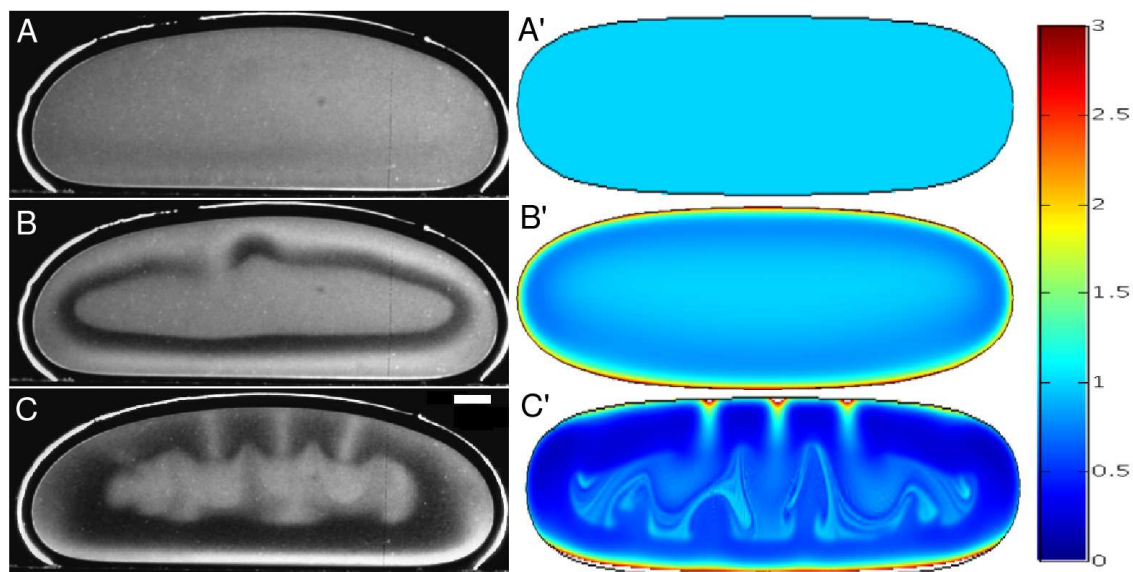


**Figure 5.8:** Self-concentration in a thin droplet, confined between glass plates, surrounded by air. Experimental observations and numerical results presented as in Fig.(5.4), with (A,A') at time  $t = 0$ , (B,B') at 200 s, and (C,C')=360 s. Scale bar is 0.5 mm.

gion in the center. Later, plumes descend from above and the accumulation layer slides down the drop meniscus, producing a clearly visible enhancement of concentration at the bottom of the meniscus beyond the local chemotactic concentration. The computations quantitatively reproduce these features.

At the high concentrations found near the contact line of sessile drops (Fig.5.9) or at the bottom of supported drops the viscous drag between the fluid and bacteria is comparable to that of the fluid on itself. A simple estimate gives the volume fraction  $\varphi^*$  at which this transition takes place. The drag force per unit volume on the suspension is  $\zeta u^b \varphi / V_b$ , with  $\zeta = 6\pi\eta R$  the drag coefficient of an equivalent sphere of radius  $R$ ,  $u^b$  the bacterial velocity, and  $V_b = 4\pi R^3/3$  the equivalent volume of a bacterium. The viscous drag force on the fluid per unit volume is  $\eta u^f / L^2$ , where  $L$  is a characteristic scale of the flow and  $u^f$  the fluid velocity. Equating these two gives

$$\varphi^* = \frac{2}{9} \left( \frac{R}{L} \right)^2 \frac{u^f}{u^b}, \quad (5.6)$$

independent of viscosity. Taking  $R \sim 2 \mu\text{m}$  as a representative bacterium radius and  $L \sim 100 \mu\text{m}$ , the thickness of the accumulation layer, and  $u^f/u^b \sim 5$  [60], then  $\varphi^* \sim 5 \times 10^{-4}$ , corresponding to a concentration  $n \sim 5 \times 10^8 \text{ cm}^{-3}$ ,

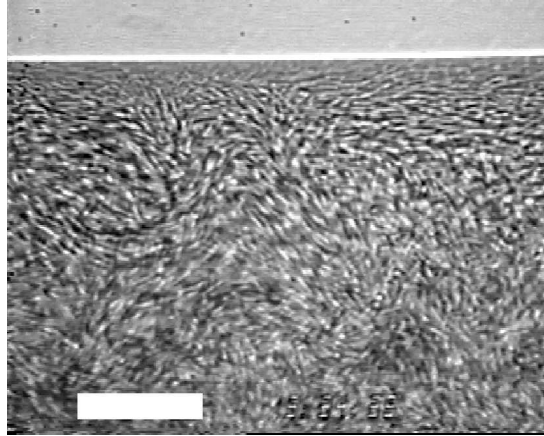


**Figure 5.9:** High concentration of bacteria near the contact line.

comparable to a typical initial homogeneous concentration in the drop. For volume fractions in excess of  $\varphi^*$ , the fluid and bacterial velocities should be treated equally; one method to accomplish this uses two-phase fluid flow []. With the low Reynolds numbers of the typical flows, the coupled dynamics of the bacterial and fluid velocities  $\mathbf{u}^b$  and  $\mathbf{u}^f$  are

$$\zeta (\mathbf{u}^f - \mathbf{u}^b) = -(1 - \varphi)\nabla p + \eta^f \nabla^2 \mathbf{u}^f \quad (5.7)$$

$$\zeta (\mathbf{u}^b - \mathbf{u}^f) = -\varphi \nabla p - \frac{D_b}{\varphi} \nabla \varphi - \Delta \rho g \hat{\mathbf{z}} + \mu r \nabla c \quad (5.8)$$

with the continuity condition,  $\nabla \cdot (\varphi \mathbf{u}^b + (1 - \varphi) \mathbf{u}^f) = 0$ . Numerical investigations of (5.7) and (5.8) coupled to the oxygen dynamics 5.1) show qualitatively similar results for the overall bioconvective flows to those obtained with the Navier-Stokes equations (5.3), but as well provide a more quantitatively correct description of the dense regime.

## 5.7 Conclusions

We have shown that the interplay of chemotaxis, buoyancy, and meniscus geometry is responsible for persistent fluid circulation and high cell densities in the neighborhood of contact lines. This circulation is strong enough to render advection dominant over diffusion and enhance the overall oxygen uptake into the medium. Driven entirely by chemotaxis and metabolism of individual cells, no explicit cell-cell communication is necessary for these phenom-

ena to occur. Nevertheless, the creation of a micro-ecological structure by a self-organized dynamic will likely influence concurrent cell-cell communication which is necessary for such processes as quorum sensing and subsequent biofilm formation [56], with its well-known complex transition from planktonic to sessile cells [53]. The geometrically-mediated concentrative mechanism described here results in approximately close-packed bacteria exhibiting rapid coherent chaotic dynamics, including collectively-driven flow of fluid through the array [60]. Our experiments have shown that the shallow fluid/air/substrate contact is a geometric constraint immobilizing bacteria. Initial cells nucleate a growing immobile assembly. The chaos of swimming concentrated planktonic cells undoubtedly transports molecular nutrients and facilitates quorum signaling adjacent to sessile individuals, supplies recruits to the sessile population, and transports tumbling, eventually settling chunks of biofilm generated elsewhere. This scenario is a setting for biofilm progression, inward from the wetting region. It is of special interest that the flow of fluid adjacent to the initially adherent cells is driven only by the dynamics of the huge number of adjacent bacteria dispersing molecular information, unlike the situation presented by Eglund *et al.* [63] where communication in an imposed flow depends on immediate adjacency. The possibility [104] that anoxia can be a negative signal for surface adhesion in *E. coli* provides further evidence that advective contributions from large-scale flows might play a role in the formation of biofilms.

## 5.8 Appendix

Here we discuss some mathematical details involving the non-dimensionalization of the governing equations. We rescale (5.1)-(5.3) to identify the dimensionless control parameters. If  $L \sim 0.1$  cm is the depth of the drop, we define the rescaled variables  $\mathbf{x} = \mathbf{r}/L$ ,  $s = D_n t/L^2$ ,  $\chi = c/c_s$ ,  $\rho = n/n_0$ ,  $\pi = L^2 p/\eta D_n$ ,  $\mathbf{v} = L\mathbf{u}/D_n$ . Defining  $\delta = D_c/D_n \sim 1 - 10$ , and  $\alpha = av_0/D_n \sim 10$ , we have

$$\chi_s + \mathbf{v} \cdot \nabla \chi = \delta \nabla^2 \chi - \rho \beta f(\chi) \quad (5.9)$$

$$\rho_s + \mathbf{v} \cdot \nabla \rho = \nabla^2 \rho - \alpha \nabla \cdot [r(\chi) \rho \nabla \chi] \quad (5.10)$$

$$\frac{1}{S_C} (\mathbf{v}_s + \mathbf{v} \cdot \nabla \mathbf{v}) = -\nabla \pi + \nabla^2 \mathbf{v} - \gamma \rho \hat{\mathbf{z}} \quad (5.11)$$

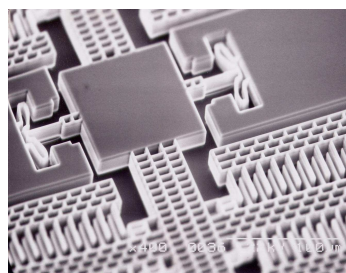
where

$$\beta = \frac{\kappa n_0 L^2}{c_s D_n} \quad Sc = \frac{\nu}{D_c} \quad \gamma = \frac{v n_0 g (\rho_b - \rho) L^3}{\eta D_n} . \quad (5.12)$$

The time  $L^2/D_n \sim 10^3$  s is that for diffusion across the drop,  $\beta \sim 10$  is the ratio of the bacterial diffusion time to that for oxygen consumption, and the Schmidt number  $Sc \sim 10^3$  measures the importance of viscosity to diffusion of oxygen. Finally,  $\gamma \sim 10^3$  is analogous to the Rayleigh number in thermal convection [137].

# Chapter 6

## Forced bodies: The Control of Particles in Micro – electrode Devices.



### 6.1 Introduction

*A promising analytical tool for analyzing organic complexes in the biology laboratory of the future is a microfluidic device commonly called a "Lab-on-a-chip". These "laboratories" are fabricated using photolithographic processes developed in the microelectronics industry to create circuits of tiny chambers and channels in a chip. They direct the flow of liquid chemical reagents just as semiconductors direct the flow of electrons. These reagents can be diluted, mixed, reacted with other reagents, or separated all on a single chip.*

These microfluidic circuits can be designed to accommodate virtually any analytic biochemical process. For example, a lab-on-a-chip for immunological assays probably would integrate sample input, dilution, reaction, and separation, whereas one designed to map enzyme fragments might have an enzymatic digestion chamber followed by a relatively long separation column. Many features of these labs-on-a-chip make them well suited for high-

throughput analyzes. Their small dimensions reduce both processing times and the amount of reagents necessary for an assay, substantially reducing costs. Just as microelectronic devices can be manufactured with many elements on a single chip, microfluidic devices can be fabricated with many channels, allowing for massively parallel chemical analyzes at a reasonable cost. They are uniquely suited to small-scale analyzes; sample volumes for a single experiment often are in the nano to picoliter range, opening the door to the possibility of analyzing components from single cells.

Relatively simple labs-on-a-chip already are being used for some nucleic acid and protein analyzes, but microfluidics technology may someday allow millions of automated biochemical experiments to be performed per day using miniscule quantities of reagents. Eventually, individual analyzes may be replaced by protocols in which tens to thousands of analytical measurements are made in parallel, either on the same or multiple samples.

To make such a future possible, new techniques must be developed to allow lab-on-a-chip devices to perform all the desirable tasks. Dielectrophoresis is one of this techniques. Dielectric particles suspended in a dielectric media become polarized in the presence of of an electric field. If the field is spatially inhomogeneous, a net force [147] known as *dielectrophoretic* (DEP) will act on the polarized particle. The dynamical behavior of particles under action of DEP force varies widely depending upon the temporal frequency and spatial configuration of the field as well as on the dielectric properties of both the medium and the particles.

Dielectrophoresis is an efficient and increasingly popular method for separating particles in microflows [87]. While in absolute terms the strength of the DEP force is rather small, at micron-sized scales it becomes a very effective means for manipulating and positioning biological macromolecules by applying relatively small voltages on a proper configuration of electrodes. DEP forces can be switched on and off to selectively capture cells, bacteria, spores, DNA, proteins, and other matter [87]. It is not difficult to envision, for example, an application in which DEP is used to capture a suspected pathogen which then be shuttled to a selected area of the microfluidic device where its DNA is extracted and analyzed.

Since the dielectrophoretic mobility of a particle scales directly with its



surface area the manipulation of smaller particles requires larger gradients of the electric fields. Nevertheless, the use of microfabricated electrodes to generate large electric field gradients has now established beyond doubt the possibility to move submicron particles by means of DEP [120, 78]. However, large electric field gradients may interact strongly with the suspending media through several electro-hydrodynamical effects generating flows which in turn will disturb the particle trajectories via drag forces. Understanding the main features of this disturbance to be able to predict and control it, is then crucial for developing applications of DEP in specific microfluidic devices. On the other hand, the combined dynamics induced by both advection and DEP is largely unexplored and therefore interesting from the point of view of basic research.

The purpose of this Chapter is to initiate the systematic study of this combined dynamics while concentrating in a case of practical interest: a DEP device consisting of a periodic array of micro-electrodes. We first introduce a model where the DEP particle dynamics produced by such arrays is perturbed by the advection due to a realistic model of the corresponding electro-hydrodynamical convective flow. By means of this model we then predict an important dynamical consequence of the perturbing flow: the appearance of zones from where particles can not escape. This trapping mechanism can have positive and negative consequences: while it spoils n-DEP transport it may improve p-DEP behavior by capturing particles away from the electrodes. Second, we propose a dynamical mechanism to break up the trapping zones, and therefore, to control the particles behavior. Finally, we perform experiments that confirm such a mechanism.

## 6.2 The Device

Experiments were conducted using a titanium based dielectrophoresis device. Fig. (6.1) shows a scanning electron microscope image of the bulk titanium-based DEP device. It consists of two components: the electrode substrate and the channel. The electrode substrate is fabricated by patterning titanium electrodes onto a bulk titanium substrate covered with an isolation layer. Two fluid reservoirs (2 millimeters in diameter) are then drilled through the bot-

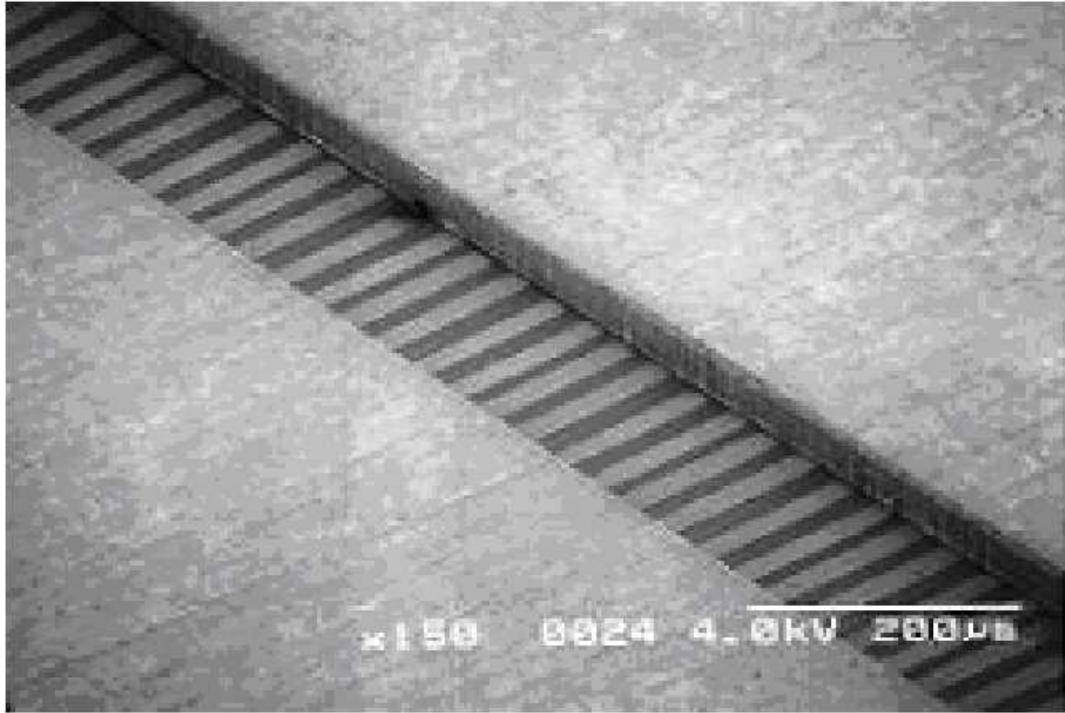


**Figure 6.1:** SEM image of the titanium DEP chip with 24 parallel electrodes sit underneath the Titanium Channel Die.

tom of the substrate to provide fluidic interconnection. The channel is formed by through-etching thin titanium foil (25 micrometers thick). Then a 7 microns thick photo-BCB polymer layer was patterned on top of the electrode substrate and on one side of the channel to form the bonding. Fig. (6.2) illustrates the assembled device. The channel is 200 microns wide and 6 millimeters long. Each electrode is 20 microns wide and has a pitch of 40 microns. The AC electric field is provided by a function generator (Wavetek model21) allowing a frequency range up to 11 MHz. The DEP properties are analyzed using an epifluorescent microscope (Nikon eclipse), a 20X water immersion lens and a CCD camera (Hamamatsu C7300-10-12NRP). For multiple frequencies we use a home made signal adder. The particles used are fluorescent polystyrene spheres (Duke Scientific) of density  $1.05 \text{ g/cm}^3$ . They have a nominal diameter of 1 micron. The dye has some conductivity properties. The particle solution used for the experiment is a dilution of particles into dionized water (initial conductivity  $2 \mu\text{S/cm}$ ). The final solution has a concentration of  $7.2 \cdot 10^9$  particles per milliliter and a conductivity of  $13 \mu\text{S/cm}$ . Before

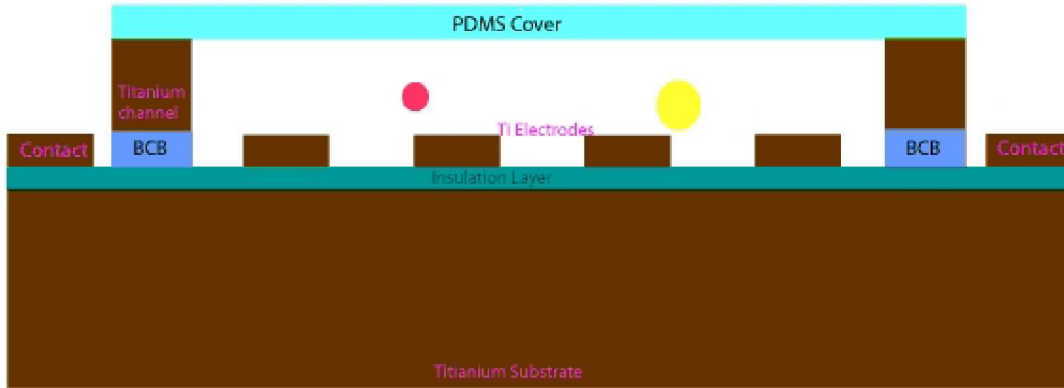


**Figure 6.2:** Schematic of the titanium DEP Chip (each electrode is 20 micron wide, and 0.5 micron thick)

the electric field is turned on, the channel is filled with the solution using a syringe pump (Harvard Apparatus 2000) and the flow is stabilized.

### 6.3 Electro-Thermal-Hydrodynamics

The dielectrophoretic force arises from the interaction of a non-uniform electric field and the dipole induced in the particle. For linear, isotropic dielectrics, the relationship between the dipole moment  $\mathbf{p}$  of a spherical particle and the electric field  $\mathbf{E}$  is given by  $\mathbf{p}(\mathbf{r}, \omega) = 4\pi a^3 \epsilon_m K(\omega) \mathbf{E}(\mathbf{r})$ , where  $E$  is the rms electric field,  $a$  is the particle radius,  $\mathbf{r}$  is the position,  $\omega$  is the angular field frequency, and  $\text{Re}[z]$  indicates the real part of the complex number  $z$ . The factor  $K(\omega)$  is a measure of the effective polarizability of the particle, known as the Clausius-Mossotti factor, given by  $K(\omega) = (\epsilon_p^* - \epsilon_m^*) / (\epsilon_p^* + 2\epsilon_m^*)$  where  $\epsilon_p^*$  and  $\epsilon_m^*$  are the complex permittivities of the particle and the medium, respectively. The complex permittivity is defined as  $\epsilon^* = \epsilon - i(\sigma/\omega)$ , where  $i = \sqrt{-1}$ ,  $\epsilon$  is the permittivity, and  $\sigma$  is the conductivity of the dielectric.

The dielectrophoretic force,  $F_{Dep}$ , on the particle due to the interaction between the induced dipole and the electric field, is given by

$$\mathbf{F}_{Dep}(\mathbf{r}, t) = (\mathbf{p}(\mathbf{r}, t) \cdot \nabla) \mathbf{E}(\mathbf{r}, t) \quad (6.1)$$

For an AC electric field of the form  $\mathbf{E}(\mathbf{r}, t) = \mathbf{E}(\mathbf{r}) \cos(\omega t)$ , the time-averaged

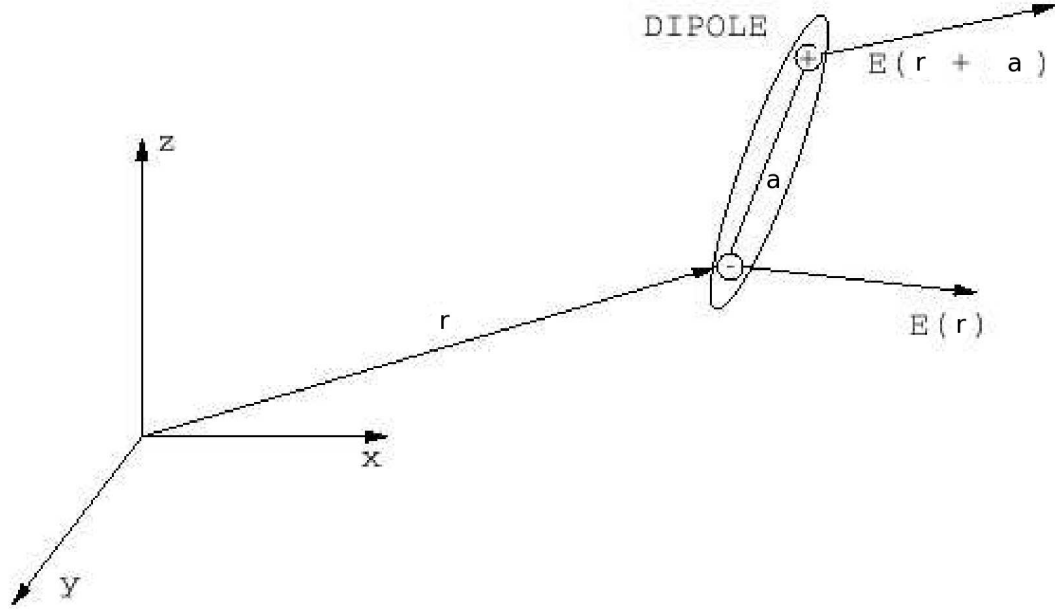


**Figure 6.3:** Dipole in non-uniform electric field.

force on the particle is given by

$$\langle \mathbf{F}_{\text{Dep}} \rangle(\mathbf{r}, t) = \lim_{T \rightarrow \infty} \frac{1}{T} \int_0^T \mathbf{F}_{\text{Dep}} dt = 2\pi a^3 \epsilon_m \text{Re}[K(\omega)] \nabla |\mathbf{E}|^2 \quad (6.2)$$

The geometry of our device represents a simple but commonly used configuration of electrodes array. The exact boundary condition implies that the normal derivative of the potential should be zero between neighboring electrodes on the boundary. The following closed-form solution of the electric field and the DEP force have been derived [49]:

$$\begin{aligned} \nabla |E|^2 &= \frac{\pi^3 V_0^2}{K^2(\cos(\pi/4))d^3} \cdot \text{Re} \left[ \begin{array}{c} izk(\bar{z})k'(z) \\ -zk(\bar{z})k'(z) \end{array} \right] \\ |E| &= \frac{\pi V_0}{K(\cos(\pi/4))d} \cdot \left[ \begin{array}{c} \text{Re} \\ \text{Im} \end{array} \right] \cdot [k(z)] \\ k(z) &= \left( \frac{z}{1 - 2z \cos(\pi/2) + z^2} \right)^{1/2} \\ z &= \exp(\pi(ix - y)/d) \end{aligned} \quad (6.3)$$

The Clausius-Mossotti factor not only depends on the dielectric properties of the particle and the medium, but also on the frequency of the applied field.

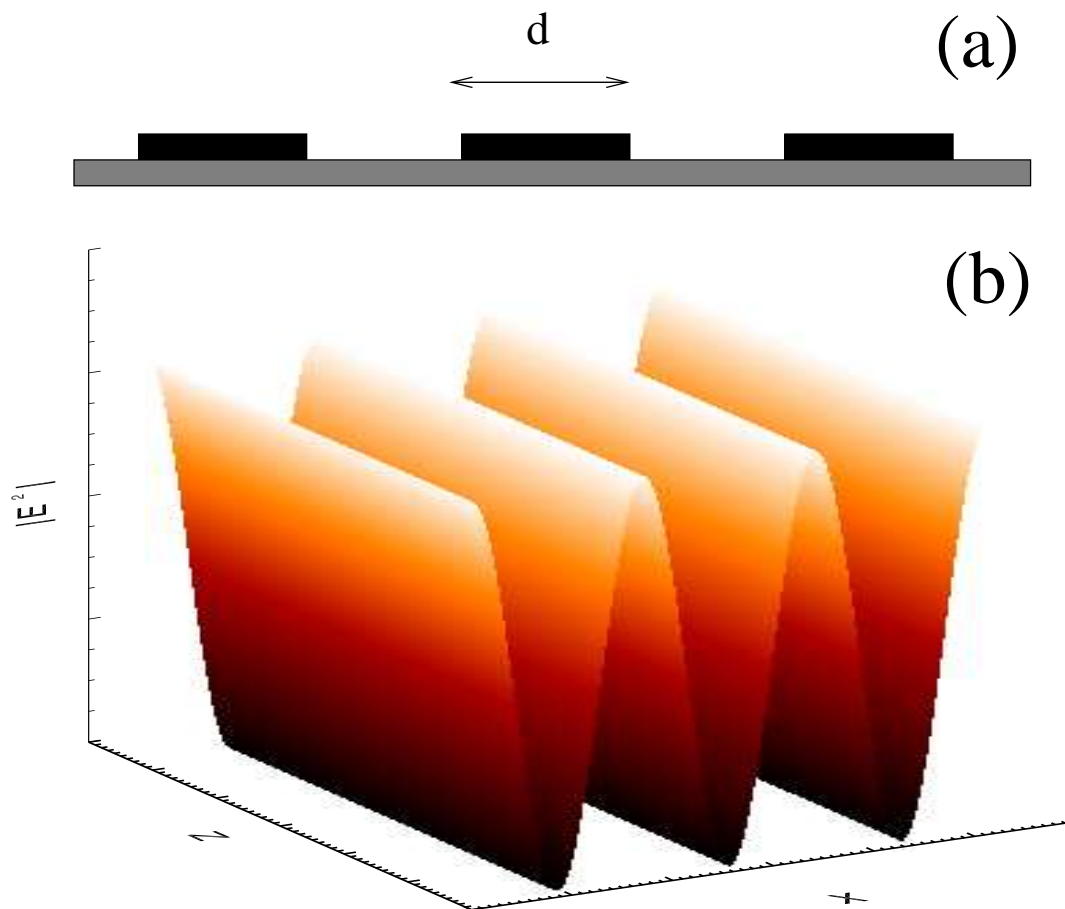


**Figure 6.4:** (a) The arrangement of an interdigitated electrode array. (b) Electric field strength,  $|E|^2$ , in the plane  $10\mu m$  above the electrode array.

Variations in this factor give rise to a DEP force that is frequency dependent and unique to each particle type. For a sphere, the real part of  $K(\omega)$  is bounded by the limits  $-\frac{1}{2} < Re[K(\omega)] < 1$  and depends on the frequency of the applied field and the complex permittivity of the medium. When  $Re[K(\omega)] > 0$  the induced force points toward the high electric field at the electrode surfaces and is known as *positive-DEP* (p-DEP). In this case, the particles are collected at the electrode edges. Conversely, when  $Re[K(\omega)] < 0$  (negative- or n-DEP), the force points in the direction of decreasing field strength and the particles are repelled from the electrodes edge (Fig. 6.5(a)).

In our configuration the electric field has local minima (negative DEP traps) above the center of the electrodes whereas it reaches the strongest values at their edges (Fig. 6.4(b)). In the absence of fluid flow, the particles expe-

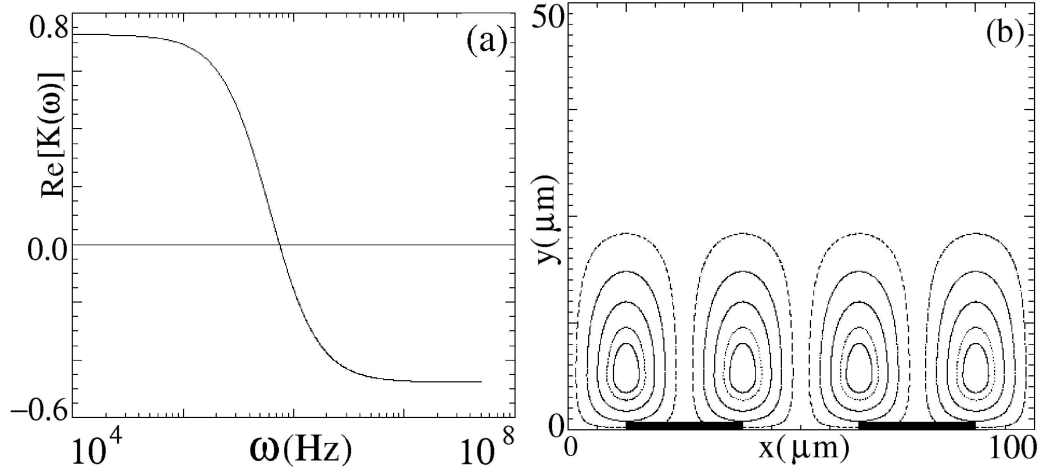


**Figure 6.5:** (a) Plot of the real part of the Clausius-Mossotti function for  $\varepsilon_m = 80\varepsilon_0$ ,  $\sigma_m = 0.001S \cdot m^{-1}$ ,  $\varepsilon_p = 2.5\varepsilon_0$  and  $\sigma_p = 0.009S \cdot m^{-1}$ . (b) Streamlines of the cellular flow used in the model.

riencing p-DEP collect at the strong field points across the electrode array. On the other hand, particles pushed away from the electrodes by n-DEP reach an equilibrium position away from the electrodes where the vertical component of the DEP force is balanced by buoyancy. Since the horizontal component decays much faster than the vertical one, in dynamical terms this equilibrium positions form, in practice, a continuous line of fixed points.

However, electric fields induce fluid motions through several mechanisms. Due to the Joule effect, for example, the fluid is non-uniformly heated and since the fluid properties are temperature dependent, gradients of density, permittivity and conductivity then arise. In a similar way as the gravitational body forces lead to natural convection, the applied electric fields acting on the permittivity and conductivity gradients generate electrical body forces that induce the so called electrothermal convection [154].

In general, the electric, temperature and velocity fields are coupled. In order to solve the temperature field, the energy balance equation must be used:

$$\rho_m c_p \frac{\partial T}{\partial t} + \rho_m c_p \mathbf{u} \nabla T = \kappa \nabla^2 T + \sigma_m E^2 \quad (6.4)$$

where  $c_p$  is the specific heat at constant pressure,  $\kappa$  is the thermal conductivity and  $\sigma_m E^2$  is the Joule heating term. Here, we have neglected the viscous dissipation term, which is of the order of  $10^{-10}$  times smaller than the Joule

heating term. For sufficiently high frequencies, we can simplify this equation to the steady state. Also, the ratio of convection of heat to heat diffusion is very small:  $\rho_m c_p \mathbf{u}d/\kappa \sim 10^{-3}$  and we can neglect the second term on the left-hand side. The temperature is therefore governed by the diffusion equation with a source term given by the time average of the Joule heating,

$$\kappa \nabla^2 T + \langle \sigma_m E^2 \rangle = 0 \quad (6.5)$$

The electrical force is given by

$$f_E = \rho_q E - \frac{1}{2} |E|^2 \nabla \varepsilon \quad (6.6)$$

where the first term corresponds to the Coulomb force (where  $\rho_q$  is the charge density), and the second term, to the dielectric force. The charge density and the electric field are described by Gauss's law

$$\rho_q = \nabla \cdot (\varepsilon E) \quad (6.7)$$

the charge conservation equation

$$\frac{\partial \rho_q}{\partial t} + \nabla \cdot (\rho_q \mathbf{u}) + \nabla \cdot (\sigma_m E) = 0 \quad (6.8)$$

and

$$\nabla \times E = 0. \quad (6.9)$$

The ratio of magnitudes of the convection current,  $\rho_q \mathbf{u}$ , to the conduction current,  $\sigma E$ , is given by the Electrical Reynolds number  $\mathbf{u}\varepsilon/\sigma d$ . For typical values, this is  $\sim 10^{-7}$  so that the second term in Eq. (6.8) can be neglected.

The relative changes in the permittivity and conductivity are small for typical temperature increments and a perturbative expansion can be performed. In the lowest order, Eqs. (6.7) and (6.8) reduce to  $\rho_q = 0$  and  $\nabla \cdot E_0 = 0$ , so that the electric potential obeys Laplace's equation. The first order charge density can then be obtained in terms of  $E_0$ .

As a result of this set of approximations, the electrical, thermal and mechanical problems are decoupled and one can solve the complete problem as follows. First, solving the electrical problem: Laplace's equation for the potential in a homogeneous medium. Second, calculating the temperature field using the solution for the electric field. And finally, using these two solutions

to compute the electrical force. Liquid motion is then governed by the Navier–Stokes equations for an incompressible fluid

$$\begin{aligned} \nabla \cdot \mathbf{u} &= 0 \\ \rho_m \left( \frac{\partial \mathbf{u}}{\partial t} + (\mathbf{u} \cdot \nabla) \mathbf{u} \right) + \nabla p &= \mu \nabla^2 \mathbf{u} + f_E + \rho_m \mathbf{g} \end{aligned} \quad (6.10)$$

that for microsystems (where the Reynolds number is usually very small  $Re \sim 10^{-6}$ ) and under the Boussineq approximation, reduces to the following average equation

$$\nabla p = \mu \nabla^2 \mathbf{u} + \langle f_E \rangle + \Delta \rho_m \mathbf{g} \quad (6.11)$$

At typical microfluidic system sizes ( $d < 300 \mu m$ ) the electrical forces dominate the buoyancy forces [47]. This flow depends on frequency of the field and two ranges can be distinguished. At frequencies smaller than the charge relaxation frequency ( $\omega \ll \sigma/\varepsilon$ ), the Coulomb force produced by the conductivity gradient dominates dragging fluid from the electrodes to the gap. On the contrary, for  $\omega \gg \sigma/\varepsilon$  the permittivity gradient makes the dielectric force dominant forcing the fluid to flow in the opposite direction. Around the charge relaxation frequency, the electrothermal force will have a minimal effect but in the DEP manipulation and/or separation of submicron particles one is usually forced to use frequencies outside this range and the fluid flow generated electrothermally has to be taken into account. In the following we will show that far from being an annoyance, this flow induce dynamical properties that can be used creatively as new mechanisms to control microparticles.

## 6.4 The Model

Several experiments and numerical simulations of the coupled electro-thermal-hydrodynamical problem [77, 80] have shown that electrothermal and electroosmotic flows consist of convective rolls centered at the electrode edges. These works provide also a reasonable idea of the strength and frequency dependence of the flow. Near the electrodes, the fluid velocity  $u_0$  ranges from 1 to  $100 \mu m \cdot s^{-1}$ , and it decays exponentially as we move away from the electrodes. On the other hand, the flow must satisfy non-slip boundary condition at the bottom of the device ( $u_x = u_y = 0$ ) and both the horizontal component of the



velocity and the normal derivative of the vertical velocity are zero at the symmetry planes ( $\mathbf{u}_x = \partial \mathbf{u}_y / \partial n = 0$ ). In order to analyze the impact of the flow on the DEP particle dynamics we introduce a simple flow model that satisfies all these conditions and mimic the cellular flow observed in devices with interdigitated array of electrodes (Fig. 6.5(b)). This flow is derived from the stream function:

$$\psi_{steady} = \mathbf{u}_0 \cdot y^2 e^{-y/\beta} \cos(\pi x) \quad (6.12)$$

so that  $\mathbf{u}$  automatically satisfies the incompressibility condition,  $\nabla \cdot \mathbf{u} = 0$ . The parameter  $\beta$  determines the position of the center of the rolls.

In a device of a characteristic length  $d \simeq 20\mu m$ , with flow velocities  $\mathbf{u}_0 \simeq 10\mu m \cdot s^{-1}$ , fluid viscosity  $\nu \simeq 10^{-6} m^2 \cdot s^{-1}$  ( $\eta = \rho\nu \simeq 10^{-3} Kg \cdot m^{-1} \cdot s^{-1}$ ), and micrometer particles  $a \simeq 1\mu m$ , the particle's Stokes number is of order  $St = (2a^2 u / 9\nu d) \simeq 10^{-6}$ , which implies that inertial effects can be neglected. Therefore, the velocity of the particles can be obtained directly from the DEP, buoyancy and drag forces. We neglect the effect of Brownian motion since it has been shown to be less of an impediment to the dielectrophoretic movement of big particles (hundreds of nm) [154] for an appropriate choice of electrode voltages. The movement of a particle in a fluid influenced by a force  $\mathbf{F}$ , is governed by

$$m \frac{d\mathbf{u}}{dt} = -\gamma(\mathbf{v} - \mathbf{u}) + \mathbf{F} \quad (6.13)$$

where  $m$  is the particle mass,  $\mathbf{v}$  the particle velocity and  $\mathbf{u}$  the fluid velocity,  $-\gamma(\mathbf{v} - \mathbf{u})$  is the drag force with  $\gamma = 6\pi\eta a$  the friction factor of the particle in the fluid. Under the action of a constant force  $\mathbf{F}$  and fluid velocity  $\mathbf{u}$ , the particle velocity is

$$\mathbf{v} = \left( \mathbf{v}_0 - \mathbf{u} - \frac{\mathbf{F}}{\gamma} \right) e^{-(\gamma/m)t} + \mathbf{u} + \frac{\mathbf{F}}{\gamma} \quad (6.14)$$

where  $\mathbf{v}_0$  is the initial velocity of the particle. The characteristic time of acceleration,  $\tau_a = m/\gamma$ , is usually much smaller than the typical time of observation ( $\sim 1$  s). For a spherical particle of mass density  $\rho_p$ ,  $\tau_a = 2\rho_p a^2 / 9\eta$ , which is smaller than  $10^{-6}$  s for cells and sub-micrometer particles. Therefore, the particle can be considered to move at its terminal velocity, given by

$$\frac{d\mathbf{r}}{dt} = \mathbf{u} + \frac{\mathbf{F}}{\gamma} = \mathbf{u} + \frac{\langle \mathbf{F}_{DEP} \rangle}{6\pi\eta a} + (\rho_p - \rho_m) \cdot \frac{2a^2}{9\eta} \cdot \mathbf{g} \quad (6.15)$$

This means that any measurement of particle velocity is a direct measure of the fluid velocity,  $u$ , plus the velocity induced by the force acting on the particle,  $F/\gamma$ . As we have discussed in previous Chapters, the acceleration process of a body in a fluid environment is much more complicated than described by the simple exponential solution (remember, for instance, the transport properties of neutrally buoyant spheres). However, the fact that the particle moves at its terminal velocity for times much greater than  $\rho_p a^2/\eta$  is still valid.

The relative importance of the three terms in the equation of motion depends basically on three parameters: the applied voltage  $V$ , the radius of the particle  $a$ , and the size of the electrode device  $d$ . The influence of fluid flow gets progressively bigger for smaller particles, and the buoyancy term becomes important only far from the electrodes where both the flow and DEP forces are smaller.

## 6.5 Results

With this simple flow model, the motion of the particles can be analyzed by using dynamical systems methods. In this way, two different dynamical phenomena are unveiled. On one hand, far from the electrodes where the fluid velocity is smaller, the flow is only a small perturbation of the no-flow state. Thus, the invariant line of fixed points where the n-DEP force balances the positive buoyancy, disintegrate into a discrete chain of interconnected saddles and nodes. Due to normal hyperbolicity [191], the invariant manifold originally formed by a continuum of fixed points is preserved with just a slight change of shape but now becomes the saddle-node connecting manifold. However, this induces a dramatic change in the dynamics since hyperbolic fixed points repel the particles which then accumulate in small regions near the nodes. This phenomenon is depicted in Figs. 6.6(a,b) where the trajectories of several particles submitted to n-DEP forces is plotted. Notice the convergence of trajectories towards equilibrium points situated above the inter-electrode gaps. This accumulation of particles in small regions above the electrodes has been observed in several experiments [79, 120], but as we see here, it can be easily understood using dynamical system methods to analyze the effects of fluid flows. Analogously, Figs.6.6(c,d) show that in the case of p-DEP, the par-

ticles that in the absence of flow tend to accumulate at the edges of the electrodes may be forced by the electrothermal flow, which is also strong in that region, to move towards the center of the electrodes and concentrate there instead. This phenomenon has been also observed experimentally [139, 154].

The second –and stronger– dynamical effect takes place closer to the electrode surfaces: the creation of a closed zone from which particles cannot escape. In Figs. 6.6(b,d) we can clearly see that there are two qualitatively different behaviors: some of the particles are trapped in closed areas above the gap between electrodes, whereas others escape from the flow influence following their destiny fixed only by the corresponding DEP force. These sets of trapped orbits resemble what is known as *Stommel retention zones* [166, 167] that have been studied in the context of plankton and nutrients dynamics in the ocean in the presence of the Langmuir circulation [22]. However, in contrast with the planktonic case, the DEP force introduces a non conservative (gradient) component in the system and the motion within the Stommel zone becomes dissipative in the dynamical systems sense. Therefore, in our case, the particles inside the trapping zone are attracted towards foci fixed points instead of circulating around centers as in the original Stommel case. A more detailed phase portrait of the dynamics described by Eq. (6.15) is plotted in fig. 6.7(a) which reveals the characteristic mentioned above. It should be noticed again that experimental evidence of the formation of stable trapping zones away from the electrodes in the p-DEP regime and in the presence of electrothermal convection has been previously reported in [80, 120].

Let us note that the magnitude of the DEP force depends on the volume of the particle whereas the Stokes force depends only on its radius. This means that the relative importance of these terms in the equation of motion Eq. (6.15) is proportional to  $a^2$ . It is then worthwhile to study the dependence of the dynamics on this parameter. It appears that for a fixed flow parameter  $u_0$  a Stommel-like zone exists only for  $a$  smaller than a critical value  $a_c$  whose dependence on the flow is shown in Fig. 6.7(b). At around  $a_c$  bifurcations involving the collision and mutual annihilation of the two foci and the two saddles occur leading to the disappearance of the trapping zones. Although the detailed scenario of these bifurcations will be presented elsewhere we illustrate here the practical impact on the particle dynamics. The right hand

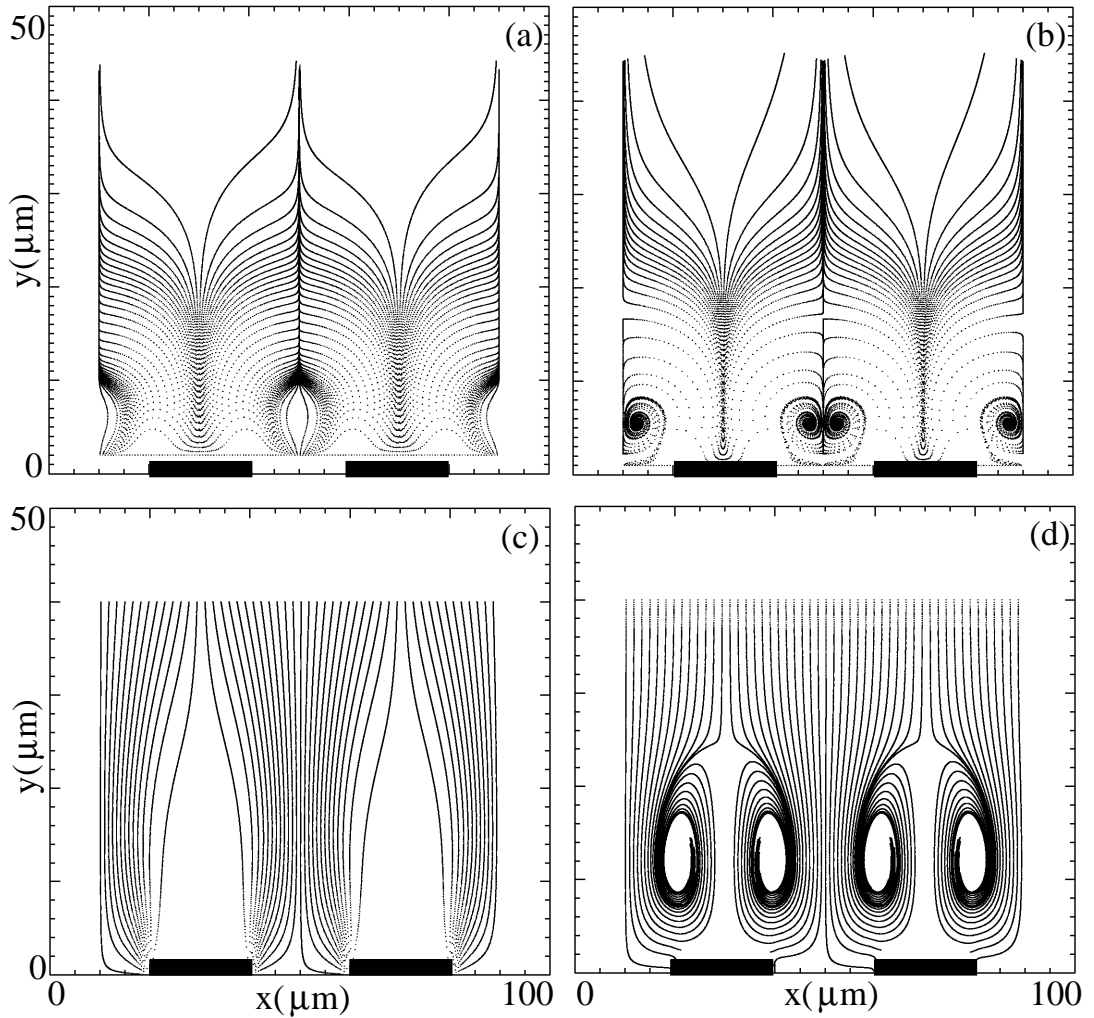


**Figure 6.6:** (a) Particle trajectories with n-DEP for point II in Fig. 6.7, corresponding to  $\omega = 5MHz$ ,  $\rho_m/\rho_p = 0.95$ ,  $\beta = 0.15d$  and  $a = 1.5\mu m$ , with a flow moving from the gap to the electrodes. (b) For point I in Fig. 6.7,  $a = 0.75\mu m$ , with the same flow as before. For the same parameters with p-DEP in (c) and (d) respectively.

side panels in Fig. 6.6 depict the dynamics showing trapping zones for both n-DEP (top) and p-DEP (bottom) for parameters taken below the bifurcations whereas the left hand side ones correspond to parameters above them and showing no signs of the former traps.

## 6.6 Breaking The Traps

In the following we show that dynamics can be also used to govern the behavior of the trapping zones. It is known that small time-dependent perturba-

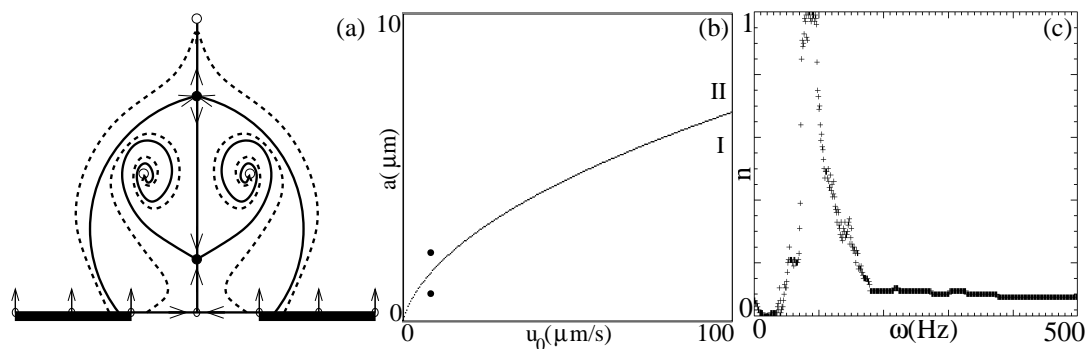


**Figure 6.7:** (a) Phase portrait showing the stable (white circles) and unstable (black circles) fixed points of the model (arbitrary scale). (b) A bifurcation diagram in the parameter space (radius of particle,  $a$ , versus fluid velocity,  $u_0$ ). In region I a Stommel kind area exists. (c) The fraction of particles,  $n$ , from one hundred initially distributed inside the Stommel zone, that escape after 10 periods, versus the frequency of the applied field.  $\epsilon = 0.1$ .

tions to steady flows can break up trapping barriers in conservative dynamical systems[133]. The same effect can be observed in our case. A simple way to introduce a time-dependent perturbation of the flow generated in micro-electrode devices is to add a small low frequency electric field to the one used in the DEP manipulation. Electrothermal and electro-osmotic forces contain both a steady term and a term that oscillates at twice the frequency of the applied electric field. The resulting flow velocity  $\mathbf{u}$  has both steady and oscillating terms too, but at sufficiently high frequencies, the oscillating terms are much smaller than the steady ones which allows us to consider only the time-averaged flow. However, if we add a small low frequency component to the applied field, a small unsteady flow will be generated together with a time-dependent DEP force.

For electrothermal convection, to ensure that the time-dependent component of the temperature gradient is non-negligible, the frequency of the applied field has to be of the same order of, or smaller than, the typical diffusion time for the temperature front. This time can be estimated from the energy balance equation [102] to be  $t_{diff} = \frac{\rho_m c_p d^2}{\kappa} \approx 10^{-3} \text{ s}$ , where  $c_p$  is the specific heat at constant pressure and  $\kappa$  the thermal conductivity of the medium. Then, electric fields of frequency smaller than 1 kHz can be used to generate the unsteady perturbation.

To model this perturbation we add a time-dependent term to the stream

function,

$$\psi = \psi_{steady} + \epsilon \cdot \mathbf{u}_0 \cdot y^2 e^{-y/\beta} \sin(\pi x) \cdot \sin(2\omega t) \quad (6.16)$$

Stommel regions will break up under these perturbations allowing a complete DEP control. A number of techniques can be used to characterize this break up: e.g. Melnikov theory can be used to investigate the spread of particles and to extract a measure of the size of the trapping regions. It is also possible to calculate an estimate of the heteroclinic lobes and, hence, quantify the transport of particles due to the time-dependent forcing [38]. Because of the fact that we have a kinematic model, we refrain from performing such analysis and concentrate on the qualitative interpretation.

In Fig. 6.7(c) the fraction of particles that escape from the trapping zone at a given time is plotted as a function of the frequency of the perturbation. Clearly there is a specific frequency value in order to achieve an optimal particles spread, and it corresponds to a frequency of the same order of the natural frequency of the system,  $\omega_0 \sim \mathbf{u}/d \sim 10 - 100\text{Hz}$ . Then the perturbation will be in synchrony with the unperturbed dynamics, and the spread of particles outside the trapping zone will be faster.

## 6.7 Comparison With Experiments

We have conducted experiments in which the whole trapping and untrapping mechanisms are clearly visualized. As Figs. 6.8(a-b) show, particles that are initially uniformly distributed in the device, are trapped above the electrodes under the joint effect of n-DEP and electro-hydrodynamical flow, once a high frequency electric field is applied. Initially, particles are uniformly suspended in the fluid and move under the Brownian agitation. When the AC electric field (10KHz, 9Vp-p) is applied (Fig. 6.8b), the particles move toward the electrodes. They accumulate at the electrodes edges and on the center. Then a 100Hz, 9Vp-p Ac signal is added. In few milliseconds (Fig. 6.8(c-d)) the trapping zone become unstable and the particles are dispersed in the fluid. Fig. (6.8e) illustrates continuous development of the perturbation. Hence, the addition of a low frequency component strongly alters the result. The trapped particles escape from the trap, bouncing around advected by the time-dependent flow. Removing the low frequency component at this moment, leave

particles untrapped, hence following their way towards the equilibrium positions. On Fig. (6.8e) we can notice that some particles are still on the electrodes edge because they are chemically bonded to the electrodes.

## 6.8 Conclusions

In summary, this simple but realistic model of dielectrophoresis in the presence of electro-hydrodynamical convection gives us ground to conjecture the presence of dynamical trapping regions. These are analogous in their origin to the Stommel zones of the problem of sedimentation in convective flows, but show a different structure due to the non-hamiltonian features of the dielectrophoretic dynamics. Nevertheless, we have shown that small time-periodic perturbations let the particles escape the traps as in the Hamiltonian case. This property, that can be easily implemented in practice by superimposing a low frequency electric field, provides a simple control tool for dielectrophoretic manipulations. The p-DEP traps described here constitute an efficient mechanism comparable to other proposed ones such as optical tweezers[92] and thermophoresis[31] but with the advantage of allowing at the same time the control of smaller particles and its implementation in smaller devices. We hope that this work opens the door to more sophisticated combinations of DEP and hydrodynamic forces for control of bioparticles.

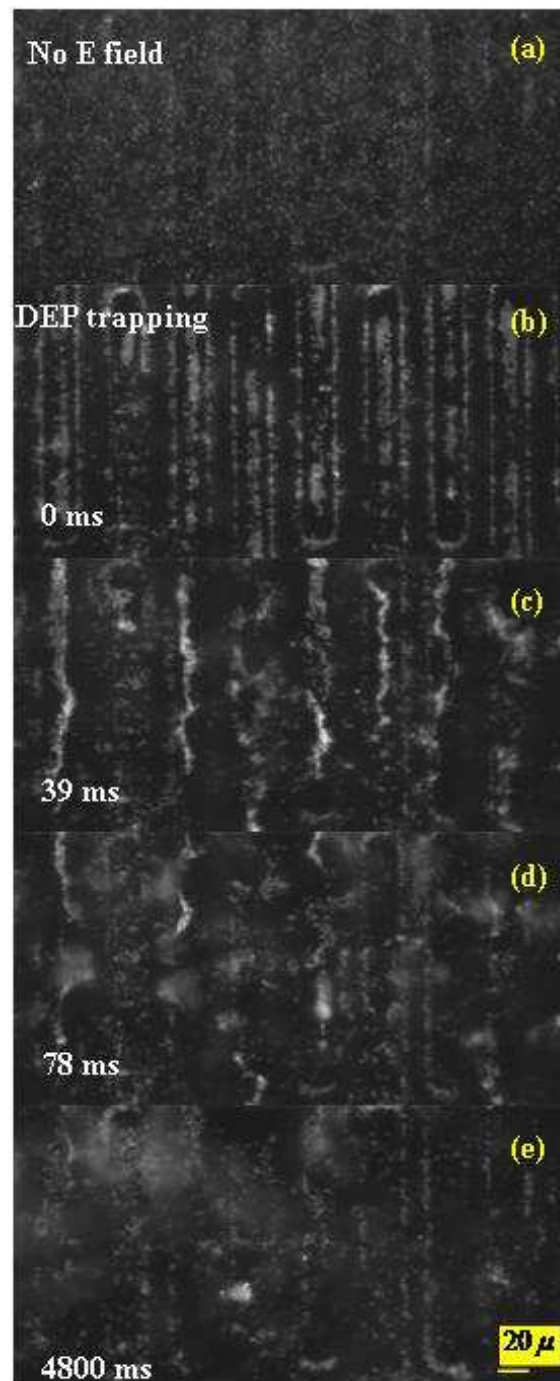


**Figure 6.8:** Image sequence of the DEP trapping and low frequency disturbance of 1 micron diameter latex beads at potential 10Vpk-pk. Main frequency is 10KHz and disturbance frequency is 100Hz. Focus plane is 6 microns above the electrodes.



# Chapter 7

## Final Remarks

We live in a fluid world. The vast majority of our body is fluid as the vast majority of our external environment is. From any single cell to complex ecosystems, we belong to a fluid reality. Hence, most of the phenomena that surround us and constitute our existence, have to do, in one way or another, with fluids. And we know they comprise a rich and complex world. This Thesis has been an exploration of that world.

We have asked ourselves questions about the dynamics of bodies in fluid flows; questions about their transport, growth, mixing, reaction, control and cooperative behavior. To answer these questions, we have developed and explored appropriate theoretical frameworks. We have analyzed and modelled a variety of instances in which the motion of a body in a fluid environment determines a given process. In the process, I believe, we have also opened new and interesting questions to be answered in the future.

We have directed our exploration towards two goals: On one hand, the solution of different open problems in which a body is suspended in a fluid. On the other hand, the exploration of an increasing complexity of the internal dynamics of the studied bodies and of the fluid–body interaction.

Our motivating problems have been of widely interdisciplinary nature. We have explored technological applications in the miniaturization industry, biological processes that determines the left–right patterning of our body plan, micro-ecological instances where cooperative behavior enhances colony survival, crystallization of inorganic substances where fluid mediated symmetry breaking events take place and subtle mechanisms that lead to an inhomogeneous distribution of passive particle in three dimensional chaotic flows.

What did I learn? First of all I learned to explore. I have learned to look for the appropriate tools in order to progress between each landmark in my road. From classical hydrodynamics to dynamical systems methods. From numerical simulations to direct experimentation. Above all, I found in the synergia of theoretical thinking, numerical simulations and laboratory experiments, the most exciting and efficient way into the scientific knowledge.

More specifically, throughout the thesis I have addressed the following questions:

- **How complex is the dynamics of simple spherical particles, passively advected by a laminar fluid flow?**

We have shown that even under the crudest simplifications, interesting and non intuitive effects appear in their dynamics. In fact, intricate but well defined structures arise in the distribution of neutrally buoyant particles suspended in three dimensional chaotic laminar flows. The bailout embedding associated with this phenomena provides a mathematical device to learn about the dynamical structures of the base flow in situations where these are very difficult to elucidate directly.

- **Why simply stirring during the crystallization of chiral inorganic chemical compounds was sufficient to produce a yield approaching 100% of just one enantiomer?**

We have been discussing chiral symmetry breaking during stirred crystallization. The nucleation of a crystal of one or other chirality is a symmetry-breaking event on the microscale, but the nonlinear autocatalytic dynamics of secondary nucleation amplify this to the macroscale, to the extent that an entire experiment may be influenced by the chirality of a single mother crystal.

- **Why is the heart almost always on the left side of our body?**

In vertebrates, a leftright bias has been shown to arise from a directional extracellular flow (nodal flow) that is generated by rotation of monocilia on the ventral surface of the embryonic node.

We have shown with an analysis of the fluid dynamics of the nodal flow in the developing embryo that the leftward flow that has been experi-

---

mentally observed is produced by the monocilia driving it being tilted toward the posterior. We have proposed a model for morphogen transport and mixing in the nodal flow, and discuss how this might initiate the development of left–right asymmetry.

- **Is there any advantage in the sophisticated social behavior observed in bacteria colonies?**

We have shown that the interplay of chemotaxis, buoyancy, and meniscus geometry is responsible for persistent fluid circulation and high cell densities in the neighborhood of contact lines. This circulation is strong enough to render advection dominant over diffusion and enhance the overall oxygen uptake into the medium. Driven entirely by chemotaxis and metabolism of individual cells, no explicit cell-cell communication is necessary for these phenomena to occur. Nevertheless, the creation of a micro-ecological structure by a self-organized dynamic will likely influence concurrent cell-cell communication which is necessary for such processes as quorum sensing and subsequent biofilm formation. The geometrically-mediated concentrative mechanism described here results in approximately close-packed bacteria exhibiting rapid coherent chaotic dynamics, including collectively-driven flow of fluid through the array.

- **How will be the biology laboratory of the future?**

Microfluidic devices commonly called a "Lab-on-a-chip" are a promising candidate. These microfluidic "laboratories" can accommodate virtually any analytic biochemical process all on a single chip.

We have developed applications of dielectrophoresis in a specific microfluidic device. At the same time, we have investigated the largely unexplored combined dynamics induced by both advection and dielectrophoresis. In this way we have initiated the systematic study of this combined dynamics while concentrating in a case of practical interest.

We have studied a simple but realistic model of dielectrophoresis in the presence of electro-hydrodynamical convection that gives us ground to conjecture the presence of dynamical trapping regions. We have shown that small time-periodic perturbations let the particles escape the traps.

This property, that can be easily implemented in practice by superimposing a low frequency electric field, provides a simple control tool for dielectrophoretic manipulations. We hope that this work opens the door to more sophisticated combinations of dielectrophoresis and hydrodynamic forces for control of bioparticles.

Science is more about asking the right questions than about give the right answers. That is at least my very personal view. By asking the right questions one opens the door to new developments that make science a fascinating human singularity.

For me this has been an exciting journey, and I consider this point just the end of one stage. Fluid's world is complex and varied. Our life develops in that world. What I have done here is just an incursion in this discipline. A life's environment in which we cannot feel strangers and in which secrets I really like to continue diving.

# Bibliography

- [1] S. C. Abrahams and J. L. Bernstein. Remeasurement of optically active  $\text{NaClO}_3$  and  $\text{NaBrO}_3$ . *Acta Cryst. B*, 33:3601–3604, 1977.
- [2] B. A. Afzelius. A human syndrome caused by immotile cilia. *Science*, 193:317–319, 1976.
- [3] B. A. Afzelius. Asymmetry of cilia of mice and men. *Int. J. Dev. Biol.*, 43:283–286, 1999.
- [4] J. C. Alexander, J. A. Yorke, Z. You, and I. Kan. Riddled basins. *Int. J. Bifurcat. Chaos*, 2:795–813, 1992.
- [5] Y. Almirantis and G. Nicolis. Morphogenesis in an asymmetric medium. *Bull. Math. Biol.*, 49:519–538, 1987.
- [6] V. I. Arnold. Sur la topologie des écoulements stationnaires des fluides parfaits. *C. R. Acad. Sci. Paris A*, 261:17–20, 1965.
- [7] K. Asakura, K. Kobayashi, Y. Mizusawa, T. Ozawa, S. Osanai, and S. Yoshikawa. Generation of an optically active octahedral cobalt complex by a chiral autocatalysis. *Physica D*, 84:72–78, 1995.
- [8] K. Asakura, D. K. Kondepudi, and R. Martin. Mechanism of chiral asymmetry generation by chiral autocatalysis in the preparation of chiral octahedral cobalt complex. *Chirality*, 10:343–348, 1998.
- [9] P. Ashwin, J. Buescu, and I. Stewart. Bubbling of attractors and synchronisation of chaotic oscillators. *Phys. Lett. A*, 193:126, 1994.
- [10] P. Ashwin, J.R. Terry, K.S. Thornburg, and R. Roy. Blowout bifurcation in a system of coupled chaotic lasers. *Phys. Rev. E*, 58:7186, 1998.

- [11] V. Astakhov, A. Shabunin, W. Uhm, and S. Kim. Multistability formation and synchronization loss in coupled hon maps: Two sides of the single bifurcational mechanism. *Phys. Rev. E*, 63:056212, 2001.
- [12] T. R. Auton, J. C. R. Hunt, and M. Prud'homme. The force exerted on a body in inviscid unsteady non-uniform rotational flow. *J. Fluid Mech.*, 197:241–257, 1988.
- [13] M. Avalos, R. Babiano, P. Cintas, J. L. Jiménez, and J. C. Palacios. From parity to chirality: Chemical implications revisited. *Tetrahedron: Asymmetry*, 11:2845–2874, 2000.
- [14] A. Babiano, J. H. E. Cartwright, O. Piro, and A. Provenzale. Dynamics of a small neutrally buoyant sphere in a fluid and targeting in Hamiltonian systems. *Phys. Rev. Lett.*, 84:5764–5767, 2000.
- [15] B. Y. Ballal and R. S. Rivlin. Flow of a Newtonian fluid between eccentric rotating cylinders: Inertial effects. *Arch. Ration. Mech. Anal.*, 62:237–294, 1976.
- [16] C. Basdevant and T. Philipovich. On the validity of the weiss criterion in two-dimensional turbulence. *Physica D*, 73:17–30, 1994.
- [17] A. B. Basset. On the motion of a sphere in a viscous liquid. *Phil. Trans. Roy. Soc. Lond.*, 179:43–63, 1888.
- [18] B. L. Bassler. *Cell*, 109:421, 2002.
- [19] G. K. Batchelor. The stress system in a suspension of force-free particles. *J. Fluid Mech.*, 41:545–570, 1970.
- [20] R. S. P. Beddington and E. J. Robertson. Axis development and early asymmetry in mammals. *Cell*, 96:195–209, 1999.
- [21] M. A. Bees and N.A. Hill. Wavelengths of bioconvection patterns. *J. Exp. Biol.*, 200:15151526, 1997.
- [22] M. A. Bees, I. Mezić, and J. McGlade. *Mathematics and Computer in Simulation*, 44:527–544, 1998.

- [23] I. J. Benczik, Z. Toroczkai, and T. Tél. Selective sensitivity of open chaotic flows on inertial tracer advection: Catching particles with a stick. *Phys. Rev. Lett.*, 89:164501, 2002.
- [24] H. C. Berg. *Random Walks in Biology*. Princeton University Press, 1983.
- [25] H. C. Berg and E.M. Purcell. *Biophys. J.*, 20:193, 1977.
- [26] M. V. Berry, N. L. Bazacs, M. Tabor, and A. Voros. Quantum maps. *Ann. Phys.*, 122:26–63, 1979.
- [27] M. D. Betterton and M. P. Brenner. *Phys. Rev. E*, 64:061904, 2001.
- [28] J. R. Blake and M.A. Sleight. Mechanics of ciliary locomotion. *Biol. Rev. Camb. Philos. Soc.*, 49:85–125, 1974.
- [29] J. Boussinesq. Sur la resistance qu'oppose un liquide indefini en repos. *C. R. Acad. Sci. Paris*, 100:935–937, 1885.
- [30] A. E. Boycott. *Nature*, 104:532, 1920.
- [31] D. Braun and A. Libchaber. *Phys. Rev. Lett.*, 89:188103, 2002.
- [32] N. A. Brown and L. Wolpert. The development of handedness in left/right asymmetry. *Development*, 109:1–9, 1990.
- [33] E. O. Budrene and H. C. Berg. *Nature*, 376:49–53, 1995.
- [34] J. Buescu. *Exotic Attractors*. Birkhauser, Boston, 1997.
- [35] T. Buhse, D. Durand, D. Kondepudi, J. Laudadio, and S. Spilker. Chiral symmetry breaking: The role of convection. *Phys. Rev. Lett.*, 84:4405–4408, 2000.
- [36] J. M. Burgers. On the motion of small particles of elongated form suspended in a viscous fluid. *K. Ned. Akad. Wet. Verhand.*, 16 (4):113, 1938.
- [37] M. Büttiker. Transport as a consequence of state-dependent diffusion. *Z. Phys. B*, 68:161, 1987.
- [38] R. Camassa and S. Wiggins. *Physical Review A*, 43:774–797, 1991.

- [39] J. Capdevila, K. J. Vogan, C. J. Tabin, and J. C. Izpisúa Belmonte. Mechanisms of left–right determination in vertebrates. *Cell*, 101:9–21, 2000.
- [40] J. H. E. Cartwright, M. Feingold, and O. Piro. Passive scalars and three-dimensional Liouvillian maps. *Physica D*, 76:22–33, 1994.
- [41] J. H. E. Cartwright, M. Feingold, and O. Piro. Global diffusion in a realistic three-dimensional time-dependent nonturbulent fluid flow. *Phys. Rev. Lett.*, 75:3669–3672, 1995.
- [42] J. H. E. Cartwright, M. Feingold, and O. Piro. Chaotic advection in three-dimensional unsteady incompressible laminar flow. *J. Fluid Mech.*, 316:259–284, 1996.
- [43] J. H. E. Cartwright, M. O. Magnasco, O. Piro, and I. Tuval. Neutrally buoyant particles and bailout embeddings in three-dimensional flows. *Phys. Rev. Lett.*, 89:264501, 2002.
- [44] J. H. E. Cartwright, Marcelo O. Magnasco, and O. Piro. Bailout embeddings, targeting of invariant tori, and the control of Hamiltonian chaos. *Phys. Rev. E*, 65:045203(R), 2002.
- [45] J. H. E. Cartwright, Marcelo O. Magnasco, and O. Piro. Noise and inertia-induced inhomogeneity in the distribution of small particles in fluid flows. *Chaos*, 12:489–495, 2002.
- [46] J. H. E. Cartwright and O. Piro. The dynamics of Runge–Kutta methods. *Int. J. Bifurcation and Chaos*, 2:427–49, 1992.
- [47] A. Castellanos, A. Ramos, A. Gonzalez, N. G. Green, and H. Morgan. *J.Phys.D: Appl.Phys.*, 36:2584, 2003.
- [48] A. Cenys, A. Namaunas, A. Tamasevicius, and T. Schneider. On-off intermittency in chaotic synchronization experiment. *Phys. Lett. A*, 213:259, 1996.
- [49] D. E. Chang, S. Loire, and I. Mezić. *J. Phys. D: Appl. Phys.*, 36:3073, 2003.



- [50] C.-Q. Cheng and Y.-S. Sun. Existence of invariant tori in three-dimensional measure preserving mappings. *Celest. Mech.*, 47:275–292, 1990.
- [51] A. A. Chernov. Protein crystals and their growth. *J. Struct. Biol.*, 142:3–21, 2003.
- [52] A. T. Chwang and T. Y.T. Wu. Hydromechanics of low-Reynolds-number flow. Part 1. Rotation of axisymmetric prolate bodies. *J. Fluid Mech.*, 63:607–622, 1974.
- [53] B. Costerton. *Proc. Natl. Acad. Sci.*, 101:16983–16984, 2004.
- [54] A. Crisanti, M. Falcioni, A. Provenzale, and A. Vulpiani. Passive advection of particles denser than the surrounding fluid. *Phys. Lett. A*, 150:79–84, 1990.
- [55] A. Cziráok, I.M. Jánosi, and J.O. Kessler. Bioconvective dynamics: dependence on organism behavior. *J. Exp. Biol.*, 203:33453354, 2000.
- [56] D. G. Davies, M. R. Parsek, J. P. Pearson, B. H. Iglewski, J. W. Costerton, and E. P. Greenberg. *Science*, 280:295–298, 1998.
- [57] R. D. Deegan, O. Bakajin, T. F. Dupont, G. Huber, S. R. Nagel, and T. A. Witten. *Nature*, 389:827–829, 1997.
- [58] R. D. Deegan, O. Bakajin, T. F. Dupont, G. Huber, S. R. Nagel, and T. A. Witten. *Phys. Rev. E*, 62:756–765, 2000.
- [59] T. Dombre, U. Frisch, J. M. Greene, M. Hénon, A. Mehr, and A. M. Soward. Chaotic streamlines in the ABC flows. *J. Fluid Mech.*, 167:353–391, 1986.
- [60] C. Dombrowski, L. Cisneros, S. Chatkaew, J. O. Kessler, and R. E. Goldstein. Self-concentration and large-scale coherence in bacterial dynamics. *Phys. Rev. Lett.*, 93:098103, 2004.
- [61] O. A. Druzhinin and L. A. Ostrovsky. The influence of the basset force on particle dynamics in two-dimensional flows. *Physica D*, 76:34–43, 1994.

- [62] J.-P. Eckmann and D. Ruelle. Ergodic theory of chaos and strange attractors. *Rev. Mod. Phys.*, 57:617–656, 1985.
- [63] P. G. Eglund, R. J. Jr. Palmer, and P. E. Kolenbrander. *Proc. Natl. Acad. Sci.*, 101:16917–16922, 2004.
- [64] D. Elhmaidi, A. Provenzale, and A. Babiano. Elementary topology of two-dimensional turbulence from a Lagrangian viewpoint and single-particle dispersion. *J. Fluid Mech.*, 257:533–558, 1993.
- [65] J. J. Essner, K. J. Vogan, M. K. Wagner, C. J. Tabin, H. J. Yost, and M. Brueckner. Conserved function for embryonic nodal cilia. *Nature*, 418:37–38, 2002.
- [66] H. Faxén. Der widerstand gegen die bewegung einer starren kugel in einer zähen flüssigkeit, die zwischen zwei parallelen ebenen wänden eingeschlossen ist. *Ann. Phys.*, 4:89–119, 1922.
- [67] M. Feingold, L. P. Kadanoff, and O. Piro. A way to connect fluid dynamics to dynamical systems: Passive scalars. In A. J. Hurd, D. A. Weitz, and B. B. Mandelbrot, editors, *Fractal Aspects of Materials: Disordered Systems*, pages 203–205. Materials Research Society, 1987.
- [68] M. Feingold, L. P. Kadanoff, and O. Piro. Diffusion of passive scalars in fluid flows: Maps in three dimensions. In R. Jullien, L. Peliti, R. Rammal, and N. Boccara, editors, *Universalities in Condensed Matter*, pages 236–41. Les Houches, Springer, 1988.
- [69] M. Feingold, L. P. Kadanoff, and O. Piro. Passive scalars, three-dimensional volume-preserving maps, and chaos. *J. Stat. Phys.*, 50:529–65, 1988.
- [70] M. Feingold, L. P. Kadanoff, and O. Piro. Transport of passive scalars: KAM surfaces and diffusion in three-dimensional Liouvillian maps. In P. Collet, E. Tirapegui, and D. Villarroel, editors, *Instabilities and Nonequilibrium Structures II*. Reidel, 1989.
- [71] F. C. Frank. On spontaneous asymmetric synthesis. *Biochim. Biophys. Acta*, 11:459–463, 1953.

- [72] M. Gad-el-Hak. The fluid mechanics of microdevices — the Freeman scholar lecture. *J. Fluids Eng.*, 121:5–33, 1999.
- [73] S. Galluccio and A. Vulpiani. *Physica A*, 212:75, 1994.
- [74] J. M. García-Ruiz. Nucleation of protein crystals. *J. Struct. Biol.*, 142:22–31, 2003.
- [75] J. Gray. The mechanism of ciliary movement. iv. photographic and stroboscopic analysis of ciliary movement. *Proc. R. Soc. Lond. Biol. Sci.*, 107:313, 1930.
- [76] G. Green. Researches on the vibration of pendulums in fluid media. *Transactions of Royal Society of Edimburgh*, 13:54–68, 1833.
- [77] N. G. Green, A. Ramos, A. Gonzalez, A. Castellanos, and H. Morgan. *J. Electrostatics*, 53:71, 2001.
- [78] N. G. Green, A. Ramos, A. Gonzalez, H. Morgan, and A. Castellanos. *Phys. Rev. E*, 66:026305, 2002.
- [79] N. G. Green, A. Ramos, and H. Morgan. *J. Phys. D*, 33:632, 2000.
- [80] N.G. Green and H. Morgan. *J. Phys. D*, 31:L25, 1998.
- [81] H. Hamada, C. Meno, D. Watanabe, and Y. Saijoh. Establishment of vertebrate left–right asymmetry. *Nature Rev. Genetics*, 3:103–113, 2002.
- [82] G. J. Hancock. The self-propulsion of microscopic organisms through liquids. *Proc. Roy. Soc. Lond. A*, 217:96–121, 1953.
- [83] J.F. Heagy, N. Platt, and S.M. Hammel. Characterization of on-off intermittency. *Phys. Rev. E*, 49:1140, 1994.
- [84] Hillesdon. *B. Math. Biol.*, 57:299–344, 1995.
- [85] J. R. Hove, R. W. Köster, A. S. Forouhar, G. Acevedo-Bolton, S. E. Fraser, and M. Gharib. Intercardiac fluid forces are an essential epigenetic factor for embryonic cardiogenesis. *Nature*, 421:172–177, 2003.

- [86] B. L. Hua and P. Klein. An exact criterion for the stirring properties of nearly two-dimensional turbulence. *Physica D*, 113:98–110, 1998.
- [87] M. P. Hughes. *Nanotechnology*, 11:124, 2000.
- [88] B. R. Hunt, E. Ott, and J. A. Yorke. Fractal dimensions of chaotic saddles of dynamical systems. *Phys. Rev. E*, 54:4819, 1996.
- [89] J. D. Jackson, editor. *Classical Electrodynamics*. Wiley, New York, 1962.
- [90] I.M. Jánosi, J.O. Kessler, and V.K. Horvth. The onset of bioconvection in suspensions of bacillus subtilis. *Phys. Rev. E.*, 58:4793–4800, 1998.
- [91] C. Jung, T. Tél, and E. Ziemniak. Applications of scattering chaos to particle transport in a hydrodynamical flow. *Chaos*, 3:555, 1993.
- [92] S. Katsura, K. Hirano, Y. Matsuzawa, K. Yoshikawa, and A. Mizuno. *Nucleic Acids Res.*, 26:4943, 1998.
- [93] E. F. Keller and L. A. Segel. *J. Theor. Biol.*, 30:225–234, 1971.
- [94] J.O. Kessler. Cooperative and concentrative phenomena of swimming microorganisms. *Contemp. Phys.*, 26:147–166, 1985.
- [95] J.O. Kessler, G.D. Burnett, and K.E. Remick. Mutual dynamics of swimming microorganisms and their fluid habitat. In P.L. Christensen, M.P. Soerensen, and A.C. Scott, editors, *Nonlinear Science at the Dawn of the 21st Century*, pages 409–426. Heidelberg: Springer, 2000.
- [96] J.O. Kessler and M.F. Wojciechowski. Collective behavior and dynamics of swimming bacteria. In J.A. Shapiro and M. Dworkin, editors, *Bacteria as Multicellular Organisms*, pages 417–450. New York: Oxford University Press, 1997.
- [97] D. K. Kondepudi, K. L. Bullock, J. A. Digits, and P. D. Yarborough. Stirring rate as a critical parameter in chiral symmetry breaking crystallization. *J. Am. Chem. Soc.*, 117:401–404, 1995.
- [98] D. K. Kondepudi, R. J. Kaufman, and N. Singh. Chiral symmetry breaking in sodium chlorate crystallization. *Science*, 250:975–976, 1990.

- [99] D. K. Kondepudi, J. Laudadio, and K. Asakura. Chiral symmetry breaking in stirred crystallization of 1,1'-binaphthyl melt. *J. Am. Chem. Soc.*, 121:1448–1451, 1999.
- [100] D. K. Kondepudi and C. Sabanayagam. Secondary nucleation that leads to chiral symmetry breaking in stirred crystallization. *Chem. Phys. Lett.*, 217:364–368, 1994.
- [101] Y.-C. Lai, T. Tél, and C. Grebogi. *Phys. Rev. E*, 48:709, 1993.
- [102] L. D. Landau and E. M. Lifshitz. *Fluid Mechanics*. Pergamon, Oxford, 1959.
- [103] R. Landauer. Motion out of noisy states. *J. Stat. Phys.*, 53:233–248, 1988.
- [104] P. Landini and A. J. B. Zehnder. *J. Bacteriol.*, 184:1522–1529, 2002.
- [105] A. J. Lichtenberg and M. A. Lieberman, editors. *Regular and Stochastic Motion*. Springer-Verlag, 1983.
- [106] J.B. Loeffler and R.B. Mefferd. Concerning pattern formation by free-swimming microorganisms. *Am. Nat.*, 86:325–329, 1952.
- [107] R. Mañé. *Ergodic Theory and Differentiable Dynamics*. Springer, 1987.
- [108] B. Martin, A. Tharrington, and X.-I. Wu. Chiral symmetry breaking in crystal growth: Is hydrodynamic convection relevant? *Phys. Rev. Lett.*, 1996.
- [109] S. F. Mason. Origins of biomolecular handedness. *Nature*, 311:19–23, 1984.
- [110] M. R. Maxey and J. J. Riley. Equation of motion for a small rigid sphere in a nonuniform flow. *Phys. Fluids*, 26:883–889, 1983.
- [111] J. McGrath, S. Somlo, S. Makova, X. Tian, and M. Brueckner. Two populations of node monocilia initiate left–right asymmetry in the mouse. *Cell*, 114:61–73, 2003.
- [112] C. McManus. *Right Hand, Left Hand*. Weidenfeld & Nicholson, 2002.

- [113] N.H. Mendelson. *Bacillus subtilis* macrofibres, colonies, and bioconvection patterns use different strategies to achieve multicellular organization. *Environ. Microbiol.*, 1:420423, 1999.
- [114] M. Mercola. Left–right asymmetry: Nodal points. *J. Cell Sci.*, 116:3251–3257, 2003.
- [115] G. Metcalfe and J. M. Ottino. Autocatalytic processes in mixing flows. *Phys. Rev. Lett.*, 72:2875–2878, 1994.
- [116] I. Mezić and S. Wiggins. On the integrability and perturbation of three-dimensional fluid flows with symmetry. *J. Nonlinear Sci.*, 4:157–94, 1994.
- [117] E. E. Michaelides. Review — the transient equation of motion for particles, bubbles, and droplets. *J. Fluids Eng.*, 119:233–247, 1997.
- [118] H. K. Moffatt. *J. Fluid Mech.*, 18:1–18, 1964.
- [119] A. E. Motter and P. S. Letelier. *Phys.Lett.A*, 285:127, 2001.
- [120] T. Muller, A. Gerardino, T. Schnelle, S. G. Shirley, F. Bordoni, G. De Gasperis, R. Leoni, and G. Fuhr. *J. Phys. D*, 29:340, 1996.
- [121] S. E. Newhouse, D. Ruelle, and F. Takens. Occurrence of strange axiom A attractors near quasiperiodic flows on  $T^m$ ,  $m \geq 3$ . *Commun. Math. Phys.*, 64:35–40, 1978.
- [122] S. Nonaka, H. Shiratori, Y. Saijoh, , and N. Hirokawa. Determination of left–right patterning of the mouse embryo by artificial nodal flow. *Nature*, 418:96–99, 2002.
- [123] S. Nonaka, Y. Tanaka, Y. Okada, S. Takeda, A. Harada, Y. Kanai, M. Kido, and N. Hirokawa. Randomization of left–right asymmetry due to loss of nodal cilia generating leftward flow of extraembryonic fluid in mice lacking KIF3B motor protein. *Cell*, 95:829–837, 1998.
- [124] S. Nonaka, S. Yoshiba, T. Goto, W. Marshall, and H. Hamada. de novo formation of left-right asymmetry by posterior tilt of nodal cilia. *submitted*, 2005.

- [125] H. E. Nusse and J. A. Yorke. *Physica D*, 36:137, 1989.
- [126] J. Nývlt, O. Söhnle, M. Matuchová, and M. Broul. *The Kinetics of Industrial Crystallization*. Elsevier, 1985.
- [127] Y. Okada, S. Nonaka, Y. Tanaka, Y. Saijoh, H. Hamada, and N. Hirokawa. Abnormal nodal flow precedes situs inversus in *iv* and *inv* mice. *Mol. Cell*, 4:459–468, 1999.
- [128] Y. Okada, S. Takeda, Y. Tanaka, J. C. Izpisa Belmonte, and N. Hirokawa. Mechanism of nodal flow: A conserved symmetry breaking event in left-right axis determination. *Cell*, 121:633–644, 2005.
- [129] A. Okubo. Horizontal dispersion of floating particles in the vicinity of velocity singularities such as convergencies. *Deep-Sea Res.*, 17:445–454, 1970.
- [130] C. W. Oseen. *Neuere Methoden und Ergebnisse in der Hydrodynamik*. Leipzig: Akad.-Verlag., 1927.
- [131] G. O’Toole, H. B. Kaplan, and R. Kolter. *Annu. Rev. Microbiol.*, 54:49–79, 2000.
- [132] E. Ott and J.C. Sommerer. Blowout bifurcations: the occurrence of riddled basins and on-off intermittency. *Phys. Lett. A*, 188:39, 1994.
- [133] J. M. Ottino. *The Kinematics of Mixing: Stretching, Chaos, and Transport*. Cambridge University Press, 1989.
- [134] S. Park, P. M. Wolanin, E. A. Yuzbashyan, P. Silberzan, J. B. Stock, and R. H. Austin. *Science*, 301:188, 2003.
- [135] L. Pasteur. *Compt. Rend.*, 26:535, 1848.
- [136] G. J. Pazour and G. B. Witman. The vertebrate primary cilium is a sensory organelle. *Curr. Opin. Cell Biol.*, 15:105–110, 2003.
- [137] T. J. Pedley and J. O. Kessler. Hydrodynamic phenomena in suspensions of swimming micro-organisms. *Annu. Rev. Fluid Mech.*, 24:313–358, 1992.

- [138] D. Perugini, G. Poli, and G. D. Gatta. Analysis and simulation of magma mixing processes in 3d. *Lithos*, 65:313–330, 2002.
- [139] R. Pethig, Y. Huang, X. B. Wang, and J. P. H Burt. *J. Phys. D*, 24:881, 1992.
- [140] R. Philips. *Crystals, Defects and Microstructures*. Cambridge University Press, 2001.
- [141] R. T. Pierrehumbert. Tracer microstructure in the large-eddy dominated regime. *Chaos, Solitons and Fractals*, 4:1091, 1994.
- [142] O. Piro and M. Feingold. Diffusion in three-dimensional Liouvillian maps. *Phys. Rev. Lett.*, 61:1799–802, 1988.
- [143] J.R. Platt. Bioconvection patterns in cultures of freeswimming organisms. *Science*, 133:17661767, 1961.
- [144] N. Platt, S.M. Hammel, and J.F. Heagy. Effects of additive noise on on-off intermittency. *Phys. Rev. Lett.*, 72:3498, 1994.
- [145] N. Platt, E.A. Spiegel, and C. Tresser. On-off intermittency: A mechanism for bursting. *Phys. Rev. Lett.*, 70:279, 1993.
- [146] M.S. Plesset and H. Winet. Bioconvection patterns in swimming microorganism cultures as an example of rayleigh-taylor instability. *Nature*, 248:441–443, 1974.
- [147] H. A. Pohl. *Dielectrophoresis*. Cambridge University Press, 1978.
- [148] S. A. Poisson. Memoire sur les mouvements simultanes d’ un pendule et de l’ air environnant. *Mem. de l’ Academie des Sciences*, 9:521–523, 1831.
- [149] B. Protas, A. Babiano, and N. K.-R. Kevlahan. On geometrical alignment properties of two-dimensional forced turbulence. *Physica D*, 128:169–179, 1999.
- [150] A. Provenzale. Transport by coherent barotropic vortices. *Annu. Rev. Fluid Mech.*, 31:55–93, 1999.



- [151] E. M. Purcell. Life at low Reynolds number. *Am. J. Phys.*, 45:3–11, 1977.
- [152] R.-Y. Qian and G. D. Botsaris. A new mechanism for nuclei formation in suspension crystallizers: The role of interparticle forces. *Chem. Eng. Sci.*, 52:3429–3440, 1997.
- [153] R.-Y. Qian and G. D. Botsaris. Nuclei breeding from a chiral crystal seed of  $\text{NaClO}_3$ . *Chem. Eng. Sci.*, 53:1745–1756, 1998.
- [154] A. Ramos, H. Morgan, N. G. Green, and A. Castellanos. *J.Phys.D: Appl.Phys.*, 31:2338, 1998.
- [155] J. M. Ribó, J. Crusats, F. Sagués, J. Claret, and R. Rubires. Chiral sign induction by vortices during the formation of mesophases in stirred solutions. *Science*, 292:2063–2066, 2001.
- [156] W. M. Roberts, J. Howard, and A. J. Hudspeth. Hair cells: Transduction, tuning, and transmission in the inner ear. *Annu. Rev. Cell Biol.*, 4:63–92, 1988.
- [157] D. Ruelle and F. Takens. On the nature of turbulence. *Commun. Math. Phys.*, 20:167–192, 1971. **23**, 343–344.
- [158] W. B. Russel, D. A. Saville, and W. R. Schowalter. *Colloidal Dispersions*. Cambridge University Press, 1989.
- [159] R. A. Satnoianu, P. K. Maini, and M. Menzinger. Parameter space analysis, pattern sensitivity and model comparison for Turing and stationary flow-distributed waves (FDS). *Physica D*, 160:79–102, 2001.
- [160] J. Schneider and T. Tél. *Ocean Dynamics*, 53:64, 2003.
- [161] J. Schneider, T. Tél, and Z. Neufeld. Dynamics of 'leaking' hamiltonian systems. *Phys. Rev. E*, 66:066218, 2002.
- [162] G. W. Sears. Fibrous growth of  $\text{NaClO}_3$ . *J. Chem. Phys.*, 26:1549–1552, 1957.
- [163] H. S. Sim and H. Schomerus. *Phys.Rev.Lett.*, 89:066801, 2002.

- [164] C. D. Stern. Fluid flow and broken symmetry. *Nature*, 418:29–30, 2002.
- [165] G. G. Stokes. On the effect of the internal friction of fluids on the motion of a pendulum. *Transactions Cambridge Phil. Society*, 9:8–106, 1851.
- [166] H. Stommel. *J. of Marine Research*, 8:24–29, 1949.
- [167] H. Stommel. *Weather*, pages 72–74, 1951.
- [168] R. F. Strickland-Constable. *Kinetics and Mechanisms of Crystallisation*. Academic Press, 1968.
- [169] D. M. Supp, S. S. Potter, and M. Brueckner. Molecular motors: the driving force behind mammalian left–right development. *Trends in Cell Biol.*, 10:41–45, 2000.
- [170] P. D. Swanson and J. M. Ottino. A comparative computational and experimental study of chaotic mixing of viscous fluids. *J. Fluid Mech.*, 213:227–49, 1990.
- [171] J. Szurgot and M. Szurgot. On the nature of growth hillocks on sodium chlorate crystals. *Cryst. Res. Technol.*, 29:829–836, 1994.
- [172] M. Szurgot and J. Szurgot. Chiral symmetry breaking in sodium chlorate crystallization from unstirred solution. *Cryst. Res. Technol.*, 30:949–956, 1995.
- [173] C. J. Tabin and K. J. Vogan. A two-cilia model for vertebrate left–right axis specification. *Genes and Dev.*, 17:1–6, 2003.
- [174] Y. Tanaka, Y. Okada, and N. Hirokawa. Fgf-induced vesicular release of sonic hedgehog and retinoic acid in leftward nodal flow is critical for leftright determination. *Nature*, 435:172 – 177, 2005.
- [175] P. Tanga and A. Provenzale. Dynamics of advected tracers with varying buoyancy. *Physica D*, 76:202–215, 1994.
- [176] B.L. Taylor, I.B. Zhulin, and M.S. Johnson. Aerotaxis and other energy-sensing behavior in bacteria. *Annu. Rev. Microbiol.*, 53:103–128, 1999.

- [177] G. I. Taylor. *Low Reynolds Number Flow*. Educational Services Incorporated, 1960. (16 mm film).
- [178] A. Thyagaraja and F. A. Haas. Representation of volume-preserving maps induced by solenoidal vector fields. *Phys. Fluids*, 28:1005–7, 1985.
- [179] J. Torgersen. Situs inversus, asymmetry and twinning. *Am. J. Human Genetics*, 2:361–370, 1950.
- [180] Z. Toroczkai, G. Károlyi, A. Péntek, T. T, and C. Grebogi. Advection of active particles in open chaotic flows. *Phys. Rev. Lett.*, 80:500–503, 1998.
- [181] A. M. Turing. The chemical basis of morphogenesis. *Phil. Trans. Roy. Soc. Lond. B*, 237:37–72, 1952.
- [182] S. C. Venkataramani, B. R. Hunt, and E. Ott. Bubbling transition. *Phys. Rev. E*, 54:1346, 1996.
- [183] S.C. Venkataramani, T.M. Antonsen, E. Ott, and J.C. Sommerer. Characterization of on-off intermittent time series. *Phys. Lett. A*, 207:173, 1995.
- [184] C. Viedma. Experimental evidence of chiral symmetry breaking in crystallization from primary nucleation. *J. Cryst. Growth*, 261:118–121, 2004.
- [185] C. Viedma. Chiral symmetry breaking during crystallization: Complete chiral purity induced by nonlinear autocatalysis and recycling. *Phys. Rev. Lett.*, 94 (6):65504, 2005.
- [186] K. J. Vogan and C. J. Tabin. A new spin on handed symmetry. *Nature*, 397:295–298, 1999.
- [187] H. Wager. On the effect of gravity upon the movements and aggregation of euglena viridis, ehrb., and other micro-organisms. *Phyl. Trans. R. Soc. Lond. B*, 201:333–390, 1911.
- [188] G. H. Wannier. A contribution to the hydrodynamics of lubrication. *Quart. Appl. Math.*, 8:1–32, 1950.

- [189] J. B. Weiss. The dynamics of enstrophy transfer in two-dimensional hydrodynamics. *Physica D*, 48:273–294, 1991.
- [190] J. Whitfield. Embryos grow with the flow. *Nature Sci. Update*, 4 July 2002.
- [191] S. Wiggins. *Normally hyperbolic invariant manifolds in dynamical systems*. Springer–Verlag, 1994.
- [192] A. N. Yannacopoulos, G. Rowlands, and G. P. King. Influence of particle inertia and Basset force on tracer dynamics: Analytical results in the small-inertia limit. *Phys. Rev. E*, 55:4148–4157, 1997.

# Declaration

This dissertation is an account of research undertaken in the Department of Interdisciplinary Physics within the Mediterranean Institute for Advanced Studies, UIB–CSIC, during the period August 2001 to July 2005. Much of the research described in this thesis was carried out in collaboration with other workers. None of the work presented in this thesis has been submitted to any other institution for any degree.



# List of publications arising from this thesis:

- AUTHORS: J. H. E. Cartwright, M. O. Magnasco, O. Piro, & I. Tuval.  
TITLE: “Noise-induced order out of chaos by bailout embedding”.  
REF. JOURNAL/BOOK: Fluctuation & Noise Lett. **2**, 161–174, 2002.  
KEY: A
- AUTHORS: J. H. E. Cartwright, M. O. Magnasco, O. Piro, & I. Tuval.  
TITLE: “Bailout embeddings and neutrally buoyant particles in three-dimensional flows”.  
REF. JOURNAL/BOOK: Phys. Rev. Lett. **89**, 264501, 2002. KEY: A
- AUTHORS: J. H. E. Cartwright, M. O. Magnasco, O. Piro, & I. Tuval.  
TITLE: “Bubbling and on–off intermittency in bailout embeddings”.  
REF. JOURNAL/BOOK: Phys. Rev. E. **68**, 016217, 2003. KEY: A
- AUTHORS: O. Piro, & I. Tuval.  
TITLE: “Bailout embedding as a Blowout bifurcation”.  
REF. JOURNAL/BOOK: Prog. Th. Phys. Supp. **150**, 465, 2003. KEY: A
- AUTHORS: I. Tuval, J. Schneider, O. Piro, & T. Tél.  
TITLE: “Opening up Fractal Structures of Three Dimensional Flows via Leaking.”.  
REF. JOURNAL/BOOK: Europhys. Lett. **65**, **5**, 633, 2004. KEY: A
- AUTHORS: J. H. E. Cartwright, O. Piro, & I. Tuval.  
TITLE: “Fluid-dynamical basis of the embryonic development of left right asymmetry in vertebrates”.  
REF. JOURNAL/BOOK: PNAS **101**, **19**, 7234, 2004. KEY: A
- AUTHORS: J. H. E. Cartwright, J. M. García-Ruiz, O. Piro, C. I. Sainz-Díaz & I. Tuval.  
TITLE: “Chiral Symmetry Breaking during Crystallization: An Advection-Mediated Nonlinear Autocatalytic Process”.  
REF. JOURNAL/BOOK: Phys. Rev. Lett. **93**, **3**, 035502, 2004. KEY: A

- **AUTHORS:** I. Tuval, L. Cisneros, C. Dombrowski, C. W. Wolgemuth, J. O. Kessler, & R. E. Goldstein.  
**TITLE:** “Bacterial Swimming and Oxygen Transport Near Contact Lines”.  
**REF. JOURNAL/BOOK:** PNAS **102**, **7**, 2277, 2005. **KEY:** A
- **AUTHORS:** I. Tuval, I. Mezic, & O. Piro.  
**TITLE:** “Control of particles in micro-electrode devices”.  
**REF. JOURNAL/BOOK:** Submitted. **KEY:** A



# Dedication

I wish to dedicate this thesis to my family; Efrat, Iosi, Mario, Flaminia, Ana, Naama, Maia, Natalia, Paloma, Noam, Diana, Galia, Yael, Tomas, Nico, Elinor, Ionatan, Anael, Cati, Dani, Monica, Pato and Carmina.



---

---

**CURRICULUM VITAE**

---

Idan  
Tuval Guefen

Version of September 2004

---

---

## CURRICULUM VITAE

---

---

SURNAME: Tuval Guefen

DATE OF BIRTH: 19 November 1976

PLACE OF BIRTH: Petah Tikvah (ISRAEL)

SEX: Male

FIRST NAMES: Idan

NATIONALITY: Spanish

---

### ACADEMIC INFORMATION

#### 1st DEGREE:

Master degree in Physics (September 2000) University of Zaragoza, Spain

#### DOCTORATE:

Ph.D. in Physics (in progress)

THESIS ADVISOR:

IMEDEA (UIB-CSIC)

Dr. Oreste Piro

---

### PROFESSIONAL SITUATION:

FPI Pre-doctoral Fellowship with IMEDEA (CSIC-UIB), from August 2001.

POSTAL ADDRESS: IMEDEA (CSIC-UIB),  
Edificio Mateu Orfila, Campus UIB,  
E-07122 Mallorca, Spain.

TELEPHONE: +34 971 172536

FAX: +34 971 173426

EMAIL: [idan@imedea.uib.es](mailto:idan@imedea.uib.es)

WWW: <http://imedea.uib.es/~idan>

---

### FOREIGN LANGUAGES

Fluent Hebrew and english, plus some Italian.

---

---

---

## PUBLICATIONS

---

KEY: B=Book; BC=Book Chapter; A=Article; R=Review; E=Editor

---

### Published in refereed journals

- AUTHORS: J. H. E. Cartwright, M. O. Magnasco, O. Piro, & I. Tuval.  
TITLE: "Noise-induced order out of chaos by bailout embedding".  
REF. JOURNAL/BOOK: Fluctuation & Noise Lett. **2**, 161–174, 2002. KEY: A
  
- AUTHORS: J. H. E. Cartwright, M. O. Magnasco, O. Piro, & I. Tuval.  
TITLE: "Bailout embeddings and neutrally buoyant particles in three-dimensional flows".  
REF. JOURNAL/BOOK: Phys. Rev. Lett. **89**, 264501, 2002. KEY: A
  
- AUTHORS: J. H. E. Cartwright, M. O. Magnasco, O. Piro, & I. Tuval.  
TITLE: "Bubbling and on–off intermittency in bailout embeddings".  
REF. JOURNAL/BOOK: Phys. Rev. E. **68**, 016217, 2003. KEY: A
  
- AUTHORS: O. Piro, & I. Tuval.  
TITLE: "Bailout embedding as a Blowout bifurcation".  
REF. JOURNAL/BOOK: Prog. Th. Phys. Supp. **150**, 465, 2003. KEY: A
  
- AUTHORS: I. Tuval, J. Schneider, O. Piro, & T. Tél.  
TITLE: "Opening up Fractal Structures of Three Dimensional Flows via Leaking".  
REF. JOURNAL/BOOK: Europhys. Lett. **65**, **5**, 633, 2004. KEY: A
  
- AUTHORS: J. H. E. Cartwright, O. Piro, & I. Tuval.  
TITLE: "Fluid-dynamical basis of the embryonic development of left right asymmetry in vertebrates".  
REF. JOURNAL/BOOK: PNAS **101**, **19**, 7234, 2004. KEY: A
  
- AUTHORS: J. H. E. Cartwright, J. M. García-Ruiz, O. Piro, C. I. Sainz-Díaz & I. Tuval.  
TITLE: "Chiral Symmetry Breaking during Crystallization: An Advection-Mediated Nonlinear Autocatalytic Process".  
REF. JOURNAL/BOOK: Phys. Rev. Lett. **93**, **3**, 035502, 2004. KEY: A

- AUTHORS: I. Tuval, L. Cisneros, C. Dombrowski, C. W. Wolgemuth, J. O. Kessler, and R. E. Goldstein.  
TITLE: "Bacterial Swimming and Oxygen Transport Near Contact Lines".  
REF. JOURNAL/BOOK: PNAS **102**, 7, 2277, 2005. KEY: A

### Submitted

- AUTHORS: I. Tuval, I. Mezic and O. Piro.  
TITLE: "Control of particles in micro-electrode devices." KEY: A

---

## CONFERENCE COMMUNICATIONS

---

- TYPE OF PARTICIPATION: Talk: 'Right Hand–Left Hand'.  
AUTHORS: J. H. E. Cartwright, O. Piro, & **I. Tuval**.  
CONFERENCE: Dynamics Days 2004.  
PLACE: Mallorca, Spain. YEAR: 2004
- TYPE OF PARTICIPATION: Talk : 'Electrothermal flow effects in dielectrophoresis'.  
AUTHORS: I. Mezic, O. Piro, & **I. Tuval**.  
CONFERENCE: APS Division of Fluid Dynamics 56th Annual Meeting 2003.  
PLACE: New Jersey, USA. YEAR: 2003
- TYPE OF PARTICIPATION: Poster: 'Inertial effects in 3D flows'.  
AUTHORS: J. H. E. Cartwright, M. O. Magnasco, O. Piro, & **I. Tuval**.  
CONFERENCE: FISES 2003.  
PLACE: Pamplona, Spain. YEAR: 2003
- TYPE OF PARTICIPATION: Poster: 'Bubbling and on–off intermittency in bailout embeddings'.  
AUTHORS: J. H. E. Cartwright, M. O. Magnasco, O. Piro, & **I. Tuval**.  
CONFERENCE: Dynamics Days 2003.  
PLACE: Mallorca, Spain. YEAR: 2003
- TYPE OF PARTICIPATION: Talk: 'Inertial effects in 3D flows'.  
AUTHORS: J. H. E. Cartwright, M. O. Magnasco, O. Piro, & **I. Tuval**.  
CONFERENCE: SIAM Conference on Applications of Dynamical Systems.  
PLACE: Utah, USA. YEAR: 2003

- TYPE OF PARTICIPATION: Talk: 'From the dynamics of Neutrally Bouyant Particles to the control of chaos'.

AUTHORS: J. H. E. Cartwright, M. O. Magnasco, O. Piro, & **I. Tuval**.

CONFERENCE: Workshop on "Dynamical Systems Methods in Mixing".

PLACE: Santa Barbara, USA. YEAR: 2003
- TYPE OF PARTICIPATION: Poster: 'Bailout embeddings and neutrally buoyant particles in three-dimensional flows'.

AUTHORS: J. H. E. Cartwright, M. O. Magnasco, O. Piro, & **I. Tuval**.

CONFERENCE: Non-Equilibrium Phenomena and Phase Transition in Complex Systems.

PLACE: Ávila, Spain. YEAR: 2002
- TYPE OF PARTICIPATION: Talk: 'Bailout embeddings and neutrally buoyant particles in three-dimensional flows'.

AUTHORS: J. H. E. Cartwright, M. O. Magnasco, O. Piro, & **I. Tuval**.

CONFERENCE: Let's Face Chaos through Nonlinear Dynamics.

PLACE: Maribor, Slovenia. YEAR: 2002
- TYPE OF PARTICIPATION: Talk: 'Fluid-dynamical basis of the embryonic development of left right asymmetry in vertebrates'.

AUTHORS: **J. H. E. Cartwright**, M. O. Magnasco, O. Piro, & I. Tuval.

CONFERENCE: FISES 2003.

PLACE: Pamplona, Spain. YEAR: 2003
- TYPE OF PARTICIPATION: Talk: 'Bailout embeddings for the control of hamiltonian chaos, and the distribution of small particles in fluid flows'.

AUTHORS: **J. H. E. Cartwright**, M. O. Magnasco, O. Piro, & I. Tuval.

CONFERENCE: Dynamics Days 2002.

PLACE: Heidelberg, Germany. YEAR: 2002
- TYPE OF PARTICIPATION: Talk: 'Inhomogeneity induced by noise: the distribution of small spherical particles swimming at random in a fluid flow'.

AUTHORS: **J. H. E. Cartwright**, M. O. Magnasco, O. Piro, & I. Tuval.

CONFERENCE: FisEs 2002.

PLACE: Tarragona, Spain. YEAR: 2002
- TYPE OF PARTICIPATION: Talk: 'Bailout embedding: A novel targetting method for KAM tori with safe forward convergence'.

AUTHORS: J. H. E. Cartwright, M. O. Magnasco, **O. Piro**, & I. Tuval.

CONFERENCE: Workshop on Hamiltonian Dynamical Systems.

PLACE: Imperial College, London, England.

YEAR: 2002

- TYPE OF PARTICIPATION: Talk: 'Structures Induced by noise and inertia in the distributions of small neutrally buoyant bodies randomly swimming in fluid flows'.

AUTHORS: J. H. E. Cartwright, M. O. Magnasco, **O. Piro**, & I. Tuval.

CONFERENCE: NoLineal 2002.

PLACE: Cuenca, Spain.

YEAR: 2002

- TYPE OF PARTICIPATION: Talk: 'The dynamics of finite size impurities in time-dependent three-dimensional incompressible flows'.

AUTHORS: J. H. E. Cartwright, M. O. Magnasco, **O. Piro**, & I. Tuval.

CONFERENCE: XXVII General Assembly de la European Geophysical Society..

PLACE: Nice, France.

YEAR: 2002

- TYPE OF PARTICIPATION: Talk: 'The emergence of structures due to noise and inertia in the distribution of finite size impurities driven by chaotic flows'.

AUTHORS: J. H. E. Cartwright, M. O. Magnasco, **O. Piro**, & I. Tuval.

CONFERENCE: International Seminar and Workshops on Chemical and Biological Activity in Flows.

PLACE: Dresden, Germany.

YEAR: 2002

- TYPE OF PARTICIPATION: Poster: 'Noise and inertia-induced inhomogeneity in the distribution of small particles in fluid flows'.

AUTHORS: **J. H. E. Cartwright**, M. O. Magnasco, **O. Piro**, & I. Tuval.

CONFERENCE: XXVII General Assembly de la European Geophysical Society..

PLACE: Nice, France.

YEAR: 2002

---

## SCHOOLS AND CONFERENCES ATTENDED

---

- CONFERENCE: MASSES: Mechanics and Symmetry Euro Summer School.  
PLACE: Peyresq, France. YEAR: September 2001



- CONFERENCE: Dinamiques no lineals d'autoorganitzacio espaciotemporal.  
PLACE: Barcelona, Spain. YEAR: Februar 2002
  - CONFERENCE: Let's Face Chaos through Nonlinear Dynamics.  
PLACE: Maribor, Slovenia. YEAR: July 2002
  - CONFERENCE: Non-Equilibrium Phenomena and Phase Transition in Complex Systems.  
PLACE: Ávila, Spain. YEAR: September 2002
  - CONFERENCE: SIAM Conference on Applications of Dynamical Systems.  
PLACE: Utah, USA. YEAR: May 2003
  - CONFERENCE: Dynamics Days 2003.  
PLACE: Mallorca, Spain. YEAR: September 2003
  - CONFERENCE: FISES 2003.  
PLACE: Pamplona, Spain. YEAR: October 2003
  - CONFERENCE: APS Division of Fluid Dynamics 56th Annual Meeting 2003.  
PLACE: New Jersey, USA. YEAR: November 2003
  - CONFERENCE: Recent Trends in Nonlinear Science.  
PLACE: Mallorca, Spain. YEAR: Februar 2004
  - CONFERENCE: Dynamics Days 2004.  
PLACE: Mallorca, Spain. YEAR: September 2004
- 
-

---

## SCIENTIFIC AND TECHNICAL ACTIVITIES

---

### Seminars given:

- TITLE: 'Bailout embeddings and neutrally buoyant particles in three-dimensional flows'.  
PLACE: IMEDEA, MALLORCA. YEAR: 2002
- TITLE: 'Right Hand–Left Hand'.  
PLACE: IMEDEA, MALLORCA. YEAR: 2004

### Stays at other institutes:

- PLACE: Dynamical Systems and Control Group, Department of Mechanical Engineering, University of California, Santa Barbara  
PERIOD: May 2003-September 2003
  - PLACE: Department of Physics, The University of Arizona, Tucson  
PERIOD: May 2004-September 2004
  - PLACE: Dynamical Systems and Control Group, Department of Mechanical Engineering, University of California, Santa Barbara  
PERIOD: June 2004
  - PLACE: Laboratory of Mathematical Physics,  
The Rockefeller University, New York. PERIOD: August 2004
- 
-